Investigating the Photophysics of Quantum Dot and Rare-Earth Doped Ferroelectric Thin Films

by

Rafaela Mendes Brinn

A dissertation submitted in partial satisfaction of the

requirements for the degree of

Doctor of Philosophy

in

Chemistry

in the

Graduate Division

of the

University of California, Berkeley

Committee in charge:

Professor A. Paul Alivisatos, Co-chair
Professor Ramamoorthy Ramesh, Co-chair
Professor Naomi Ginsberg
Professor Alexander Katz

Spring 2024

Investigating the Photophysics of Quantum Dot and Rare-Earth Doped Ferroelectric Thin Films

Abstract

Investigating the Photophysics of Quantum Dot and Rare-Earth Doped Ferroelectric Thin Films

by

Rafaela Mendes Brinn

Doctor of Philosophy in Chemistry

University of California, Berkeley

Professor A. Paul Alivisatos, Co-chair

Professor Ramamoorthy Ramesh, Co-chair

This dissertation is composed of 7 chapters discussing optical studies performed in thin film samples. These studies are separated in two parts. Part I focuses on studies performed on quantum dot monolayer thin films while Part II discusses work on erbium doped ferroelectric thin films. Part I will have 4 chapters: Chapter 1 is an introductory chapter on quantum dots' structural and optical properties, Chapter 2 is a quantitative study on the recombination rates of QD thin films with different shell thicknesses, Chapter 3 will discuss incorporation of atomic dopants to engineer quantum dots of a specific size and energy and finally Chapter 4 will provide a brief conclusion on the work done as well as outlook on future avenues of controlling the photophysics of QD thin film. Part II will have 3 additional chapters: Chapter 5 will expand on fundamental concepts of rare-earth doped ferroelectric thin films, Chapter 6 will contain a study on tuning erbium emission via epitaxial strain engineering of the ferroelectric thin film matrix and Chapter 7 will contain concluding thoughts on this part of the dissertation and provide outlooks on potential strategies to further manipulate erbium emission. To briefly expand more on the projects discussed in Chapter 2,3,and 6:

In Chapter 2, we measure the photoluminescence quantum yield of self-assembled quantum dot monolayer thin films and quantify their radiative and nonradiative rates. The recombination rates of core/shell quantum dot self-assembled monolayer superlattices are systematically compared to their colloidal solution counterparts. Both the radiative and nonradiative rates of these quantum dots were found to be enhanced in the thin film samples. The increase in nonradiative rate is expected and can be attributed to the stripping of ligands from the nanocrystal surface as well as energy transfer in close-packed solid-state samples. In contrast, the increase in radiative rate in the film reveals a change in the fundamental optical properties of quantum dot films, suggesting that the oscillator strength of

the nanocrystals increases in the films compared to in solution. The increase in oscillator strength is likely due to changes in the organic ligand shell coverage and its effect on the electronic band structure of the quantum dot.

In Chapter 3, we study exciton diffusion lengths in micron-sized superlattices where Te-doped CdSe:Te/CdS nanocrystals serve as the building blocks. These nanocrystals are synthesized colloidally with 5% of Te dopant stoichiometrically added during the seeded growth synthesis of wurtzite CdSe nanocrystals. Through this colloidal synthesis, we can make nanocrystals with a much broader and red-shifted emission than their undoped counterparts, proving that the Te-dopant has been successfully incorporated in the CdSe matrix. A thin hexagonal CdS shell is then grown around the Te-doped CdSe core forming a dot-in-plate (or nut in bolt) shape. Using elemental mapping techniques we characterize the distribution of elements in our CdSe:Te/CdS core/shell nanocrystals. Based on their shape, these nanocrystals can self-assemble into a highly ordered 2D superlattice structure with a heterogeneous energy landscape. Using Stimulated Emission Depletion (STED) microscopy, we measure the exciton diffusion lengths in these superlattices to elucidate the role of the Te-dopant in transport.

In Chapter 6, we discuss how erbium doped materials are powerful candidates for quantum information sciences due to their long electron and nuclear spin coherence times, as well as telecom-wavelength emission. By selecting host materials with interesting, controllable properties, we introduce a new parameter that can be used to study Er^{3+} emission. In this work, we study erbium (Er^{3+})-doped $PbTiO_3$ thin films. $PbTiO_3$ is a well-studied ferroelectric material with known methods of engineering different domain configurations through epitaxial strain. Through changing the domain configurations of the $PbTiO_3$ thin films, we create radically different crystal fields around the Er^{3+} dopant. This is resolved through changes in the Er^{3+} resonant fluorescence spectra, tying the optical properties of the defect directly to the domain configurations of the ferroelectic matrix. Additionally, a second set of peaks are observed for films with in-plane polarization. We hypothesize these results to be due to either the Er^{3+} substituting different sites of the $PbTiO_3$ crystal or due to differences in charges between the Er^{3+} dopant and the original substituent ion. Understanding the relationship between the Er^{3+} emission and the epitaxial strain of the ferroelectric matrix lays the pathway for future optical studies of spin manipulation through altering ferroic order parameters.

To my family and friends

Thank you for your endless support through this process

&

To Cronk the cat for making sure I got plenty of breaks while writing this Dissertation.

Contents

List of Figures

List of Tables

Acknowledgments

For the last half a decade I have split my time between the Hildebrand Hall dungeon and the Imaging Facilities up the hill at the Molecular Foundry making samples, collecting data, and designing experiments. This journey was extraordinarily tumultuous due to a worldwide pandemic starting in March of my first year shortly followed by not one but both of my research advisers leaving UC Berkeley for jobs at different universities. Although at times this process felt very isolating, I want to acknowledge all the people that helped me along the way to get to this point in my career.

During my first semester, I took Quantum Mechanics and Thermodynamics and Statistical Mechanics as well as taught Chem 4A. I would like to thank Can Uzundal, Jon Fernandes, Ryan Reynolds, Juanes Arias-Martinez, Erika Riffe, David Bain, Eric Haugen, Brittany Stinger and Angelique Amado for all the long hours we spent on problem sets–either doing them or grading them. I'm thankful that we were able to continue our friendship beyond that initial semester. I truly appreciate all the Warriors games I went with Can, the coffees I grabbed with Jon, the movies I watched with Ryan, the bike rides I went with Juan and the badminton I played with David, Eric, and Erika. I want to especially thank Brittany Stinger who not only started this journey with me but also was a wonderful roommate for our first 4 years and neighbor for our last year in the program. I am incredibly grateful for our friendship and all the memories we made in 1327 MLK Way.

Shortly after arriving at Berkeley, I found a home in the Alivisatos research group. I would first off like to thank Professor Paul Alivisatos for giving me the opportunity to learn and do research in the lab space where so many great minds got their start. I appreciate the conversation I had on the first day of orientation with Dr. Ethan Curling and Dr. Priscilla Pieters where they convinced me to join the group. I ended up officially joining a couple months later with Han Lee and Sam Gleason who became great friends throughout this process. Once I started in the group, I received great mentorship from Dr. Justin Ondry and Professor Chang Yan, from whom I learned so much. When things in lab were not always working, I am thankful to have my Self-Assembly Subgroup (SASies) to talk science and brainstorm ideas with Dr. Priscilla Pieters and Dr. Abdullah Abbas; it was fun to have a laugh here and there when it felt like the worse of times. I would also like to thank Professor Vida Jamali, Dr. Jakob Dahl, and Dr. Jason Calvin for helpful scientific discussions and career advice. Thank you to Dr. Michelle Crook, Dana Byrne, and Amanda Brewer for our de-stressing craft nights and for hanging up my connect-the-dots and still life art in their offices/homes. I am thankful for collaborations with Professor Naomi Ginsberg and her students Professor Rongfeng Yuan and Dr. Trevor Roberts. It was wonderful to work on such an interesting project with them. Lastly, I would like to thank Negest Williams for making sure I was taken care off financially during my entire time at Berkeley.

Additionally, I am thankful for the conversations I had with Professor Zakaria Al Balushi, Dr. Emory Chang, Dr. Archana Raja, and Dr. Jeff Urban once I learned the Alivisatos group was leaving UC Berkeley. I am incredibly grateful to have ultimately meet Professor Ramamoorthy Ramesh who gave me the opportunity to stay at Berkeley and work on a fascinating research project. I am grateful to have learned so much from members of the Ramesh group: Professor Lucas Caretta, Piush Behera, Pravin Kavle and Dr. Peter Meisenheimer. Peter especially was an incredible, supportive mentor. I am thankful for the opportunity to design and construct a spectroscopy setup in Dr. Archana Raja's lab at the Molecular Foundry and for all of the support I received from Dr. Medha Dandu, Dr. Elyse Barre, Dr. Daria Blach, Dr. Artiom Skripka and Dr. Ed Barnard during the process. Additionally, I would like to thank Professor Paul Stevenson for all of his help getting me to the finish line.

Lastly, I would like to thank the friends I have met at Berkeley: Eva Gerber and Nathan Lin who I sang and danced with at the Eras Tour; Isaac Harris who I could always count on seeing at BERC events; Magan Powell, Nugent Lew and Dr. Saehyun Choi for all the fun game nights. Additionally, I am thankful for my best friends from high school for always checking in on me: Ariel Sabatini, Julie Benbasset, Clecy Romen, and Amrita Mitra. Visiting them over the last 5 years was always a highlight. Thank you to Professor Andrew Crowther who played a key role in my development as a scientist and researcher. And of course, thank you to Alyssa Meurer for being a great partner and listener when I needed to complain the most during the last two and a half years. Last but not least I want to thank my family: Ana and Andrew Brinn, Juliana Brinn and Alda Fernandes Mendes for all of their support and phone calls when I needed them most. The memories I have made in the last 5 years will be cherished forever. I am truly grateful for everyone I meet during graduate school and look forward to seeing all we do next.

Part I

Part One: Photophysics of Quantum Dot Monolayer Thin Films

Chapter 1

Structural and Optical Properties of Quantum Dot Thin Films and Their Electronic Dynamics

1.1 Overview of Quantum Dots

Quantum dots are semiconducting nanocrystals that have size tunable optical properties. This behavior was fairly unexpected since it was assumed that a material's properties are inherently due to its elemental composition. However, when synthesising materials in the nanometer size range, a quantum effect occurs that makes the properties of the material tunable based on their size. The discovery of quantum dots revolutionized the field of semiconductors and nanotechnology. Quantum dots recently gained additional worldwide recognition from the Royal Swedish Academy of Sciences awarding Moungi G. Bawendi, Louis E. Brus and Aleksey I. Ekimov the 2023 Chemistry Noble Prize for the discovery and synthesis of quantum dots.[105]

In the early 1980s in the former Soviet Union, Ekimov was recognized for observing size-dependent quantum effects in copper chloride nanoparticles which he grew in glassy matrices.[54] Alexander Efros used Ekimov's discovery to develop a general theory on the effect of size quantization on optical absorption for a class of semiconductors.[52] A few years later at Bell Laboratories in the United States, Brus was the first scientist to replicate this size-dependent quantum effects in a colloidal solution of cadmium sulfide nanocrystals.[142, 27] Lastly, in 1993 Bawendi with Christopher Murray and David Norris perfected the chemical synthesis of cadmium chalcogenide quantum dots via the hot injection method.[114] The hot injection method allowed for the formation of highly crystalline quantum dots with low defect densities, optical properties, and optimal photostability at room temperature. This allowed quantum dots to be implemented in a myriad of applications. These discoveries laid the foundation for research groups worldwide investigating different size dependent proper-

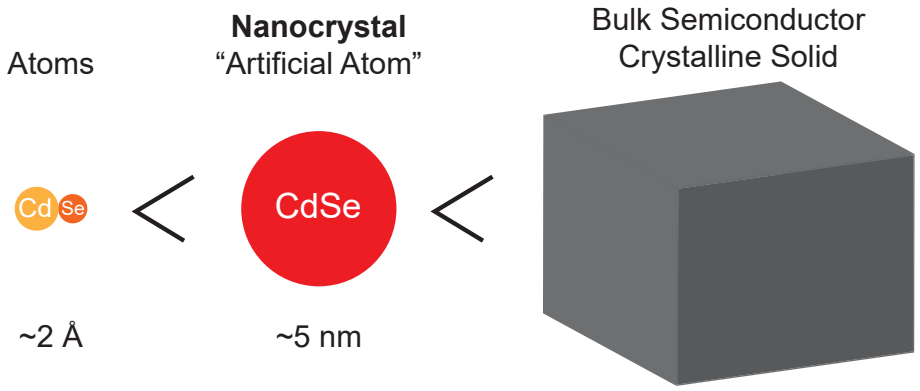

Figure 1.1: **Size comparison of molecular bonds, nanocrystals and bulk materials**

ties and transformations[3], optimizing quantum dot emission efficiency[69] and engineering shape control of nanocrystals[106] and heterostructured nanocrystals.[37]

One of the many reasons quantum dots are interesting materials is because they have discrete energy levels similar to isolated atoms. In the molecular level, two atoms come together to form a molecule with a length scale of a few angstroms. On the opposite side of the material spectrum, bulk crystalline solids are composed of millions of atoms and are often sizes that can be observed by the naked eye. Nanocrystals are composed of a few hundred atoms resulting in sizes in the nanometer regime (Fig. 1.1). Similarly, nanocrystals have an electronic structure with similar components to the atomic scale and bulk semiconductor materials. For that reason they can be thought of as “artificial atoms”. Additionally, they can form superlattices or supercrystals with ordered structural properties where each quantum dot acts like an atom in a solid crystal further making them comparable to atomic species.

In the next few sections, I will delve into the structural and optical properties of quantum dots. Then, I will discuss strategies to create highly ordered mesoscale materials using quantum dots as building blocks. Finally, I will discuss the interesting electronic dynamics that arise from the formation of these structures.

1.2 A Chemist’s View on Semiconductors

As mentioned in the previous section, quantum dots are semiconducting nanocrystals. Before delving into the properties of QDs, let us first discuss semiconductors broadly and how we can connect it to the molecular principles developed in introductory chemistry courses. The

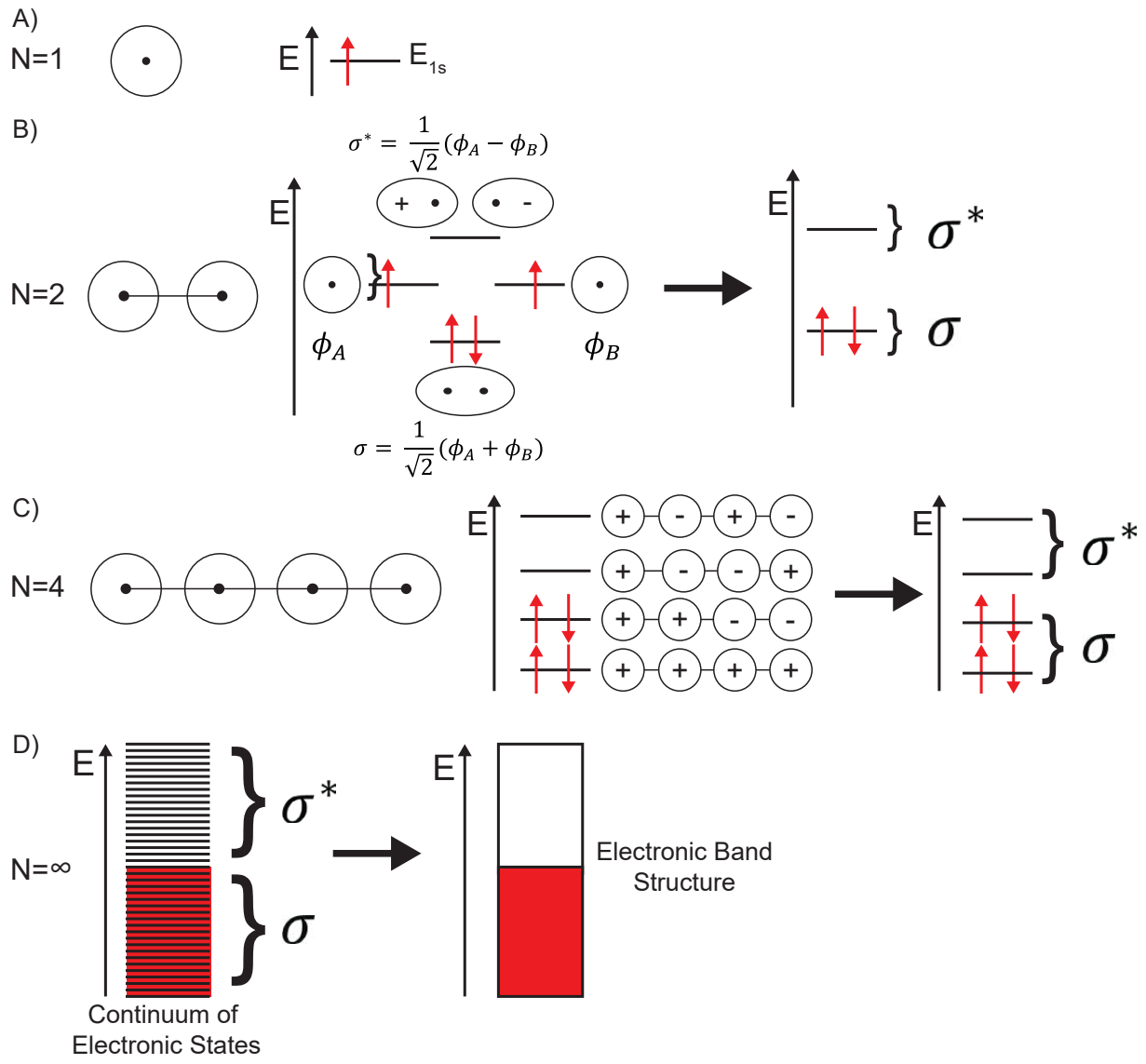

Figure 1.2: **Connecting Molecular Orbital Diagrams to Material Band Structures.** **A** Energy level diagram for N=1 atom. **B** Hybridization of atomic energy levels between N=2 atoms. **C** Energy level diagram for N=4 atoms in a chain. **D** Energy level diagram for $N = \infty$ atoms in a chain. Every atom is assumed to have one electron in its $1s$ orbitals.

foundation of chemistry is understanding how atomic species interact via bonding through the sharing of electrons. If we begin by thinking about bonding from the conventional atomic and molecular wisdom, we can directly translate that knowledge to bulk crystalline solid material.

The simplest way to begin this comparison is to consider a material composed of N atoms in a chain with 1 electron in the $1s$ orbital, similar to Hydrogen. If N=1, the one electron will populate the energy level that corresponds to the $1s$ orbital of that specific atom (Fig. 1.2A). If N=2, the energy levels of the $1s$ orbitals for each atom labeled as Φ_A and Φ_B will hybridize to form what is known as a bonding (σ) and antibonding (σ^*) energy level (Fig. 1.2B). From the Aufbau principle we know that electrons in the ground state will populate lower energy levels first. Hence, in a N=2 molecular orbital diagram both electrons from the atomic $1s$ orbitals populate the lower energy σ molecular energy levels. The σ^* molecular orbital is located at a higher energy because the electron density between the two nuclei in the molecule is less favorable than if the two atoms were not bonded at all. This results in what is known as a node between the two atoms as the molecular orbital changes from positive to negative due to the unequal sharing of electrons. If we add principles of quantum mechanics to the diagram, we can describe the the σ molecular orbital wavefunction as $\sigma = 1/(\sqrt{2})(\Phi_A+\Phi_B)$ and the (σ^*) molecular orbital wavefunction as $\sigma^* = 1/(\sqrt{2})(\Phi_A-\Phi_B)$.

If N= 4, we can have 4 unique hybridized energy levels based on the interactions between the atoms (Fig. 1.2C). For example, the most energetically favorable interaction is if the 4 atoms have a uniform sharing of electrons and no antibonding nodes are present. This configuration will be the lowest energy level in the system. If only one antibonding node exists between the 4 atoms, there are still two favorable bonding interactions between adjacent atoms resulting in the second most energetically favorable configuration. The third lowest energy level is if two antibonding nodes exist between the 4 atoms with only one favorable bonding interaction between the atoms. The most unfavorable and highest energy configuration is if there are antibonding nodes between each atom. Similarly to the N=2 diagram above, the $1s$ electrons will populate the lower energy levels. The populated and unpopulated states in this diagram will be analogous to the bonding σ and antibonding σ^* molecular orbitals respectively.

If $N \to \infty$ then there are an infinite number of hybridized energy levels making up the energy diagram of the system (Fig. 1.2D). These energy levels are so closely spaced together in energy that instead of thinking of them as discrete energy levels, they can be thought of as a continuum of electronic states. The continuum of states is referred to as bands. For our $1s$ orbital example, half of those states will be filled with the electrons from the $N = \infty$ atoms. Those filled states make-up what is known as the valence band, which is analogous to σ orbitals in our molecular orbital diagram. The remaining unpopulated energy states form the conduction band, which is analogous to the σ^* orbitals. Since bulk crystalline solid materials are composed of millions of atoms, instead of thinking about their energy diagram

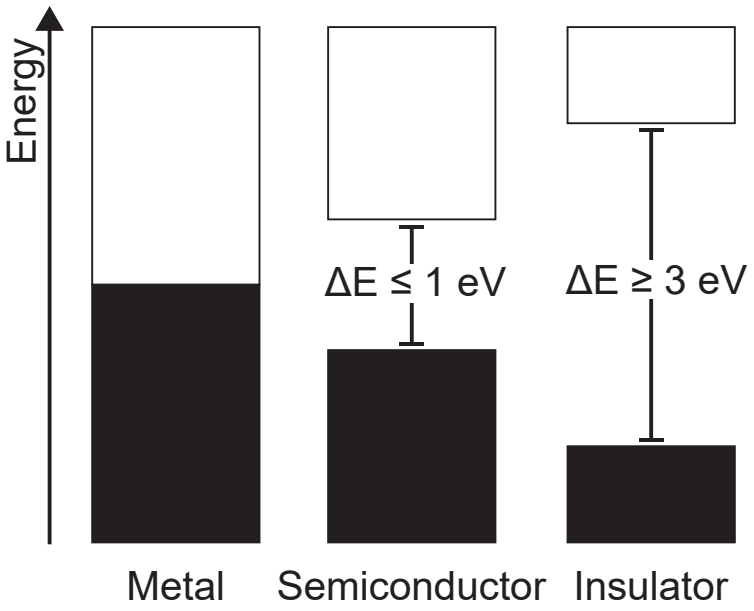

Figure 1.3: **Simplified Band Structure Diagram of Metals, Semiconductors, and Insulators**

as discrete states, we discuss it in the context of their electronic band structure. A similar analysis can also be done with p- and d- orbitals.

The electronic band structure is material dependent and is not always a full continuum of electronic states as represented in Figure 1.2D. Metals like gold and aluminum have an extended band structure where there is no separation between the valence and conduction band edges. For this reason, metals are great conductors because electrons can thermally access higher energy unpopulated states in the conduction band. More relevant to the work discussed in this dissertation, certain materials do not have an extended band structure, but rather have a gap in energy between the valence and conduction band edges. That difference in energy is referred to as the bandgap (ΔE) of the material. If $\Delta E \leq$ 1eV, the material is considered a semiconductor. Common semiconductors are silicon and germanium. If $\Delta E \geq$ 3eV, the material is considered an insulator. Common insulators are rubber and plastic (Fig. 1.3).

The band structure diagram shown in Figure 1.3 provides a qualitative picture of the energy levels however it is not representative of the density of states (DOS) of a material system. The DOS depicts the number of electronic states occupied within a system at a particular energy and temperature. For a 3D bulk crystalline semiconductor, the DOS can be described by a parabolic function (DOS$\propto \sqrt{E}$) where the DOS continuously increases

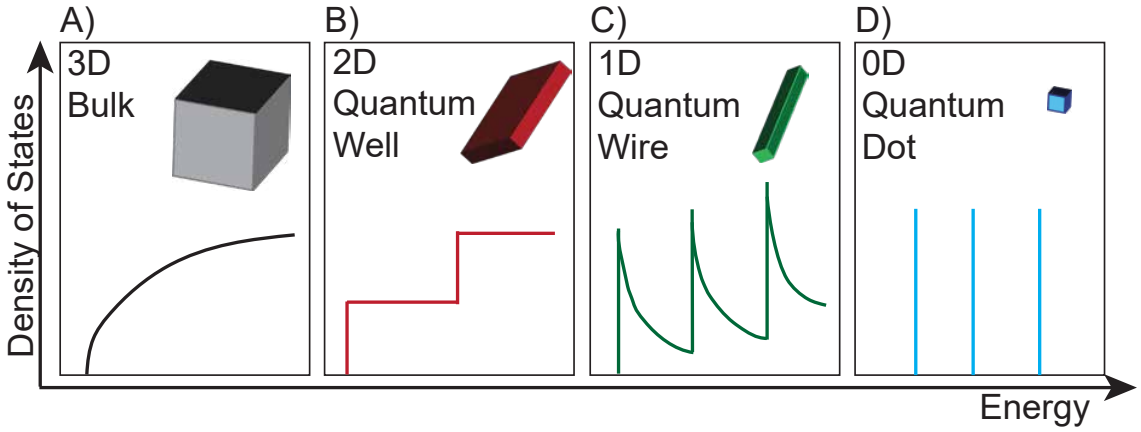

Figure 1.4: **Density of States Diagram for Confined Materials**. Density of State diagrams for **A** 3D Bulk material has no confinement, **B** 2D quantum well is confined in one axis, **C** a 1D quantum wire is confined in two axis and **D** a 0D quantum dots is confined in all axis

with increasing the energy of the system (Fig. 1.4A) If we constrain the degrees of freedom of the electron, the DOS changes quite significantly. A 2D system with the electron motion being confined in one direction can be modeled as a quantum well with its DOS forming a step function that does not depend on energy (DOS$\propto E^0$=constant) (Fig. 1.4B). Due to the quantization of energy in the confined direction, electrons are forced to occupy a planar region. By confining an additional degree of freedom, we have a 1D quantum wire which has a sharp DOS followed by a decay where DOS decreases with increasing energy (DOS$\propto E^{-1/2}$) (Fig. 1.4C). With all 3 degrees of freedom being confined, the result is a 0D quantum dot where electrons have no free motion and its energy is quantized in all three directions resulting in discrete energies similar to molecules which can be described by a delta function (DOS$\propto \delta(E)$) (Fig. 1.4D).[3] Given that quantum dots have some size distribution, the delta function may actually be slightly broadened.

Semiconducting Nanocrystals

Now that we have discussed the general band structure of semiconductor materials, we can begin to discuss how we can tune the electronic structure of nanocrystal due to their quantum phenomenon. As mentioned previously, quantum dots have a few hundred atoms and hence fall in between the size regime of molecules composed of a few atoms and bulk semiconductors that have millions of atoms. We have also discussed how quantum dots have discrete energy levels instead of a continuum of states. We can tune these energy levels by changing the size of the QD. By increasing the size of a QD, more atoms are inevitably

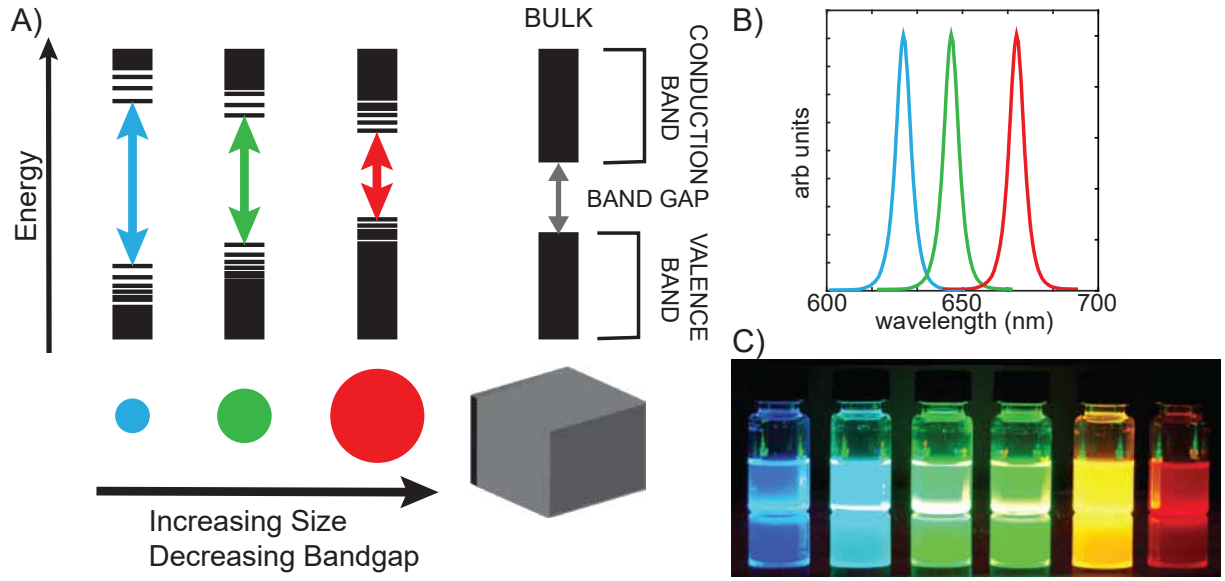

Figure 1.5: **Size Dependent Quantum Effects. A** Diagram of increasing energy gap of quantum dots with size. **B** Emission of quantum dots of different sizes. **C** Quantum dots size can be tunes so they can emit all over the visible range.

present in the material. That means more energy levels and electrons are present in the material system. With additional energy levels, the bandgap of the QD will decrease until the bulk bandgap limit of the material is reached. At this point the quantum confinement no longer occurs, and instead we have the traditional semiconductor band structure (Fig. 1.5A).

Within the size regime where the quantum phenomena effect is true, different QDs of a specific material composition but different sizes will emit at different energies. By changing the bandgap of the material, we change the energy of an electronic transition. We can visualize that change in Figure 1.5B where smaller QDs (blue) emit at higher energy (shorter wavelengths) than larger QDs (red) that emit at lower energy (longer wavelength). For CdSe QDs, in order to have the quantum confinement required to have strong size dependent electronic properties, we can tune the size from 2 nm (blue) to 6 nm (red). This allows us tune the emission of QDs all across the visible spectrum (Fig. 1.5C) resulting in QDs of different colors.

It is important to note that despite having tunability in emission by changing the QD size, there are still minimum and maximum energies that are synthetically able to be achieved. These limits are restricted by the material itself and its electronic configuration. There are a wide range of materials with known quantum dot synthetic preparation that emit from the UV to the infrared region (Fig. 1.6).[134] Therefore when engineering QDs for a specific

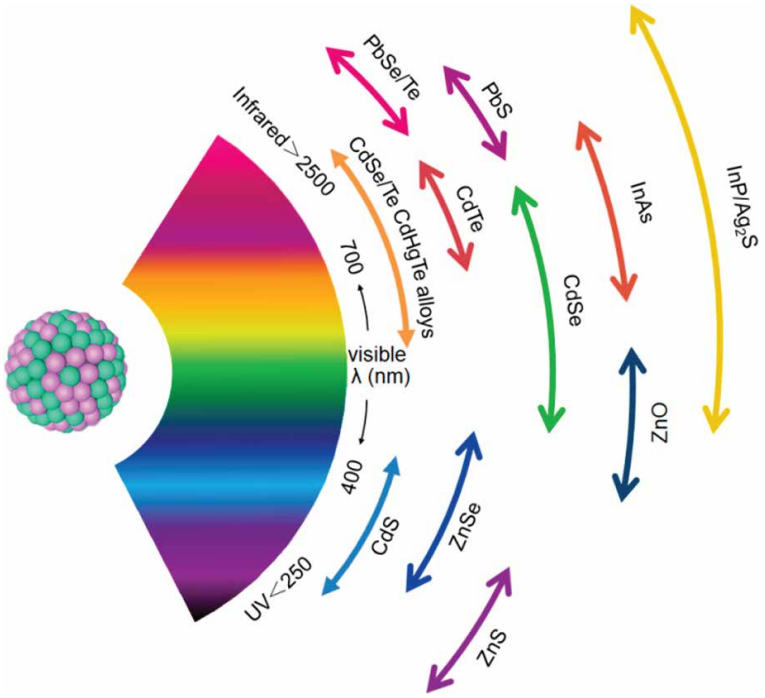

Figure 1.6: **Emission Tunability of Quantum Dots Composed of Different Materials**. Reproduced from [134]

energy application, selecting the correct material system is equally as important as synthesizing the QD to the appropriate size.

1.3 Colloidal Synthesis and Crystal Structure of Nanocrystals

In order to make QDs with a narrow size distribution and single crystal structure to have desirable applications, a colloidal synthesis via a hot injection method has been widely used.[31] The prototypical QD (CdSe) is grown from a solution of cadmium carboxylate salt typically made via the reaction of cadmium oxide (CdO) and octadecylphosphonic acid (ODPA) in trioctylphosphine oxide (TOPO) under Ar gas at 330 °C to form a Cd-ODPA complex. The temperature of the reaction flask is then increased to 380 °C at which point a syringe filled with trioctylphosphine selenide (TOP-Se) is quickly injected (Fig. 1.7A). The reaction then proceeds for some time until QDs are grown to a particular size. In the reaction scheme of the hot injection synthesis, the monomer concentration rapidly increases with the hot injection until the nucleation threshold is reached (Fig. 1.7B). Once this threshold is reached, rapid

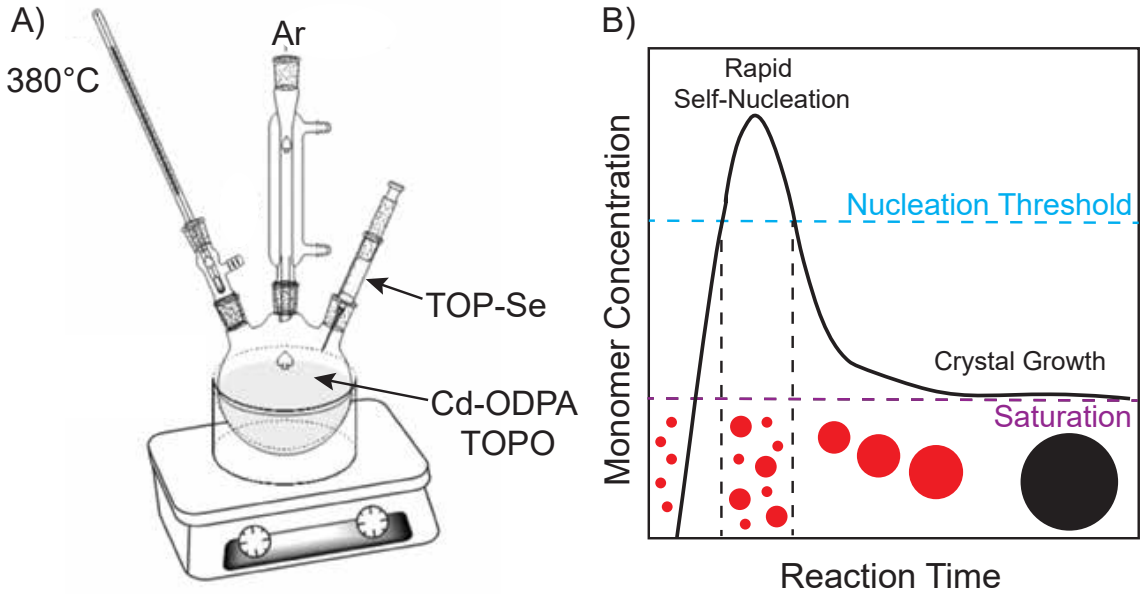

Figure 1.7: **Colloidal synthesis of nanocrystals. A** Simplified diagram of experimental set up for hot injection synthesis of quantum dots. **B** Reaction scheme of colloidal synthesis of QDs with a narrow size distribution. Hot injection reaction diagram adapted from [134].

self-nucleation occurs in which nanocrystals begin forming. At this point, both monomers and small nanocrystals exist in solution. Once the nucleation step has consumed enough monomers so the concentration is below the threshold, the crystal will continue to grow until the reaction is terminated. Due to higher surface energy, smaller nanocrystals grow faster allowing the solution to have a uniform size distribution once the reaction is stopped. If the reaction is not stopped, a saturation point is reached in which the crystal no longer grows. At this point the nanocrystal is large enough that its optical properties will be similar to the bulk semiconductor and its quantum confinement will not be as strong as smaller QDs.

Through small modifications to the hot injection reaction, we can control the crystal structure of QDs. QDs composed of binary compounds of groups II-VI (CdSe,CdS, and CdTe) and III-V (InP, GaAs, and GaN) have a tetragonal bonding geometry with either a cubic zinc-blende (Fig. 1.8A) or hexagonal wurtzite crystal structure (Fig. 1.8B).[3] Materials composed of IV-VI (Pb based chalcogenides) compounds typically have the rock salt crystal structure (Fig. 1.8C). Another class of semiconducting nanocrystals are known as perovskite nanocrystals which are named after the perovskite crystal structure. This class of nanocrystals are tertiary compounds formed with an ABX_3 composition where typically A= cesium, methylammonium (MA), or formamidinium (FA), B = lead or tin; and X = chloride, bromide, or iodide.[132] Although perovskite nanocrystals usually have a cubic perovskite

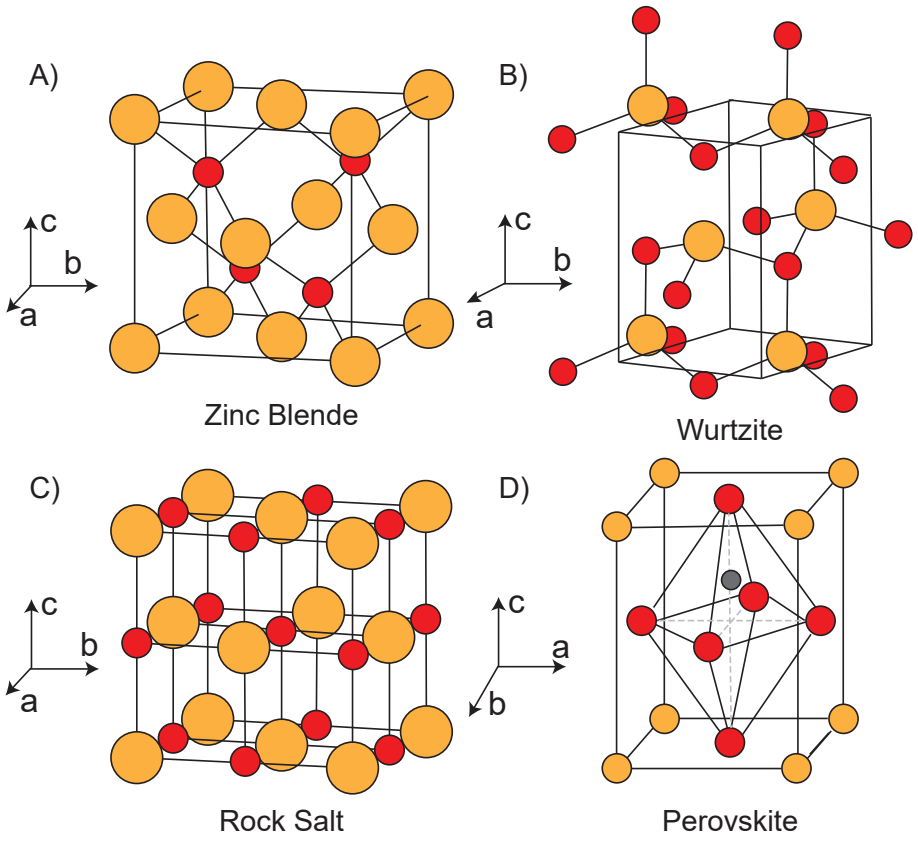

Figure 1.8: **Common Semiconductor Crystal Structures** Crystal structure for **A** zinc blende, **B** wurtzite, **C** rock salt and **D** perovskite crystals.

structure, in Figure 1.8D we instead show a distorted tetragonal perovskite crystal which is a common structure for oxide complexes[140] which will be discussed in future chapters. We can characterize the crystal structure of a QD sample via X-ray diffraction.

Through careful theoretical and experimental studies, the structure of the QD surface at the atomic level has been generated allowing us to better understand the complex functionalities of QDs.[185] In Figure 1.9, the atomic structure of PbS shows faceted regions within the QD surface. There are also organic ligands attached to the surface which are an innate part of the QD colloidal synthetic preparation. The organic ligand shell plays an additional role in confinement as it passivates surface sites in the nanocrystal that would otherwise be charged and result in surface trap states. The ligand shell can be tuned to contain either long- or short-chained carbon groups,[5, 87] functional groups like electron donating and withdrawing groups,[61, 89, 58, 29] and DNA.[188, 36] Additionally colloidal synthetic routes have also been developed to engineer QD heterostructures like a core/shell[37] and a

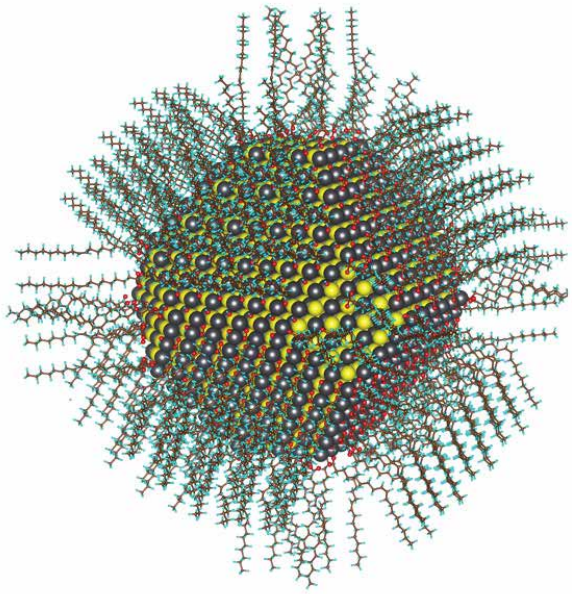

Figure 1.9: **Atomic Structure of a Quantum Dot Surface.** Quantum dot surface with faceted features and organic ligands passivating the surface.Reproduced from [185]

quantum well/quantum dot structure[38] where the radial composition of the material can be modified. Also, QDs with anisotropic shapes such as dot in rod,[130] dot in plate,[167, 32, 35] tetrapods,[106, 107] pyramids and bi-pyramids[159] have also been achieved beyond the conventional spherical geometry. The tunability in size, ligand, radial composition and shape through colloidal synthesis make quantum dots unique semiconductors that can have diverse structures unlike traditional semiconductors developed through traditional vacuum deposition routes.

1.4 Designing Larger Scale Quantum Dot-Based Materials

QDs can be synthesized colloidally with narrow size distributions, interesting shapes and functional heterostructures. However, in order to use this nanotechnology in modern day devices, we need to design large scale solid systems using QDs as building blocks. There have been several different reported techniques that can pattern QDs onto periodic locations with high accuracy and precision[93, 98] including inkjet printing,[66] photolithography,[182] and transfer printing.[95] However, these techniques tend to be highly involved and require

specialized instrumentation.

There are some simpler strategies to engineer QD based solid materials at the benchtop level. The simplest procedure is through dropcasting where QDs dispersed in solvent are deposited onto a substrate using a pipet. Over time the solvent evaporates, drying the QDs into a solid structure. The resulting film will not be very uniform, with different regions being thicker, and having a lot of vacant areas (Fig. 1.10A). The thickness of the film can be modulated by changing the concentration of the solvent deposited on the substrate surface. To achieve uniform QD coverage a spin coating technique is preferred where the substrate is placed on a rotating platform, which helps the colloidal solution fully coat the substrate before the solvent evaporates. The resulting films will have uniform coverage of randomly arranged QDs (Fig. 1.10B). Besides the concentration of solution, we can also tune the rotation rate of the platform that will ultimately play a role on the thickness of the film. Spin coating can be used to form ordered monolayer films if a patterned substrate is used.[14]

To routinely form ordered, uniform films, a self-assembly procedure is needed.[49] In the self-assembly process, the QDs dispersed in a non-polar solvent are deposited on top of a polar solvent inside a Teflon well. Over time as the non-polar solvent evaporates, enthalpic and entropic forces will make the QDs form a spatially ordered structure at the air-liquid interface. We can delay the evaporation of the non-polar solvent by covering the well with a cover slip allowing for the QDs to become more ordered. We can then transfer the QD assemblies to a substrate by simply scooping them up with tweezers. This allows for the formation of QD thin films with high spatial ordering and uniform coverage (Fig. 1.10C). This technique also provides us with additional parameters to tune, like time and the solvent system to optimize the film formation. Because of their highly ordered and uniform nature, these self-assembled films are considered 2D superlattices, which are ideal material systems to study how local spatial order affects electronic dynamics in QD ensembles.[125]

1.5 Exciton Dynamics in Quantum Dot Solids

An exciton is an electron-hole pair that temporarily exists in a material system. When energy is inserted into a material via a laser pulse, an electronic transition occurs causing an electron to move from a lower energy ground state (or from the valence band in a semiconductor) to a higher energy excited state (or from the conduction band in a semiconductor). In the ground state, the vacancy that persists where the electron once was has a positive charge associated with it and is referred to as a hole. Electrostatic Coulomb attraction forces bind the negative charged electron and the positive charged hole, forming an exciton. After some time, the electron can eventually relax back to the hole in a process referred to as recombination. If the exciton bound state does not persist and the electron and hole pair do not recombine, the electron and holes are known as charge carriers.

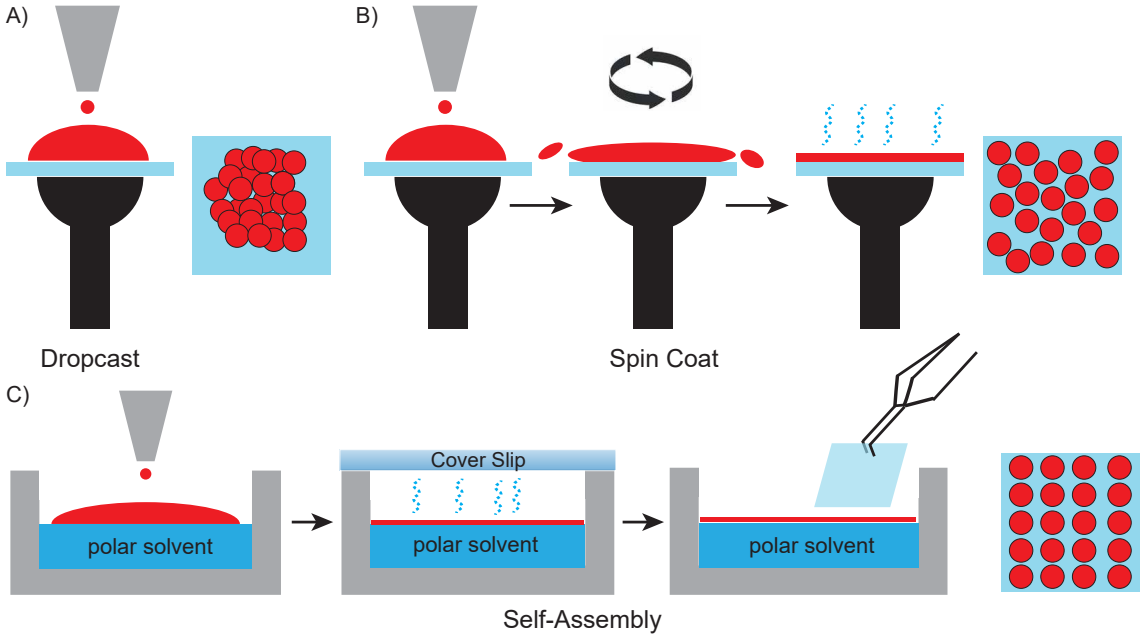

Figure 1.10: **Formation of Quantum Dot Based Solids.** Techniques to form quantum dot solids include **A** dropcasting, **B** spin coating and **C** self-assembly

Before discussing exciton dynamics in quantum dot solids, we must first consider how quantum confinement affects an exciton within a QD. A photoexcited species in a QD behavior is similar to a particle-in-a-box quantum model.[27] We are particularly interested in QD core/shell heterostructures as the shell acts like an insulating layer and enhances the luminescence of the nanocrystals. Depending on the material composition of the core and the shell, three different type of heterostructures can exist: 1) type I, 2) quasi-type II and 3) type II.[135] When a QD is photoexcited and an exciton forms, the confinement of the electron and hole wavefunction in the core vs shell that exist in the material depends on the mismatch of energy levels of the two materials. For a type I heterostructure like CdSe/ZnS core/shell, there is a large mismatch between the core and shell energy levels so that the core material has a higher energy ground state and lower energy excited state than the shell material. In this configuration, both the electron and hole wavefunctions will be localized in the core (Fig. 1.11A). The opposite can also be true where the exciton favors the shell. In a quasi-type II heterostructure like CdSe/CdS core/shell, the hole wavefunction is still localized in the core as in the type I configuration but the mismatch between excited energy levels of the core and shell materials is small enough that the electron wavefunction can overcome that energy barrier and become delocalized in both the core and shell (Fig. 1.11B). Coulombic forces between the positively charged hole wavefunction and the negatively charged electron wavefunction will affect the delocalization of the electron wavefunction but nonetheless it is able to become delocalized. In a type II heterostructure like CdSe/ZnTe core/shell, the

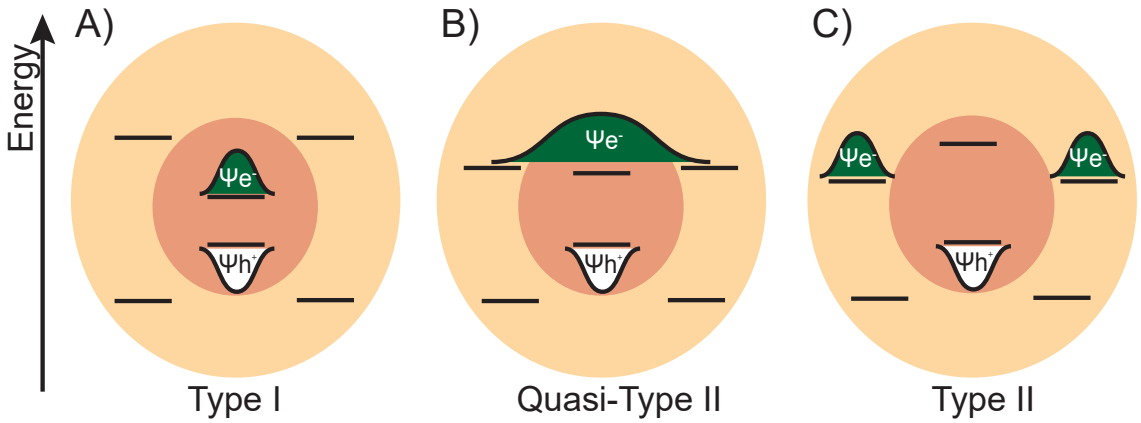

Figure 1.11: **Band Structure of Core/Shell Heterostructures.** Quantum dot heterostuctures can either have a **A** Type I, **B** Quasi type II and **C** type II heterojunctions

mismatch of energy levels is in a way that the hole is localized in the core and the electron wavefunction is localized in the shell (or vice versa) (Fig. 1.11C). Although it is possible to engineer structures where the electron and/or hole wavefunctions are localized in the shell, that tends to be an unfavorable configuration as unpassivated surface atoms can create surface states to trap either wavefunctions which ultimately decreases the brightness of the nanocrystal.

Once an exciton is generated within a QD, it will temporarily exist before eventual recombination of the electron and hole wavefunctions. There are a few different pathways to explain how exciton recombination occurs in QDs.[135] The most valuable mechanism, because we can measure it, is when an electron-hole pair recombine radiatively resulting in the emission of a photon (Fig. 1.12A). The energy of this photon ($h\nu$), which we can detect via photoluminescence measurements corresponds to the bandgap of the QD. The other mechanisms are all considered to be non-radiative because a photon is not emitted. In an Auger recombination, the energy released during the recombination process is absorbed by either an excited electron so it moves to a higher excited state or by a hole that moves to a lower energy state (Fig. 1.12B). It is important to note that in order for the Auger recombination mechanism to occur, two or more photoexcited species need to exist in one QD system. In a trap assisted (Shockley-Read-Hall) recombination mechanism, the electron becomes localized in a different mid bandgap energy state before eventually recombining to the ground state (Fig. 1.12C). This type of recombination mechanism is mostly relevant to systems with a dopant or defect in their lattice structure which we will discuss in Chapter 3. Similarly, unpassivated atomic sites in the QD surface create trap states where the electron relaxes back to the ground state using surface mediated recombination mechanisms (Fig. 1.12D). If an electron becomes trapped in a surface state, it is possible for it to eventually become un-trapped and recombine radiatively resulting in delayed emission also known as

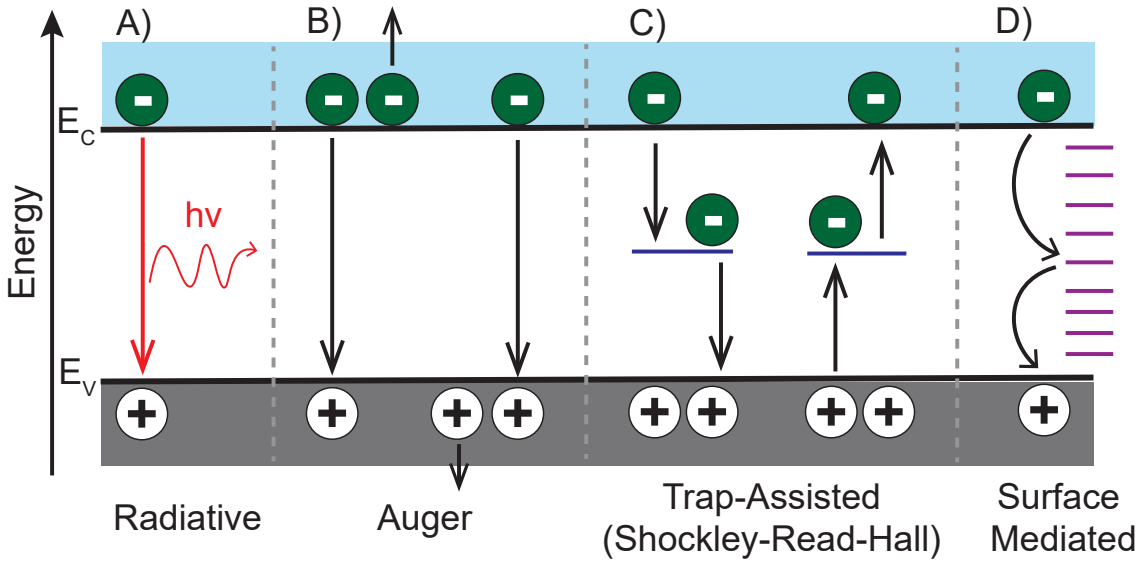

Figure 1.12: **Recombination Mechanisms A** Radiative recombination resulting with the emission of a photon. Non-radiative mechanisms like **B** Auger,**C** Trap-assisted (Shockley-Read-Hall) and **D** surface mediated recombination

blinking. These non-radiative pathways will eventually release energy from the nanocrystal system via phonons through lattice vibrations resulting in thermal energy loss.

Once QDs are in a close-packed solid, interpaticle interactions can affect the charge carrier dynamics prior to recombination.[63] Since electrons and holes are always inclined to move to lower and higher energy states, respectively, there are additional pathways for electrons through energy transfer mechanisms. Despite trying to colloidally synthesize fairly uniform nanocrystals, there will always be some variation in size that directly correlates to their emission and bandgap energies. As discussed earlier, larger QDs will have smaller energy bandgaps and may act as acceptors in energy transfer processes from a smaller donor QD. In a system with adjacent QDs separated by a distance (r) represented in Figure 1.13A, the orange (donor) QD is smaller and has a larger bandgap than the red (acceptor) QD. If energy is absorbed (purple arrow) by the orange QD an exciton is generated in that nanocrystal. The exciton can either recombine in the orange QD and emit energy (PL_{Donor}) or it can "hop" from the orange to the red QD (ET, yellow arrow). The exciton can then recombine in the red QD and emit energy ($PL_{Acceptor}$).

The exciton transfers between QDs via a hopping mechanism are known as Förster resonance energy transfer (FRET). FRET occurs through a coupling of the transition dipole moments of neighboring QDs. The FRET rate (k_{ET}) is dictated by r (Fig. 1.13B) of neigh-

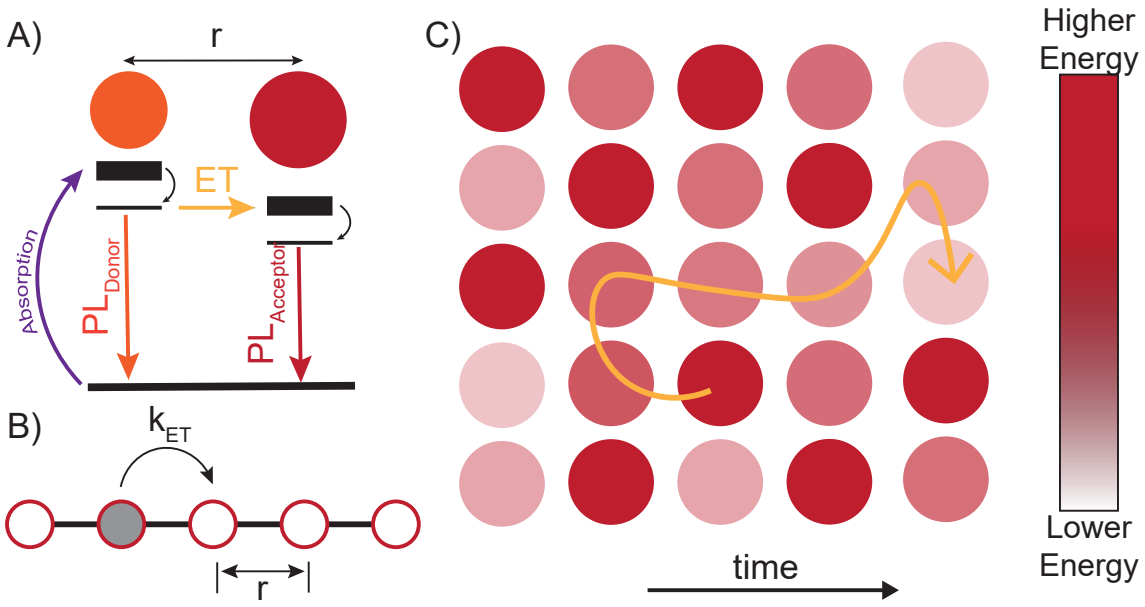

Figure 1.13: **Exciton Transfer in Quantum Dot Solids. A** Two neighboring quantum dots separates by some distance (r) with different sizes can experience energy transfer (ET) if energy is absorbed (purple arrow) by smaller nanocrystal (orange). Recombination can then occur in the larger nanocrystal (red). **B** Simple diagram of energy transfer via hopping mechanism in an array of atoms. The rate of the energy transfer (k_{ET}) is dictated by r. **C** Exciton transport mechanism in an ordered superlattice of quantum dots.

boring nanocrystals and can be described by the following equation:

$$k_{ET} = 1/\tau(r_0/r)^6 \tag{1.1}$$

where τ is the lifetime of the donor QD and r_0 is the distance for which the likelihood of FRET occurring is 50%. This distance is dictated by several factors including spectral overlap between the donor QD emission and the acceptor QD absorption.

In a QD superlattice where an array of QDs with some size distribution are randomly arranged, excitons will hop from higher to lower energy bandgap nanocrystals over time before eventually recombining (Fig. 1.13C, yellow arrow).[176] In Chapter 3, we will further discuss spatiotemporal techniques that are used to study energy migration and quantify exciton hopping lengths.

1.6 The Importance of Rational Design in Quantum Dot Based Technology

In the previous sections, we discussed the history of QDs, their controllable size and tunable optical properties. These properties make QDs desirable candidates in a wide range of applications such as light emitting diodes, displays,[41] biological labeling,[59] photovoltaics,[53, 73] and next-generation lasers.[88] Through discovering strategies to embed QDs in different materials and creating high-scale devices additional applications can be realized.[105, 98] However, understanding how energy propagates in QD based materials is equally as important as engineering large-scale devices. Through rational design of QD based technology and altering the structure of QDs, we can not only produce devices with unique patterns but also influence electron dynamics.[60]

In the next two chapters we will discuss two case studies where, using rational design of quantum dot based thin films, we were able to study interesting electronic behavior. In Chapter 2, through modulation of the CdS shell, we were able to quantify and compare the recombination rates of different CdSe/CdS core/shell quantum dots in colloidal solution and monolayer thin film to understand how these rates change in different mediums. In Chapter 3 through the incorporation of a Te atomic defect within the CdSe matrix, we created quantum dots that albeit small, emit at wavelengths beyond the bulk limit. Through forming highly ordered superlattices with this defect, we were able to study how energy dissipates in a heterogeneous energy landscape. Both of these studies allow us to improve our understanding of how the structure of QD based materials influences energy dynamics which is helpful to consider during rational design of QD based technology for different applications.

Chapter 2

Quantitative comparison of recombination rates of core/shell quantum dots in colloidal solutions and self-assembled monolayer superlattices

2.1 Introduction

Colloidal quantum dots (QDs) are nanoscale crystallites of semiconducting materials where spatial confinement enables tunable electronic properties such as, bright, narrow, size tunable, photoluminescence[37, 3] and excellent photostability.[126] With these properties, QDs are excellent candidates for emitters in light emitting diodes,[146] color converters in displays,[72, 43] photosensitizers in QD-based solar cells,[161, 53, 25] and fluorescent tags in bioimaging.[4, 189, 59] However, incomplete understanding on the factors and mechanisms governing the relationship between the radiative and non-radiative channels limits rational design for QD technology.[98] The implementation of QD technology for these applications critically depends on understanding the key parameters of photoluminescence: the photoluminescence quantum yield (PLQY), radiative rate (Γ_r) and non-radiative rate (Γ_{nr}) which are all interrelated according to the following equation: PLQY = $\Gamma_r/(\Gamma_r+\Gamma_{nr})$. The PLQY of a material determines the efficiency of a photoexcited process by measuring the ratio of the photons emitted versus photons absorbed. Whereas the Γ_r and Γ_{nr} measure how long a photoexcited process exists before the electron and hole recombine either radiatively with the emission of a photon or non-radiatively through defect mediated processes until the eventual emission of heat/phonons. In many applications that benefit from high PLQY of QDs there is a need to promote radiative and suppress non-radiative pathways.[77] This is well understood for many QD materials in solution however most practical applications require

them to be in the solid state.

QD solids and films are useful in device fabrication and technology. There has been significant progress to control the structure of self-assembled 2D or 3D QD superlattices[1, 117, 118] for optimized device performance.[98, 80, 46, 172] Among a range of different self-assembly mechanisms,[21] the self-assembly of QDs at the liquid-air interface has been shown to reproducibly form well-ordered superlattices with high packing densities.[1] Although the structure of these superlattices can be well-controlled, understanding of the photoluminescence properties of these thin films is limited due to the challenge of determining the PLQY and hence Γ_r and Γ_{nr} of low volume materials with sufficient high signal to noise ratios. CdSe/CdS core/shell QDs are a model system to conduct monolayer thin film PLQY measurements in an integrating sphere due to their prevalence in the literature and bright tunable emission properties.[37, 69, 12, 128, 2, 125]Previous work studying Γ_r of CdSe/CdS core/shell QD colloidal solutions have shown that the core size has a modest effect on Γ_r but increasing shell thickness results in a decreasing in Γ_r due to decreasing electron-hole wavefunction overlap.[71] Studies on quantum solids have predominantly investigated multilayer films with a focus on studying exciton diffusion.[2, 62, 149, 92] A recent study on core/shell QD monolayer thin films studied exciton transport using spatiotemporal techniques to elucidate electrodynamic mechanisms.[176] However, these studies have not reported how Γ_r changes between colloidal solution and thin films.

Herein, we compare Γ_r and Γ_{nr} of QD monolayer thin films to their counterparts in colloidal solutions. We experimentally determine Γ_r and Γ_{nr} of the monolayer thin films by measuring the PLQY of the QD monolayer thin films reproducibly with high accuracy using a solid-state sample holder in an integrating sphere (Fig. A.1). We study a series of CdSe/CdS core/shell QDs which we can systematically vary the Γ_r and Γ_{nr} by changing the CdS shell thickness. We observed that both the Γ_r and Γ_{nr} increase in the thin film samples compared to their colloidal solution counterparts. The increase in Γ_{nr} has been attributed to well-studied energy transfer processes in QD solids[2, 128, 125, 131, 157] as well as the presence of trap states.[133, 87, 61] However, it is a surprising result that Γ_r is increased in the thin films. Even though there are techniques such as shell growth[37, 40] and ligand engineering[87, 28, 11] to reduce QD surface trap states, the presence of charge trapping states is a natural part of the QD surface.[87, 61, 166] We hypothesize potential mechanisms to explain the increase in Γ_r in the thin films by evaluating the quasi type-II electronic band structure of core/shell QDs. We particularly focus on the effect of unpassivated surface sites on energy levels and electron wavefunction delocalization. These results imply that there is the potential to engineer trap states to yield optimal performance besides the conventional wisdom of completely removing trapping states.

2.2 Materials and Methods

Chemicals

Cadmium oxide (CdO, $\geq$ 99.99%, Sigma Aldrich), octadecylphosphonic acid (ODPA, 99%, PCI Synthesis), trioctylphosphine oxide (TOPO, 99%, Sigma Aldrich), trioctylphosphine (TOP, 99%, Strem), selenium powder (Se, 99.999%, Sigma Aldrich), oleic acid (OA, 90% tech grade, Sigma Aldrich), oleylamine (OAm, 70% tech grade, Sigma Aldrich), octanethiol (OctSH, $\geq$ 98.5%, Sigma Aldrich),1-octadecene (ODE, 90% tech grade, Sigma Aldrich), N, N-dimethylformamide (DMF, anhydrous 99%, Sigma-Aldrich), toluene (anhydrous 99.5%, Sigma Aldrich), acetone (anhydrous, 99.5%, Sigma Aldrich), hexanes (mixture of isomers, anhydrous 95%, Sigma Aldrich), n-octane (98%, reagent grade, Sigma Aldrich). 0.2 M $Cd(oleate)_2$ in ODE precursor was prepared using a previously reported procedure.[69] Briefly, appropriate amounts of CdO, OA, and ODE were degassed for about two hours under vacuum at 110 °C until all gases and water had evolved. The reaction was then heated to 240 °C under argon for ∼30 minutes until a clear, slightly yellow, solution forms. The flask was then cooled to 110 °C and degassed a second time for an additional 1-2 hours to remove additional water. The solution was stored in an argon-filled glovebox.

Wurtzite-CdSe Core Nanocrystals

CdSe core nanocrystals were synthesized by modifying a known procedure.[31] Briefly, 120 mg CdO, 560 mg ODPA, 6 g TOPO were degassed under vacuum in a 50 mL round-bottom flask at 150 °C for 1 hour. The mixture was then heated to 330 °C under argon gas and maintained at 330 °C until solution turned clear indicating formation of a complex (∼2-3 hours). Upon completion of complex formation, 3 g of TOP was injected in the solution and then the temperature was raised to 360 °C. A solution of 116 mg of Se in 0.72 g TOP was swiftly injected when temperature approached 360 °C. Upon injection, CdSe nanocrystals were formed and were allowed to grow for 1 minute to produce small, uniform cores. Solution was then rapidly cooled with compressed air to 120 °C before injecting 10 mL of anhydrous toluene and transferring to an inert atmosphere. The nanocrystals were cleaned in an inert environment with successive precipitation and redispersion using acetone and hexane respectively and were stored in 3 ml of hexane. Concentrations were determined by a previously reported empirical formula[175] and size was determined via TEM image analysis (Fig A.2).

CdSe/CdS core/shell Nanocrystals

A CdS shell of different shell thicknesses was grown around the CdSe nanocrystals using a previously reported preparation.[37] The shell growth was done by first degassing under vacuum 3 mL of ODE, 3 mL of OAm in a 25 mL round-bottom flask at 110 ºC for 30 mins.

Then, 100 nmol of CdSe cores were added and the solution was heated to 310 ^{o}C under Ar. When the temperature reached 240 ^{o}C, injections of Cd and S precursor solutions in ODE started at a rate of 3 ml/hr using a syringe pump. The Cd and S precursor solutions contained different amounts of 0.20 mM $Cd(OA)_2$ and OctSH in ODE based on the desired shell thickness. Upon completion of the precursor injections, the reaction was maintained at 310 ^{o}C for 10 minutes, then cooled rapidly using compressed air to room temperature. Successive precipitation and redispersed using acetone and hexane respectively were done twice to clean the nanocrystals capped with OA and OAm before they were stored in hexane in an inert atmosphere.

Self-assembly of Nanocrystals Superlattice

Formation of nanocrystal superlattice was performed using a previously published self-assembly method.[49] Monolayer nanocrystal superlattices were formed at the liquid-air interface at room temperature. The nanocrystal stock solution was diluted in octane to a proper concentration to obtain monolayer coverage. Approximately, 50 uL of diluted nanocrystal solution was drop-casted on top of 1 mL of DMF in a 1 cm^2 square Teflon well. The well was covered with a glass cover slip to slow solvent evaporation rate overnight. The self-assembled superlattice was scooped onto a plasma cleaned glass cover slip for optical measurements or a Cu 400 mesh standard carbon TEM grid for structural characterization.

TEM Characterization and Image Analysis

Transmission Electron Microscopy was used to characterize nanocrystal superlattices using a FEI Tecnai T20 S-TWIN TEM operating at 200 kV with a LaB6 filament. TEM images were collected using a Gatan Rio 16IS camera with full 4k by 4k resolution using the drift correction feature. TEM samples were scooped from self-assembly well onto Electron Microscopy Sciences CF400-Cu 400 mesh standard carbon TEM grids. Sizing distribution curves were generated from TEM images of >2000 nanoparticles using a custom written MATLAB script in which the details have been previously reported.[25] Image analysis and Fourier transformation of image was performed on ImageJ software.

Optical Characterization of Colloidal Nanocrystal Samples

Steady-state absorbance spectra were collected in octane with a Shimadzu UV-3600 double beam spectrometer operating with 1 nm slits. Steady-state photoluminescence, time-resolved photoluminescence, time resolved emission spectra, and fluorescence anisotropy measurements were done using a Picoquant Fluotime 300 Spectrometer with a time-correlated single photon counting apparatus, a PMA 175 detector and a LDH-P-C-405 diode laser with a 407.7 nm excitation wavelength. TRPL measurements were done with 50 ps laser pulse width and a repetition rate of 10 MHz. Multiexciton generation is not considered for these

measurements since the average number of excitons per pulse is $\ll 1$. TRES measurements were done by measuring the PL after a 0.5-50 ns delay post excitation pulse. The fluorescence anisotropy measurements were performed by rotating the emission polarizer from 0-90° and collecting the number of counts at the center wavelength.

Photoluminescence Quantum Yield of Quantum Dot Samples

PLQY was measured using a home-built integrating sphere setup that has been discussed in detail in previous work.[69] Briefly, a Fianium SC450 pulsed supercontinuum laser provided a white light source with an average power of 4 W for a wavelength range of 410-2500 nm. The excitation light passes through two monochromators, a Princeton Instruments SP150 and a Princeton Instruments SP275, for wavelength selection resulting in an excitation bandwidth of <0.5 nm. The monochromatic excitation beam then passes through a beam splitter. Some light goes into a calibrated Si photodiode to measure the power while most of it goes through a 25 mm entrance port of a 135 mm Spectralon integrating sphere from LabSphere. Samples were held on the opposite side of the entrance port in a custom built Spectralon circular cuvette holder. The direct reflection beam was blocked by a baffle while the diffuse light was able to exit the sphere. Once the diffused light exited the integration sphere, it was focused onto the entrance slit of a Princeton Instruments SP2300 monochromator with a 300 g/mm grating blazed at 500 nm. The resultant spectrum was detected using a TE cooled for spectral position using a Ne lamp and sensitivity using a NIST-traceable radiometric calibration lamp from Ocean Optics (model HL3-plus, serial number 089440003). Blank and sample measurements were done with at least 5 repetitions for each wavelength to produce PLQY error bars. Solution samples were dispersed in octane and measured in a custom cuvette while monolayer thin films were measured using 3D-printed solid state sample holder (Fig A.1A).

2.3 Results

Characterization of Quantum Dot Monolayer Superlattices

In this work, we focus on three CdSe/CdS core/shell QD samples. There are well-reported synthetic methods to colloidally synthesize CdSe/CdS core/shell QDs with high PLQY at different core sizes and shell thickness.[37] The CdSe/CdS QD has a quasi-type-II heterostructure due to the band offset of CdSe and CdS. In a photoexcited CdSe/CdS QD, the hole wavefunction is largely localized in the CdSe core, and the electron wavefunction is delocalized into the CdS shell.[56] Although Coulombic attractions between the negatively charged electron wavefunction and positively charged hole wavefunction confine the exciton, un-passivated charged atomic sites on the QDs surface could result in charge carrier trap

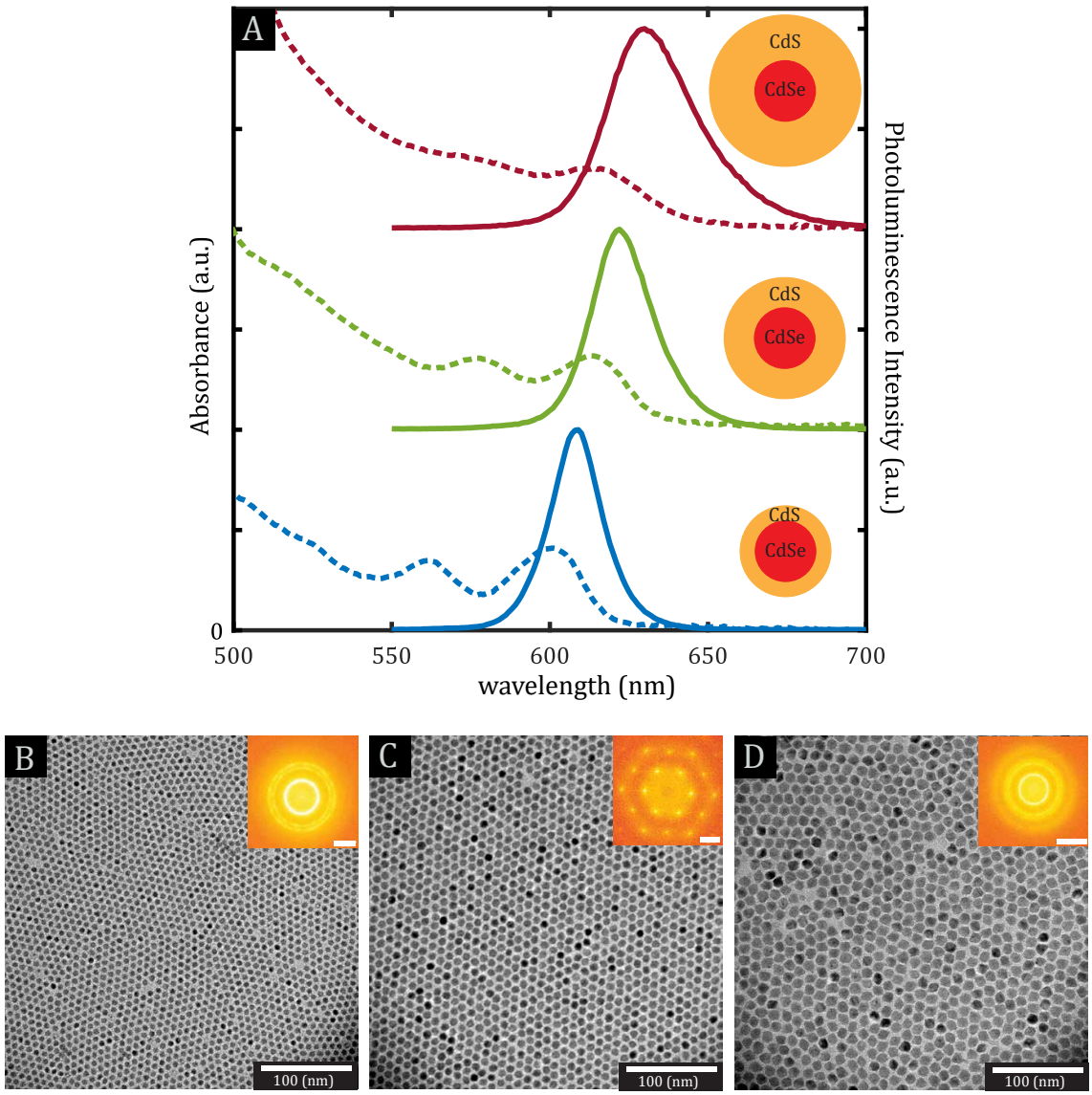

Figure 2.1: **Optical and Structural Characterization of QD Samples. A** Absorption (dashed) and photoluminescence (solid) spectra of CdSe/3MLCdS(blue), CdSe/6MLCdS (green), and CdSe/9MLCdS (red) QDs in colloidal solution. TEM images of self-assembled superlattices of **B** CdSe/3MLCdS, **C** CdSe/6MLCdS, and **D** CdSe/9MLCdS with Fast Fourier transform analysis shown in inset (inset scale bar is 50 nm^{-1} for inset in **B** and **D** and 100 nm^{-1} for inset in **C**).

state.[12, 56] CdSe/CdS QDs are synthesized to have organic ligands passivating the surface. These ligands can sometimes be removed from the surface depending on the local environment to reach thermodynamic equilibrium.[28] One way to decrease the charge trapping is by increasing the shell thickness of the QDs until sufficient passivation of the hole wavefunction.[61] However, after a certain threshold in shell thickness, further increasing the shell will worsen the wavefunction overlap as the electron delocalizes into the CdS shell where it can become trapped in a shallow surface trap.[69] Not all charge carrier trapping results in non-radiative recombination, some trappings are reversible and can result in a delayed exciton emission.[136] Hence, by changing the shell thickness of a QD we can systematically change the wavefunction overlap and observe how Γ_r and Γ_{nr} change.

The CdSe cores in all core/shell QDs studied have the same diameter (D) of 3.4 nm. We then grow different thicknesses of CdS shell onto these cores. These samples have 3 ($D = 6.5$ nm), 6 ($D = 8.5$ nm) and 9 ($D = 12.6$ nm) monolayers (ML) of CdS shell where 1 monolayer of shell is 0.416 nm (Fig. 2.1A and A.2). These shell thicknesses were chosen to study samples with weak, intermediate and strong wavefunction confinement respectively. The samples will be referred to as CdSe/3MLCdS, CdSe/6MLCdS, and CdSe/9MLCdS accordingly based on their shell thickness. The thickness of the CdS shell changes the optical properties of the samples. As a thicker shell is grown, we observed that the PL peak energy shifts to longer wavelengths (Fig. 2.1A and Table 2.1) due to increasing electron wavefunction delocalization into the CdS shell. Similarly, the absorption peak also shifts to longer wavelength with the shell growth (Fig. A.3).

Next, we use the self-assembly method to form monolayer superlattice thin films in the liquid-air interface.[119] The structure of these monolayer superlattices was studied using transmission electron microscopy (TEM). The TEM images of these superlattices show that we can achieve high-monolayer coverage at micron length scales with some spatial order (Fig. 2.1B-D and Fig. A.4). By performing Fast Fourier transform analysis of the TEM images (Fig. 2.1B-D inset), we can observe the superlattice ordering in each sample. The CdSe/6MLCdS superlattice has hexagonal packing structure at micron length scales represented by the hexagonal spots on the Fourier transform of the image (Fig. 2.1C, inset). At this magnification, the CdSe/3MLCdS and CdSe/9MLCdS superlattices do not appear to have obvious long-range order but rather are composed of small, ordered domains (Fig. A.5A and C). At higher magnification, the Fourier transform of the TEM images of CdSe/3MLCdS and CdSe/9MLCdS samples show a similar hexagonal packing structure to the CdSe/6MLCdS (Fig. A.5B and D). Despite the difference in spatial ordering length scales, a given QD likely only interacts with its nearest neighbors[176] which does not vary between the sample. Hence, all thin film samples have the same short-range spatial ordering which is the most important comparison for our analysis.

Table 2.1: Optical characterization values from Figure 2.2 of QD samples in colloidal solution (sol) and monolayer thin films (film)

Sample	x_0 (nm)	τ_{avg} (ns)	PLQY	Relative Decrease in PLQY
CdSe/3MLCdS$_{sol}$	608.3 ± 0.2	22.3 ± 0.8	$62.2 \pm 1.4\%$	86.8%
CdSe/3MLCdS$_{film}$	610.2 ± 0.1	5.2 ± 0.3	$8.2 \pm 2.4\%$	
CdSe/6MLCdS$_{sol}$	623.0 ± 0.2	40.6 ± 1.5	$69.9 \pm 1.6\%$	28.6%
CdSe/6MLCdS$_{film}$	622.3 ± 0.1	20.3 ± 0.45	$49.9 \pm 5.2\%$	
CdSe/9MLCdS$_{sol}$	632.5 ± 0.1	202.8 ± 2.1	$82.6 \pm 1.9\%$	20.8%
CdSe/9MLCdS$_{film}$	628.8 ± 0.1	55.8 ± 0.8	$65.4 \pm 6.6\%$	

Photoluminescence Properties of QDs: Colloidal Solution versus Monolayer Superlattices

We measured the PLQY (Fig. 2.2A) of the three samples, both for colloidal solution (solid lines) and for the self-assembled superlattice (dashed line). The PLQY of the sample increases with shell thickness with the CdSe/9MLCdS having the highest PLQY and CdSe/3MLCdS having the lowest PLQY. That is expected because with increased shell thickness, the more the hole wavefunction is shielded from surface trapping states, the less probable it becomes for a charge carrier to be trapped in an un-passivated surface state. Relative to their colloidal solution counterparts, the PLQY of the self-assembled monolayer superlattice thin films decreases. For CdSe/6MLCdS, the PLQY decreases by 28.6% from 69.9% to 49.9% while it decreases by 20.8% from 82.5% to 65.3% for CdSe/9MLCdS. CdSe/3MLCdS showed the greatest decrease in PLQY with an 86.8% decrease (from 62.5% to 8.2%) (Table 2.1). CdSe/3MLCdS showed the greatest decrease in PLQY with an 86.8% decrease (from 62.5% to 8.2%). This decrease in PLQY is expected because of an increase in non-radiative recombination processes such as energy transfer/exciton diffusion to nearest neighbors[125] and loss of ligands passivating the QD surface during the self-assembly process.[48] The largest decrease from colloidal solution to monolayer thin films is for the CdSe/3MLCdS sample where any removal of ligands from the surface leads to an increase in probability of charge carrier trapping since the CdSe core is not as shielded by the CdS shell as for the other samples.

Steady-state PL measurements (Fig. 2.2B) of the three monolayer superlattices (dashed curve) do not have a significant energy shift compared to their colloidal solution (solid curve) counterparts. Typically, a key signature of energy transfer caused by exciton diffusion in QDs is a peak shift to longer wavelengths in PL[2] which we do not observe. That is potentially due to the narrow size distribution of the sample. Due to the monodispersity of the samples, there is less downhill energy funneling as has been observed in past studies.[92, 2, 62, 131] Additionally, the emission peaks are also narrower for the thin films which is due to size-selective assembly during the film formation.

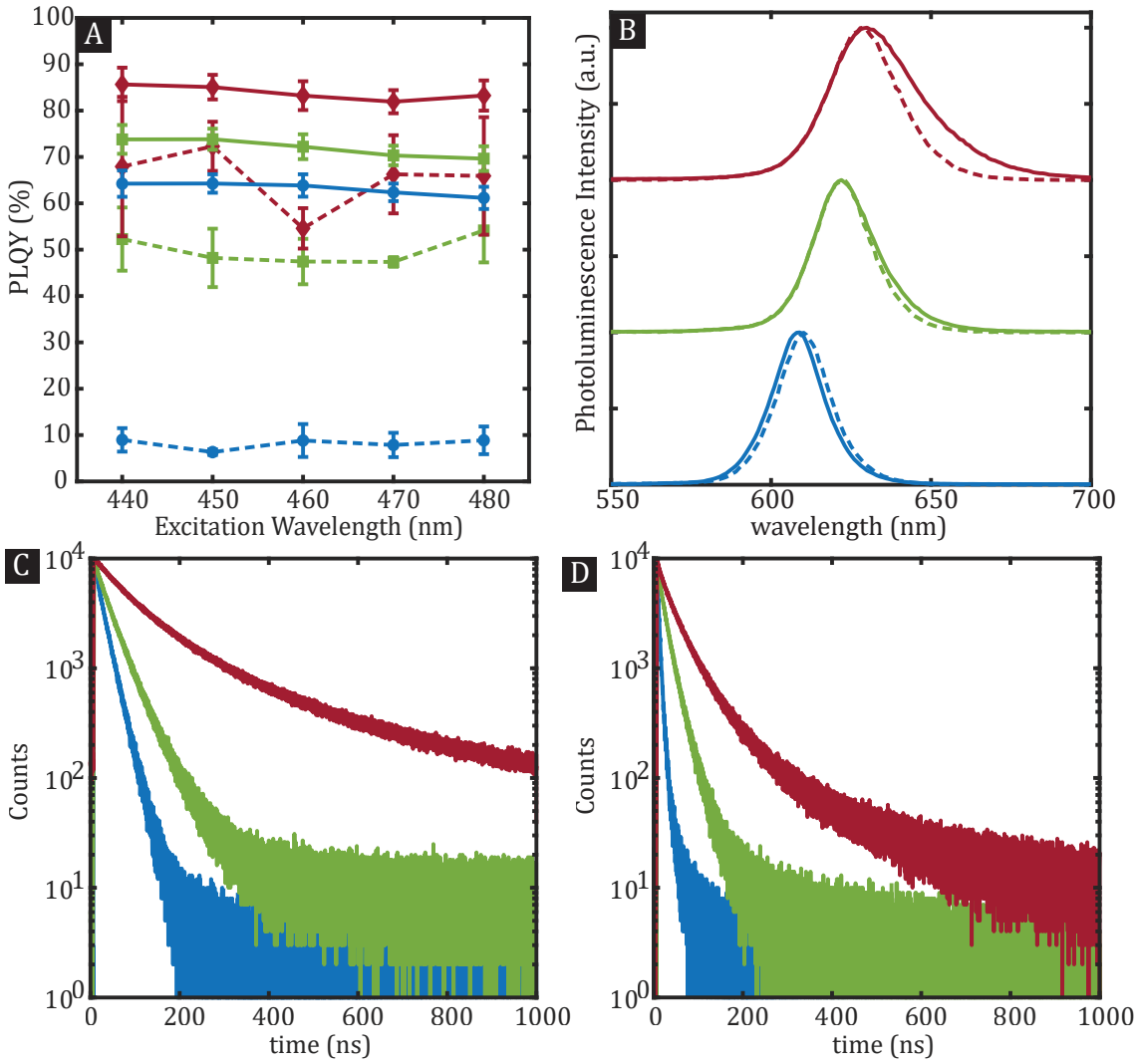

Figure 2.2: **Optical Characterization of QD Monolayer Thin Films. A** PLQY values at different excitation wavelengths for QD samples in colloidal solution (solid) and monolayer thin films (dashed) **B** Steady-state photoluminescence spectra of QD monolayer thin films (dashed) and colloidal solution (solid). Time-resolved photoluminescence spectra of QD samples in **C** colloidal solution and **D** monolayer thin films. CdSe/3MLCdS samples are shown in blue, CdSe/6MLCdS in green and CdSe/9MLCdS in red for all four panels

We further compared the time-resolved photoluminescence (TRPL) at the maximum emission wavelength for both the colloidal solution and monolayer thin films (Fig. 2.2C and 2.2D, respectively). The first two decades of the TRPL spectra of each sample were fit to different exponential functions to determine the best fit (Fig. A.6). A biexponential decay function was selected to best represent the colloidal solution and monolayer thin film data (stretched exponential function also fit monolayer thin film TRPL data well) and the weighted average lifetime (τ_{avg}) of each sample was determined (Section A.6). The τ_{avg} of each sample increases with shell thickness. In colloidal solution, CdSe/3MLCdS has the shortest lifetime (22.3 ns, blue), followed by CdSe/6MLCdS (40.6 ns, green) and lastly CdSe/9MLCdS (202.8 ns, red) (Fig. 2.2B, Table 2.1). The τ_{avg} values of the monolayer thin films also follow the same trend. However, the τ_{avg} of these superlattices is much shorter than in colloidal solution. For the CdSe/3MLCdS, τ_{avg} decreases by a factor of over 4 (to 5.2 ns), by a factor of 2 (to 20.3 ns) for CdSe/6MLCdS and by a factor of almost 3 (to 55.8 ns) for CdSe/9MLCdS (Table 2.1). Previous reports have attributed this trend of decreasing PLQY and τ from solution to solid state quantum dot films to loss of ligands and exciton diffusion which are known to increase Γ_{nr}.[2] However, to unravel the changes in Γ_r we need to couple the τ_{avg} and PLQY values to further discuss the recombination rates of these samples quantitatively.

Comparison of Recombination Rates

By extracting τ_{avg} from the TRPL curves and the PLQY of the monolayer thin films, we can calculate Γ_r (Fig. 2.3A) and Γ_{nr} (Fig. 2.3B) for the three samples. The recombination rates were calculated using τ and PLQY values and the mathematical relationships $\Phi=\Gamma_r/(\Gamma_r+\Gamma_{nr})$ and $\Gamma_{Tot}= \Gamma_r+ \Gamma_{nr}=\tau^{-1}$ where Φ is the PLQY and τ is the weighted average of biexponential fit (Section A.6). We can manipulate these equations to solve for the recombination rates directly: $\Gamma_r=\Phi/\tau$ and $\Gamma_{nr}= \tau^{-1}$-Γ_r.

Each data point in Figure 2.3A and 2.3B corresponds to the recombination rate determined from each trial of the PLQY measurement (Fig. A.7) of the thin film sample and the average TRPL value (Table 2.1). The average recombination rate is also shown with error bars corresponding to the average and standard deviation of the PLQY measurements from the different trials. Neither Γ_r nor Γ_{nr} change as a function of excitation wavelength.

For the colloidal solution samples, a monotonic decrease in Γ_r and Γ_{nr} is observed with increasing shell thickness (Fig. 2.3C-D, Table 2.3). This trend of decreasing rates follows the expected behavior that increasing shell thickness improves the confinement of the hole wavefunction to the CdSe core and decreases the probability of charge carrier trapping in the QD surface.[12, 69]

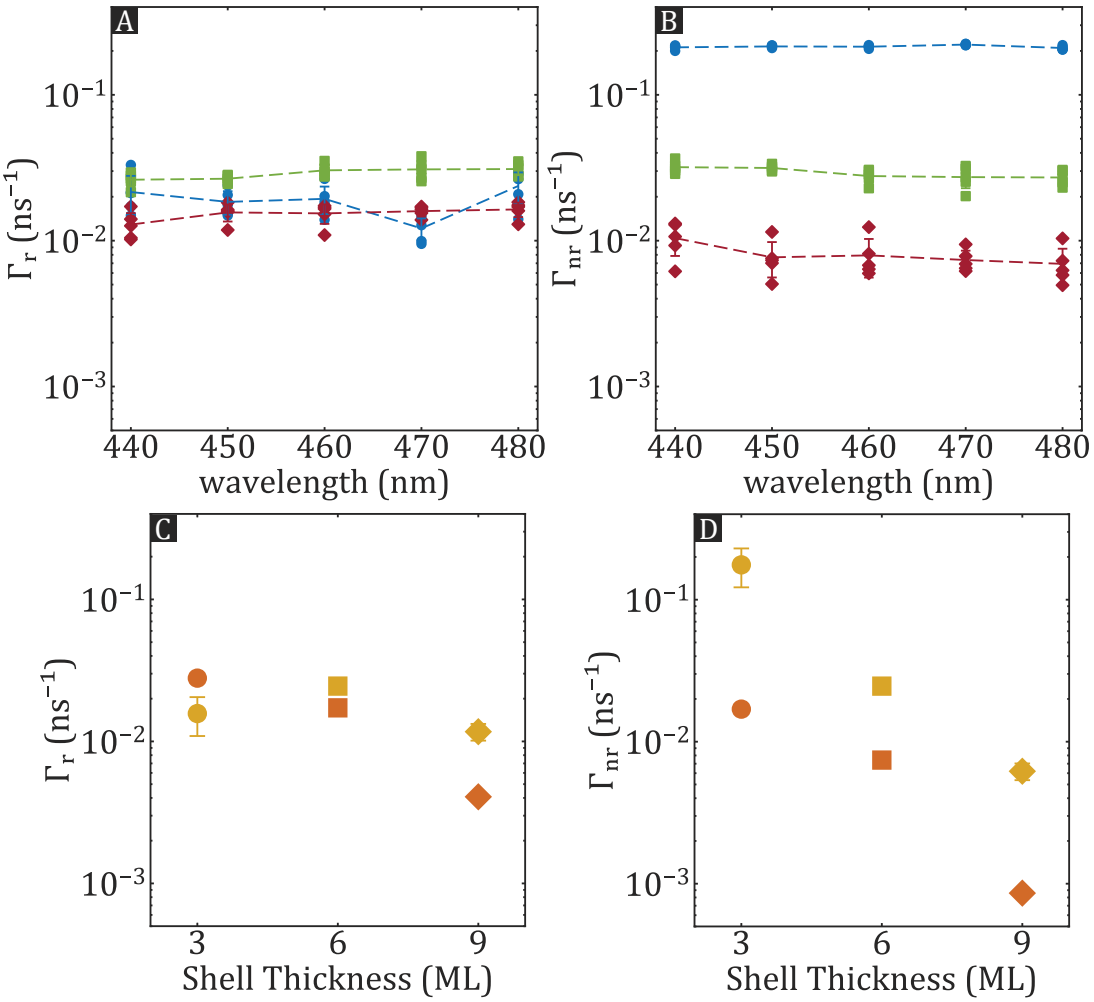

Figure 2.3: **Recombination Rates for QD Monolayer Thin Films and in Colloidal Solution.** **A** $\Gamma_r$and **B** $\Gamma_{nr}$for CdSe/3MLCdS (blue circle), CdSe/6MLCdS (green square), and CdSe/9MLCdS (red diamond) monolayer thin films at different excitation wavelengths. Each data point corresponds to values from different PLQY measurement. Average rate shown via data point with error bars corresponding to standard deviation based on the different PLQY trials. **C** $\Gamma_r$and **D** $\Gamma_{nr}$of colloidal solution (orange) vs monolayer thin film (yellow) for the three different QD samples as a function of shell thickness. Corresponding y-axis error bars come from uncertainty of TRPL fits and PLQY measurements.

Table 2.2: Recombination rates of quantum dot samples in colloidal solution (sol) and monolayer thin films (film).

Sample	Γ_r $(10^{-2}\ ns^{-1})$	$\Gamma_{nr}(10^{-2}\ ns^{-1})$
CdSe/3MLCdS$_{sol}$	2.8 ± 0.1	1.70 ± 0.04
CdSe/3MLCdS$_{film}$	1.6 ± 0.5	17.6 ± 5.4
CdSe/6MLCdS$_{sol}$	1.72 ± 0.07	0.74 ± 0.03
CdSe/6MLCdS$_{film}$	2.4 ± 0.3	2.5 ± 0.3
CdSe/9MLCdS$_{sol}$	0.41 ± 0.01	0.086 ± 0.002
CdSe/9MLCdS$_{film}$	1.2 ± 0.2	0.62 ± 0.08

For the self-assembled monolayer thin film, the CdSe/6MLCdS had the highest Γ_r followed by the CdSe/3MLCdS and the CdSe/9MLCdS having similar Γ_r (with overlapping standard deviations). The Γ_{nr} of the monolayer thin films decreases with increasing shell thickness as expected since thicker shell increases confinement of hole wavefunction and decreases non-radiative pathways.

We can also compare Γ_r (Fig. 2.3C) and Γ_{nr} (Fig. 2.3D) of the monolayer thin films to their colloidal solution counterparts. The recombination rate values for the colloidal solution and the monolayer thin film are tabulated in Table 2.3. The only recombination rate that is smaller for the monolayer thin film than in colloidal solution is Γ_r for the CdSe/3MLCdS sample. This same trend is observed even if we use a stretched exponential function to fit the TRPL data of the thin films (Fig. A.8). Given that the CdSe/3MLCdS sample has the thinnest shell, the electron is more likely to get momentarily trapped in an un-passivated surface trap state before recombining radiatively.[136] For CdSe/6MLCdS and CdSe/9MLCdS, Γ_r increases in the monolayer thin films compared to colloidal solution. The Γ_{nr} increased for all monolayer thin film samples likely due to an increase in un-passivated surface sites and energy transfer (see Discussion).

Although the CdS shell and organic ligand shell passivating the QD surface has been reported to minimize the dark fraction or blinking of QDs, there could still be some QDs within a single batch with a higher dark fraction of emission.[37, 135] The dark fraction of QDs can reduce the PLQY but will not affect in the TRPL data which may influence the calculated Γ_r value.[71] To account for this issue, the PLQY of the different colloidal solutions and thin films and used the average PLQY for the recombination rate calculations with the standard deviation reported as error. The reported error will account for some dark fraction of QDs. Additionally, the dark fraction of QDs in a single batch is random. Since the same batch of QDs was used for the measurements in colloidal solution and monolayer thin films, we expect the fraction of dark counts to be similar in both solution and film. Hence, comparing the radiative rate ratio of monolayer thin films with colloidal solution will still hold.

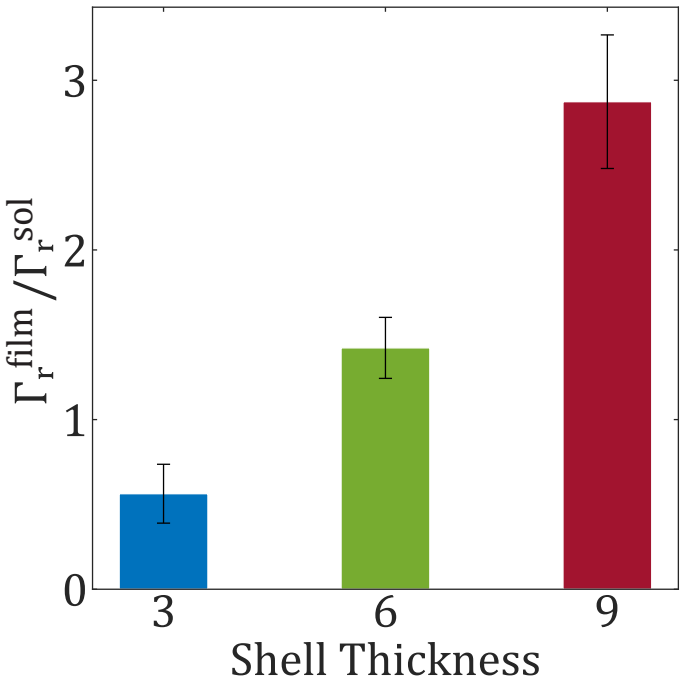

Figure 2.4: **Radiative Rate Ratio for all Three QD Samples.** Error bars were determined based on Γ_r uncertainties shown in Table 2.3.

By comparing the radiative rate ratio of the monolayer thin film with colloidal solution ($\Gamma_r{}^{film}/\Gamma_r{}^{sol}$, Fig. 2.4), we observe that that the ratio increases steeply with increasing shell thickness. For CdSe/3MLCdS, the ratio is < 1 (0.57), which we attribute to ligands being stripped from QD surface causing charge carriers to be trapped by a surface trap state as discussed above. For CdSe/6MLCdS and CdSe/9MLCdS, the ratio is >1 with the Γ_r being enhanced 1.4× for the CdSe/6MLCdS monolayer thin film and an enhancement of 2.9× for the CdSe/9MLCdS monolayer thin films than in colloidal solution. To understand the increase in Γ_r for the CdSe/6MLCdS and CdSe/9MLCdS, we must consider the electronic band structure of the core/shell QD and the role of the surface organic ligands.

2.4 Discussion

Although the PLQY and TRPL of the monolayer thin films decreased compared to the colloidal solution samples, both Γ_r and Γ_{nr} for the monolayer thin films mostly increased except

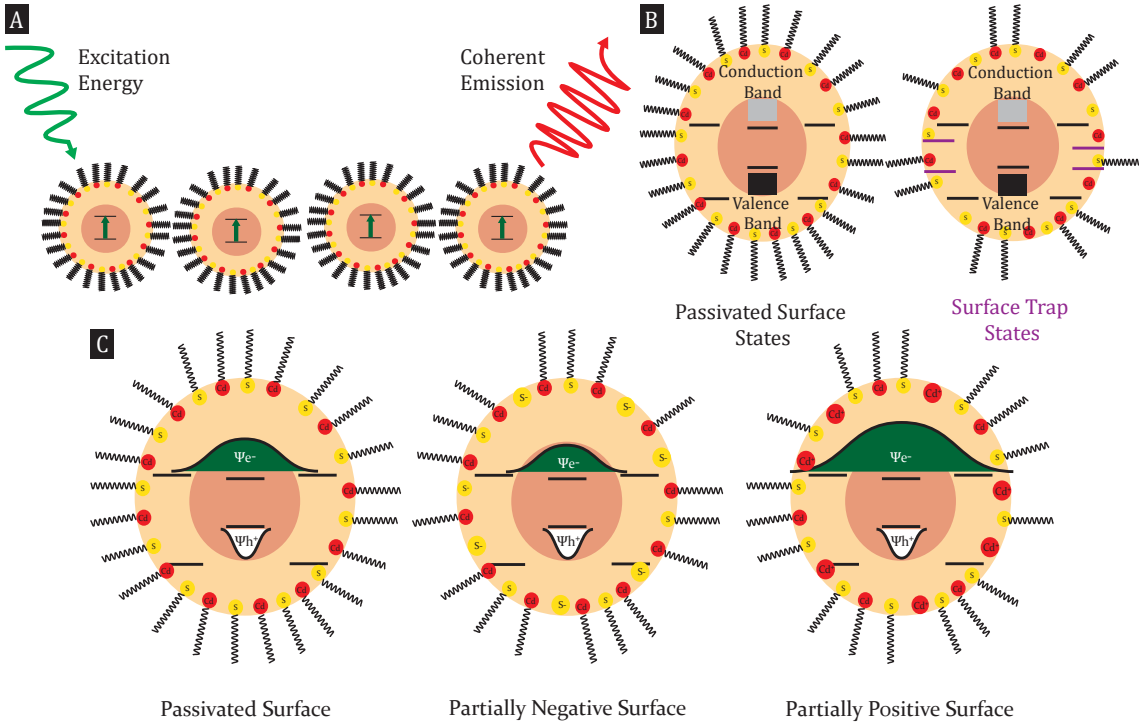

Figure 2.5: **Potential Mechanism for Increase in Γ_r for Quasi–Type II CdSe/CdS core/shell QD. A** Coherent emission due to alignment of transition dipole moments. **B** Electronic band structure diagram for a QD with a fully passivated surface(left) and after the introduction of surface trap states due to unpassivated atomic surface sites (right). **C** Electron-hole wavefunction diagram with a fully passivated surface (left), a partially negative surface (center), and a partially positive surface (right). Red atoms on QD surface correspond to Cd sites and yellow atoms correspond to S sites.

for Γ_r for the CdSe/3MLCdS monolayer thin film. The increase in Γ_{nr} for the CdSe/CdS monolayer thin films from the colloidal solution counterpart is expected since the process of Forster resonance energy transfer (FRET) has been observed for close-packed nanocrystal solids.[2, 128] The FRET hopping rate scales with $(1/R)^6$ where R is the distance between QDs. In colloidal solution the average inter-particle distance is a few hundred nanometers (two orders of magnitude larger than the diameter of the QDs). The local spatial order of the monolayer thin films allows for the inter-particle distance in these ordered domains to be dictated by the length of the ligand passivating the QD surface.[63] The short interparticle distance allows for FRET to occur since it is mediated by dipole-dipole coupling between QDs.[157] Time resolved emission spectra (TRES) of the monolayer thin films does not show a significant red shift over time as expected for systems undergoing FRET (Fig. A.9). This lack of red-shift could be due to the monodispersity in QD size resulting in a film with a

homogeneous energy landscape.[73] Additionally, the increase in Γ_{nr} for the films could be due to the partial loss of passivating ligand from the surface of the nanocrystal.[150] Inherent to the self-assembly process at the liquid-air interface, as the non-polar dispersing solvent evaporates, the organic non-polar ligands (oleylamine and oleic acid) on the surface of the QD interact with the polar solvent (DMF).[16] This unfavorable interaction can detach ligand molecules from the nanocrystal surface, leaving behind un-passivated charged surface atoms (Cd^+ or S^-) and charged molecules to interact with the polar solvent which is thermodynamically more favorable.

The increase in Γ_{nr} for monolayer thin film samples has not been reported in the past as this is the first direct PLQY measurement of a monolayer thin film. To better understand this behavior, the Γ_r equation from Fermi's golden rule needs to be considered:

$$\Gamma_r = \frac{\omega^3 n|\mu_{12}|^2}{3\pi\epsilon_0\hbar c^3} \tag{2.1}$$

The three variables that change for each sample are the emission frequency (ω), index of refraction (n) and transition dipole moment (μ). The emission frequency has not changed from solution to thin film as no significant photoluminescence peak shift is measured. The index of refraction does change significantly between solution and thin film. The solution measurements were done in octane solvent (n=1.4) while the thin films are composed of inorganic material (CdSe n=2.59 and CdS n=2.53), organic ligand (oleic acid and oleylamine, n=1.45), air (n=1.0), and the glass cover slip substrate (n= 1.5). To determine the refractive index of the monolayer thin film, the effective medium approximation was used to approximate n for the thin film (Section A.10).[81] Briefly, the binary image of the TEM superlattices was used where the white pixels were the QDs (inorganic material, n ∼2.55) and the black pixels were some combination of the organic ligands (n=1.4) and air (n=1.0). The increase in Γ_r for the thin films is greater than the change in n despite being directly proportional in eq. 2.1. Therefore, the change in n of the monolayer thin films alone does not explain the increase in Γ_r. Additionally, we also consider a change in μ from colloidal solution to thin film (Fig. A.11 and A.12) but effective mass modeling is needed to quantify an increase in transition dipole moment and its effect on Γ_r.[71]

Since the increase in Γ_r for the monolayer thin film is not solely due to a change in environment, there must be a fundamental change occurring in the optical properties of the QDs. For the CdSe/3MLCdS monolayer thin film, Γ_r is smaller than it is in solution. Since the CdSe/3MLCdS sample has the thinnest shell, the electron can become trapped in an un-passivated surface site, until it eventually becomes un-trapped and recombines radiatively in a surface mediated recombination mechanism.[69, 33, 184] In this case, the emission will be delayed, resulting in a smaller Γ_r.[136]

We consider possible models to explain the increase in Γ_r for the other two samples with a thicker shell. For example, the arrangement of QDs in a monolayer with high spatial order

can lead to a coupling of transition dipole moments resulting in coherent emission (Fig 2.5A). An analogous coupling of vibrational motion in nanocrystal superlattices resulting in a collective phononic state has been reported.[78] Additionally, optical coherent behavior such as superradiance has been reported for quantum dot ensembles[145] and superfluorescence has been reported in lead halide perovskite nanocrystals.[139] However, superfluorescence has only been reported in nanocrystals with comparable radiative lifetime and dephasing times[163] whereas the dephasing time of shelled CdSe QDs has been reported to be many orders of magnitude shorter than their radiative lifetime.[110, 82] Additionally, characteristic signatures of coherent coupling like shifts in photoluminescence energy and a small Γ_{nr} is not observed in the thin films. We then consider the quasi type-II electronic band structure of CdSe/CdS QDs composed of localized energy levels as well as a continuum of states that make up the valence and conduction bands (Fig. 2.5B, left). However, if ligands are removed from the surface of the QD, unpassivated atomic sites can introduce trap states to the electronic structure of the QD (Fig 2.5B, right). The introduction of trap states can change the hybridization of localized energy levels with the extended continuum of states in the QD system[83] which can alter the transition dipole moment and ultimately Γ_r. We have observed that removing ligands from the QD surface affects both Γ_r and Γ_{nr} in colloidal solution (Fig. A.13-A.15).

Unpassivated surface sites can also shift the delocalization of the electron wavefunction.[89, 58] In an ideal, fully passivated QD, the hole wavefunction is localized in the CdSe core while the electron wavefunction can be delocalized in the shell until eventual exciton recombination due to Coulombic attractions (Fig. 2.5C, left).[12, 56, 138, 17] Ligand removal during the self-assembly process can cause the QD surface to become partially charged which can alter the overlap integral with electron and hole wave functions similarly to quantum-confined Stark effects that have been reported in single nanoparticles.[123, 20] Even if the QD surface is partially charged, the monolayer thin film will remain charge neutral as the interleaving surfactant ligands remain to balance the charges hence why quantifying the QD ligand coverage in the thin films is challenging. Further consideration of a partially charged QD surface model is useful for strategic engineering QD based devices. If the QD surface is partially negatively charged, electron-electron repulsion will compress the electron wavefunction, increasing its overlap with the hole wavefunction (Fig. 2.5C, center). This type of mechanism results in an increase in Γ_r as shown in colloidal solution (Fig. A.15) which is beneficial for designing materials with brighter emission. On the other hand, if ligands are removed so that the QD surface is partially positive, the electron wavefunction can be further delocalized into the CdS shell potentially leading to charge carrier trapping (Fig. 2.5C, right). Computational methods have been developed to quantify electron and hole wavefunction overlap in core/shell QDs[12, 56, 71] which in the future can be applied to samples with different ligand shell coverage. Although the delocalization of the wavefunction may not be symmetrical since it depends on the distribution of unpassivated surface sites and since the trapping can be reversible,[136] engineering a partially positively charged QD surface would be a beneficial design for QD systems for charge transfer processes.

To confirm our proposed mechanisms for the increase in Γ_r, future work systematically modulating the ligand shell of the QD system with different chemical species such as electron withdrawing groups is required. Although developing a method to suppress non-radiative pathways remains the biggest obstacle to engineering bright QD monolayer thin films, these mechanisms provide some insight for rationally designing nanotechnology.

2.5 Conclusion

In conclusion, the PLQY and the recombination rates of CdSe/CdS core/shell QD monolayer thin films have been experimentally determined. We observed an increase in the Γ_r for the monolayer thin films relative to the colloidal solutions, which is not fully explained by the change in the QD environment, but rather by a fundamental change in the material. For the CdSe/6MLCdS and CdSe/9MLCdS monolayer thin films, our measurement capacity reveals that Γ_r is larger compared to that in solution, which can be due to a change in the QD electronic structure due to the removal of ligands attached to passivated surface sites during the self-assembly process. Although Γ_r increases for two of the monolayer thin films, Γ_{nr} is greater for all monolayer thin films compared to solution. Improving the control of ligand coverage on the QD surface in the monolayer thin films will be instrumental in engineering monolayer thin films with high Γ_r. For instance, it would be desirable if trap sites could be engineered so that the increment of Γ_r outcompetes the increment of Γ_{nr}.

Chapter 3

Incorporating Atomic Defects into Quantum Dots During Colloidal Synthesis for Specific Energy Applications

This work was a result of a fruitful collaboration with members of Professor Naomi Ginsberg's research group, specifically, Dr. Trevor Roberts and Professor Rongfeng Yuan. Collaborating with such wonderful scientists was a highlight of my graduate studies. The results of this collaboration were published in Science Advances in 2023.[176] In this chapter, I will discuss in more detail the synthesis, structural characterization, and elemental composition of Te-doped CdSe/CdS QDs.

3.1 Introduction

In Chapter 1, we discussed how we can tune quantum dot's (QD) emission based on their size, allowing for materials of the same composition to have vastly different properties. Along with their tunable electronic properties, QDs have bright and narrow photoluminescence and excellent photostability which makes them excellent candidates for displays,[74] LEDs,[43, 41] or lasers.[88, 67] However, there are limitations on the spectral range for which we can reasonably tune a given material's emission. These limitations are determined by the bulk bandgap of the material. For instance, the bulk bandgap of CdSe is 1.74 eV (712 nm).[26] Therefore, engineering QDs that emit in the 700 nm region is challenging as we are approaching the bulk limit. In order to so, we have to grow QDs to a large size and compromise on engineering nanocrystals with a particular structure, size and shape.

Synthetic strategies can be used to overcome those limitations through chemical trans-

formations. Post-synthetic, cation exchange reactions have been reported where the cations ligated within a QD are substituted with different ones in solution.[50, 120, 111] This exchange reaction is fairly simple and provides a powerful way to tune the nanocrystal composition and phase. However, an anion exchange analogue has not been demonstrated due to the larger size of the atoms and lower diffusivity of the lattice anions, which leads to slow reaction kinetics and poor structure retention.[18] An alternative route to engineer QDs with different anionic compositions is by introducing dopants during the high-temperature colloidal synthesis.[57]

Investigating defects in colloidal quantum dot systems has been an active area of research for decades. Although the literature mainly focuses on identifying and eliminating defects to improve material purity, there are many benefits of incorporating defects like dopants to alter the electronic and optical structure of colloidal systems to tune transport. Generally, dopants introduce midgap states in the system that allow for new pathways for optical excitation and recombination.[10] In colloidal quantum dot solids, the main form of transport has been identified as exciton transport due to the quantum confinement of charge carriers.[63, 2] In core/shell systems, the shell isolates the electronic excited states within the core of the nanocrystal. By adding small amounts of Te dopants to a CdSe QD, we expect that hole trap states will be engineered to the electronic structure of the nanocrystal.[9] Isolated defects are unlikely to electronically couple to the lattice, but Te has been shown to couple to the CdSe host matrix as if it was CdTe.[176] Uniform distribution of Te into the CdSe will instead change the bandgap of the material rather than introduce isolated states. Although studies have been conducted on trap-related emission of CdSe: Te nanocrystals,[57] the effect of the Te-dopant on transport has yet to be studied. By extending this study of Te-doped CdSe nanocrystals to QD-based solids, we can engineer structures with spatial order but heterogeneous energy landscapes to investigate the role of Te-dopants in exciton transport.

Herein, we report the preparation of CdSe:Te/CdS QD monolayer superlattices as a platform to study the role of defects in exciton transport. We synthesize Te-doped CdSe by altering the precursors used in the colloidal synthesis. By changing the ratio of Te- and Se-precursor during the hot injection step, we can engineer CdSe QDs with different amounts of Te dopants, but with uniform size distribution, wurtzite crystal structure, and broad, red-shifted emission. We compare the optical and structural properties of the Te-doped CdSe QDs with that of undoped CdSe QDs with similar emission. Elemental mapping is used to quantify the average amount of Te-dopant in the QD samples. By growing a 3 monolayer (ML) hexagonal CdS shell around the doped and undoped QDs we engineer a system that is capable of assembling into monolayer superlattices with long-range spatial order. Through Time-Resolved Ultrafast Stimulated Emission Depletion (TRUSTED) microscopy, we study the spatiotemporal evolution of charge carriers in these superlattices to elucidate the role of dopants in exciton transport.

3.2 Materials and Methods

Chemicals:

Cadmium oxide (CdO, $\geq$ 99.99%, Sigma Aldrich), octadecylphosphonic acid (ODPA, 99%, PCI Synthesis), trioctylphosphine oxide (TOPO, 99%, Sigma Aldrich), trioctylphosphine (TOP, 99%, Strem), selenium powder (Se, 99.999%, Sigma Aldrich), tellurium powder (Te, 99.8%, Sigma Aldrich), oleic acid (OA, 90% tech grade, Sigma Aldrich), oleylamine (OAm, 70% tech grade, Sigma Aldrich), 1-octadecene (ODE, 90% tech grade, Sigma Aldrich), n, n-dimethylformamide (DMF, anhydrous 99%, Sigma-Aldrich), toluene (anhydrous 99.5%, Sigma Aldrich), acetone (anhydrous, 99.5%, Sigma Aldrich), hexanes (mixture of isomers, anhydrous 95%, Sigma Aldrich), n-octane (98%, reagent grade, Sigma Aldrich). 0.2 M Cd(oleate)2 in ODE precursor was prepared using a previously reported procedure1. Briefly, appropriate amounts of CdO, OA, and ODE were degassed for about two hours under vacuum at 110 °C until all gases and water had evolved. The reaction was then heated to 240 °C under argon for 30 minutes until a clear, slightly yellow, solution forms. The flask was then cooled to 110 °C and degassed a second time for an additional 1-2 hours to remove additional water. The solution was stored in an argon-filled glovebox.

X-Ray Diffraction

X-ray diffraction was measured of nanocrystal sample drop-casted on a silicon substrate. XRD was collected on a Bruker Phaser D2 diffractometer with a Cu kα source operated at 30 kV and 10 mA with a 160 SSD detector. Diffraction measurements were done from 20° to 60° 2θ with increments of 0.01° with an integration time of 3 s/step.

TEM Characterization and Image Analysis

Transmission Electron Microscopy was used to characterize nanocrystal superlattices using a FEI Tecnai T20 S-TWIN TEM operating at 200 kV with a LaB6 filament. TEM images were collected using a Gatan Rio 16IS camera with full 4k by 4k resolution using the drift correction feature. TEM samples were scooped from self-assembly well onto Electron Microscopy Sciences CF400-Cu 400 mesh standard carbon TEM grids. Sizing distribution curves were generated from TEM images of >2000 nanoparticles using a custom written MATLAB script in which the details have been previously reported.[25] Image analysis and Fourier transformation of image was performed on ImageJ software.

Optical Characterization of Colloidal Nanocrystal Samples

Steady-state absorbance spectra were collected in octane with a Shimadzu UV-3600 double beam spectrometer operating with 1 nm slits. Steady-state photoluminescence, time-resolved photoluminescence, time resolved emission spectra, and fluorescence anisotropy measurements were done using a Picoquant Fluotime 300 Spectrometer with a time-correlated single photon counting apparatus, a PMA 175 detector and a LDH-P-C-405 diode laser with a 407.7 nm excitation wavelength. TRPL measurements were done with 50 ps laser pulse width and a repetition rate of 10 MHz. Multiexciton generation is not considered for these measurements since the average number of excitons per pulse is $<<1$. TRES measurements were done by measuring the PL after a 0.5-50 ns delay post excitation pulse. The fluorescence anisotropy measurements were performed by rotating the emission polarizer from 0-90° and collecting the number of counts at the center wavelength.

Self-assembly of Nanocrystals Superlattice

Formation of QD superlattices (QDSL) was performed using a previously published self-assembly method[49]. Monolayer nanocrystal superlattices were formed at the liquid-air interface at room temperature.The nanocrystal stock solution was diluted in octane to a proper concentration to obtain monolayer coverage. Approximately, 50 μL of diluted nanocrystal solution was drop-casted on top of 1 mL of DMF in a 1 cm^2 square Teflon well. The well was covered with a glass cover slip to slow solvent evaporation rate overnight. The self-assembled superlattice was scooped onto a plasma cleaned glass cover slip for optical measurements or a Cu 400 mesh standard carbon TEM grid for structural characterization.

STEM-EDS Characterization and Analysis

Elemental composition analysis of nanocrystals was performed at the National Center for Electron Microscopy, Molecular Foundry, Lawrence Berkeley National Laboratory. Samples were drop-casted on ultrathin 400 mesh carbon Cu TEM grids and left under vacuum to remove any excess solvent and oxygen plasma treated. High-angle annular dark field HAADF-STEM and STEM-EDS maps was collected on the FEI TitanX 60-300 microscope using a FEI low-background double-tilt holder. HAADF-STEM was measured at 300 kV with a beam convergence semiangle of 10 mrad using a Gatan HAADF detector. STEM-EDS mapping was acquired at 300 kV with a screen current of $\sim$ 2 nA using four windowless silicon drift detectors with a total solid angle of 0.7 steradians and 140 eV energy resolution. STEM-EDS maps were collected using the Bruker Esprit software for 5-10 minutes utilizing drift correction. Quantification of the elemental composition of each sample was done using the Bruker Esprit software using the Cliff–Lorimer method for each element: Cd K-series,

Se K-series, S K-series, Te L-series.

Time-Resolved Emission Spectra

The sample was pumped by a 470 nm (Picoquant diode laser) laser with ∼100 ps temporal resolution. Photoluminescence spectra from 550 to 750 nm were collected in a Picoquant FluoTime 300 Fluorometer at normal incidence with wavelength step size of 2.5 nm for the CdSe:Te/CdS QDSL sample. Luminescent photons were collected by a photomultiplier tube detector, and the factory-set wavelength-dependent response of the photomultiplier tube was used as a calibration curve to correct the individual spectra. The peak emission wavelength was extracted by fitting the peak in the time-dependent photoluminescence spectra to a Gaussian function.[176]

Time-Resolved Ultrafast Stimulated Emission Depletion

TRUSTED[127] is used in a home-built confocal microscope with a 63 x 1.4 numerical aperture Plan Apo Leica objective (HC PL APO 63×/1.40 oil CS2, Leica Material #11506350). The excitation and depletion laser pulse trains at 200 kHz were derived from third-harmonic and second-harmonic noncollinear optical parametric amplifiers (Light Conversion), respectively, pumped by a 10-W Light Conversion PHAROS regeneratively amplified laser system with a fundamental wavelength of 1030 nm. The 25-fJ excitation pulse was centered at 550 nm with 20 nm bandwidth, and the two 125 pJ depletion pulses were centered at 740 nm with a bandwidth set to 16 nm. Both the pump and depletion (STED) pulses were fiber-coupled into single-mode polarization-maintaining fibers to produce high-quality Gaussian modes. A vortex phase mask (RPC Photonics VPP-1a) was then used to generate the annular depletion pulse beam mode. The pulses were then directed through a quarter waveplate positioned to circularly polarize the depletion pulses. During the experiment, the sample is rastered with a PI Nano scanning piezoelectric stage (P-545.3C7) in steps of 15 μm over a 60-μm by 60-μm area. Data from the resulting 25 spatial locations are averaged to improve the signal-to-noise ratio. Epifluorescence is collected between 687.5 and 712.5 nm through dichroic mirrors and emission filters (three 700/25 filter from Edmund Optics) and is focused onto a fast-gated SPAD detector with a 200 ps rise time (A. Tosi, SPAD lab, Politecnico di Milano; PicoQuant) controlled by a Picosecond Delayer (MPD) that is triggered just after the arrival of the second depletion pulse to eliminate fluorescence occurring before the definition of the detection volume. We phase-lock the detection data stream to the timing of an optical chopper (Newport 3501) placed in the excitation pulse line, so that we may separately determine the photon count rates during the "excitation on" and "excitation off" chopper phases for multiple cycles. The count rates obtained during these open and closed phases of the chopper are each corrected for the classic pile-up effect with a simple Poisson correction factor before we take the difference of the two to isolate the count rate that is attributed to

the modulated excitation pulse only. The second STED pulse is separately modulated with a shutter so that data collected when this pulse is blocked can be used as a reference and control. The signal versus delay time obtained when this second depletion pulse is unblocked is divided by the signal versus delay time observed when it is blocked. The resulting data are then normalized to the extrapolated value of this ratio at zero delay time to calculate the fraction of remaining excitations in the detection volume as a function of the delay time.[176]

3.3 Incorporation of Te dopants in Quantum Dots

Synthesis of Doped Quantum Dots

Previous work on Te-doped CdSe nanocrystals [57, 8] report introducing Te to a known CdSe synthesis by adding small amounts of tellurium precursor during the hot injection step of the reaction. By changing the molar ratio of Te to Se, we can alter the amount of Te-dopant in the CdSe QD. In this work, we follow a similar approach but using a CdSe colloidal synthesis procedure that is known to yield a narrow size distribution of nanoparticles[31] which is desirable in order to form highly-ordered superlattices.

Wurtzite CdSe:Te{X%} Nanocrystals:
Te-doped CdSe core nanocrystals were synthesized by modifying a similar procedure for undoped CdSe nanocrystals.[31] Briefly, 120 mg CdO, 560 mg ODPA, 6 g TOPO were degassed under vacuum in a 50 mL round-bottom flask at 150 °C for 1 hour. The mixture was then heated to 320 °C under argon gas and maintained at 320 °C until solution turned clear indicating formation of a complex. Upon completion of complex formation, 3 g of TOP was injected in the solution and then the temperature was raised to 360 °C. A solution of the appropriate ratio of Se and Te totaling 1.5 mmol in 0.72 g TOP was swiftly injected when the temperature approached 360 °C. Upon injection, CdSe nanocrystals were formed and were allowed to grow for 90 seconds to produce large, uniform cores. The solution was then rapidly cooled with compressed air to 120 °C before injecting 10 mL of anhydrous toluene and transferring to an inert atmosphere. The nanocrystals were cleaned in an inert environment with successive precipitation and redispersion using acetone and hexane respectively and were stored in 3 mL of hexane. Concentrations were determined by a previously reported empirical formula[79] and size was determined via TEM image analysis.

In order to understand the incorporation of Te dopants during the hot injection process of the colloidal synthesis of CdSe QDs, different samples were synthesized with varying amounts of Te dopant. Samples with 2%, 5%, and 7% of Te were synthesized by varying the Se:Te precursor ratios (Table 3.1). The amounts of Se precursor (Se powder) and of Te precursor (Te powder) were determined stoichiometrically so the total amount of precursor is 1.5 mM. The precursors were then colloidally dispersed in TOP before being injected into

Table 3.1: CdSe:Te{X%} Precursor Amounts

CdSe:Te{X%}	Te powder (mg)	Se powder (mg)
0	0	120
2	2.4	114.0
5	6.0	111.6
7	8.4	117.6

the reaction flask.

Hexagonal CdSe:Te{X%}/CdS core/shell Nanoplates:
An insulating hexagonal CdS shell, typically 3 ML thick, was grown around the Te-doped CdSe nanocrystals to improve their luminescence using a previously reported preparation.[119] The anisotropic shell growth was grown by first degassing under vacuum 3 mL of ODE, 3 mL of OAm and 100 nmol of CdSe cores in a 25 mL round-bottom flask at 110 °C for 30 mins. The solution was then heated to 310 °C under Ar. When the temperature reached 240 °C, injections of Cd and S precursor solutions in ODE started at a rate of 3 mL/hr using a syringe pump. The Cd precursor solution contained 4 mL of 0.20 mM $Cd(OA)_2$ and the S precursor contained ∼25 mg of S powder in 3 g of TOP. Upon completion of the precursor injections, the reaction was maintained at 310 °C for 10 minutes, then cooled rapidly using compressed air to room temperature. Successive precipitation and redispersed using acetone and hexane respectively were done to clean the nanocrystals capped with OA and OAm before they were stored in 2 mL hexane in an inert atmosphere.

Size Analysis

A size analysis of the QDs is performed using Transmission Electron Microscopy (TEM) images (Fig. 3.1, left) of CdSe QDs with 2% (Fig. 3.1A), 5% (Fig. 3.1B) , and 7% (Fig. 3.1C) Te dopant concentration to generate a distribution of the diameter (Fig. 3.1A-C, middle left) and feret diameter (Fig. 3.1A-C, middle right) of the ensemble of nanocrystals for each sample. The distribution in diameter assumes that the nanocrystals are isotropic and fits an outline of a circle around each nanocrystal reporting the diameter of the outlined circles. On the other hand, the distribution of ferret diameter considers any anisotropic shapes of nanocrystals and reports the longest distance across the nanocrystals, performing no fitting of the nanocrystal into a particular shape. The difference between the diameter and feret diameter of the nanocrystal ensemble corresponds to how spherical the nanocrystals are (Fig. 3.1, right). The higher the difference between the diameter and the feret diameter, the greater the deviation of the shape of the nanocrystal to a circle. All diameters and feret diameters reported from the size analysis are within uncertainty of each other. Hence, these QDs can be considered to be the same size even though they have different amounts of dopant.

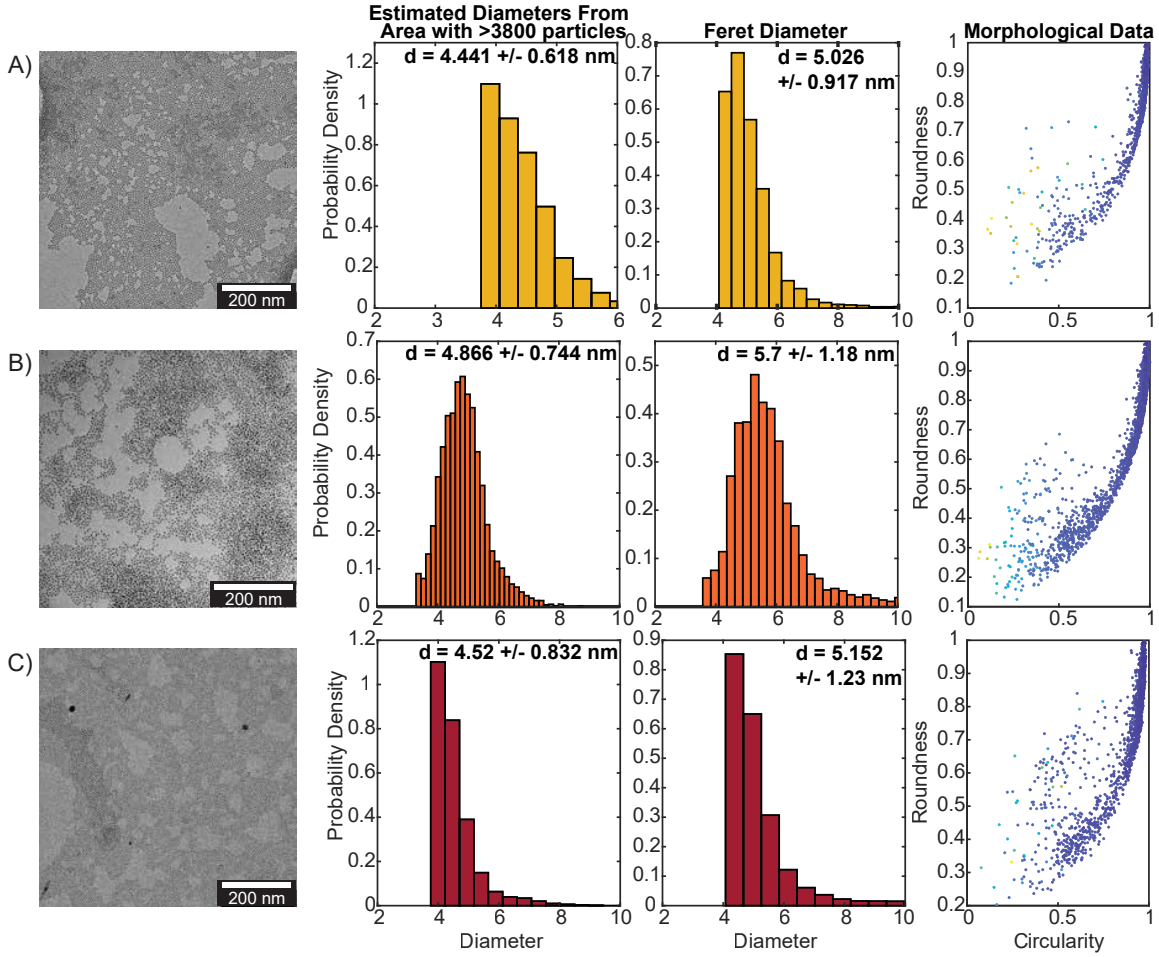

Figure 3.1: **Size Analysis of Transmission Electron Microscopy Images.** TEM images and corresponding size analysis with estimated diameter, feret diameter and morphological data of **A** CdSe:Te{2%}, **B** CdSe:Te{5%}, and **C** CdSe:Te{7%} QDs.

Traditionally, the size distribution of a colloidal CdSe QD sample can be measured through its optical properties, primarily its absorbance and photoluminescence. The wavelength of the first excitonic absorption peak and the absorbance at that peak of a colloidal solution of known concentration can be used to calculate the extinction coefficient and the diameter of the nanoparticle sample using previously reported equations [175]. Whereas the linewidth of the photoluminescence (PL) peak of the nanocrystals corresponds to the size distribution of the QD sample. Given that the emission of QD can be tuned with size, samples with a broader PL linewidth have a larger size distribution whereas samples with a narrower PL linewidth have a smaller size distribution. In Figure 3.1 we observe that

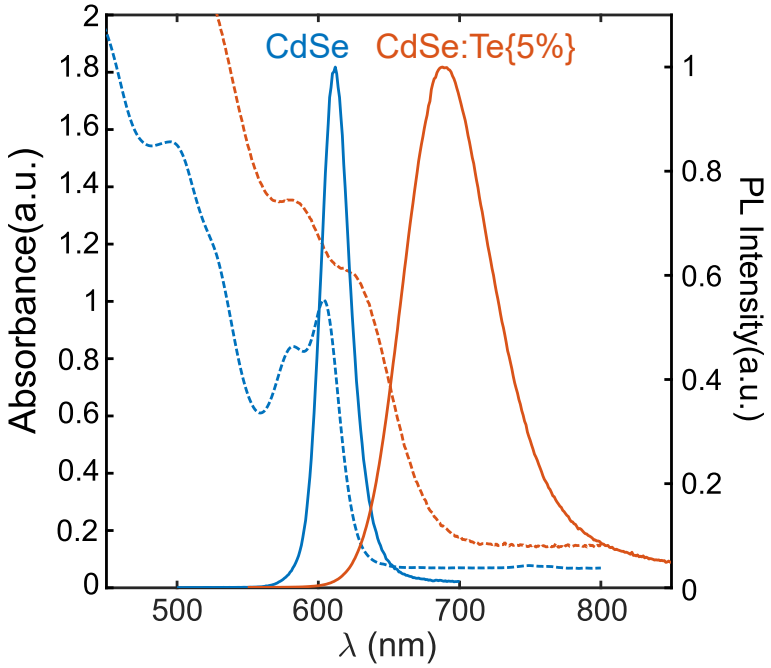

Figure 3.2: **Absorbance and Photoluminescence of Undoped and Doped CdSe QDs.** Absorbance (dashed) and PL (solid) of CdSe (blue) and CdSe:Te{5%} (orange)

the Te-doped QDs have a similar, narrow size distribution regardless of the amount of Te-dopant. However, the absorbance and PL peak of a Te-doped CdSe QDs (Fig. 3.2, orange) is much more red-shifted and broader than undoped CdSe QDs (Fig. 3.2, blue). Therefore, the only way to measure the size distribution of doped QDs is through microscopy image analysis.

X-Ray Diffraction

From the powder X-ray diffraction patterns, we observe that the incorporation of Te atoms in the CdSe matrix does not significantly affect the CdSe crystal structure of the nanocrystal (Fig. 3.3). CdSe and CdTe quantum dots can be synthesized to have either a wurtzite (wz-) or a zinc blende (zb-) crystal structure. The quantum dots used in the work have been prepared by modifying a known high-temperature synthesis of wz-CdSe[31]. It has been reported that when synthesized at high temperatures, the zb-CdTe crystal structure is favored over wz-CdTe.[107] The wz-CdSe XRD peaks are shown in a dashed line. All wurtzite peaks are present for the Te-doped and undoped CdSe quantum dots. As we increase the amount of Te dopant in the CdSe host matrix, we observe a broadening of the diffraction peaks due to minor change in the lattice parameter due to Te having a larger atomic radius than Se. For the CdSe:Te{7%} sample that has the most Te dopants, the broadening of the peaks

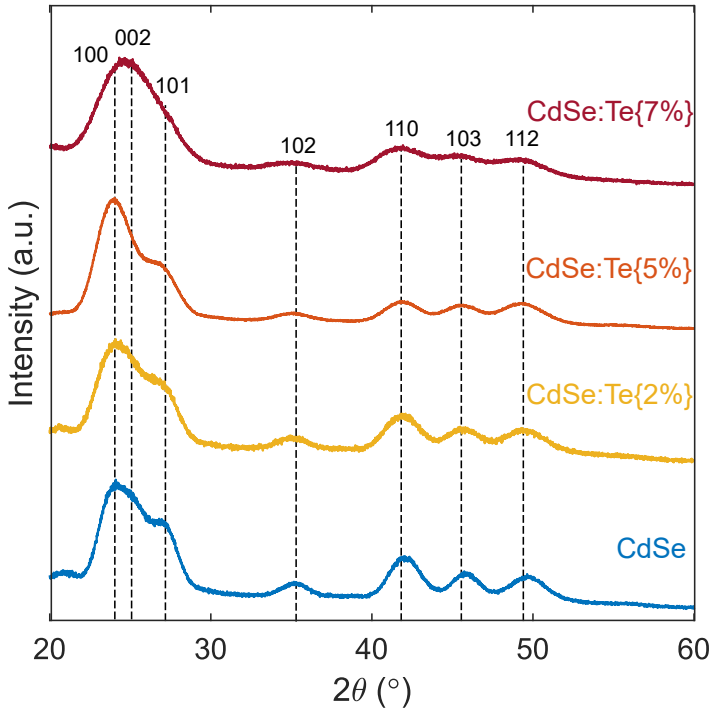

Figure 3.3: **X-Ray Diffraction of Undoped and Doped CdSe QDs.** XRD of wurtzite CdSe (blue), CdSe:Te{2%} (yellow), CdSe:Te{5%} (orange), and CdSe:Te{7%}(red) QDs. Wurtzite peaks reported in dashed lines.

leads to a merging of the 101 and 002 peaks. The presence of the other wz-CdSe peaks (102,110,103,112) shows that the Te dopant at these dopant levels does not significantly change the crystal structure of the wz-CdSe nanocrystals. We also do not observe any signature zb-CdTe XRD peaks in the XRD measurements. Based on these measurements, we can conclude that the Te is likely incorporated into the CdSe matrix as a dopant as opposed to the formation of a CdSe:CdTe alloy.

Optical Properties of Te-Doped Quantum Dots

Despite having similar sizes, crystal structure and shell thickness, the amount of Te dopant drastically changes the optical properties of the samples. For the undoped CdSe/CdS QD the first exciton absorption peak is well-defined at 625 nm (1.98 eV) and the PL is fairly homogeneous with a PL peak at 632 nm (1.96 eV) and a FWHM of 13 nm (0.04 eV) (Fig. 3.4A). As we increase the amount of Te-dopant in the CdSe core, the first exciton absorption

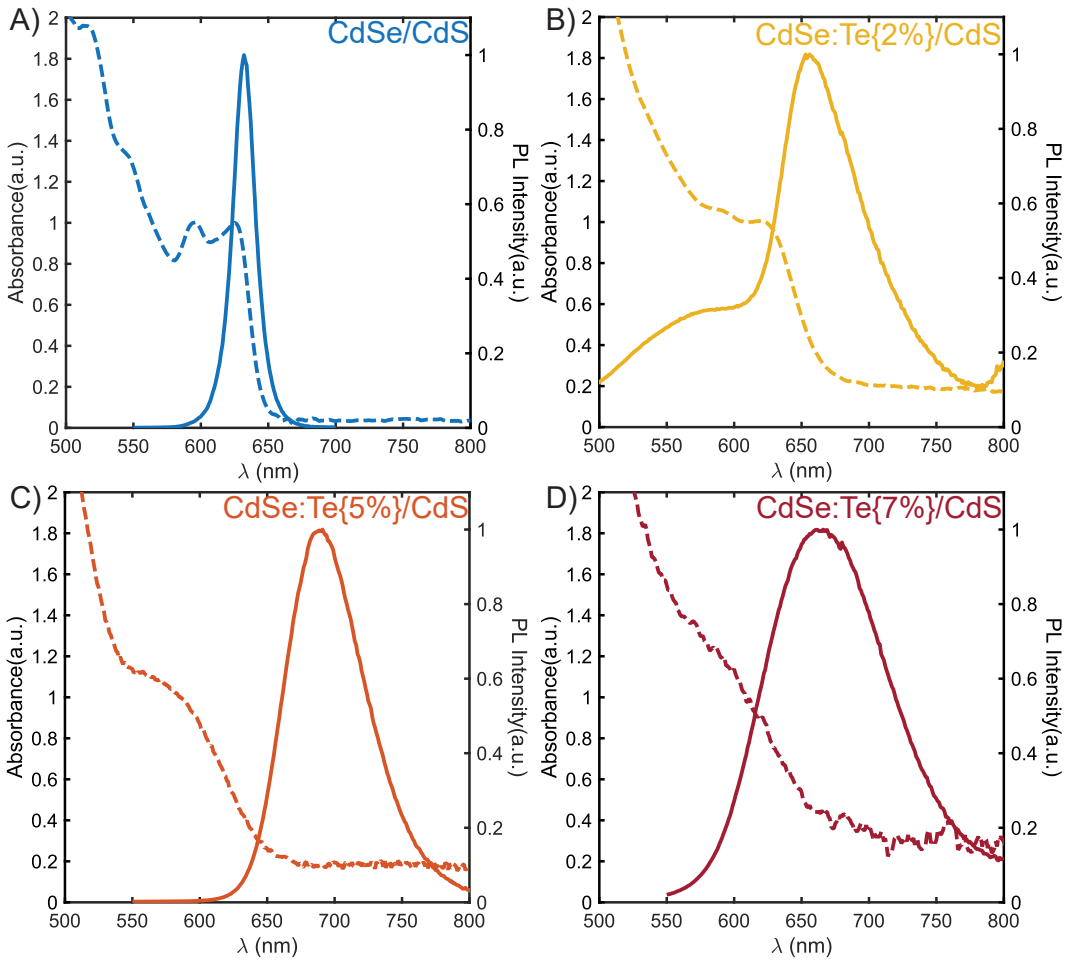

Figure 3.4: **Absorbance and Photoluminescence of Undoped and Doped CdSe QDs.** Absorbance (dashed) and PL (solid) spectra of **A** CdSe/CdS, **B** CdSe:Te{2%}/CdS, **C** CdSe:Te{5%}/CdS, and **D** CdSe:Te{7%}/CdS.

peak becomes less defined, the PL peak redshifts and becomes broader with a longer red tail. The increase in spectral linewidth with doping is likely a result of several Te atoms per CdSe QD core creating a distribution of traps within a band gap.[57] For the CdSe:Te{2%}/CdS sample, the first exciton absorbance peak is close to that of the undoped sample at 623 nm (1.99 eV), but its PL peak is fairly different (Fig. 3.4B). There appears to be one peak at 575 nm (2.16 eV) and another at 656 nm (1.89 eV). That is likely due to heterogeneous incorporation of Te within the QDs in the sample. The peak at 656 nm is much broader and inhomogeneous than the undoped sample with a longer red tail. The homogeneous linewidth is 28 nm (0.08 eV) and the inhomogeneous linewidth is 43 nm (0.12 eV). For the CdSe:Te{5%}/CdS sample, the first exciton absorbance peak is much less defined and ap-

pears more blue shifted than for the undoped and 2% doped sample at about 584 nm (2.12 eV). We do only observe one PL peak for the 5% sample centered at 688 nm (1.80 eV) with a homogeneous linewidth of 29 nm (0.07 eV) and inhomogeneous linewidth of 41 nm (0.10 eV) similar to the 2% doped sample (Fig. 3.4C). The CdSe:Te{7%}/CdS sample does not have a distinguishable first exciton absorbance peak. It has one PL peak centered at 664 nm (1.87 eV) but the peak has a homogeneous linewidth of 51 nm (0.14 eV) and inhomogeneous linewidth of 60 nm (0.16 eV) (Fig 3.4D). Single-particle emission spectroscopy of Te-doped CdSe QDs have also shown an increase in the distribution of peak energies and spectral widths with doping.[176] Since the increase in spectral features is true for both the single QD and the QD ensemble, we can assume that the Te dopant has been incorporated homogeneously within the CdSe core. The incorporation of Te-dopants into the CdSe core drastically changes the absorbance and PL of the material, however besides the first exciton absorbance peak becoming less defined, these properties do not change systematically.

Te-Doped Quantum Dot Superlattices

Formation of QD superlattices (QDSL) was performed using a previously published self-assembly method.[49] Monolayer nanocrystal superlattices were formed at the liquid-air interface at room temperature. We can image the spatial ordering of the QDSL using TEM (Fig. 3.5). We can compare how the Te-incorporated in the CdSe core affects the formation of the QDSL. In Figure 3.5A, a QDSL composed of undoped CdSe/3MLCdS shows uniform close-packed monolayer coverage at large length scales. Different domains with local spatial ordering are also present. In the Te-doped sample, a similar QDSL image is observed (Fig. 3.5B) which means the incorporation of the Te dopant does not affect the self-assembly process. Additionally, we obtain the same uniform monolayer coverage for both undoped (Fig. 3.5C) and doped (Fig. 3.5D) samples with a thicker shell. The thicker shell means the QDs are slightly larger and therefore the domains of local spatial ordering are larger as well. From the TEM images of the QDSL we can see that regardless of Te-incorporation or QD size differences due to shell thickness, the local environment for each QD in the QDSL is identical. In other words, each QD has the same number of nearest neighbors in the QDSL.

High Resolution Transmission Electron Microscopy

HRTEM was performed on the QD superlattices to confirm the nanocrystal shape, ordering and crystallographic alignment. For the CdSe:Te{5%}/3MLCdS samples studied, we measured these highly spatially ordered superlattices (Fig. 3.6A). Based on the fast Fourier transform (FFT) inset of the image we also observe crystallographic ordering since there are discrete points in the FFT instead of rings that are often observed in disordered systems. By zooming into a smaller section of the image (Fig. 3.6B), we better observe the crystallographic alignment of these QDs as the discrete points are localized in a specific

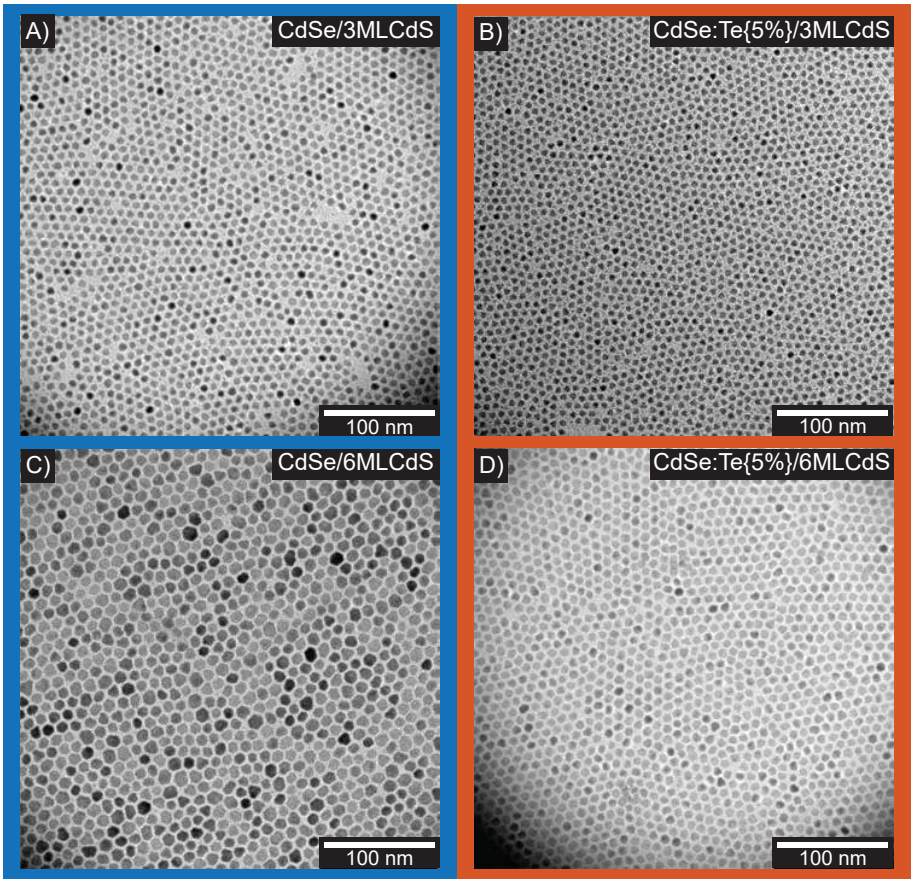

Figure 3.5: **Transmission Electron Microscopy Images of QD Superlattices.** TEM images of QDSLs of **A** CdSe/3MLCdS, **B** CdSe:Te{5%}/3MLCdS, **C** CdSe/6MLCdS, and **D** CdSe:Te{5%}/6MLCdS.

region showing that there is interparticle crystallographic alignment. The image of one CdSe:Te{5%}/3MLCdS QD (Fig. 3.6C) shows only two points in the FFT that match the regions in the FFT of the wider view images. From these images we observe that the QDs have both great spatial ordering and crystallographic ordering with the *c*-axis of the QD being perpendicular to the substrate and the *a*-axis mutually aligned in-plane. We performed these same analysis for the CdSe:Te{5%}/6MLCdS QDs and observed a similar trend (Fig. 3.6D-F). Since the CdSe:Te{5%}/6MLCdS QDs are larger than the CdSe:Te{5%}/3MLCdS, the HRTEM images have better resolution and contrast, making it easier to see the QD edges and understand the nanocrystal shape. From the HRTEM of the CdSe:Te{5%}/6MLCdS sample (Fig. 3.6D-F), we can see that these QDs have a hexagonal prism shape as opposed to an isotropic circular shape.

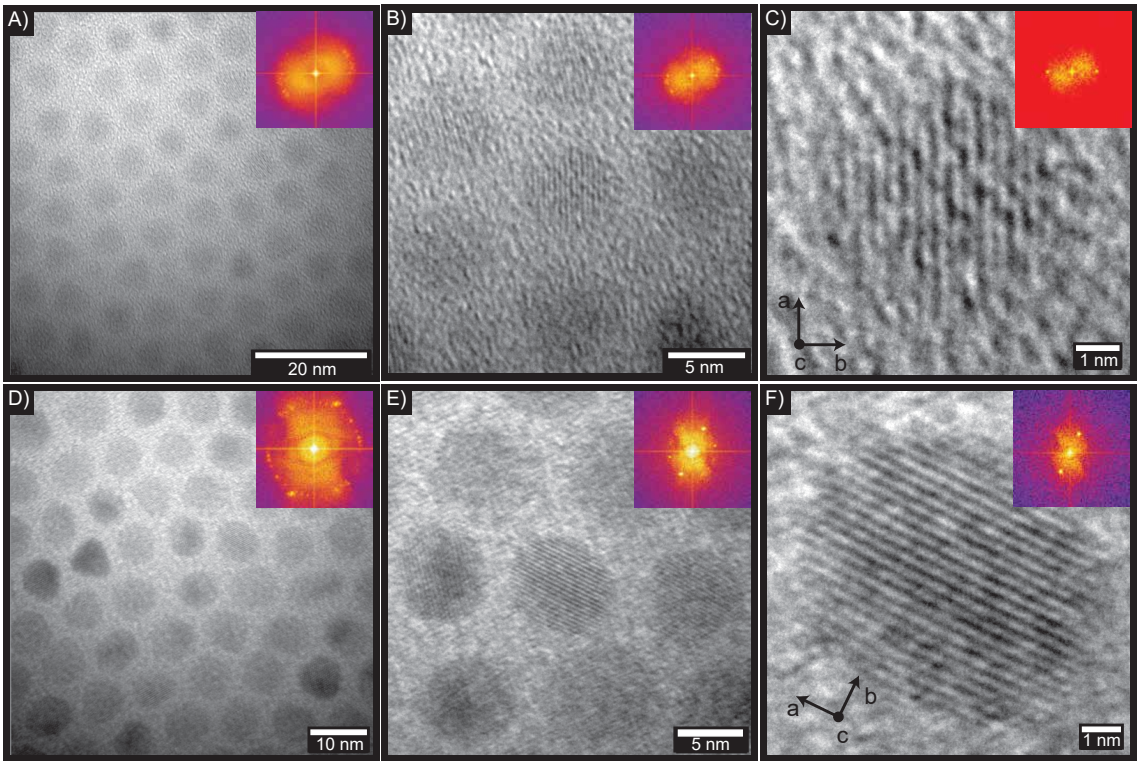

Figure 3.6: **High-Resolution TEM Images of QDSL.** HRTEM of the CdSe:Te{5%}/3MLCdS QDSL with increasing magnification so **A** 100 QDs, **B** 10 QDs, and **C** 1 QD can be observed. The same images are present for the CdSe:Te{5%}/6MLCdS sample **D-F**. The corresponding fast Fourier transforms of the images are shown in the inset.

3.4 Elemental Analysis of Doped Quantum Dots using STEM EDS

Scanning Transmission Microscopy Energy Dispersion Spectroscopy

Elemental composition analysis of nanocrystals was performed at the National Center for Electron Microscopy, Molecular Foundry, Lawrence Berkeley National Laboratory. By performing Energy Dispersive Spectroscopy in a scanning transmission electron microscope (STEM-EDS) we can measure the interaction of the microscope's high-energy electron beam with the atoms in our QDs. The electron from the STEM bean can collide with an inner shell electron of the atom resulting in the emission of the inner core electron and an inner shell vacancy. In order to occupy that inner shell vacancy, an outer shell electron relaxes and

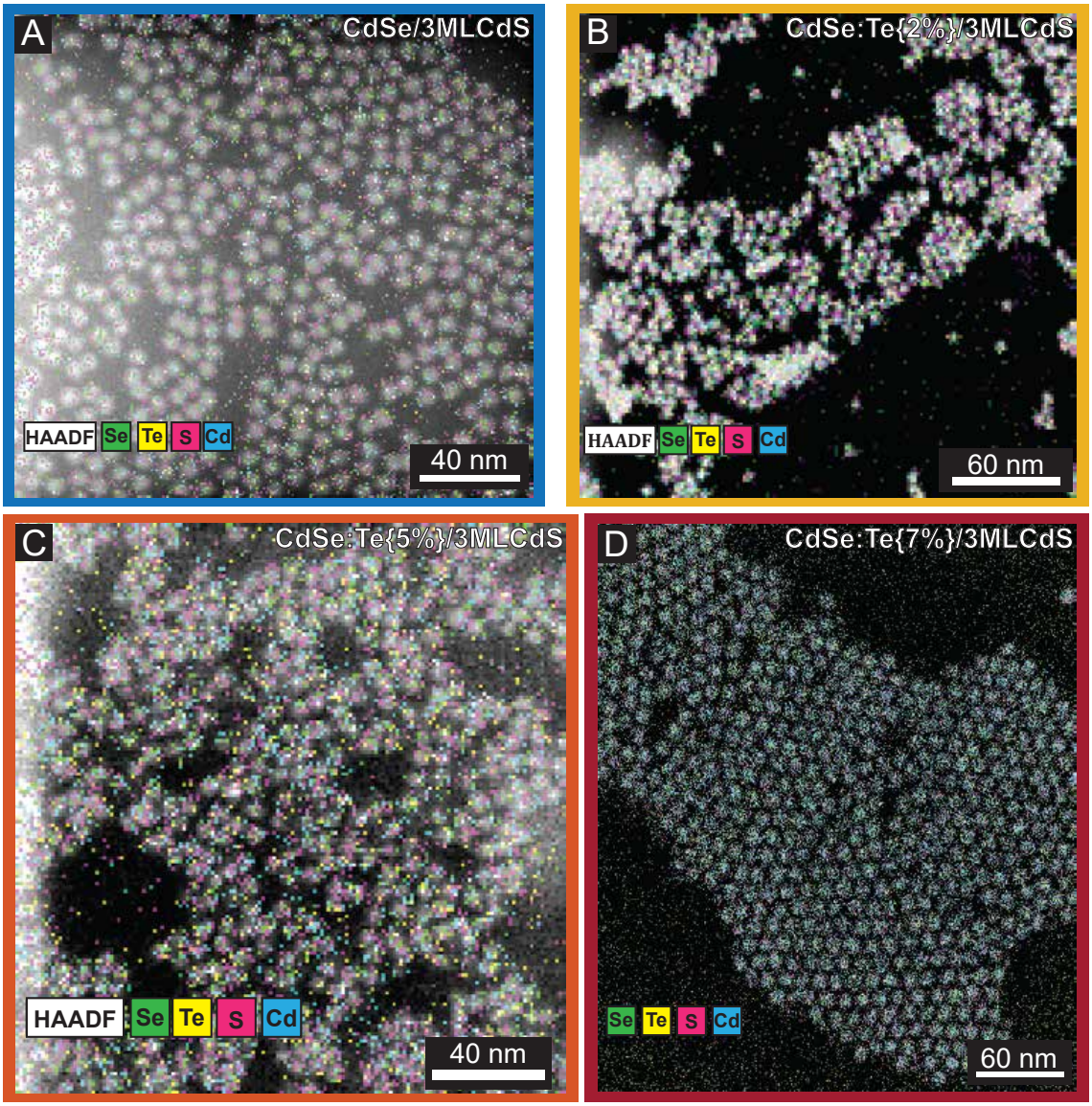

Figure 3.7: **STEM-EDS Elemental Maps Undoped and Doped CdSe/CdS QDs.** Elemental maps of **A** undoped CdSe/CdS nanocrystals **B** and 2%, **C** 5%, and **D** 7% Te doped CdSe/CdS. The maps are overlaid on top of the HAADF images for clarity.

emits a characteristic X-ray equivalent to the electronic transition. This emission is collected into a silicon drift detector that measures the energies and intensities of the X-rays at each pixel. Since these x-rays are characteristic for each element, we can use this information to identify and quantify the elements present in the sample. These measurements are much easier to do with larger samples, however by imaging regions with uniform QD monolayer

coverage that we can identify using the high-angle annular dark field (HAADF) imaging, we are able to perform these measurements on our samples.

The detected X-ray energies and intensities from our STEM-EDS measurements can be used to generate an elemental map so we can visualize and characterize the spatial distribution of the elemental composition of our samples. In Figures 3.7A-D, the STEM-EDS maps of the undoped, 2%-doped, 5%-doped, and 7%-doped CdSe/3MLCdS nanocrystals, respectively. For the undoped CdSe/3MLCdS (Fig. 3.7A) most of the signal detected was the Se K-series, S K-series and Cd K-series with some signal detected from Te L-series. As the Te-dopant is introduced into the sample, signal is detected from the Te L-series. The greater the amount of Te dopant in the sample, the more Te L-series signal is detected (Fig. 3.7B-D), as expected. Since the core/shell QDs have a diameter between 6-7 nm, we are limited by the pixel resolution of the detector and cannot obtain spatial information about whether the dopant is located deep inside the CdSe core or in the core/shell interface. Future studies investigating larger Te-doped core/shell nanocrystals are required to gather that information. However from these elemental maps we can confirm the presence of Te dopants in the QDs and quantify the amount of Te-dopant in each sample.

Elemental Analysis

By comparing the energy dispersion spectra of the undoped (Fig. 3.8A) and the 5% doped (Fig. 3.8B) samples, we further confirm that we have successfully incorporated Te into the QDs. We particularly focus on the region of the spectra where we expect signal from the Te L-series and Cd K-series. The L-series are the X-ray signals that correspond to electronic transitions to the second lowest energy level (n=2) as opposed to the K-series which correspond to electronic transitions to the lowest energy level (n=1). The Cd K-series located at 3.133 keV is present for both samples and the Te L-series at 3.769 keV is only present for the sample with Te dopants as expected. Te L-series signal present in Figure 3.8A likely comes from intrinsic measurement error and was accounted for in the baseline correction of the analysis.

Table 3.2 shows the results of the Cliff-Lorimer analysis of the four samples with different amounts of Te-dopant. All four samples have the same CdS shell thickness. For the three Te-doped samples, the percentage of Te detected is higher than the expected value in atomic %. The % of Te in the sample was calculated by diving the % of Te by the sum of % of Te and % of Se detected for each sample: (% of Te)/(% of Te + % of Se). This equation is used determine the % of Te in the sample because the Te atom is expected to replace the Se atom in the CdSe matrix. The CdSe:Te{5%}/3MLCdS sample has the closest measured at% of Te (6.15%) to the expected value (5%). The CdSe:Te{2%}/3MLCdS sample had an at% of Te of 5.79%, about 3% higher than expected while the CdSe:Te{7%}/3MLCdS had the greatest at% of Te of 20.82%, nearly 13% higher than expected. It is important to note that the

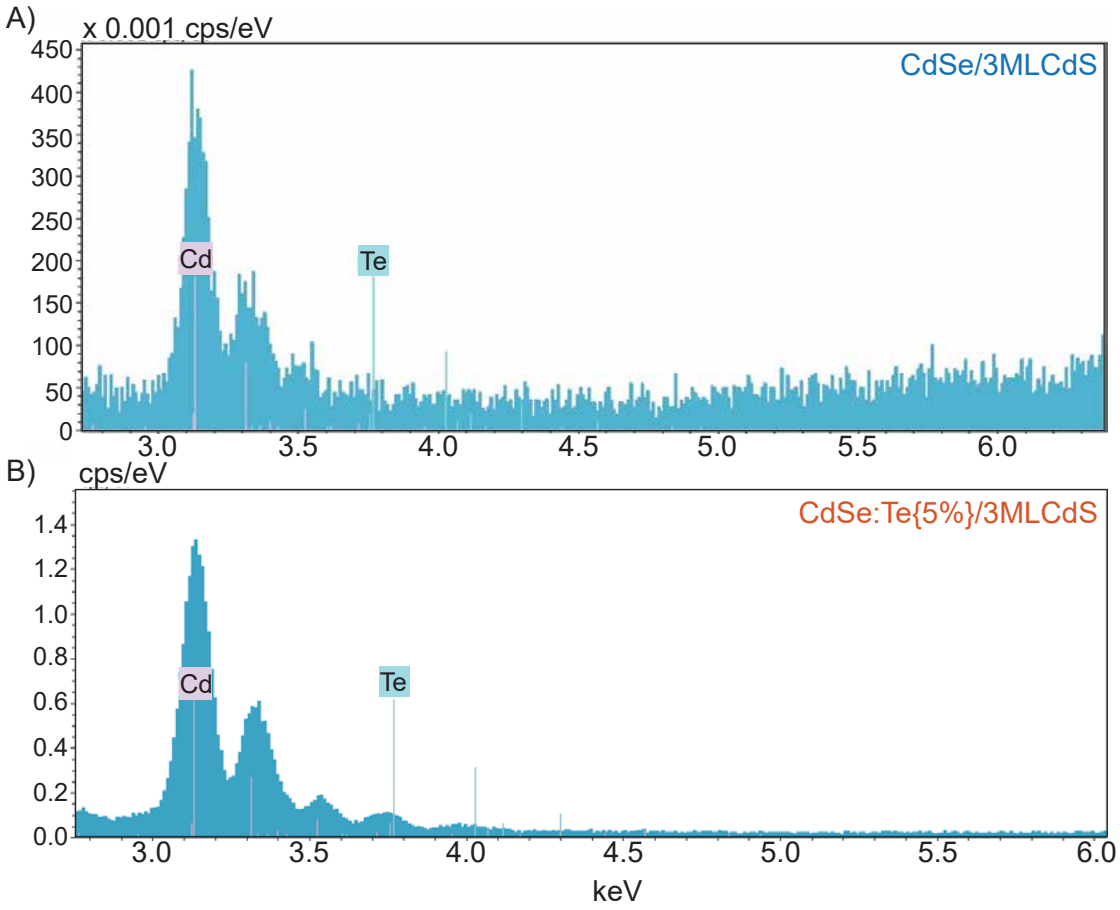

Figure 3.8: **Energy Dispersion Spectra of Undoped and Doped CdSe/CdS QDs.** EDS focused on region for Te L-series for **A** undoped CdSe/3MLCdS and for **B** CdSe:Te{5%}/3MLCdS.

Table 3.2: Quantifying the atomic composition of each sample using the Cliff–Lorimer method for each element: Cd K-series, Se K-series, S K-series, Te L-series.Values present correspond to the normalized atomic %.

Element	CdSe/CdS	CdSe:Te{2%}/CdS	CdSe:Te{5%}/CdS	CdSe:Te{5%}/CdS
Cadmium	73.93	74.32	86.17	55.08
Sulfur	14.56	14.23	8.52	34.41
Tellurium	0	0.66	0.33	2.19
Selenium	11.51	10.79	4.99	8.32
% of Te	**0**	**5.79**	**6.15**	**20.82**
% Error	0	1.04	2.26	2.32

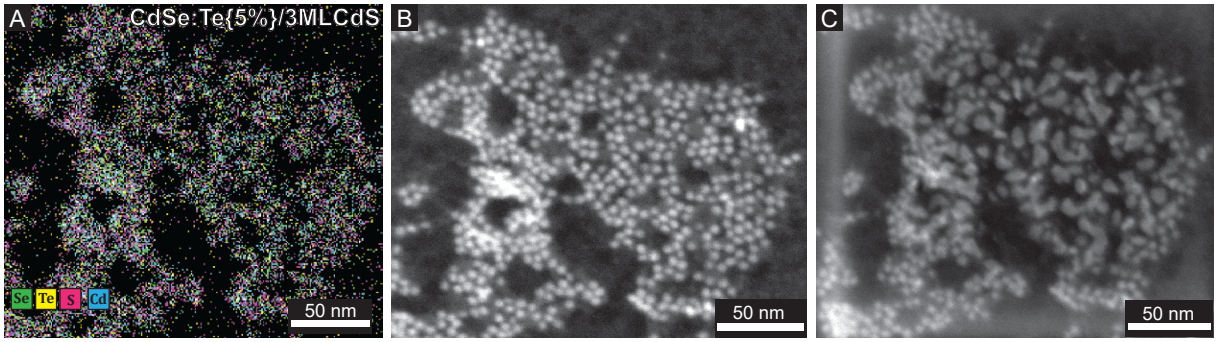

Figure 3.9: **Sample Damage After STEM-EDS Measurement. A** STEM-EDS Map of CdSe:Te{5%}/3MLCdS and its corresponding HAADF images **B** pre-map acquisition and **C** post-map acquisition.

error of % of Te in the sample is fairly large likely due to the small size of the nanocrystal. The expected amount of % of Te is included in the error of the detected % of Te for the CdSe:Te{5%}/3MLCdS but not for the other two Te-doped samples. The analysis done on the undoped CdSe/3MLCdS sample did not detect any Te in the sample. Future studies are needed to further understand the incorporation of the Te dopant in the CdSe nanocrystal.

Sample Damage

The resolution and number of counts acquired for the STEM-EDS map (Fig. 3.9A) measurement was limited by acquisition time due to sample damage. For example, Figure 3.9B shows the HAADF image of the sample before STEM-EDS map collection and Figure 3.9C shows the HAADF image of the sample post STEM-EDS collection. After 5 minutes of acquisition with a screen current of 1.12 nA, significant damage of the sample was observed. Whereas the individual nanocrystals are distinguishable in the pre-STEM-EDS map HAADF image (Fig. 3.9B), the nanocrystals appear clumped together and are indistinguishable in the post-STEM-EDS map (Fig. 3.9C). If the sample becomes too damaged during the measurement, it will drift and the map becomes unusable.

3.5 Probing Electronic Dynamics in a Doped Quantum Dot Based System

Note: The data in this section was measured by Dr. Rongfeng Yuan and Dr. Trevor Roberts in Prof. Naomi Ginsberg's research group to understand the electron dynamics of this mate-

rial system. They have graciously given me permission to discuss their results.

Time Resolved Emission Spectra (TRES)

In a close-packed QD solid system, it has been reported that an exciton can migrate from one QD to another as long as it is moving to a lower energy site.[92] In Figure 3.10A, we show a schematic of this process in our QDSL where an exciton (red star) migrates from a higher energy QD (light blue) to a lower energy QD (darker blue) over time represented by a magenta arrow. One way to track how the exciton migrates in a QD solid is by tracking the exciton energy at different time intervals via time resolved emission spectra (TRES). TRES of the CdSe:Te{5%}/3MLCdS QDSL shows a redshift in peak energy emission with increasing time delay (Fig. 3.10B). In Figure 3.10C, we show the associated time resolved mean energy loss corresponding to the difference between the average emission energy at each time delay after a 100 ps photoexcitation at 470 nm and the peak emission energy at zero time delay. This analysis was done on both the CdSe:Te{5%}/3MLCdS QDs in colloidal solution (pink circle) and in QDSL (red triangle) as well as the CdSe/3MLCdS in colloidal solution (light blue square) and in QDSL (dark blue triangles). For both samples, the QDSL has a more pronounced dynamic redshift (9.8 meV for CdSe/3MLCdS and 80 meV for CdSe:Te{5%}/3MLCdS) compared to their colloidal solution counterpart ($\sim$0 meV for CdSe/3MLCdS and 15 meV for CdSe:Te{5%}/3MLCdS). The initial decrease in average exciton energy as a function of time for the QDSLs is expected due to interactions among QDs The CdSe:Te{5%}/3MLCdS sample has a greater magnitude of redshift over exciton lifetime than the undoped sample both in colloidal solution and in QDSL. The large redshift for the CdSe:Te{5%}/3MLCdS QDSL suggests a heterogeneous energetic landscape despite being composed of QDs with a uniform size distribution whereas the undoped QDSL has a narrower energy distribution.

Time-Resolved Ultrafast Stimulated Emission Depletion Microscopy (TRUSTED)

Another method to study exciton dynamics in QDSLs is through time-resolved ultrafast stimulated emission depletion (TRUSTED) microscopy.[127] TRUSTED allows us to monitor the spatiotemporal expansion of an exciton population after local photoexcitation by reporting the fraction of excitons remaining at a specified time delay. A schematic of a TRUSTED experiment is shown in Figure 3.11A where an initial population of excitons (black circles) are generated via a picosecond diffraction-limited 550 nm pump pulse (blue) and not quenched by a nearly incident 100 ps 740 nm annular "STED" pulse (yellow). After a time delay, a second identical annular STED pulse quenches additional excitons (red circles) that migrated to the annular region (yellow) illuminated by the STED pulse. The remaining excitons that are not quenched by the STED pulse can then be plotted as a function of time

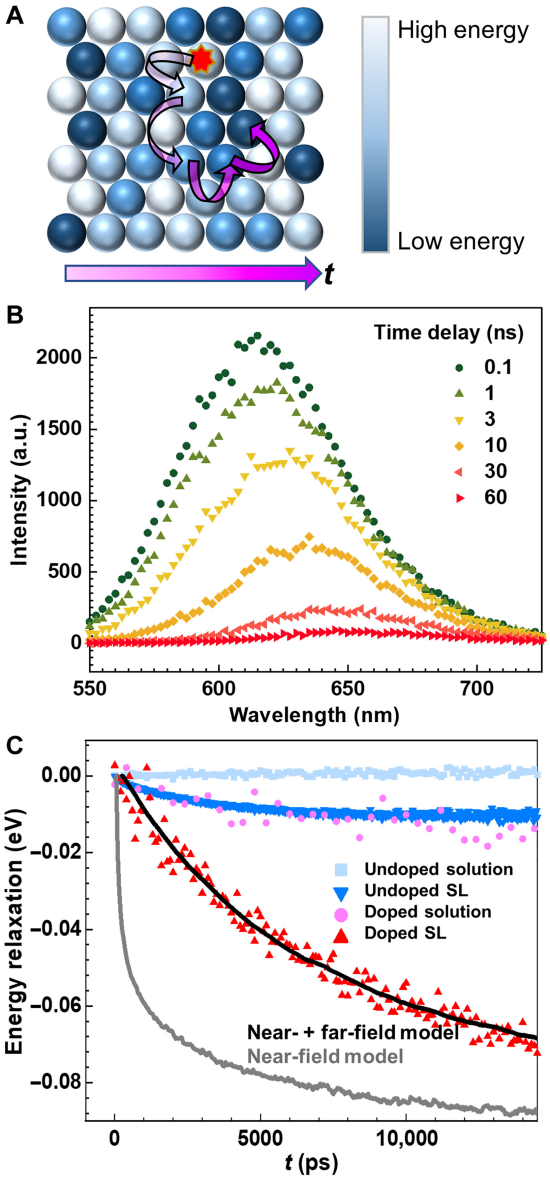

Figure 3.10: **Tracking Exciton Dynamics Energetically via TRES. A** Diagram of exciton (red star) hopping from a high-energy QD (light blue) to a low energy QD (dark blue). Time is indicated with increasingly deep magenta. **B** Time-dependent photoluminescence spectra at select time delays after photoexcitation of a CdSe:Te{5%}/3MLCdS QDSL. **C** TRES of CdSe:Te{5%}/3MLCdS QD solution (pink circles) and QDSLs (red triangles) track the decay of mean exciton energy. CdSe/3MLCdS solution (light blue squares) and QDSL (dark blue triangles) counterparts are shown for reference. Simulated energy decay from spatial-spectral dynamics of near-field (gray) and near-field plus far-field (black) models is also shown. Reproduced from [176]

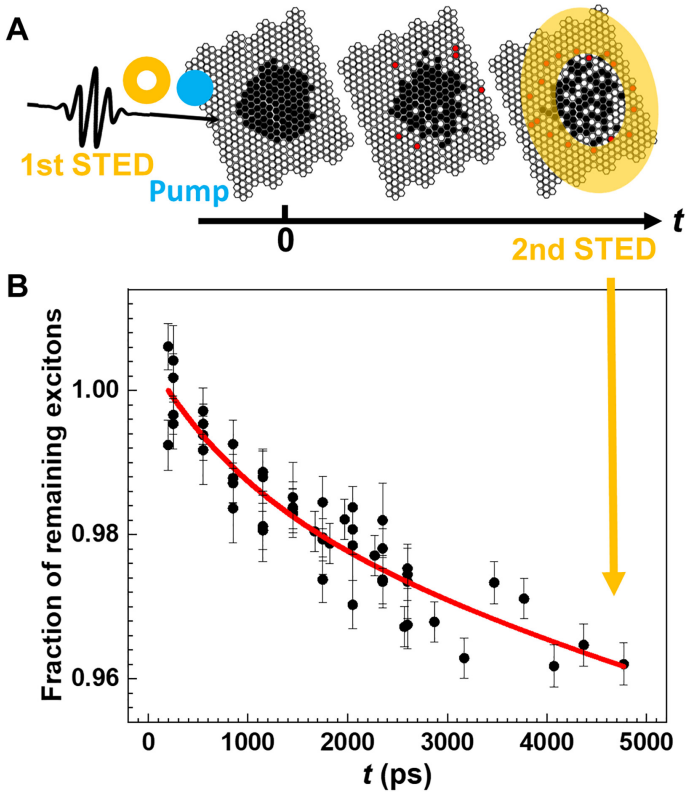

Figure 3.11: **Spatial tracking of exciton dynamics via TRUSTED. A** Schematic of a TRUSTED protocol. **B** Measured TRUSTED fraction of remaining excitons (black points) decays as a function of time delay between first and second STED pulse arrivals is fit (red) using an exponentially decaying diffusivity model. Decreasing fraction corresponds to exciton diffusion. Reproduced from [176]

(Fig. 3.11B).

In Figure 3.11B, the horizontal axis is the time delay between the first and second STED pulses. The vertical axis is calculated as the ratio of the PL intensity with and without the second STED pulse, and then normalized to its initial value to construct the "fraction of remaining excitons" in the detection volume. A decaying signal means that excitons move spatially outward between the time delay of the two STED pulses, and the slope of the decay depends on the rate at which excitons travel. By fitting the data to a time-dependent diffusivity model (red curve), we measure that the initial diffusivity to be $4.6 \pm 2.5 \times 10^{-}3$ cm^2/s with a decay rate of k=0.0008 $\pm$ 0.0010 $ps^{-}1$. From the TRES we know the exciton proceeds to lower energy sites over time which means the number of acceptor sites concomitantly decreases resulting in a time-dependent reduction in energy transfer rate. This decay

can be approximated with an exponentially decaying exciton diffusivity model (additional detail in reference [176]) so the long-time diffusivity is $1.5 \pm 1.2 \times 10^{-3}$ cm^2/s. The extent of exciton transport is 35 ± 6 nm within the 5 ns TRUSTED measurement time window and is $\sim$47 nm over the QD lifetime.

By combining the information from TRES on the rate of the mean energy change at much longer time delay window and from TRUSTED direct spatiotemporal measurements, a kinetic Monte Carlo simulation model of exciton transport elucidates a composite transport mechanism that includes both near field FRET and far-field emission/reabsorption contributions. Further discussion on this composite electrodynamic mechanism can be found in reference [176]. Through this comprehensive study of exciton transport mechanism in Te-doped CdSe/CdS QDSLs, a more unified framework to characterize energy transport in QD-based solids is uncovered which can be directly applied to rational design of optoelectronic materials.

3.6 Conclusions

Introducing Te dopants during the hot injection step of the colloidal synthesis of CdSe quantum dots allows for the implementation of the impurity within the CdSe matrix. We can reasonably control the amount of dopant by altering the amount of Te:Se precursor used. Although we observed no change to the crystal structure, size and shape of the QDs, we measured vastly different optical properties such as changes in the first exciton absorbance peak, PL peak energy and homogeneous and inhomogeneous linewidths. Through the STEM-EDS measurements, we were able to confirm the presence of Te in the QDs and quantify the amount of dopant in each sample. Our collaborators in the Ginsberg group performed TRES and TRUSTED measurements on the Te-doped QDSL to elucidate a composite transport mechanism to understand how energy migrates in this material system. Although additional pathways can be explored like temperature and reaction time to have finer control on dopant concentration, we have shown a method to form highly ordered QDSL composed of bright QDs with atomic defects to alter its emission beyond the bulk bandgap limit. This work provides an alternative pathway to further tune the optical properties of a nanocrystal system without compromising on a desired structure, size and/or shape.

Chapter 4

Conclusion and Outlook

4.1 Conclusion

In Chapter 1 we discussed key concepts to understand the fundamental structural and optical properties of QDs. We also discussed how we can use QDs as building blocks to engineer complex structures with long range order and their corresponding electronic dynamics. In Chapter 2, we discussed the first comparison of recombination rates between QDs in highly ordered monolayer thin films and their colloidal solution counterparts by directly measuring the PLQY of the thin films which has been historically challenging. In these measurements, we observed an unexpected increase in radiative rate and hypothesized different mechanisms to explain this behaviour. In Chapter 3, we engineered a Te-doped QD system that we were able to use as the building block for a monolayer superlattice. Using techniques like TRES and TRUSTED we were able to elucidate the electrodynamic mechanism of exciton transport in this system. Both of these works have provided an improvement in the fundamental physics of energy propagation in QD based monolayer thin films.

4.2 Outlook

With the foundational studies laid out in these two projects, future work can be done attempting to control the mechanisms we discussed. The most obvious method would be through altering the inter-particle distance in these superlattices which will ultimately affect its exciton transport. One way to do this is by modulating the ligand shell surrounding the QDs.[5, 87] For example, the QDs discussed in Chapters 2 and 3 are passivated with oleic acid and oleylamine ligands which have a relatively long 18-carbon chain. Successful $in-situ$ ligand exchange strategies during the self-assembly process have been developed where ligands with shorter carbon chains like decanoic acid (10-carbon chain), butyric acid (4-carbon chain), and formic acid (1-carbon change) are used to decrease the inter-particle

distance and enhance exciton transport.[48]

Additionally, through ligand engineering, we could select molecules with desired functionalizations such as electron withdrawing or donating groups[61, 89, 58, 29] to understand how that affects the confinement of the electron wavefunction and ultimately the radiative rate of the material. Work has also been done studying how engineering dynamic vs static ligand environments around the QD surface affect their luminescence.[11, 30] Extending this concept to thin films to observe how dynamic ligand environments affect energy transport mechanism would be interesting.

Lastly, we could manipulate the interparticle interactions mechanically using a polymer film like polydimethylsiloxane (PDMS). PDMS is silicone polymer that acts like an elastic solid similar to rubber. By transferring the QD monolayer superlattice to PDMS[86, 121, 131, 124] and applying mechanical strain on the polymer in a particular axis, we could alter the interparticle distance in one direction. This would allow us to do interesting studies where we could modulate the interparticle spacing in QD based materials in 1 dimension. These proposed studies will allow for further understanding how the structure of QD superlattice thin films influences their energy dynamics.

Part II

Part Two: Tuning Erbium Emission by Altering Properties of Host Material Matrix

Chapter 5

Rare-Earth Doped Ferroelectric Thin Films

In Chapter 3, we discussed a study on atomic defects influencing the properties of its host material. In this section we want to apply that concept to rare-earth doped ferroelectric thin films to do the inverse. Instead of using dopants to change the properties of the host material system, we aim to manipulate degrees of freedom of the host material to control the properties of the dopant. However, in order to do so we needed to choose a host material with known tunable parameters that can readily incorporate dopants and select a dopant with desirable properties for us to study. We ultimately choose erbium-doped lead titanate thin films as prototypical material systems to perform these studies. Before discussing the study performed, we must first expand on introductory concepts related to this project.

5.1 A Chemist's View on Electricity and Magnetism

In Chapter 1, we discussed exciton dynamics in QD based materials. An exciton, made up of a negatively charged particle (electron) and a positively charged "particles" (hole) will eventually recombine due to attractive forces between the charges. Although holes are thought of as positively charged "particles", in reality they are abstract vacancies that are considered to be positively charged in comparison to the negatively charged electrons surrounding it. There are however subatomic positive charged particles known as protons that we did not discuss in Chapter 1. Let us now extend this concept of attractive forces to electrons and protons in the context of electricity and magnetism.

If we consider two stationary point charges in space, we can describe the electrostatic force between them by Coulomb's Law:

$$F = kq_1q_2/r^2 \tag{5.1}$$

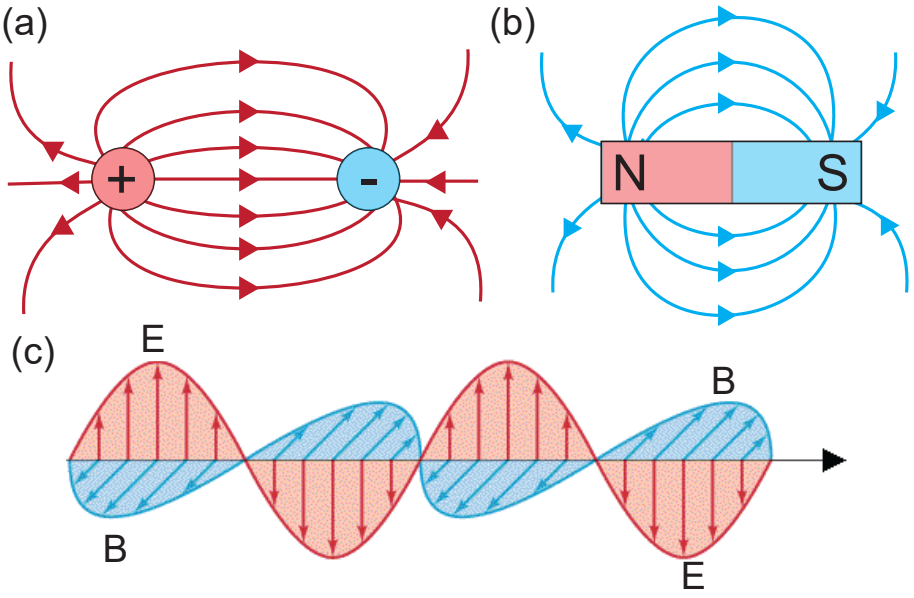

Figure 5.1: **Electric and Magnetic Forces. a** Simple diagram of electric field between two equal but opposite point charges. **b** Simple diagram of magnetic field around a bar magnet. **c** Diagram of electromagnetic wave composed of an oscillating electric field (E, red) and a oscillating magnetic field (B, blue) perpendicular to each other. Figures were adopted from reference [55].

where k is the electrostatic constant (8.99×10^{9} kg·m^3/s^2·coul^2), r is the distance between the two charges and q_1 and q_2 are point charges where a proton or electron have a charge of $\pm1.602\times10^{-19}$ Coulombs. If q_1 and q_2 have the same charge, the electrostatic force will be repulsive. However, if the charges are opposite (Fig. 5.1a), not only is the force attractive but also an electric field ($\vec{E}$) will be created by the point charges. $\vec{E}$ can be described by eq. 5.1 as the capacity of the force of a charge that can be exerted on another charged object. From eq. 5.1, we know that the force will be greater for charges with a greater magnitude and shorter inter particle distance.

A magnetic field ($\vec{B}$) describes the magnetic influence on moving electric charges (electric currents) and magnetic materials varying over time (Fig. 5.1b). Magnets are composed of a north pole (N) and a south pole (S) with $\vec{B}$ always looping from N to S. The simple diagram of a magnetic field around a bar magnet (Fig. 5.1b) looks fairly similar to the diagram of an electric field between point charges (Fig. 5.1a) because both fields are created by two poles otherwise known as dipole fields. Since magnetic fields vary with location, it is challenging to describe them with a simple equation. Instead it is represented by a vector field where a vector is assigned at each point in space. A magnetic force constant (μ =1.26×10^{-6}T)

is used to describe $\vec{B}$. This constant can be thought of as analogous to the k constant for $\vec{E}$. We can additionally think of $\vec{B}$ and $\vec{E}$ as interrelated since changing $\vec{E}$ creates a $\vec{B}$ and changing $\vec{B}$ creates an $\vec{E}$.

Since electricity and magnetism are so closely related, $\vec{E}$ and $\vec{B}$ are usually combined as electromagnetic forces. The force on an electric charge is dependent on position, speed, and direction. The $\vec{E}$ describes the force on a stationary charge independent of motion whereas the $\vec{B}$ is proportion to both the speed and direction of the charge. By combining the two force fields, we can describe the force on a point charge q moving with a velocity v with the Lorentz force equation:

$$F = q(\vec{E} + v \times \vec{B}) \tag{5.2}$$

Although this formula was derived by Hendrik Lorentz in 1895, it is suggested in the work of James Clerk Maxwell who derived four partial differential equations known as Maxwell's equations in 1864 to describe the relationship between electricity and magnetism. Maxwell is also credited with hypothesizing the concept that an oscillating $\vec{B}$ will produce an oscillating $\vec{E}$ perpendicular to its path. The opposite will be true where an oscillating $\vec{E}$ produces an oscillating $\vec{B}$ at a right angle resulting in an endless cycle. The two fields would travel together in space and time constantly regenerating each other to make a self-sustaining electromagnetic wave (Fig. 5.1c). Maxwell was able to calculate that the speed of that hypothetical wave using the k and μ force constants is equivalent to the speed of light, suggesting that light is an electromagnetic wave.[55]

5.2 Ferroic Order

Electric and magnetic fields can be used to manipulate the properties of crystals based on their structures and phase transitions. Certain crystal have physical characteristics that allows them to exhibit spontaneous properties with application of external fields. If a crystal has two or more phases of a property that are orientation stable and readily shift from each other with the application of external fields, the crystal is considered to be "ferroic". There are four primary ferroic orders: ferroelasticity, ferroelectricity, ferromagnetism, and ferrotordicity that describe how the crystal changes with stress, electric field, magnetic field, and toroidal field, respectively. The primary ferroic properties can form domains of different ordered states.[99]

Ferroelasticity

Ferroelasticity is the mechanical equivalent to the other ferroic orders. When stress is applied to a ferroelastic material, a phase change occurs where either crystal structure or orientation

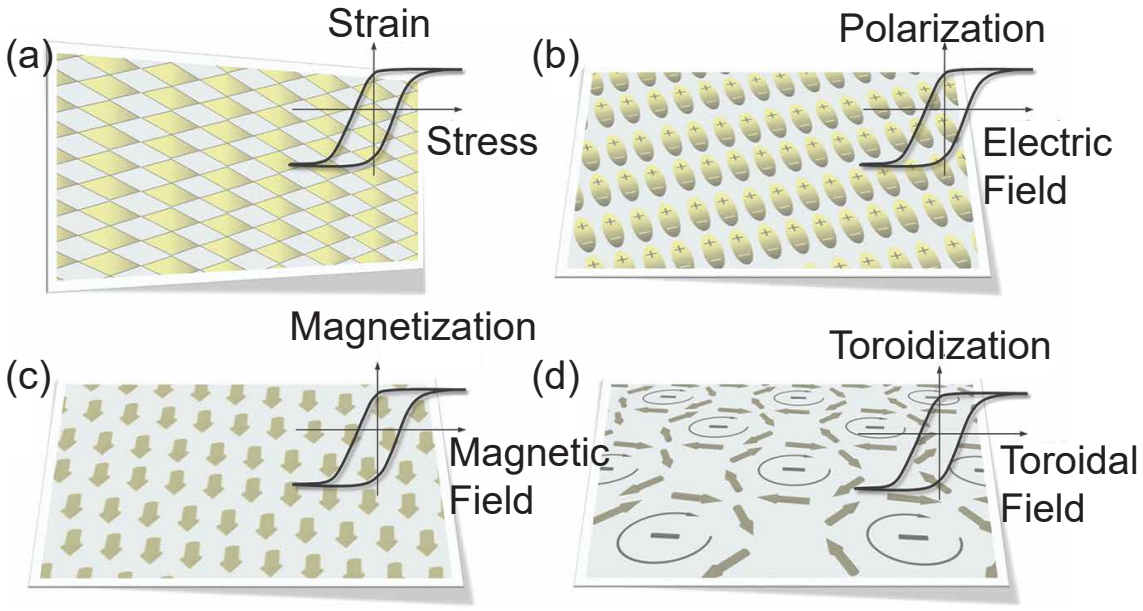

Figure 5.2: **Different types of Ferroic Order.** Diagrams of the four types of ferroic properties: **a** ferroelasticity, **b** ferroelectricity, **c** ferromagnetism and **d** ferrotoroidicity. Reproduced from [99].

is altered, resulting in spontaneous strain (ρ) (Fig. 5.2a). For example, lead halide perovskite single crystals have exhibited ferroelastic properties due to a phase transitions from a cubic to tetragonal to orthorhombic crystal structures under external stress.[15]

Ferroelectricity

Ferroelectricity is when a material develops a spontaneous electric polarization (P), which can be switched with the application of an $\vec{E}$ (Fig. 5.2b). A ferroelectric material will have a nonlinear relationship between P and $\vec{E}$ unlike dielectric materials. Materials that show some enhanced nonlinear polarization are known as paraelectric materials. Due to symmetry considerations, ferroelectric materials are also piezoelectric and pyroelectric which means that the material is spontaneously polarized with stress and temperature, respectively. The spontaneous polarization of ferroelectric materials is a result of its internal electric dipoles being coupled to the material lattice. Most ferroelectric phase transitions will exhibit behaviors due to an ion being displaced from its equilibrium position and creating an electric dipole moment in the structure like in $BaTiO_3$[183] and $PbTiO_3$[44] and/or order-disorder transition where the electric dipole moment's orientation changes with temperature like in

$NaNO_2$.[76]

Ferromagnetism

Ferromagnetism is when a spontaneous alignments of spins results in a magnetic moment (M) that can be switched with the application of a $\vec{B}$ (Fig. 5.2c). This induced magnetization via $\vec{B}$ is known as magnetic permeability. There are several types of magnetic materials that can be distinguished: Ferromagnetism is the strongest type of magnetization since M is aligned and oriented in the same direction. Antiferromagnetism is when a material has domains of opposing M of the same magnitude so no spontaneous magnetization occurs. Ferrimagnetism is similar to antiferromagnetism, except the domains have M with different magnitudes so the material does have spontaneous magnetization. Other weaker types of magnetism are paramagnetism where materials are weakly affected by an external $\vec{B}$ and diamagnetism where the material is repelled by $\vec{B}$. Materials that exhibit ferromagnetism are typically compounds with iron,[169] cobalt,[180] nickel,[153] and certain rare-earth elements.[75]

Ferrotordicity

Ferrotordicity is the fourth type of primary ferroic order where a material can experience a vortex-like alignment of spins with toroidization (Fig. 5.2d). This toroidization can be switched by a toroidal field of the form $\vec{E} \times \vec{B}$. Ferrotoroidics are challenging to measure and therefore difficult to characterize experimentally.[64]

5.3 Multiferroics

Materials that have 2 or more primary ferroic orders in the same phase are known as multiferroics. There are different subsets of multiferroic materials.[154, 99] For example materials with a coupling between their electrical and magnetic properties have magnetoelectricity; those with a coupling between magnetic and elastic properties have magnetoelasticity; and coupling between elastic and electrical properties results in piezoelectricity (a term that we discussed above in the ferroelectric section) (Fig. 5.3a). This coupling is powerful because it provides pathways to control one property with a different degree of freedom. The most promising application of multiferroics is magnetoelectric materials, which provide an avenue to control magnetism by electric fields which are a few orders of magnitude less energy intensive than traditional magnetic fields.[34, 104]

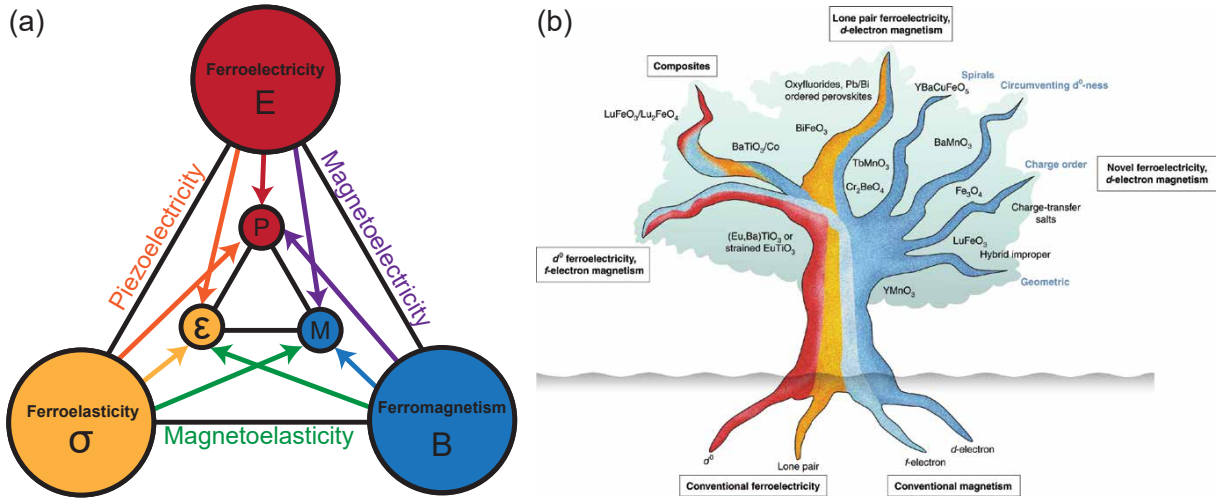

Figure 5.3: **Multiferroic Material.** **a** Combination of 2 primary ferroic orders results in different types of multiferroic behavior. **b** Multiferroic family tree reproduced from [154].

Since ferromagnetic materials are favored by partially filled d-orbitals while ferroelectricity is favored by transition metals with empty d-orbitals, engineering magnetoelectric materials is challenging. The most promising and widely studied prototypical multiferroic material, $BiFeO_3$ (BFO), is the only single crystal material with large ($\sim$90 μCcm^{-2}) ferroelectric polarization to exhibit magnetoelectric properties at room temperature.[165] The large polarization of BFO is driven by the lone pair ferroelectricity of Bi^{3+} $6s^2$ electrons, and its robust antiferromagnetism comes from the $3d$ electrons of Fe.[70] Similar routes outlined in the multiferroic family tree (Fig. 5.3b)[154] can be used to circumvent the chemical contradictions between ferroelectric and magnetic properties to engineer magnetoelectric materials. For example, materials with d^0 ferroelectricity and f-electron magnetism like $(Eu,Ba)TiO_3$ alloys[144] and pure $EuTiO_3$[94] have been shown to be magnetic and ferroelectric. Additionally, strong coupling has been observed in composite multiferroic architectures where a superlattice of non-magnetic ferroelectric and non-ferroelectric ferromagnetic material are combined via layer-by-layer growth. Lastly, alternative multiferroics have been established with materials exhibiting novel ferroelectricity through unconventional routes to lifting the inversion center and conventional d-electron magnetism.[154]

Through engineering magnetoelectric materials, we can study the physics between spin-charge coupling by manipulating the magnetization of materials with long-range magnetic order. However, if we can understand the fundamental limits of the magnetoelectric coupling, we can extend this concept to the quantum level. This allows us to establish an additional route to multiferroic-like coupling where isolated spins are incorporated in a ferroelectric medium. Electric field manipulation of spins has been reported in Fe^{3+}-doped

$PbTiO_3$ (PTO) single crystals.[97] Fe^{3+} has a high spin (s=5/2) $3d^5$ electronic structure and replaces the Ti^{4+} site in PTO which is a prototypical ferroelectric. Using Electron Paramagnetic Resonance (EPR) measurements, it was observed that the ferric ion spins are aligned perpendicular to the ferroelectric polar axis which can readily be manipulated via electric field. In this work they measured spin coherence lifetimes of 8.7 μs at 3.5 K. These values need to be improved in order to use these materials as a platform for different quantum and spintronic applications. Selecting different dopants with higher spin-orbit coupling provides a solution to improve these properties. Spin-orbit coupling is the mechanism that assists a spin flip through using the orbital angular momentum of outer electrons to interact with the spin of an excited electron. This coupling is desirable for technological applications.

5.4 Rare Earth Ions

Rare-earth ions (REIs) are the 17 metallic ions that make up the lanthanide series in the periodic table with the addition of Yttrium (Y) and Scandium (Sc).[187] These ions have unpaired f-electrons, high spin-orbit coupling, and luminescent properties that makes them desirable in diverse applications such as laser,[156] displays,[45] low carbon electronics,[186] magnetic materials,[75] etc... Trivalent REIs have partially filled $4f$ shells that are shielded by outer filled $5s^2$ and $5p^6$ shells. This results in inner shell $4f$-$4f$ transitions with narrow spectral lines that span from the infrared to the vacuum ultraviolet.[101] The spectra of REI are fairly complex due to large number of low lying levels from the unpaired $4f$ shells. However, these transitions have been well studied both theoretically and shown experimentally.[42] A Dieke diagram reports the energy levels of trivalent REI in the in the energy range from 0-40$\times 10^3$ cm^{-1} (Fig. 5.4a). Even when REI are doped into a crystal, the $4f$ levels are shielded enough that the host-lattice interactions are weak perturbations to the free ion levels. Experimentally, since REI have narrow spectral lines, changes in its spectrum can be detected in different crystal environments.[65]

Instead of discussing the Dieke diagram for all trivalent REIs included, we will focus our discussion on the REI relevant to Chapter 6 of this dissertation. Although Erbium (Er^{3+}) will be our primary focus, we will also discuss systems that include Dysprosium (Dy^{3+}), Gadolinium (Gd^{3+}) and Neodymium (Nd^{3+}) (Fig.5.4b). In particular, we are interested in the energy levels around 6.5$\times 10^3$ cm^{-1} shown in a dashed line in Figure 5.4b. This energy level corresponds to the lowest energy state for (Er^{3+}) which we will probe in Chapter 6. By considering the Dieke diagram in this energy range, we can assess potential quenching of Er^{3+} emission as well as upconversion, which is common for systems that include more than one REI. In this energy regime, we see that both Dy^{3+} and Nd^{3+} have energy levels in this range that could potentially affect the Er^{3+} emission. On the other hand, Gd^{3+} does not have any energy levels in this region with its lowest energy level being at 30$\times 10^3$ cm^{-1} (in the UV-Range) so its unlikely for there to be energy transfer interactions between Er^{3+} and

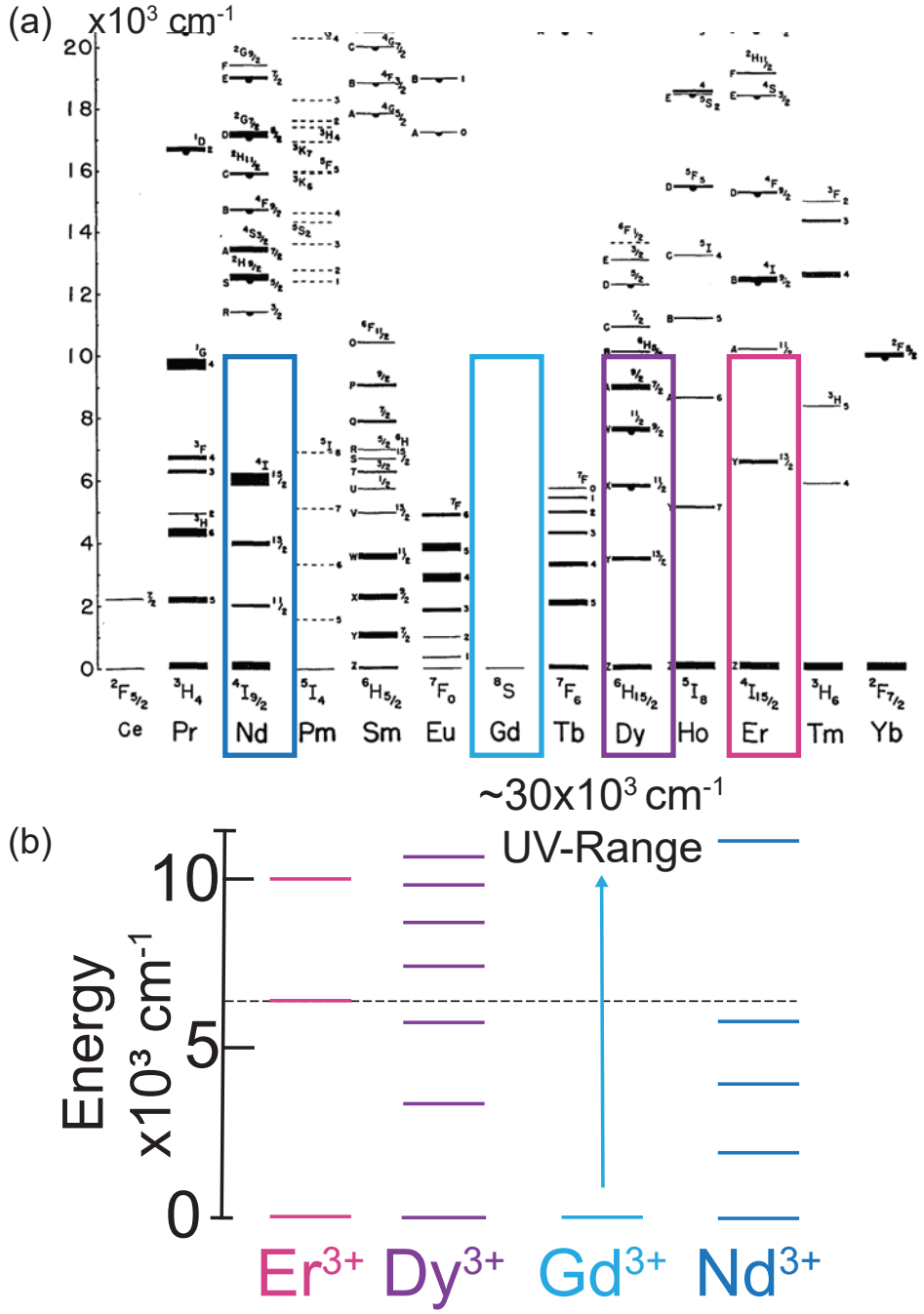

Figure 5.4: **Rare-Earth Ion transitions.** **a** Dieke diagram for trivalent REI from 0 to $20{\times}10^3$ cm^{-1}. **b** Dieke diagram focused on the REI trivalent species of interest for Chapter 6. Dieke diagram reproduced from [42].

Gd^{3+}. This diagram may be useful to revisit while reading the *Second Site Identification* section in Chapter 6.

Erbium

As mentioned above, erbium will be the primary REI studied in Chapter 6. Er^{3+} is fairly stable, abundant and safe because it does not oxidize as quickly as other REI. Pure erbium is ferromagnetic below 19 K, antiferromagnetic between 19-80 K and paramagnetic above 80 K. From the Dieke diagram we know that Er^{3+}emits and absorbs in the visible, ultraviolet and near infrared spectral range and emits at around ∼1540 nm (6.5×10^3 cm^{-1}) depending on its local environment.[42] This wavelength, which is part of the telecom band is important for optical communications as single mode optical fibers have a minimal loss in this spectral range. Additionally, Er^{3+} has been reported to have been successfully implanted in a wide range of materials with different coordination environments such as cubic MgO, non-cubic and nonpolar TiO_2 and $PbWO_4$ and polar symmetries ZnO. [155] Due to their long optical and spin coherence times (23 ms in $CaWO_4$),[91] telecom-wavelength spin-photon interfaces,[137] and frequency-selective control of ions in different sites,[39] erbium based materials make desirable candidates for quantum information networks.[186]

5.5 Engineering Ferroelectric Thin Films

We are particular interested in engineering Er^{3+}-doped thin films where the host material is a well studied ferroelectric like $PbTiO_3$ (PTO). Er^{3+}-doped PTO thin films can be epitaxially deposited by introducing the Er^{3+} dopant during the film growth process.[155] These films are engineered using a physical vapor deposition technique known as pulsed laser deposition.

Pulsed Laser Deposition

Pulsed laser deposition (PLD) is a technique where a high-power pulsed laser beam is focused onto a target composed of the desired material inside a vacuum chamber (Fig. 5.5). The particles from the target are vaporized in a plasma plume and are deposited as a thin film on a substrate. PLD is typically done in ultra high vacuum chambers, at high temperatures, and in the presence of a background gas such as oxygen.[100] Although the diagram of PLD is simplified in Figure 5.5,[19] the mechanism of the laser-target interaction resulting in the deposition of a film is fairly complex. Small differences in deposition conditions can alter the crystallinity, uniformity and stoichiometry of the films. At first a laser pulse is absorbed at the target surface and the energy from that pulse is converted from electronic excitation

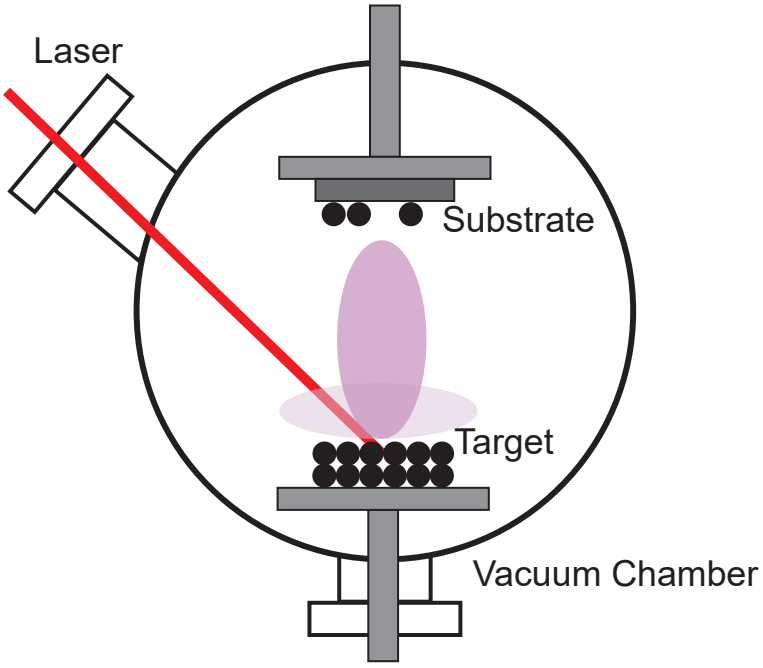

Figure 5.5: **Diagram of Pulsed Laser Deposition.** Adapted from [19].

into thermal, chemical and mechanical energy resulting in evaporation, ablation, plasma formation and exfoliation of the target. The ejected particles surround the vacuum chamber in the form of a plume until being deposited on a heated substrate. The deposition of the film on the substrate can be tuned through several parameters like laser energy and pulse as well as substrate surface temperature and roughness. Once PLD conditions have been optimized, different targets can be used to engineer materials with unique architectures and compositions.[174]

Epitaxial Strain Engineering

Beyond optimizing PLD conditions, different amount of epitaxial strain can be engineered on a thin film via substrate selection.[44] Once a thin film is deposited on a substrate, we can characterize its crystal structure and lattice constants via X-ray diffraction (XRD). However the substrates the films are deposited on are also made up of crystalline materials. Most of the time, the lattice constants of the substrate are not equivalent to that of the deposited film.[85] The mismatch in lattice parameters between a substrate and a perovskite oxide crystal for examples affect the strain of the film in either one of two ways: 1) if the lattice constant of the substrate is smaller than that of the perovskite, the thin film will experience

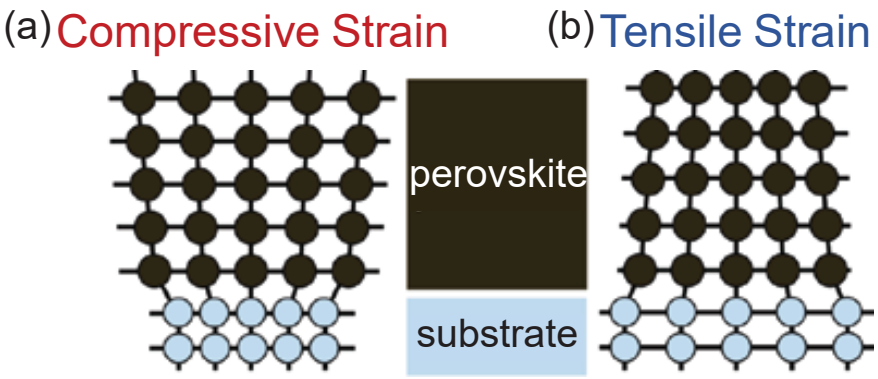

Figure 5.6: **Epitaxial Strain Engineering of Thin Films. a** Diagram showing in-plane compressive strain on a film grown on a substrate with a smaller lattice constant. **b** Diagram showing in-plane tensile strain on a film grown on a substrate with a larger lattice constant. Adapted from [68].

in-plane compressive strain (Fig. 5.6a) or 2) if the lattice constant of the substrate is larger than that of the perovskite, the film will experience in-plane tensile strain (Fig. 5.6b).[68]

PTO has a tetragonal perovskite crystal structure (Fig. 1.8d) with its c-axis lattice constant being larger than its $a = b$ axis lattice constant. When the lattice constant of the substrate is large (> 3.95 Å), the PTO film will prefer to form domains where c is in the plane of the film (c-oriented) to relax the elastic energy. Conversely, when the lattice constant of the substrate is small (< 3.95 Å), the PTO will form domains where c is preferentially normal to the film plane (a-oriented). By comparing the relative intensities of the XRD peaks that correspond to different domain configurations, we can quantify the domain ratio of the thin films. These domain ratios have been directly related with the amount of epitaxial strain engineered on PTO thin film. [44] This will be further discussed in the *Epitaxial Strain Engineering* section in Chapter 6.

5.6 Applications of Rare-Earth doped Ferroelectric Thin Films

Rare-earth doped ferroelectric thin films provide a platform that can be used in various applications. REI-based materials have gained a lot of attention as potential qubits for quantum information applications due to their excellent coherent properties.[65] On the other hand, multiferroic materials have the potential to transform low-power spintronics.[154] Through

combining these two applications by engineering rare-earth spins in a ferroelectric material, we can realize applications in both of those fields and begin to study how we can tune different degrees of freedom of the host material to control the properties of REI.[97] Since REI are known to have luminescent properties, we have the opportunity to probe the changes in REI emission optically.[155] Although we can engineer rare-earth doped ferroelectric films, understanding its properties still require some fundamental studies. In Chapter 6, we will discuss a case study of how altering the epitaxial strain of Er^{3+}-doped PTO films affects the Er^{3+}emission.

Chapter 6

Epitaxial Strain Tuning of Er^{3+}in Ferroelectric Thin Films

6.1 Introduction

Rare-Earth ions (REI) are attractive photon sources in a broad range of applications, such as LEDs,[116] displays,[13] lasers,[156] optical fibers,[45] and medical devices.[6] The self-contained, environmentally-insensitive nature of the $4f$ electrons[101] makes them attractive systems for storing and manipulating quantum information, demonstrated by impressive coherence properties in both optical and spin degrees of freedom.[160, 65, 90, 186]

In particular, Er^{3+} defects are a potentially powerful system due to their long electron[91] and nuclear spin coherence times,[141] as well as telecom-wavelength emission ($\sim$1.5 μm) [137]. The "atom-like" properties of Er^{3+} allow it to retain many of these desirable properties across a wide range of materials and coordination environments such as yttrium-based crystals,[23, 22] TiO_2,[129] MgO, ZnS,$PbWO_4$, MoO_3, and ZnO.[155]. This is particularly attractive from a materials design perspective, providing us with the opportunity to choose host materials with additional degrees of freedom (e.g., strain or polarization), or with controllable parameters to systematically study the dependence of Er^{3+} on its local environment.

One class of materials which may offer new functionality for controlling these REI defects are ferroelectric materials. Ferroelectric materials are also piezoelectric, offering multiple pathways to control the Er^{3+} emission by manipulation of different order parameters,[171] and thus the local crystal field of the defect site. Recent work on Fe^{3+} doped $PbTiO_3$ single crystals has demonstrated that the anisotropy of the Fe spins can be controlled by rotation of the electric dipole in $PbTiO_3$,[97] highlighting the potential of ferroelectric control, while acoustic manipulation with piezoelectric materials have been used to coherently manipulate Er^{3+} defects.[115]

$PbTiO_3$ is a ferroelectric perovskite oxide with many desirable properties, such as large spontaneous polarization[168, 102] and, in thin-film form, crystal lattice parameters which can be finely tuned through judicious choice of substrate.[44] The ability to manipulate the lattice environment with externally-applied fields offers the potential for acoustic control and transduction of quantum states.[115, 7, 152] $PbTiO_3$ also has a bandgap of 3.88 eV at room temperature[178] which is much greater than the Er^{3+} telecom emission. Perovskite oxides like $PbTiO_3$which have been doped with transition metal[97] or REIs[155] can have interacting charge, spin, orbital and lattice degrees of freedom. Since the distortion of the perovskite lattice is directly coupled to the ferroelectric polarization in $PbTiO_3$,[108] strain coupling of ferroelectricity and perhaps even multiferroic orders can be realized. However, many deleterious processes (e.g., fast spin relaxation or optical branching ratios) are extremely sensitive to the detailed energy level structure; realizing the full potential of this class of defects in active materials requires a thorough understanding of the interactions between the host lattice and the defect crystal field levels.

In this work, we demonstrate coupling of the Er^{3+} emission to the epitaxial strain of the host matrix at both liquid helium and liquid nitrogen temperatures. By systematically changing the epitaxial strain of the host lattice via substrate selection, we change the crystal field of the defect, allowing us to systematically explore optical properties and site occupancy. We use resonant fluorescence spectroscopy to study the telecom-wavelength ${}^4I_{13/2} \rightarrow {}^4 I_{15/2}$ transition for Er^{3+}. We are able to demonstrate the dependence of peak position, linewidth, and intensity on substrate strain and domain configuration. Moreover, we observe a second, distinct set of peaks in some substrates. Through understanding the effect of epitaxial strain on Er^{3+} emission, we provide a blueprint to how to study the control of Er^{3+} emission with strain using resonant fluorescence spectroscopy.

6.2 Methods

Epitaxial $PbTiO_3$ films

100 nm thick thin films of Er^{3+}-containing $PbTiO_3$ (PTO) were deposited via pulsed laser deposition from an Er containing precursor using $\sim$2 mJ cm^{-2} laser energy at 590 °C and 100 mTorr process O_2. The Er^{3+} concentration is nominally 0.01% (at.%). Samples were deposited on substrates with a range of lattice constants in order to generate a wide range of strain environments. The substrates are $(La_{0.18}Sr_{0.82})(Al_{0.59}Ta_{0.41})O_3$ (LSAT), $SrTiO_3$ (STO), $DyScO_3$ (DSO), $GdScO_3$ (GSO), and $NdScO_3$ (NSO). The strain and domain orientation of the samples were characterized from CuK_α X-ray diffraction (XRD) spectra about the 001 peak, using the ratio of the $d_c = 4.11$ Å and $d_a = 3.92$ Å peaks as the $c : a$ domain fraction (Figure 6.1d,e).

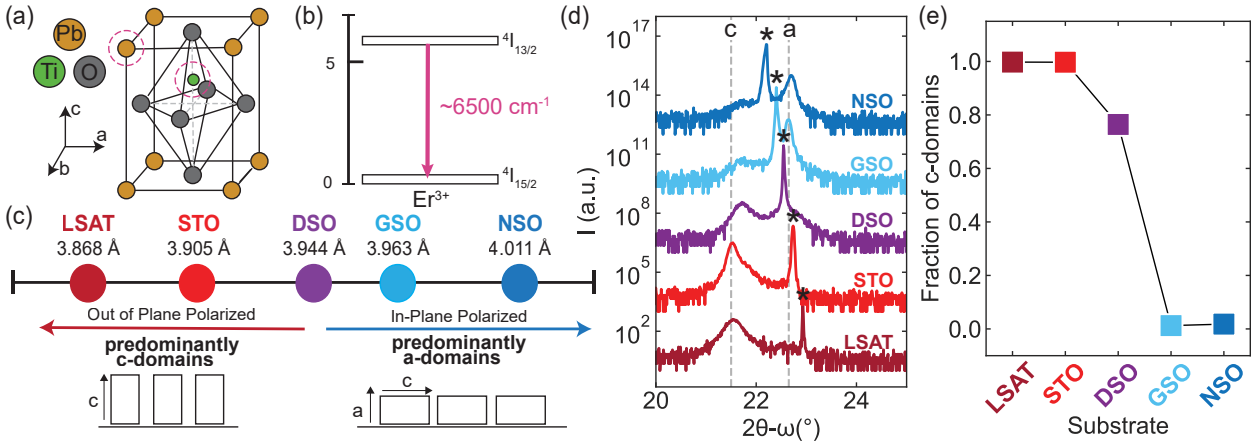

Figure 6.1: **Er^{3+}-doped PTO a** Diagram of the tetragonal PTO unit cell with the two sites the Er^{3+} dopant can replace (the A- and B-site) outlined in a pink dashed line. **b** $^4I_{13/2} \rightarrow ^4 I_{15/2}$ transition of the Er^{3+} ion with an emission of ∼6500 cm^{-1} in the near-IR. **c** When epitaxially deposited on different substrates, the tetragonal PTO will take on different domain configurations to relax the epitaxial strain of the substrate, ultimately leading to either primarily OOP or primarily IP polarized films. **d** X-ray diffraction spectra showing the average domain configuration of different films. The peaks at $2\theta - \omega =\sim 21.5°$ and $\sim 22.6°$ correspond to c- and a-oriented polarizations, respectively. Substrate peak is marked with an *. **e** This $c : a$ ratio can then be quantified from the intensity of the peaks in **d**.

Resonant Fluorescence Spectroscopy

Resonant Fluorescence Spectroscopy measurements were done at the Molecular Foundry located at the Lawrence Berkeley National Laboratory. Samples were excited using a Newport Velocity Tunable (TLB-6300-LN) laser with a nominal linewidth of ≤300 kHz (narrower than any feature discussed here). The excitation passed through a polarizing beam-splitter and the fluorescence with polarization orthogonal to the excitation was detected to suppress scattered laser light. Resonant excitation scheme was designed using Thorlabs Optical Choppers. The emission was dispersed on to an InGaAs AndorCCD camera connected to a Princeton Instruments SpectroPro 300 with a spectral resolution of 0.1 nm (0.8 cm^{-1}) (Fig. B.1).

All measurements were done in a Janis ST-500 cryostat at either 7 K (liquid He) or 77 K (liquid N_2), with temperature control from a Lakeshore cryogenic temperature controller (Model 325) to enable temperature-dependent measurements.

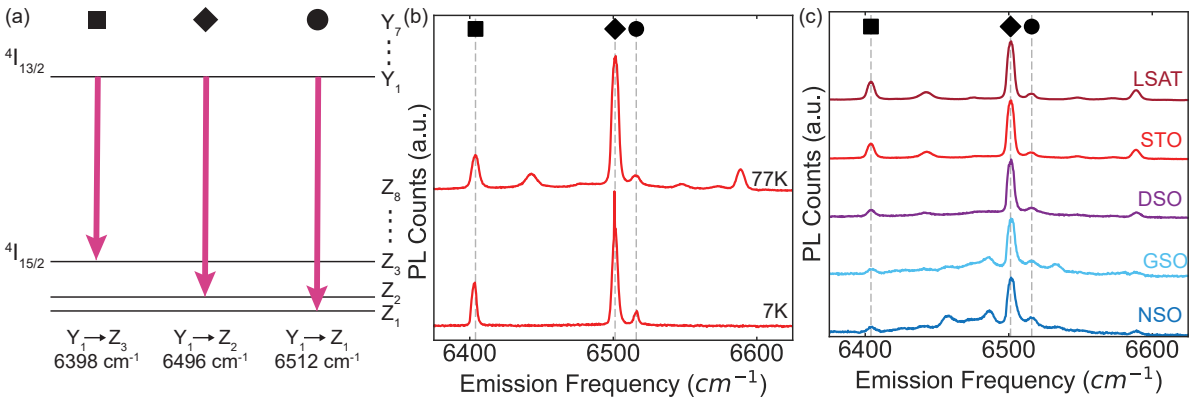

Figure 6.2: **Er^{3+} Telecom Transitions. a** Diagram of the energy levels for the $^4I_{13/2} \rightarrow ^4I_{15/2}$ transitions. Z and Y refer to the lower and upper manifolds, respectively. **b** Er^{3+} emission observed for 6500 cm^{-1} excitation at 77 K and 6515 cm^{-1} excitation at 7 K in Er^{3+}-doped PTO on STO. **c** Er^{3+} emission for the 5 films observed for 6500 cm^{-1} at 77 K.

6.3 Epitaxial Strain Engineering

To systematically study the effect of strain environment on the Er^{3+} optical properties, we select a wide-bandgap, anisotropic host that can be tuned through epitaxial strain. PTO is a tetragonally distorted perovskite (Fig. 6.1a) ferroelectric with a significant $c : a$ (4.11 Å: 3.91 Å) ratio, where the ferroelectric polarization P is tied to the c-axis of the unit cell. This tetragonal distortion of the unit cell translates to a tetragonal distortion of the crystal field around the Er^{3+} dopant that can substitute either the A (Pb^{2+}) or B (Ti^{4+}) site in the perovskite structure as outlined with a dashed pink line in Figure 6.1a. We hypothesize that this results in different emission profiles from the defect that are tied to the direction of P. We probe the telecom-wavelength $^4I_{13/2} \rightarrow ^4I_{15/2}$ transition for Er^{3+} at 6500 cm^{-1} (Fig. 6.1b). Because $c : a$ is large, using thin film techniques the orientation of P, with respect to the film geometry, can be effectively tuned using standard thin film techniques such as epitaxial strain. [44]

When the lattice constant of the substrate is large (> 3.95 Å), the PTO film will prefer to form domains where c is in the plane of the film (c-oriented) to relax the elastic energy. Conversely, when the lattice constant of the substrate is small (< 3.95Å), the PTO will form domains where c is preferentially normal to the film plane (a-oriented). This is illustrated in Figure 6.1c. Because these c- and a-oriented domains are defined by different lattice constants, this difference is also apparent in XRD. Thus, by varying the growth substrate, we are able to not only systematically vary strain, but also change the domain configuration of the sample.

The fraction of c- and a-domains can be quantified from XRD using the ratio of the film peaks at 21.5° (c, 001) and 22.6° (a, 100) (Fig. 6.1d). By integrating the c- and a-domain peaks in the XRD analysis, we can quantify the phase fraction of each sample (Fig. 6.1e). From this analysis, we can see that samples deposited on LSAT and STO substrates posses majority c-domains, while samples on GSO and NSO substrates have majority a-domains. Between these extremes, the lattice constant of DSO is comparable to the mean of the c and a axes of PTO, thus the structure is split between the two configurations.

6.4 Telecom Emission in Erbium-doped PTO

We can detect the Er^{3+} incorporated within the PTO crystal structure through its luminescence. The Er^{3+} ground state ($^4I_{15/2}$) is composed of 8 crystal field levels while the first excited state ($^4I_{13/2}$) is composed of 7 crystal field levels. At elevated temperatures, we expect a highly congested spectrum which is difficult to distinguish and identify due to a combination of broad linewidths and thermally excited states. However, at temperatures where the thermal energy, k_BT, is small relative to the crystal splittings, we expect simpler spectra arising only from the sparser range of thermally-populated states. Our analysis focuses on emission from the Y_1 level to the 3 lowest ground states: Z_1 (circle), Z_2 (diamond), and Z_3 (square) (Fig. 6.2a). We observe emission broadly consistent with previous measurements at 4 K for Er^{3+}-doped PTO on $SrTiO_3$ substrate with peaks at 6512 cm^{-1} ($Y_1 \rightarrow Z_1$), 6496 cm^{-1} ($Y_1 \rightarrow Z_2$) and 6398 cm^{-1} ($Y_1 \rightarrow Z_3$),[155] though our systematic variation of substrate allows us to identify new, subtle trends.

At 7 K, only transitions from the (Y_1) excited state are observed; the long excited state lifetime (3.9 ms)[155] ensures the excited state crystal field levels follow a Boltzmann distribution, so only the Y_1 has any appreciable population. However, at 77 K, additional peaks emerge that correspond to new thermally accessible crystal field levels in the excited state (Fig. 6.2b). The three transitions from the (Y_1) level to the the 3 lowest ground states can be identified for all 5 samples (LSAT, STO, DSO, GSO, NSO) at 77 K (Fig. 6.2c). We note, however,that there is significant variation in peak intensity, the presence of other transitions, and even the frequency of the transitions.

To explore these variations and develop a more detailed description of the luminescence of the Er^{3+}-doped PTO films, excitation-emission spectral maps (Fig. 6.3) were measured for all 5 samples. In these spectral maps, we can visualize the connection between different excitation and emission peaks. A purple, diagonal line where the emission and excitation frequencies are equivalent is present for all five samples which corresponds to residual laser scattering. To visualize the change in PL counts from the sample, the intensity is normalized

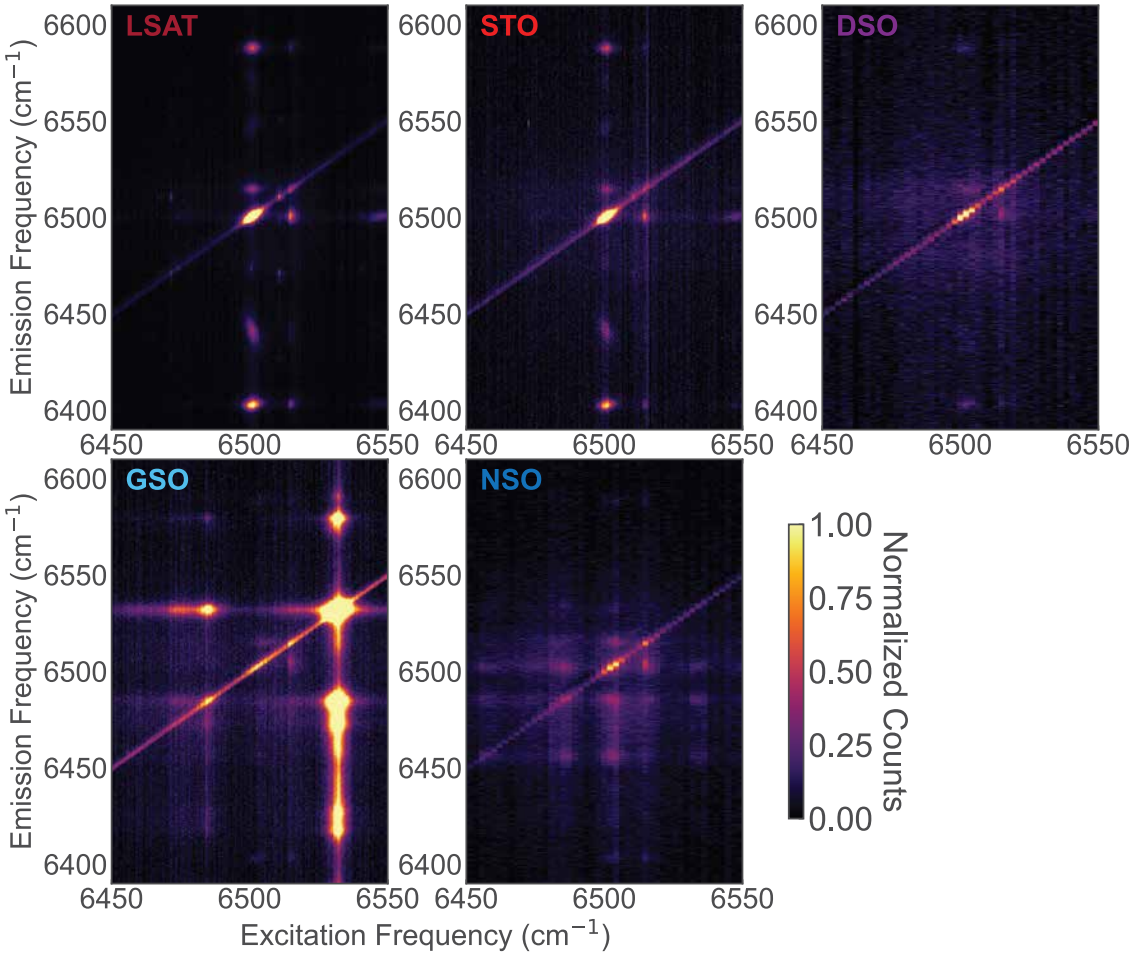

Figure 6.3: **Excitation-Emission Spectral Maps.** Spectral maps for all 5 samples. Intensity of spectral maps has been normalized to maximum intensity at 6500 cm^{-1}. Spectral maps were done at 77 K.

to the 6500 cm^{-1} emission peak when excited at 6500 cm^{-1}.

From this data, we can see the full complexity of the Er^{3+} photoluminescence. For the Er^{3+}-doped PTO sample on GSO, intense emission is detected at an excitation frequency of 6533 cm^{-1} and 6486 cm^{-1} which is not observed for the other samples. This emission, however, comes from the substrate itself (discussed later), presumably from trace contamination of Er^{3+} in the substrate similar to previous observations of unexpected background Er^{3+} emission.[170] An additional set of peaks is observed in Er^{3+}-doped PTO on NSO at an emission frequency of 6457 cm^{-1} and 6486 cm^{-1} which are excited by frequencies *not* observed in other samples or in the substrate. The assignment of these peaks is discussed

later.

6.5 Strain-Dependent Parameters

From our data, we can directly compare the changes in the Er^{3+} emission as a function of the PTO domain configuration imposed on the thin film by the substrate. We find that intensity, peak position, and linewidth are all impacted by the choice of substrate.

First, we visualize the difference in intensity, peak linewidth and frequency by comparing the PL from the Er^{3+}-doped PTO on STO and DSO samples at 7 K. We focus on the three peaks that are present at 7 K which correspond to the Y_1 to Z_1 transition (Fig. 6.4a), the Y_1 to Z_2 transition (Fig. 6.4b), and the Y_1 to Z_3 transition (Fig. 6.4c). We find a clear trend in intensity across our substrate series which is consistent across the three peaks we plot: the intensity of the peaks increases in the order NSO<GSO<DSO<STO<LSAT, which is also the order of *c*-domain fraction (Fig. B.2). This trend is observed at both 7 K (Fig. B.2a) and 77 K (Fig. B.2b). These samples were grown from the same PLD target, in the same chamber, during the same growth run, so we rule out different Er^{3+} compositions as a factor.

We also observe changes in the peak position and linewidth as a function of sample, as illustrated in Figure 6.4. We find that the emission peaks tend to shift to higher energies as the fraction of *c*-domains decreases; this trend is clearly observable by inspection at 7 K, but is also present in the 77 K data. This shift to higher energy is also accompanied by a broadening of the peaks.

To quantify these change, we fit the three transitions in the emission spectra using a Gaussian curve with a linear background (Fig. B.3-B.9) and compare the differences in PL intensity (Fig. 6.4d,g), emission frequency (Fig. 6.4e,h) and peak linewidth (Fig. 6.4f,i) for the samples at 7 K (Fig. 6.4d-e) and 77 K (Fig. 6.4g-i). Peak fit results are reported in Tables B.1 and B.2. The PL intensity of the peaks for the sample on DSO are normalized in respect to those of STO at 7 K (Fig. 6.4d). The same normalization was done for the 77 K data set but in respect to the peaks for the sample on LSAT instead (Fig. 6.4g). All of the transitions' peaks intensities decrease as the fraction of *c*-domains approaches 0. At 77 K, the PL counts decreases on average for the three transitions by 57% for the STO sample, 86% for the DSO sample, 92% for GSO and 91% for the NSO sample.

Additionally, the change in peak position for each transition is compared by subtracting that particular transition with either that of the sample on STO for the 7 K data set (Fig. 6.4e) or the sample on LSAT for the 77 K data set (Fig. 6.4h). As the fraction of *c*-domains decreases, the emission frequency increases. The change is more drastic for the 7 K data set where the emission frequency increases by at least 0.58 cm^{-1} for the Y_1 to Z_1

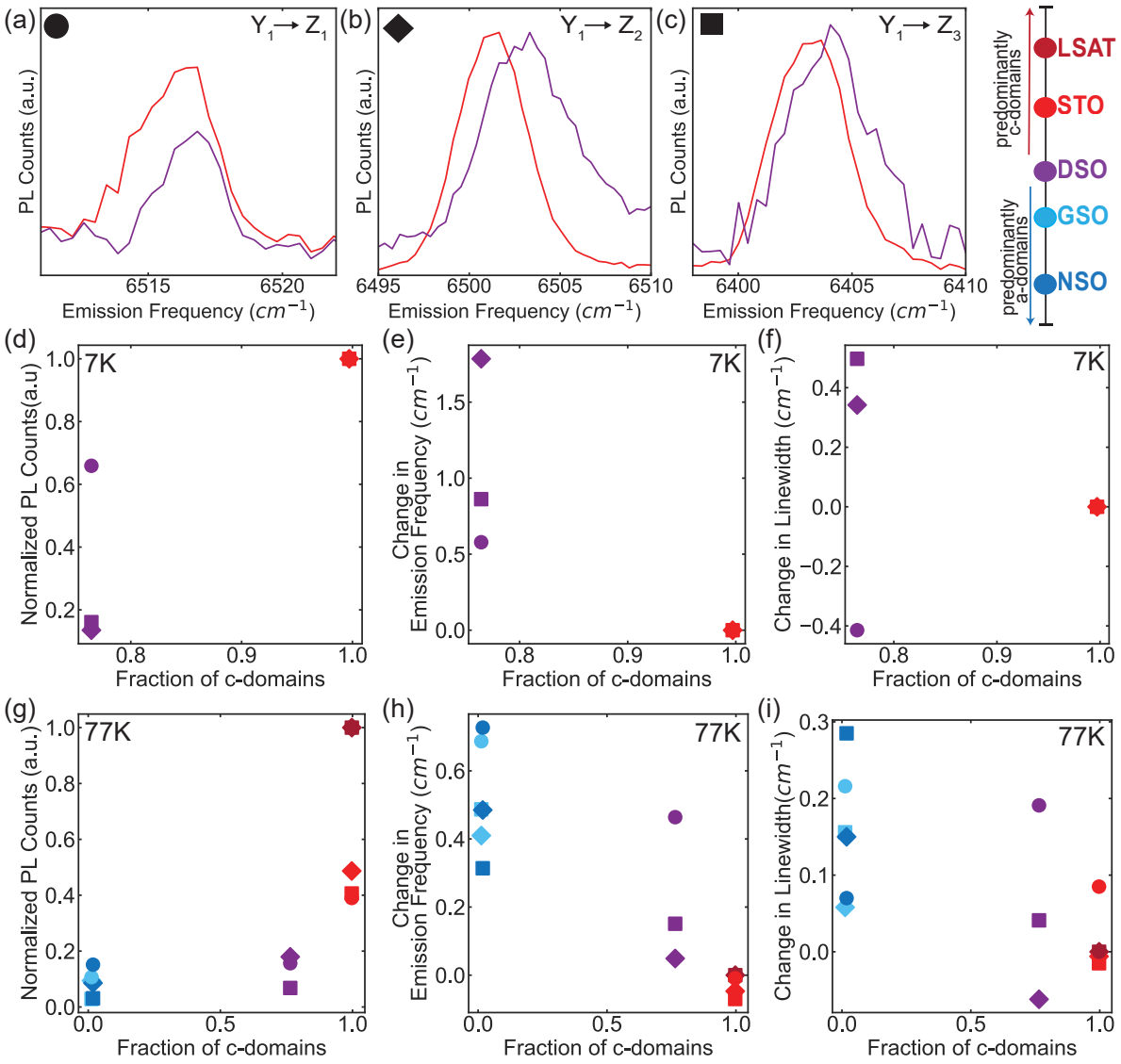

Figure 6.4: **Changes in Er^{3+}Emission a** Emission corresponding to Y_1 to Z_1,**b** Y_1 to Z_2 and **c** Y_1 to Z_3 transitions for Er^{3+}-doped PTO on STO (red) and DSO (purple) samples at 7 K. **d** Change in counts, **e** emission frequency and **f** peak linewidth for Er^{3+}-doped PTO sample on STO and DSO at 7 K. As well as, the **g** Change in counts, **h** emission frequency and **i** peak linewidth for Er^{3+}-doped PTO sample on the 5 substrates at 77 K. A color reference is provided for easy substrate identification. Measurements done at 7 K were excited at 6515 cm^{-1} and measurements done at 77K were excited at 6500 cm^{-1}.

transition and at most 1.78 cm^{-1} for the Y_1 to Z_2 transitions. At 77 K, the change in emission frequency for the samples with predominantly a-domains vary between 0.31 cm^{-1} for the Y_1 to Z_3 transition and 0.73 cm^{-1} for the Y_1 to Z_2 transition both for the sample on NSO.

Similarly, the change in linewidth for each sample is compared by subtracting that sample's linewidth with either the sample on STO for the 7 K data set (Fig. 6.4f) or the sample on LSAT for the 77 K data set (Fig. 6.4i). Overall, as the fraction of c-domain decreases, the change in linewidth of the samples increases. The only exceptions are the Y_1 to Z_1 transition for the Er^{3+}-doped PTO sample on DSO which changes by -0.41 cm^{-1} at 7 K and the Y_1 to Z_2 transition for the Er^{3+}-doped PTO on DSO which changes by -0.06 cm^{-1} at 77 K. However, it is important to note that both those transitions are at resonance with the excitation frequency. Additionally, the changes in linewidth are smaller than the spectrometer resolution (0.8 cm^{-1}), hence these values may be an underestimations of the true change in linewidth. Yet again, the change is more drastic at 7 K than at 77 K. Overall, the samples with a higher fraction of c-domains have brighter peak intensities, lower energy emission frequencies and narrower linewidths.

We consider whether these trends could be artifacts from slightly different temperatures due to differences in sample mounting *etc...* by comparing our data to temperature-dependent measurements (Fig. B.10-B.12). In the 10-50 K range, the PL counts increases for all 3 peaks up until a threshold temperature of 35 K in which the PL counts then decrease in intensity and continue to decrease at the liquid N_2 temperature regime. This turnover arises from the depopulation of the Z_1 ground state once other crystal field levels are thermally excited. The change in PL counts with temperature is much more gradual than the observed changes across samples; for the trends we observe to arise from sample mounting we would require implausibly-large variations of $\approx$25 K across our datasets.

Similarly, both the change in emission frequency and change in linewidth increase gradually with temperature for both temperature regimes. In the liquid He temperature regime, the changes in emission frequency and linewidth discussed above are not included in the temperature dependent data. At most, a change in emission frequency of 0.47 cm^{-1} for the Y_1 to Z_3 transition and a change in linewidth of 0.27 cm^{-1} for the Y_1 to Z_1 transition are observed at 55 K. In the liquid N_2 temperature regime, the changes in emission frequency and linewidth discussed above occur between 110 K-150 K and 90 K-110 K, respectively. These temperatures are unlikely to be reached in the cryostat during the measurement without external voltage. Therefore, the trends we observe in Figure 6.4 are due to different domain configuration imposed by epitaxial strain on the thin film through the substrate and not because of differences in thermal conditions.

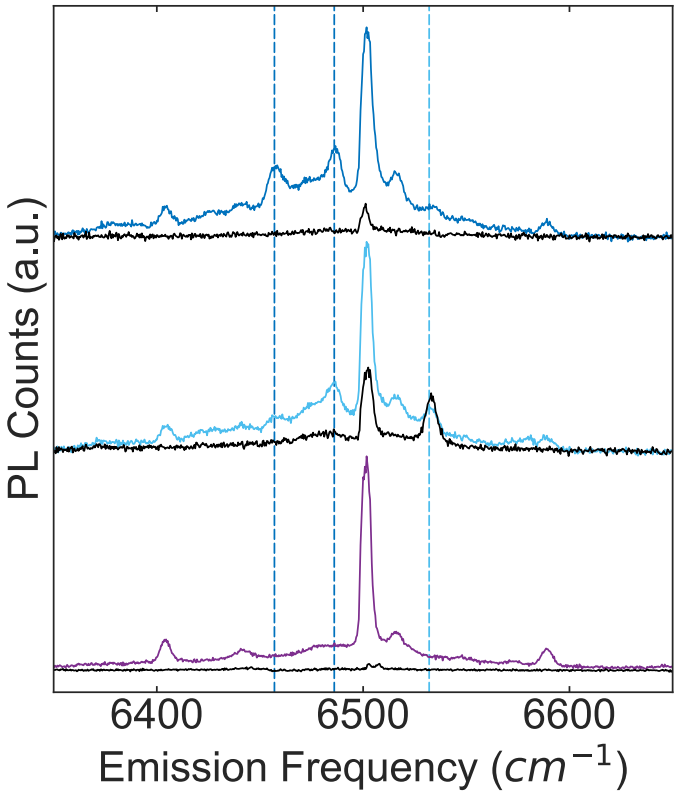

Figure 6.5: **Rare Earth Emission from Substrates** PL for the Er^{3+} doped PTO samples deposited on DSO (purple), GSO (light blue) and NSO (dark blue) are compared to the that of their respective substrates (black) when excited at 6500 cm^{-1}. Dashed lines represent frequencies for different set of peaks present in GSO (light blue dashed) and NSO (dark blue dashed).

6.6 Second Site Identification

In our analysis so far, we have focused on peaks that were previously reported in Er^{3+}-doped PTO on STO.[155] However, we also observe peaks in GSO (Fig. B.13) and NSO (Fig. B.14) which have not been previously reported. We determine that the intense peaks in GSO arise from the substrate (Fig. 6.5). Given the unique emission range of Er^{3+},[42] we assume these peaks come from Er^{3+} contamination in the substrate itself, a known problem with REI materials.[162, 170] None of the other substrates used displayed the same intense background signal.

Table 6.1: Additional Peaks in Er^{3+}-doped PTO on GSO and NSO

GSO			NSO		
Frequency (cm^{-1})	Intensity (arb. units)	Linewidth (cm^{-1})	Frequency (cm^{-1})	Intensity (arb. units)	Linewidth (cm^{-1})
6456.43	225.48	5.06	6457.36	500.08	3.21
6485.71	417.52	3.01	6486.44	618.70	2.84
6533.38	346.06	3.07	6534.84	141.58	3.27

The new peaks in NSO (Fig. 6.5), however, are not present in the substrate-only sample, demonstrating that they arise from the Er^{3+}-doped PTO layer itself. These peaks reported in Table 6.1 are not present in the samples with a high fraction of *c*-domains (LSAT, STO and DSO). We see features consistent with this second site in GSO, but the large background of the substrate signal makes definitive statement difficult.

Additionally, we compared the emission of the Er^{3+}-doped PTO samples and their substrates when exciting at a resonant frequency to those additional peaks (Fig B.15). When we excite the Er^{3+}-doped PTO on GSO sample with 6533 cm^{-1} excitation (Fig. B.15a), a different set of peaks are present which do not match the peaks at 6500 cm^{-1} excitation. However, the new set of peaks is also present in the PL spectra of the GSO substrate when excited at 6533 cm^{-1}. Hence, we further confirm that these additional peaks are due to Er^{3+} impurities in the GSO substrate. These second set of peaks have different frequencies than the peaks for Er^{3+}-doped PTO due to the Er^{3+} experiencing different local coordination environments.

Similarly, to evaluate the identity of the peak at 6457$cm^{-1}$for the NSO sample, we excite both the Er^{3+}-doped PTO on NSO sample and the NSO substrate with a 6457 cm^{-1}excitation frequency (Fig. B.15b). For the NSO sample, peaks at 6485$cm^{-1}$and 6500$cm^{-1}$are also present which match peaks present at a 6500 cm^{-1}excitation frequency. The NSO substrate does not have any additional peaks beyond the one at 6457cm^{-1}which is due to some residual laser scattering.

Since Er^{3+}-doped PTO on GSO is also predominantly *a*-domains, we also measure its PL at 6457 cm^{-1}excitation and compare it with the GSO substrate (Fig. B.15c). However due to the bright luminescence of the Er^{3+}impurities in the GSO substrate, it is difficult to differentiate whether the emission at this excitation frequency is from the Er^{3+} in PTO or the Er^{3+} in the GSO.

6.7 Discussion

We consider potential origins of this different family of peaks in terms of perturbations to the local crystal field. One potential explanation is that the charge compensation required to host Er^{3+} in a lattice of Pb^{2+} and Ti^{4+} charges is different; for example, local *vs* non-local charge compensation, or even different charge compensation configurations, can give rise to distinct sets of peaks.[158] Alternatively, there are two different cation sites the Er^{3+} could occupy, each with a different crystal field environment (A site or B site in the perovskite structure of $PbTiO_3$) (Fig. 6.1a).

While our spectroscopic results do not allow us to definitely distinguish between these scenarios, we hypothesize that occupancy of the A site *and* B site is the origin of the two sets of peaks. Vacancies within the PTO crystal (the most likely charge compensation mechanism) have been extensively studied.[151, 173, 148] Oxygen vacancies, which are the most common, are highly mobile[103] making them unlikely to be localized around a particular Er^{3+} dopant.[24, 181] Moreover, ESR measurements have shown that rare-earth ions can substitute into the A or B site of $BaTiO_3$,[51] where the thermodynamic driving force is the ionic radius of the ion relative to the site. This is consistent with our observation that the population of these sites changes as we tune the epitaxial strain and lattice parameter of the film with different substrates.

6.8 Conclusion

To conclude, we have shown that Er^{3+} emission can be tuned by epitaxial strain engineering via substrate selection. Epitaxially depositing Er^{3+}-doped PTO films at similar conditions on substrates with varying lattice parameters permits for fabrication of thin films of the same composition but different domain configurations. This allowed for a direct comparison of how strain engineering in these films affects the Er^{3+} emission in the telecom spectral range. We observed that films with predominantly *c*-domains have narrower linewidths, emit at lower energies and have a brighter luminescence than films with predominantly *a*-domains. Additionally, samples that have predominantly *a*-domains showed additional peaks that correspond to Er^{3+} transitions. The set of peaks for the Er^{3+}-doped PTO on GSO sample correspond to Er^{3+} impurities in the GSO substrate itself. However, the set of peaks for the sample on NSO does not come from the NSO substrate and hence must be from the deposited Er^{3+}-doped PTO. This different set of peaks can either be due to Er^{3+} replacing a different site in the PTO crystal and/or due to some charge compensation effects. This work lays a foundation to how strain engineering through epitaxial fabrication of samples plays a role in controlling the emission of REI. Opening up the pathway to manipulating the Er^{3+} emission via controlling the ferroelectic order parameter of the host film.

Chapter 7

Conclusion and Outlook

7.1 Conclusion

In this part of the dissertation, we discussed the benefits and properties of erbium-doped ferroelectric thin films. In Chapter 5, we expand on the fundamental concepts needed to understand why ferroelectric films and rare earth ions (REIs) are interesting materials to study as well as why combining them is beneficial. In Chapter 6, we discussed the ability to tune the Er^{3+} emission intensity, frequency, and linewidth through engineering ferroelectric thin films with different amounts of epitaxial strain. Additionally, we observed an additional set of peaks that are only present on samples with predominantly *a*-domains (in-plane polarization). Although for one sample those peaks were identified to be from REI impurities in the substrate, that was not the case for the other sample. We hypothesized that these spectral differences are because the Er^{3+} experiences different local crystal field environments either due to different atomic site substitution and/or charge compensation effects. This work lays a foundation to how epitaxial strain engineering during thin film deposition plays a role in tuning the emission of REI which is important to consider in future studies as Er^{3+}-doped PTO thin films will always have some amount of strain.

7.2 Outlook

Although understanding the effect of thin film epitaxial strain on Er^{3+} emission is helpful to fully understand thin film engineering strategies, the ideal application of this material system is electric field manipulation of the the Er^{3+} ions. Through applying an external electric field, we can manipulate the ferroelectric order of the thin film which will directly influence the local crystal field environment experienced by the Er^{3+}.

The most straightforward method to do these measurements is by using a sample with predominantly *c*-domains (out of plane polarization) and applying an in-plane electric field.

Experimentally, we expect to be able to probe this by measuring the changes in the emission spectra of Er^{3+}. However, the changes in the Er^{3+} emission from out of plane polarization to in plane polarization will be fairly similar to local thermal heating of the sample despite those processes being physically drastically different. A state-of-the-art cryostat instrument with excellent control of thermal conditions will be necessary to decouple the thermal conditions and the influence of the external electric field. Another potential solution is to engineer a way to apply an out-of-plane electric field on a sample with in-plane polarization. However, the lithography required for the device fabrication would be fairly complex.

PTO was an ideal system to perform these initial characterization techniques since it is a ferroelectric material that has been well-studied.[44] However, PTO thin films are known to have high leakage currents resulting in polarization retention loss.[113] There are engineering techniques that can be used to fabricate films with different architectures to minimize stray fields. For example, $PbSrTiO_3$ bilayer heterostructures can alternate from a mixed phase to predominantly *c*-domains resulting in an electric analogue of an exchange-spring interaction. Through variations in strontium content and thickness of the layers additional control on the switching properties of the bilayer system is obtained.[84] Although future work is required, these avenues provide routes to achieve the goals of leveraging the ferroelectric order of a host material to manipulate REI qubits for quantum networks and low-power spintronic applications.

Bibliography

[1] Abdullah S. Abbas et al. "Observation of an Orientational Glass in a Superlattice of Elliptically-Faceted CdSe Nanocrystals". In: *ACS Nano* 16.6 (June 2022), pp. 9339–9347. ISSN: 1936086X. DOI: 10.1021/ACSNANO.2C02014/ASSET/IMAGES/LARGE/NN2C02014{_}0005.JPEG. URL: https://pubs.acs.org/doi/full/10.1021/acsnano.2c02014.

[2] Gleb M. Akselrod et al. "Subdiffusive exciton transport in quantum dot solids". In: *Nano Letters* 14.6 (2014), pp. 3556–3562. ISSN: 15306992. DOI: 10.1021/nl501190s.

[3] A. P. Alivisatos. "Perspectives on the physical chemistry of semiconductor nanocrystals". In: *Journal of Physical Chemistry* 100.31 (1996), pp. 13226–13239. ISSN: 00223654. DOI: 10.1021/jp9535506.

[4] A. Paul Alivisatos, Weiwei Gu, and Carolyn Larabell. "Quantum Dots as Cellular Probes". In: *https://doi.org/10.1146/annurev.bioeng.7.060804.100432* 7 (July 2005), pp. 55–76. ISSN: 15239829. DOI: 10.1146/ANNUREV.BIOENG.7.060804.100432. URL: https://www.annualreviews.org/doi/abs/10.1146/annurev.bioeng.7.060804.100432.

[5] Nicholas C. Anderson et al. "Ligand Exchange and the Stoichiometry of Metal Chalcogenide Nanocrystals: Spectroscopic Observation of Facile Metal-Carboxylate Displacement and Binding". In: *Journal of the American Chemical Society* 135.49 (Dec. 2013), pp. 18536–18548. DOI: 10.1021/JA4086758. URL: https://pubs.acs.org/doi/full/10.1021/ja4086758.

[6] P. Ascenzi et al. "Rare earth elements (REE) in biology and medicine". In: *Rendiconti Lincei* 31.3 (Sept. 2020), pp. 821–833. ISSN: 17200776. DOI: 10.1007/S12210-020-00930-W/FIGURES/8. URL: https://link.springer.com/article/10.1007/s12210-020-00930-w.

[7] S. Ashhab et al. "Two-level systems driven by large-amplitude fields". In: *Physical Review A - Atomic, Molecular, and Optical Physics* 75.6 (June 2007), p. 063414. ISSN: 10502947. DOI: 10.1103/PHYSREVA.75.063414/FIGURES/6/MEDIUM. URL: https://journals.aps.org/pra/abstract/10.1103/PhysRevA.75.063414.

[8] Assaf Avidan and Dan Oron. "Large Blue Shift of the Biexciton State in Tellurium Doped CdSe Colloidal Quantum Dots". In: *Nano Letters* 8.8 (Aug. 2008), pp. 2384–2387. DOI: 10.1021/NL801241M. URL: https://pubs.acs.org/doi/full/10.1021/nl801241m.

[9] Assaf Avidan and Dan Oron. "Large blue shift of the biexciton state in tellurium doped CdSe colloidal quantum dots". In: *Nano Letters* 8.8 (Aug. 2008), pp. 2384–2387. ISSN: 15306984. DOI: 10.1021/nl801241m. URL: https://pubs.acs.org/sharingguidelines.

[10] Assaf Avidan, Iddo Pinkas, and Dan Oron. "How Quickly Does a Hole Relax into an Engineered Defect State in CdSe Quantum Dots". In: *ACS Nano* 6.4 (Apr. 2012), pp. 3063–3069. DOI: 10.1021/NN204690P. URL: https://pubs.acs.org/doi/full/10.1021/nn204690p.

[11] Arunima D Balan et al. "Unsaturated Ligands Seed an Order to Disorder Transition in Mixed Ligand Shells of CdSe/CdS Quantum Dots". In: *ACS Nano* 13 (2019), p. 37. DOI: 10.1021/acsnano.9b03054. URL: www.acsnano.org.

[12] Arunima D. Balan et al. "Effect of Thermal Fluctuations on the Radiative Rate in Core/Shell Quantum Dots". In: *Nano Letters* 17.3 (2017), pp. 1629–1636. ISSN: 15306992. DOI: 10.1021/acs.nanolett.6b04816.

[13] John Ballato, John S. Lewis, and Paul Holloway. "Display Applications of Rare-Earth-Doped Materials". In: *MRS Bulletin* 24.9 (1999), pp. 51–56. ISSN: 0883-7694. DOI: 10.1557/S0883769400053070. URL: https://www.cambridge.org/core/journals/mrs-bulletin/article/display-applications-of-rareearthdoped-materials/F013B84D4B7B696A0F38BDC09CD6C424.

[14] Meneka Banik and Rabibrata Mukherjee. "Fabrication of Ordered 2D Colloidal Crystals on Flat and Patterned Substrates by Spin Coating". In: *ACS Omega* 3.10 (2018), pp. 13422–13432. ISSN: 24701343. DOI: 10.1021/acsomega.8b02002.

[15] Maryam Bari et al. "Ferroelastic Domains and Effects of Spontaneous Strain in Lead Halide Perovskite CsPbBr3". In: *Chemistry of Materials* 35.17 (Sept. 2023), pp. 6659–6670. ISSN: 15205002. DOI: 10.1021/ACS.CHEMMATER.3C00579/ASSET/IMAGES/LARGE/CM3C00579{_}0012.JPEG. URL: https://pubs.acs.org/doi/full/10.1021/acs.chemmater.3c00579.

[16] William J Baumgardner, Kevin Whitham, and Tobias Hanrath. "Confined-but- Connected Quantum Solids via Controlled Ligand Displacement". In: 13 (2013). DOI: 10.1021/nl401298s. URL: https://pubs.acs.org/sharingguidelines.

[17] Moungi G Bawendi, Michael L Steigerwald, and Louis E Brus. "The Quantum Mechanics of Larger Semiconductor Clusters ("Quantum Dots")". In: *Annu. Rev. Phys. Chem* 41 (1990), pp. 477–96. URL: www.annualreviews.org.

[18] Brandon J. Beberwyck, Yogesh Surendranath, and A. Paul Alivisatos. "Cation exchange: A versatile tool for nanomaterials synthesis". In: *Journal of Physical Chemistry C* 117.39 (Oct. 2013), pp. 19759–19770. ISSN: 19327447. DOI: 10.1021/JP405989Z/ASSET/IMAGES/MEDIUM/JP-2013-05989Z{_}0004.GIF. URL: https://pubs.acs.org/doi/full/10.1021/jp405989z.

[19] D. Benetti et al. "Combined magnetron sputtering and pulsed laser deposition of TiO 2 and BFCO thin films". In: *Scientific Reports 2017 7:1* 7.1 (May 2017), pp. 1–9. ISSN: 2045-2322. DOI: 10.1038/s41598-017-02284-0. URL: https://www.nature.com/articles/s41598-017-02284-0.

[20] Andreas Biebricher, Markus Sauer, and Philip Tinnefeid. "Radiative and nonradiative rate fluctuations of single colloidal semiconductor nanocrystals". In: *Journal of Physical Chemistry B* 110.11 (Mar. 2006), pp. 5174–5178. ISSN: 15206106. DOI: 10.1021/JP060660B/ASSET/IMAGES/LARGE/JP060660BF00004.JPEG. URL: https://pubs.acs.org/doi/full/10.1021/jp060660b.

[21] Michael A. Boles, Michael Engel, and Dmitri V. Talapin. "Self-assembly of colloidal nanocrystals: From intricate structures to functional materials". In: *Chemical Reviews* 116.18 (2016), pp. 11220–11289. ISSN: 15206890. DOI: 10.1021/acs.chemrev.6b00196.

[22] Thomas Böttger et al. "Effects of magnetic field orientation on optical decoherence in Er3+: Y2 SiO5". In: *Physical Review B - Condensed Matter and Materials Physics* 79.11 (Mar. 2009), p. 115104. ISSN: 10980121. DOI: 10.1103/PHYSREVB.79.115104/FIGURES/4/MEDIUM. URL: https://journals.aps.org/prb/abstract/10.1103/PhysRevB.79.115104.

[23] Thomas Böttger et al. "Optical decoherence and spectral diffusion at 1.5 μm in Er3+: Y2 SiO5 versus magnetic field, temperature, and Er3+ concentration". In: *Physical Review B - Condensed Matter and Materials Physics* 73.7 (Feb. 2006), p. 075101. ISSN: 10980121. DOI: 10.1103/PHYSREVB.73.075101/FIGURES/7/MEDIUM. URL: https://journals.aps.org/prb/abstract/10.1103/PhysRevB.73.075101.

[24] Isaac Bredeson et al. "Dimensional control of defect dynamics in perovskite oxide superlattices". In: *Physical Review Materials* 2.3 (Mar. 2018), p. 035401. ISSN: 24759953. DOI: 10.1103/PHYSREVMATERIALS.2.035401/FIGURES/5/MEDIUM. URL: https://journals.aps.org/prmaterials/abstract/10.1103/PhysRevMaterials.2.035401.

[25] Noah D. Bronstein et al. "Quantum Dot Luminescent Concentrator Cavity Exhibiting 30-fold Concentration". In: *ACS Photonics* 2.11 (Aug. 2015), pp. 1576–1583. ISSN: 23304022. DOI: 10.1021/ACSPHOTONICS.5B00334/ASSET/IMAGES/PH-2015-00334Q{_}M004.GIF. URL: https://pubs.acs.org/doi/full/10.1021/acsphotonics.5b00334.

[26] Immanuel. Broser et al. *Landolt-Börnstein Zahlenwerte und Funktionen aus Naturwissenschaften und Technik: Neue Serie*. Springer, 1982. ISBN: 9783540113089. URL: https://link.springer.com/book/9783540113089.

[27] L. E. Brus. "Electron–electron and electron-hole interactions in small semiconductor crystallites: The size dependence of the lowest excited electronic state". In: *The Journal of Chemical Physics* 80.9 (May 1984), pp. 4403–4409. ISSN: 0021-9606. DOI: 10.1063/1.447218. URL: /aip/jcp/article/80/9/4403/625821/Electron-electron-and-electron-hole-interactions.

[28] Jason J Calvin et al. "Thermodynamics of the Adsorption of Cadmium Oleate to Cadmium Sulfide Quantum Dots and Implications of a Dynamic Ligand Shell". In: *J. Phys. Chem. C* 2022 (1295). DOI: 10.1021/acs.jpcc.2c04223. URL: https://doi.org/10.1021/acs.jpcc.2c04223.

[29] Jason J. Calvin et al. "Thermodynamic Investigation of Increased Luminescence in Indium Phosphide Quantum Dots by Treatment with Metal Halide Salts". In: *Journal of the American Chemical Society* 142.44 (Nov. 2020), pp. 18897–18906. DOI: 10.1021/JACS.0C08954. URL: https://pubs.acs.org/doi/full/10.1021/jacs.0c08954.

[30] Jason J. Calvin et al. "Thermodynamics of Composition Dependent Ligand Exchange on the Surfaces of Colloidal Indium Phosphide Quantum Dots". In: *ACS Nano* 15.1 (Jan. 2021), pp. 1407–1420. DOI: 10.1021/ACSNANO.0C08683. URL: https://pubs.acs.org/doi/full/10.1021/acsnano.0c08683.

[31] Luigi Carbone et al. "Synthesis and micrometer-scale assembly of colloidal CdSe/CdS nanorods prepared by a seeded growth approach". In: *Nano Letters* 7.10 (2007), pp. 2942–2950. ISSN: 15306984. DOI: 10.1021/nl0717661.

[32] Elsa Cassette et al. "Colloidal CdSe/CdS dot-in-plate nanocrystals with 2D-polarized emission". In: *ACS Nano* 6.8 (2012), pp. 6741–6750. ISSN: 19360851. DOI: 10.1021/nn3024255.

[33] Lucia Cavigli et al. "Volume versus surface-mediated recombination in anatase TiO2 nanoparticles". In: *Journal of Applied Physics* 106.5 (Sept. 2009), p. 53516. ISSN: 00218979. DOI: 10.1063/1.3211291/371222. URL: /aip/jap/article/106/5/053516/371222/Volume-versus-surface-mediated-recombination-in.

[34] P. Chandra et al. "Scaling of the Coercive Field with Thickness in Thin-Film Ferroelectrics". In: *Ferroelectrics* 313 (2004), pp. 7–13. ISSN: 00150193. DOI: 10.1080/00150190490891157. URL: https://www.tandfonline.com/doi/abs/10.1080/00150190490891157.

[35] Himani Chauhan, Yogesh Kumar, and Sasanka Deka. "New synthesis of two-dimensional CdSe/CdS core@shell dot-in-hexagonal platelet nanoheterostructures with interesting optical properties". In: *Nanoscale* 6.17 (2014), pp. 10347–10354. ISSN: 20403372. DOI: 10.1039/c4nr01264j.

[36] Chi Chen et al. "Ultrafast dense DNA functionalization of quantum dots and rods for scalable 2D array fabrication with nanoscale precision". In: *Science Advances* 9.32 (Aug. 2023). ISSN: 23752548. DOI: 10.1126/SCIADV.ADH8508/SUPPL{_}FILE/SCIADV.ADH8508{_}SM.PDF. URL: https://www.science.org/doi/10.1126/sciadv.adh8508.

[37] Ou Chen et al. "Compact high-quality CdSe-CdS core-shell nanocrystals with narrow emission linewidths and suppressed blinking". In: *Nature Materials* 12.5 (2013), pp. 445–451. ISSN: 14761122. DOI: 10.1038/nmat3539.

[38] Siming Chen et al. "Hybrid quantum well/quantum dot structure for broad spectral bandwidth emitters". In: *IEEE Journal on Selected Topics in Quantum Electronics* 19.4 (2013). ISSN: 1077260X. DOI: 10.1109/JSTQE.2012.2235175.

[39] Songtao Chen et al. "Parallel single-shot measurement and coherent control of solid-state spins below the diffraction limit". In: *Science* 370.6516 (Oct. 2020), pp. 592–595. ISSN: 10959203. DOI: 10.1126/SCIENCE.ABC7821/SUPPL{_}FILE/ABC7821-CHEN-SM.PDF. URL: https://www.science.org/doi/10.1126/science.abc7821.

[40] Yongfen Chen et al. ""Giant" multishell CdSe nanocrystal quantum dots with suppressed blinking". In: *Journal of the American Chemical Society* 130.15 (Apr. 2008), pp. 5026–5027. ISSN: 00027863. DOI: 10.1021/JA711379K/SUPPL{_}FILE/JA711379K-FILE003.PDF. URL: https://pubs.acs.org/doi/full/10.1021/ja711379k.

[41] v. L. Colvin, M. C. Schlamp, and P. A. Allvlsatos. "Light-emitting diodes made from cadmium selenide nanocrystals and a semiconducting polymer". In: *Nature* 370.6488 (1994), pp. 354–357.

[42] H. M. Crosswhite and G. H. Dieke. "The Spectra of the Doubly and Triply Ionized Rare Earths". In: *Applied Optics, Vol. 2, Issue 7, pp. 675-686* 2.7 (July 1963), pp. 675–686. ISSN: 2155-3165. DOI: 10.1364/AO.2.000675. URL: https://opg.optica.org/viewmedia.cfm?uri=ao-2-7-675&seq=0&html=true%20https://opg.optica.org/abstract.cfm?uri=ao-2-7-675%20https://opg.optica.org/ao/abstract.cfm?uri=ao-2-7-675.

[43] Xingliang Dai et al. "Quantum-Dot Light-Emitting Diodes for Large-Area Displays: Towards the Dawn of Commercialization". In: *Advanced Materials* 29.14 (Apr. 2017), p. 1607022. ISSN: 1521-4095. DOI: 10.1002/ADMA.201607022. URL: https://onlinelibrary.wiley.com/doi/full/10.1002/adma.201607022%20https://onlinelibrary.wiley.com/doi/abs/10.1002/adma.201607022%20https://onlinelibrary.wiley.com/doi/10.1002/adma.201607022.

[44] Anoop R. Damodaran et al. "Three-State Ferroelastic Switching and Large Electromechanical Responses in PbTiO3 Thin Films". In: *Advanced Materials* 29.37 (Oct. 2017), p. 1702069. ISSN: 1521-4095. DOI: 10.1002/ADMA.201702069. URL: https://onlinelibrary.wiley.com/doi/full/10.1002/adma.201702069%20https:

//onlinelibrary.wiley.com/doi/abs/10.1002/adma.201702069%20https://onlinelibrary.wiley.com/doi/10.1002/adma.201702069.

[45] M. Dejneka and B. Samson. "Rare-earth-doped fibers for telecommunications applications". In: *MRS Bulletin* 24.9 (Sept. 1999), pp. 39–45. ISSN: 08837694. DOI: 10.1557/S0883769400053057/METRICS. URL: https://link.springer.com/article/10.1557/S0883769400053057.

[46] Kerong Deng et al. "Self-assembly of anisotropic nanoparticles into functional superstructures". In: *Chem. Soc. Rev* 49 (2020), p. 6002. DOI: 10.1039/d0cs00541j.

[47] Benjamin T Diroll et al. "Smectic Nanorod Superlattices Assembled on Liquid Subphases: Structure, Orientation, Defects, and Optical Polarization". In: *Chem. Mater* 27 (2015), p. 55. DOI: 10.1021/acs.chemmater.5b00355. URL: https://pubs.acs.org/sharingguidelines.

[48] Angang Dong, Yucong Jiao, and Delia J. Milliron. "Electronically coupled nanocrystal superlattice films by in situ ligand exchange at the liquid-air interface". In: *ACS Nano* 7.12 (2013), pp. 10978–10984. ISSN: 19360851. DOI: 10.1021/nn404566b.

[49] Angang Dong et al. "Binary nanocrystal superlattice membranes self-assembled at the liquid–air interface". In: *Nature 2010 466:7305* 466.7305 (July 2010), pp. 474–477. ISSN: 1476-4687. DOI: 10.1038/nature09188. URL: https://www.nature.com/articles/nature09188.

[50] Hee Son Dong et al. "Cation exchange reactions in ionic nanocrystals". In: *Science* 306.5698 (Nov. 2004), pp. 1009–1012. DOI: 10.1126/SCIENCE.1103755. URL: www.sciencemag.org/cgi/content/full/306/5698/1005/.

[51] Timothy D. Dunbar et al. "Electron paramagnetic resonance investigations of lanthanide-doped barium titanate: Dopant site occupancy". In: *Journal of Physical Chemistry B* 108.3 (Jan. 2004), pp. 908–917. ISSN: 15206106. DOI: 10.1021/JP036542V/ASSET/IMAGES/LARGE/JP036542VF00014.JPEG. URL: https://pubs.acs.org/doi/full/10.1021/jp036542v.

[52] A. L. Efros and Al. L. Efros. "Interband light absorption in semiconductor spheres". In: *Sov. Phys. Semicond.* 16.7 (1982), pp. 772–775. URL: https://www.researchgate.net/publication/279890805.

[53] Carissa N. Eisler et al. "Photonic Luminescent Solar Concentrator Design for High Efficiency, Low Cost Multijunction Photovoltaics". In: *Frontiers in Photonics* 3.July (2022), pp. 1–10. DOI: 10.3389/fphot.2022.932913.

[54] A. I. Ekimov and A. A. Onushchenko. "Quantum Size Effect in Three-Dimensional Microscopic Semiconductor Crystals". In: *JETP Letters* 118.1 (Dec. 2023), S15–S17. ISSN: 10906487. DOI: 10.1134/S0021364023130040/FIGURES/3. URL: https://link.springer.com/article/10.1134/S0021364023130040.

[55] *Electricity & Magnetism*. URL: https://faculty.wcas.northwestern.edu/infocom/Ideas/electric.html.

[56] Hagai Eshet, Michael Grünwald, and Eran Rabani. "The electronic structure of CdSe/CdS Core/shell seeded nanorods: Type-I or quasi-type-II?" In: *Nano Letters* 13.12 (2013), pp. 5880–5885. ISSN: 15306984. DOI: 10.1021/nl402722n. URL: https://pubs.acs.org/sharingguidelines.

[57] Thomas Franzl et al. "CdSe:Te nanocrystals: Band-edge versus Te-related emission". In: *Journal of Physical Chemistry C* 111.7 (Feb. 2007), pp. 2974–2979. ISSN: 19327447. DOI: 10.1021/jp067166s. URL: https://pubs.acs.org/sharingguidelines.

[58] Matthew T Frederick, Victor A Amin, and Emily A Weiss. "Optical Properties of Strongly Coupled Quantum DotLigand Systems". In: (2013). DOI: 10.1021/jz301905n. URL: https://pubs.acs.org/sharingguidelines.

[59] Aihua Fu et al. "Semiconductor quantum rods as single molecule fluorescent biological labels". In: *Nano Letters* 7.1 (Jan. 2007), pp. 179–182. ISSN: 15306984. DOI: 10.1021/NL0626434/SUPPL{_}FILE/NL0626434SI20061110{_}064653.AVI. URL: https://pubs.acs.org/doi/abs/10.1021/nl0626434.

[60] F. Pelayo García de Arquer et al. "Semiconductor quantum dots: Technological progress and future challenges". In: *Science (New York, N.Y.)* 373.6555 (Aug. 2021). ISSN: 10959203. DOI: 10.1126/SCIENCE.AAZ8541/ASSET/C3AC7CAD-9110-4FD1-85BA-03C145F887FC/ASSETS/IMAGES/LARGE/SCIENCE.AAZ8541-F6.JPG. URL: https://www.science.org/doi/10.1126/science.aaz8541.

[61] Carlo Giansante and Ivan Infante. "Surface Traps in Colloidal Quantum Dots: A Combined Experimental and Theoretical Perspective". In: *Journal of Physical Chemistry Letters* 8.20 (Oct. 2017), pp. 5209–5215. ISSN: 19487185. DOI: 10.1021/ACS.JPCLETT.7B02193/ASSET/IMAGES/LARGE/JZ-2017-02193Q{_}0005.JPEG. URL: https://pubs.acs.org/doi/full/10.1021/acs.jpclett.7b02193.

[62] Rachel H. Gilmore et al. "Charge Carrier Hopping Dynamics in Homogeneously Broadened PbS Quantum Dot Solids". In: *Nano Letters* 17.2 (2017), pp. 893–901. ISSN: 15306992. DOI: 10.1021/acs.nanolett.6b04201.

[63] Naomi S. Ginsberg and William A. Tisdale. "Spatially resolved photogenerated exciton and charge transport in emerging semiconductors". In: *Annual Review of Physical Chemistry* 71 (2020), pp. 1–30. ISSN: 0066426X. DOI: 10.1146/annurev-physchem-052516-050703.

[64] Stephanie Gnewuch and Efrain E. Rodriguez. "The fourth ferroic order: Current status on ferrotoroidic materials". In: *Journal of Solid State Chemistry* 271 (Mar. 2019), pp. 175–190. ISSN: 0022-4596. DOI: 10.1016/J.JSSC.2018.12.035.

[65] Philippe Goldner, Alban Ferrier, and Olivier Guillot-Noël. "Rare Earth-Doped Crystals for Quantum Information Processing". In: *Handbook on the Physics and Chemistry of Rare Earths* 46 (Jan. 2015), pp. 1–78. ISSN: 0168-1273. DOI: 10.1016/B978-0-444-63260-9.00267-4.

[66] Zhenkun Gu et al. "Direct-Writing Multifunctional Perovskite Single Crystal Arrays by Inkjet Printing". In: *Small* 13.8 (Feb. 2017), p. 1603217. ISSN: 1613-6829. DOI: 10.1002/SMLL.201603217. URL: https://onlinelibrary.wiley.com/doi/full/10.1002/smll.201603217%20https://onlinelibrary.wiley.com/doi/abs/10.1002/smll.201603217%20https://onlinelibrary.wiley.com/doi/10.1002/smll.201603217.

[67] Jun Guan et al. "Quantum Dot-Plasmon Lasing with Controlled Polarization Patterns". In: *ACS Nano* 14.3 (Mar. 2020), pp. 3426–3433. ISSN: 1936086X. DOI: 10.1021/ACSNANO.9B09466/ASSET/IMAGES/LARGE/NN9B09466{_}0005.JPEG. URL: https://pubs.acs.org/doi/full/10.1021/acsnano.9b09466.

[68] Hyeon Han et al. "Lattice strain-enhanced exsolution of nanoparticles in thin films". In: *Nature Communications 2019 10:1* 10.1 (Apr. 2019), pp. 1–8. ISSN: 2041-1723. DOI: 10.1038/s41467-019-09395-4. URL: https://www.nature.com/articles/s41467-019-09395-4.

[69] David A Hanifi et al. "Redefining near-unity luminescence in quantum dots with photothermal threshold quantum yield". In: *Science* 1202.March (2019), pp. 1199–1202.

[70] Nicola A. Hill. "Why are there so few magnetic ferroelectrics?" In: *Journal of Physical Chemistry B* 104.29 (July 2000), pp. 6694–6709. ISSN: 15206106. DOI: 10.1021/JP000114X/ASSET/IMAGES/MEDIUM/JP000114XE00002.GIF. URL: https://pubs.acs.org/doi/full/10.1021/jp000114x.

[71] Maxwell P. Hoffman et al. "Mapping the effect of geometry on the radiative rate in core/shell QDs: core size dictates the conduction band offset". In: *RSC Advances* 11.57 (Nov. 2021), pp. 35887–35892. ISSN: 2046-2069. DOI: 10.1039/D1RA07556J. URL: https://pubs.rsc.org/en/content/articlehtml/2021/ra/d1ra07556j%20https://pubs.rsc.org/en/content/articlelanding/2021/ra/d1ra07556j.

[72] Chuanhui Huang et al. "Effect of structure : A new insight into nanoparticle assemblies from inanimate to animate". In: 1959.May (2020).

[73] Hehe Huang et al. "High-Efficiency Perovskite Quantum Dot Photovoltaic with Homogeneous Structure and Energy Landscape". In: (2023). DOI: 10.1002/adfm.202210728. URL: https://onlinelibrary.wiley.com/doi/10.1002/adfm.202210728.

[74] Yu Ming Huang et al. "Advances in Quantum-Dot-Based Displays". In: *Nanomaterials 2020, Vol. 10, Page 1327* 10.7 (July 2020), p. 1327. ISSN: 2079-4991. DOI: 10.3390/NANO10071327. URL: https://www.mdpi.com/2079-4991/10/7/1327/htm%20https://www.mdpi.com/2079-4991/10/7/1327.

[75] W. Hübner and K. Bennemann. "Simple theory for spin-lattice relaxation in metallic rare-earth ferromagnets". In: *Physical Review B* 53.6 (Feb. 1996), p. 3422. ISSN: 1550235X. DOI: 10.1103/PhysRevB.53.3422. URL: https://journals.aps.org/prb/abstract/10.1103/PhysRevB.53.3422.

[76] Mizuhiko Ichikawa, Torbjoörn Gustafsson, and Ivar Olovsson. "Is NaNO2 a pure order–disorder type ferroelectric?" In: *Solid State Communications* 123.3-4 (July 2002), pp. 135–139. ISSN: 0038-1098. DOI: 10.1016/S0038-1098(02)00207-7.

[77] Ankit Jain et al. "Atomistic Design of CdSe/CdS Core-Shell Quantum Dots with Suppressed Auger Recombination". In: *Nano Letters* 16.10 (2016), pp. 6491–6496. ISSN: 15306992. DOI: 10.1021/acs.nanolett.6b03059.

[78] Maximilian Jansen, William A. Tisdale, and Vanessa Wood. "Nanocrystal phononics". In: *Nature Materials 2023 22:2* 22.2 (Jan. 2023), pp. 161–169. ISSN: 1476-4660. DOI: 10.1038/s41563-022-01438-4. URL: https://www.nature.com/articles/s41563-022-01438-4.

[79] Jacek Jasieniak et al. "Re-examination of the size-dependent absorption properties of CdSe quantum dots". In: *Journal of Physical Chemistry C* 113.45 (2009), pp. 19468–19474. ISSN: 19327447. DOI: 10.1021/JP906827M/SUPPL{_}FILE/JP906827M{_}SI{_}001.PDF. URL: https://pubs.acs.org/doi/abs/10.1021/jp906827m.

[80] Cameron Jennings et al. "Self-Assembled InAs/GaAs Coupled Quantum Dots for Photonic Quantum Technologies". In: *Advanced Quantum Technologies* 3.2 (Feb. 2020), p. 1900085. ISSN: 2511-9044. DOI: 10.1002/QUTE.201900085. URL: https://onlinelibrary.wiley.com/doi/full/10.1002/qute.201900085%20https://onlinelibrary.wiley.com/doi/abs/10.1002/qute.201900085%20https://onlinelibrary.wiley.com/doi/10.1002/qute.201900085.

[81] Matthew J. Jurow et al. "Tunable Anisotropic Photon Emission from Self-Organized CsPbBr3 Perovskite Nanocrystals". In: *Nano Letters* 17.7 (July 2017), pp. 4534–4540. ISSN: 15306992. DOI: 10.1021/ACS.NANOLETT.7B02147/SUPPL{_}FILE/NL7B02147{_}SI{_}001.PDF.

[82] Cherie R. Kagan et al. "Colloidal Quantum Dots as Platforms for Quantum Information Science". In: *Chemical Reviews* 121.5 (Mar. 2021), pp. 3186–3233. ISSN: 15206890. DOI: 10.1021/ACS.CHEMREV.0C00831/ASSET/IMAGES/MEDIUM/CR0C00831{_}M012.GIF. URL: https://pubs.acs.org/doi/full/10.1021/acs.chemrev.0c00831.

[83] Khaled Karrai et al. "Hybridization of electronic states in quantum dots through photon emission". In: *Nature 2003 427:6970* 427.6970 (Jan. 2004), pp. 135–138. ISSN: 1476-4687. DOI: 10.1038/nature02109. URL: https://www.nature.com/articles/nature02109.

[84] Pravin Kavle et al. "Exchange-Interaction-Like Behavior in Ferroelectric Bilayers". In: *Advanced Materials* 35.39 (Sept. 2023), p. 2301934. ISSN: 1521-4095. DOI: 10.1002/ADMA.202301934. URL: https://onlinelibrary.wiley.com/doi/full/10.1002/adma.202301934%20https://onlinelibrary.wiley.com/doi/abs/10.1002/adma.202301934%20https://onlinelibrary.wiley.com/doi/10.1002/adma.202301934.

[85] Hui Seon Kim and Nam Gyu Park. "Importance of tailoring lattice strain in halide perovskite crystals". In: *NPG Asia Materials 2020 12:1* 12.1 (Dec. 2020), pp. 1–14. ISSN: 1884-4057. DOI: 10.1038/s41427-020-00265-w. URL: https://www.nature.com/articles/s41427-020-00265-w.

[86] LeeAnn Kim et al. "Contact Printing of Quantum Dot Light-Emitting Devices". In: *Nano Letters* 8.12 (Dec. 2008), pp. 4513–4517. DOI: 10.1021/NL8025218. URL: https://pubs.acs.org/doi/full/10.1021/nl8025218.

[87] Nicholas Kirkwood et al. "Finding and Fixing Traps in II-VI and III-V Colloidal Quantum Dots: The Importance of Z-Type Ligand Passivation". In: *Journal of the American Chemical Society* 140.46 (Nov. 2018), pp. 15712–15723. DOI: 10.1021/JACS.8B07783.

[88] V. I. Klimov et al. "Optical gain and stimulated emission in nanocrystal quantum dots". In: *Science* 290.5490 (Oct. 2000), pp. 314–317. ISSN: 00368075. DOI: 10.1126/SCIENCE.290.5490.314/ASSET/E9CD3695-0E77-46CF-8AF5-367699CC53FA/ASSETS/GRAPHIC/SE3908896004.JPEG. URL: https://www.science.org/doi/10.1126/science.290.5490.314.

[89] Kathryn E Knowles et al. "Colloidal Quantum Dots: Think Outside the (Particle-in-a-)Box". In: *J. Phys. Chem. Lett* 3 (2012), p. 56. DOI: 10.1021/jz2013775. URL: https://pubs.acs.org/sharingguidelines.

[90] Nathalie Kunkel and Philippe Goldner. "Recent Advances in Rare Earth Doped Inorganic Crystalline Materials for Quantum Information Processing". In: *Zeitschrift für anorganische und allgemeine Chemie* 644.2 (Feb. 2018), pp. 66–76. ISSN: 1521-3749. DOI: 10.1002/ZAAC.201700425. URL: https://onlinelibrary.wiley.com/doi/full/10.1002/zaac.201700425%20https://onlinelibrary.wiley.com/doi/abs/10.1002/zaac.201700425%20https://onlinelibrary.wiley.com/doi/10.1002/zaac.201700425.

[91] Marianne Le Dantec et al. "Twenty-three-millisecond electron spin coherence of erbium ions in a natural-abundance crystal". In: *Science Advances* 7.51 (Dec. 2021), p. 9786. ISSN: 23752548. DOI: 10.1126/SCIADV.ABJ9786/SUPPL{_}FILE/SCIADV.ABJ9786{_}SM.PDF. URL: https://www.science.org/doi/10.1126/sciadv.abj9786.

[92] Elizabeth M.Y. Lee and William A. Tisdale. "Determination of exciton diffusion length by transient photoluminescence quenching and its application to quantum dot films". In: *Journal of Physical Chemistry C* 119.17 (Apr. 2015), pp. 9005–9015. ISSN: 19327455. DOI: 10.1021/jp512634c.

[93] Gwang Heon Lee et al. "Recent Advances in Patterning Strategies for Full-Color Perovskite Light-Emitting Diodes". In: *Nano-Micro Letters 2023 16:1* 16.1 (Dec. 2023), pp. 1–39. ISSN: 2150-5551. DOI: 10.1007/S40820-023-01254-8. URL: https://link.springer.com/article/10.1007/s40820-023-01254-8.

[94] June Hyuk Lee et al. "A strong ferroelectric ferromagnet created by means of spin–lattice coupling". In: *Nature 2010 466:7309* 466.7309 (Aug. 2010), pp. 954–958. ISSN: 1476-4687. DOI: 10.1038/nature09331. URL: https://www.nature.com/articles/nature09331.

[95] Changhong Linghu et al. "Transfer printing techniques for flexible and stretchable inorganic electronics". In: *npj Flexible Electronics 2018 2:1* 2.1 (Oct. 2018), pp. 1–14. ISSN: 2397-4621. DOI: 10.1038/s41528-018-0037-x. URL: https://www.nature.com/articles/s41528-018-0037-x.

[96] Guiju Liu et al. "Atomic Identification of Interfaces in Individual Core@shell Quantum Dots". In: *Advanced Science* 8.22 (Nov. 2021). ISSN: 21983844. DOI: 10.1002/ADVS.202102784. URL: /pmc/articles/PMC8596122/%20/pmc/articles/PMC8596122/?report=abstract%20https://www.ncbi.nlm.nih.gov/pmc/articles/PMC8596122/.

[97] Junjie Liu et al. "Coherent electric field manipulation of Fe3+ spins in PbTiO3". In: *Science Advances* 7.10 (Mar. 2021). ISSN: 23752548. DOI: 10.1126/SCIADV.ABF8103/SUPPL{_}FILE/ABF8103{_}SM.PDF. URL: https://www.science.org/doi/10.1126/sciadv.abf8103.

[98] Mengxia Liu et al. "Colloidal quantum dot electronics". In: *Nature Electronics* (1928). DOI: 10.1038/s41928-021-00632-7. URL: https://doi.org/10.1038/s41928-021-00632-7.

[99] Thomas Lottermoser and Dennis Meier. "A short history of multiferroics". In: *Physical Sciences Reviews* 6.2 (Feb. 2021). ISSN: 2365659X. DOI: 10.1515/PSR-2020-0032/ASSET/GRAPHIC/J{_}PSR-2020-0032{_}FIG{_}002.JPG. URL: https://www.degruyter.com/document/doi/10.1515/psr-2020-0032/html.

[100] Douglas H. Lowndes et al. "Synthesis of novel thin-film materials by pulsed laser deposition". In: *Science* 273.5277 (Aug. 1996), pp. 898–903. ISSN: 00368075. DOI: 10.1126/science.273.5277.898.

[101] Jacques Lucas et al. "Introduction to Rare Earth Luminescent Materials". In: *Rare Earths* (Jan. 2015), pp. 251–280. DOI: 10.1016/B978-0-444-62735-3.00014-0.

[102] Wenhui Ma and Aize Hao. "Electric field-induced polarization rotation and ultrahigh piezoelectricity in PbTiO3". In: *Journal of Applied Physics* 115.10 (Mar. 2014), p. 104105. ISSN: 10897550. DOI: 10.1063/1.4868320/397216. URL: /aip/jap/article/115/10/104105/397216/Electric-field-induced-polarization-rotation-and.

[103] B. K. Mani, C. M. Chang, and I. Ponomareva. "Atomistic study of soft-mode dynamics in PbTiO3". In: *Physical Review B - Condensed Matter and Materials Physics* 88.6 (Aug. 2013), p. 064306. ISSN: 10980121. DOI: 10.1103/PHYSREVB.88.064306/FIGURES/3/MEDIUM. URL: https://journals.aps.org/prb/abstract/10.1103/PhysRevB.88.064306.

[104] Sasikanth Manipatruni, Dmitri E. Nikonov, and Ian A. Young. "Beyond CMOS computing with spin and polarization". In: *Nature Physics 2018 14:4* 14.4 (Apr. 2018), pp. 338–343. ISSN: 1745-2481. DOI: 10.1038/s41567-018-0101-4. URL: https://www.nature.com/articles/s41567-018-0101-4.

[105] Liberato Manna. "The Bright and Enlightening Science of Quantum Dots". In: *Nano Letters* 23.21 (Nov. 2023), pp. 9673–9676. ISSN: 15306992. DOI: 10.1021/ACS.NANOLETT.3C03904. URL: https://pubs.acs.org/doi/full/10.1021/acs.nanolett.3c03904.

[106] Liberato Manna, Erik C Scher, and A Paul Alivisatos. "Synthesis of Soluble and Processable Rod-, Arrow-, Teardrop-, and Tetrapod-Shaped CdSe Nanocrystals". In: (2000). DOI: 10.1021/JA003055. URL: https://pubs.acs.org/sharingguidelines.

[107] Liberato Manna et al. "Controlled growth of tetrapod-branched inorganic nanocrystals". In: *Nature Materials 2003 2:6* 2.6 (May 2003), pp. 382–385. ISSN: 1476-4660. DOI: 10.1038/nmat902. URL: https://www.nature.com/articles/nmat902.

[108] Lane W Martin and Andrew M Rappe. "Thin-film ferroelectric materials and their applications". In: *Nature Publishing Group* 1 (2016), p. 16087. DOI: 10.1038/natrevmats.2016.87. URL: www.nature.com/natrevmats.

[109] João R. Martins et al. "Statistical Analysis of Photoluminescence Decay Kinetics in Quantum Dot Ensembles: Effects of Inorganic Shell Composition and Environment". In: *Journal of Physical Chemistry C* 126.48 (Dec. 2022), pp. 20480–20490. ISSN: 19327455. DOI: 10.1021/ACS.JPCC.2C06134/ASSET/IMAGES/LARGE/JP2C06134{_}0006.JPEG. URL: https://pubs.acs.org/doi/full/10.1021/acs.jpcc.2c06134.

[110] Francesco Masia et al. "Spin-flip limited exciton dephasing in CdSe/ZnS colloidal quantum dots". In: *Physical Review Letters* 108.8 (Feb. 2012), p. 087401. ISSN: 00319007. DOI: 10.1103/PHYSREVLETT.108.087401/FIGURES/3/MEDIUM. URL: https://journals.aps.org/prl/abstract/10.1103/PhysRevLett.108.087401.

[111] Noga Meir et al. "Revisiting the Anion Framework Conservation in Cation Exchange Processes". In: *Chemistry of Materials* 28.21 (Nov. 2016), pp. 7872–7877. DOI: 10.1021/ACS.CHEMMATER.6B03332. URL: https://pubs.acs.org/doi/full/10.1021/acs.chemmater.6b03332.

[112] Rebecca Momper et al. "Kinetic Control over Self-Assembly of Semiconductor Nanoplatelets". In: (2023). DOI: 10.1021/acs.nanolett.9b05270. URL: https://dx.doi.org/10.1021/acs.nanolett.9b05270.

[113] A. Morelli et al. "Polarization retention loss in PbTi O3 ferroelectric films due to leakage currents". In: *Journal of Applied Physics* 102.8 (Oct. 2007), p. 84103. ISSN: 00218979. DOI: 10.1063/1.2794859/375915. URL: /aip/jap/article/102/8/084103/375915/Polarization-retention-loss-in-PbTiO3.

[114] C. B. Murray, D. J. Norris, and M. G. Bawendi. "Synthesis and Characterization of Nearly Monodisperse CdE (E = S, Se, Te) Semiconductor Nanocrystallites". In: *Journal of the American Chemical Society* 115.19 (Sept. 1993), pp. 8706–8715. ISSN: 15205126. DOI: 10.1021/JA00072A025/ASSET/JA00072A025.FP.PNG{_}V03. URL: https://pubs.acs.org/doi/abs/10.1021/ja00072a025.

[115] Ryuichi Ohta et al. "Observation of Acoustically Induced Dressed States of Rare-Earth Ions". In: *Physical Review Letters* 132.3 (Jan. 2024), p. 036904. ISSN: 10797114. DOI: 10.1103/PHYSREVLETT.132.036904/FIGURES/4/MEDIUM. URL: https://journals.aps.org/prl/abstract/10.1103/PhysRevLett.132.036904.

[116] R. P. de Oliveira, J. Benvenuti, and D. C.R. Espinosa. "A review of the current progress in recycling technologies for gallium and rare earth elements from light-emitting diodes". In: *Renewable and Sustainable Energy Reviews* 145 (July 2021), p. 111090. ISSN: 1364-0321. DOI: 10.1016/J.RSER.2021.111090.

[117] Justin C Ondry et al. "Trade-offs between Translational and Orientational Order in 2D Superlattices of Polygonal Nanocrystals with Differing Edge Count". In: *Nano Letters* 22 (2022), pp. 389–395. DOI: 10.1021/acs.nanolett.1c04058. URL: https://doi.org/10.1021/acs.nanolett.1c04058.

[118] Justin C Ondry et al. "Trade-offs between Translational and Orientational Order in 2D Superlattices of Polygonal Nanocrystals with Differing Edge Count". In: *Nano Letters* 22 (2022), pp. 389–395. DOI: 10.1021/acs.nanolett.1c04058. URL: https://doi.org/10.1021/acs.nanolett.1c04058.

[119] Justin C. Ondry et al. "Colloidal Synthesis Path to 2D Crystalline Quantum Dot Superlattices". In: *ACS Nano* (2020). ISSN: 1936-0851. DOI: 10.1021/acsnano.0c07202.

[120] Justin C. Ondry et al. "Colloidal Synthesis Path to 2D Crystalline Quantum Dot Superlattices". In: *ACS Nano* 15.2 (Feb. 2021), pp. 2251–2262. ISSN: 1936086X. DOI: 10.1021/ACSNANO.0C07202/ASSET/IMAGES/MEDIUM/NN0C07202{_}M003.GIF. URL: https://pubs.acs.org/doi/full/10.1021/acsnano.0c07202.

[121] Taejong Paik et al. "Hierarchical Materials Design by Pattern Transfer Printing of Self-Assembled Binary Nanocrystal Superlattices". In: *Nano Letters* 17.3 (2017), pp. 1387–1394. ISSN: 15306992. DOI: 10.1021/acs.nanolett.6b04279.

[122] Lars-Olof Pålsson and Andrew P Monkman. "Measurements of Solid-State Photoluminescence Quantum Yields of Films Using a Fluorimeter". In: (). DOI: 10.1002/1521-4095(20020517)14:10<757::AID-ADMA757>3.0.CO;2-Y. URL: https://onlinelibrary.wiley.com/terms-and-conditions.

[123] Kyoungwon Park et al. "Single molecule quantum-confined Stark effect measurements of semiconductor nanoparticles at room temperature". In: *ACS Nano* 6.11 (Nov. 2012), pp. 10013–10023. ISSN: 19360851. DOI: 10.1021/NN303719M/SUPPL{_}FILE/NN303719M{_}SI{_}001.PDF. URL: https://pubs.acs.org/doi/full/10.1021/nn303719m.

[124] Vesselin N. Paunov and Olivier J. Cayre. "The gel trapping technique - A novel method for characterization of the wettability of microparticles and replication of particle monolayers". In: *Materials Research Society Symposium Proceedings*. Vol. EXS. 2. Springer, Dordrecht, 2004, pp. 149–151. DOI: 10.1007/1-4020-3562-4{_}35. URL: https://link-springer-com.libproxy.berkeley.edu/chapter/10.1007/1-4020-3562-4_35.

[125] Lintao Peng et al. "Influence of local structures on the energy transfer efficiencies of quantum-dot films". In: *Physical Review B* 102.3 (July 2020), p. 035437. ISSN: 24699969. DOI: 10.1103/PhysRevB.102.035437. URL: https://journals.aps.org/prb/abstract/10.1103/PhysRevB.102.035437.

[126] Xiaogang Peng et al. "Epitaxial Growth of Highly Luminescent CdSe/CdS Core/Shell Nanocrystals with Photostability and Electronic Accessibility". In: *Journal of the American Chemical Society* 119.30 (July 1997), pp. 7019–7029. ISSN: 00027863. DOI: 10.1021/JA970754M. URL: https://pubs.acs.org/doi/abs/10.1021/ja970754m.

[127] Samuel B. Penwell et al. "Resolving ultrafast exciton migration in organic solids at the nanoscale". In: *Nature Materials 2017 16:11* 16.11 (Sept. 2017), pp. 1136–1141. ISSN: 1476-4660. DOI: 10.1038/nmat4975. URL: https://www.nature.com/articles/nmat4975.

[128] Erika Penzo et al. "Long-Range Exciton Diffusion in Two-Dimensional Assemblies of Cesium Lead Bromide Perovskite Nanocrystals". In: *ACS Nano* 14.6 (June 2020), pp. 6999–7007. ISSN: 1936086X. DOI: 10.1021/acsnano.0c01536. URL: https://pubs.acs.org/doi/full/10.1021/acsnano.0c01536.

[129] Christopher M. Phenicie et al. "Narrow Optical Line Widths in Erbium Implanted in TiO2". In: *Nano Letters* 19.12 (Dec. 2019), pp. 8928–8933. ISSN: 15306992. DOI: 10.1021/ACS.NANOLETT.9B03831/SUPPL{_}FILE/NL9B03831{_}SI{_}001.PDF. URL: https://pubs.acs.org/doi/full/10.1021/acs.nanolett.9b03831.

[130] Anatolii Polovitsyn et al. "Synthesis of Anisotropic CdSe/CdS Dot-in-Giant-Rod Nanocrystals with Persistent Blue-Shifted Biexciton Emission". In: *ACS Photonics* 5.11 (Nov. 2018), pp. 4561–4568. DOI: 10.1021/ACSPHOTONICS.8B01028. URL: https://pubs.acs.org/doi/full/10.1021/acsphotonics.8b01028.

[131] Ferry Prins et al. "Spatially resolved energy transfer in patterned colloidal quantum dot heterostructures". In: *ACS Applied Materials and Interfaces* 6.5 (Mar. 2014), pp. 3111–3114. ISSN: 19448252. DOI: 10.1021/am500197n. URL: www.acsami.org.

[132] Loredana Protesescu et al. "Nanocrystals of Cesium Lead Halide Perovskites (CsPbX3, X = Cl, Br, and I): Novel Optoelectronic Materials Showing Bright Emission with Wide Color Gamut". In: *Nano Letters* 15.6 (June 2015), pp. 3692–3696. ISSN: 15306992. DOI: 10.1021/NL5048779/SUPPL{_}FILE/NL5048779{_}SI{_}001.PDF. URL: https://pubs.acs.org/doi/full/10.1021/nl5048779.

[133] Chaodan Pu and Xiaogang Peng. "To Battle Surface Traps on CdSe/CdS Core/Shell Nanocrystals: Shell Isolation versus Surface Treatment". In: *Journal of the American Chemical Society* 138.26 (2016), pp. 8134–8142. ISSN: 15205126. DOI: 10.1021/jacs.6b02909.

[134] Yuan Pu et al. "Colloidal Synthesis of Semiconductor Quantum Dots toward Large-Scale Production: A Review". In: *Industrial and Engineering Chemistry Research* 57.6 (Feb. 2018), pp. 1790–1802. ISSN: 15205045. DOI: 10.1021/ACS.IECR.7B04836/ASSET/IMAGES/LARGE/IE-2017-048366{_}0011.JPEG. URL: https://pubs.acs.org/doi/full/10.1021/acs.iecr.7b04836.

[135] Freddy T. Rabouw and Celso de Mello Donega. "Excited-State Dynamics in Colloidal Semiconductor Nanocrystals". In: *Topics in Current Chemistry 2016 374:5* 374.5 (Aug. 2016), pp. 1–30. ISSN: 2364-8961. DOI: 10.1007/S41061-016-0060-0. URL: https://link.springer.com/article/10.1007/s41061-016-0060-0.

[136] Freddy T. Rabouw et al. "Delayed Exciton Emission and Its Relation to Blinking in CdSe Quantum Dots". In: *Nano Letters* 15.11 (Nov. 2015), pp. 7718–7725. ISSN: 15306992. DOI: 10.1021/ACS.NANOLETT.5B03818/ASSET/IMAGES/NL-2015-03818M{_}M007.GIF. URL: https://pubs.acs.org/doi/full/10.1021/acs.nanolett.5b03818.

[137] Mouktik Raha et al. "Optical quantum nondemolition measurement of a single rare earth ion qubit". In: *Nature Communications 2020 11:1* 11.1 (Mar. 2020), pp. 1–6. ISSN: 2041-1723. DOI: 10.1038/s41467-020-15138-7. URL: https://www.nature.com/articles/s41467-020-15138-7.

[138] Gabriele Rain et al. "Probing the Wave Function Delocalization in CdSe/CdS Dot-in-Rod Nanocrystals by Time-and Temperature-Resolved Spectroscopy". In: (2011). ISSN: 4031-4036. DOI: 10.1021/nn2005969. URL: www.acsnano.org.

[139] Gabriele Rainò et al. "Superfluorescence from lead halide perovskite quantum dot superlattices". In: *Nature* 563.7733 (2018), pp. 671–675. ISSN: 14764687. DOI: 10.1038/s41586-018-0683-0.

[140] Ramamoorthy Ramesh and Darrell G. Schlom. "Creating emergent phenomena in oxide superlattices". In: *Nature Reviews Materials* 4.4 (2019), pp. 257–268. ISSN: 20588437. DOI: 10.1038/s41578-019-0095-2. URL: http://dx.doi.org/10.1038/s41578-019-0095-2.

[141] Miloš Rancic et al. "Coherence time of over a second in a telecom-compatible quantum memory storage material". In: *Nature Physics 2017 14:1* 14.1 (Sept. 2017), pp. 50–54. ISSN: 1745-2481. DOI: 10.1038/nphys4254. URL: https://www.nature.com/articles/nphys4254.

[142] R. Rossetti, S. Nakahara, and L. E. Brus. "Quantum size effects in the redox potentials, resonance Raman spectra, and electronic spectra of CdS crystallites in aqueous solution". In: *The Journal of Chemical Physics* 79.2 (July 1983), pp. 1086–1088. ISSN: 0021-9606. DOI: 10.1063/1.445834. URL: /aip/jcp/article/79/2/1086/776583/Quantum-size-effects-in-the-redox-potentials.

[143] Shrawan Roy et al. "Measurement of Quantum Yields of Monolayer TMDs Using Dye-Dispersed PMMA Thin Films". In: ().

[144] K. Z. Rushchanskii et al. "A multiferroic material to search for the permanent electric dipole moment of the electron". In: *Nature Materials 2010 9:8* 9.8 (July 2010), pp. 649–654. ISSN: 1476-4660. DOI: 10.1038/nmat2799. URL: https://www.nature.com/articles/nmat2799.

[145] Michael Scheibner et al. "Superradiance of quantum dots". In: *Nature Physics* 3.2 (2007), pp. 106–110. ISSN: 17452481. DOI: 10.1038/nphys494.

[146] M C Schlamp, Xiaogang Peng, and A P Alivisatos. "Improved efficiencies in light emitting diodes made with CdSe(CdS) core/shell type nanocrystals and a semiconducting polymer". In: *Journal of Applied Physics* 82.11 (1997), pp. 5837–5842. DOI: 10.1063/1.366452. URL: https://doi.org/10.1063/1.366452.

[147] Jon A. Schuller et al. "Orientation of luminescent excitons in layered nanomaterials". In: *Nature Nanotechnology 2013 8:4* 8.4 (Mar. 2013), pp. 271–276. ISSN: 1748-3395. DOI: 10.1038/nnano.2013.20. URL: https://www.nature.com/articles/nnano.2013.20.

[148] Sheyla Serrano et al. "Oxgen-vacancy defects in PbTiO3 and BaTiO3 crystals: a quantum chemical study". In: *https://doi.org/10.1117/12.515777* 5122 (Aug. 2003), pp. 287–294. DOI: 10.1117/12.515777. URL: https://www.spiedigitallibrary.org/conference-proceedings-of-spie/5122/0000/Oxgen-vacancy-defects-in-PbTiO3-and-BaTiO3-crystals--a/10.1117/12.515777.full%20https://www.spiedigitallibrary.org/conference-proceedings-of-spie/5122/0000/

Oxgen-vacancy-defects-in-PbTiO3-and-BaTiO3-crystals--a/10.1117/12.515777.short.

[149] Wenbi Shcherbakov-Wu and William A. Tisdale. "A time-domain view of charge carriers in semiconductor nanocrystal solids". In: *Chemical Science* 11.20 (2020), pp. 5157–5167. ISSN: 20416539. DOI: 10.1039/c9sc05925c.

[150] Yi Shen et al. "Quantum Yield Regeneration: Influence of Neutral Ligand Binding on Photophysical Properties in Colloidal Core/Shell Quantum Dots". In: *ACS Nano* 9.3 (Mar. 2015), pp. 3345–3359. DOI: 10.1021/ACSNANO.5B00671. URL: https://pubs.acs.org/doi/full/10.1021/acsnano.5b00671.

[151] Takahiro Shimada et al. "Multiferroic Vacancies at Ferroelectric PbTiO3 Surfaces". In: *Physical Review Letters* 115.10 (Sept. 2015), p. 107202. ISSN: 10797114. DOI: 10.1103/PHYSREVLETT.115.107202/FIGURES/3/MEDIUM. URL: https://journals.aps.org/prl/abstract/10.1103/PhysRevLett.115.107202.

[152] M. P. Silveri et al. "Quantum systems under frequency modulation". In: *Reports on Progress in Physics* 80.5 (Apr. 2017), p. 056002. ISSN: 00344885. DOI: 10.1088/1361-6633/aa5170. URL: https://iopscience.iop.org/article/10.1088/1361-6633/aa5170%20https://iopscience.iop.org/article/10.1088/1361-6633/aa5170/meta.

[153] J. C. Slater. "The Ferromagnetism of Nickel". In: *Physical Review* 49.7 (Apr. 1936), p. 537. ISSN: 0031899X. DOI: 10.1103/PhysRev.49.537. URL: https://journals.aps.org/pr/abstract/10.1103/PhysRev.49.537.

[154] N. A. Spaldin and R. Ramesh. "Advances in magnetoelectric multiferroics". In: *Nature Materials 2019 18:3* 18.3 (Feb. 2019), pp. 203–212. ISSN: 1476-4660. DOI: 10.1038/s41563-018-0275-2. URL: https://www.nature.com/articles/s41563-018-0275-2.

[155] Paul Stevenson et al. "Erbium-implanted materials for quantum communication applications". In: *Physical Review B* 105.22 (June 2022), p. 224106. ISSN: 24699969. DOI: 10.1103/PHYSREVB.105.224106/FIGURES/9/MEDIUM. URL: https://journals.aps.org/prb/abstract/10.1103/PhysRevB.105.224106.

[156] Y. Sun et al. "Recent progress in developing new rare earth materials for hole burning and coherent transient applications". In: *Journal of Luminescence* 98.1-4 (July 2002), pp. 281–287. ISSN: 0022-2313. DOI: 10.1016/S0022-2313(02)00281-8.

[157] Anna Synak et al. "Förster Energy Transfer in Core–Shell Nanoparticles: Theoretical Model and Monte Carlo Study". In: *The Journal of Physical Chemistry C* (Aug. 2021), pp. 125–18517. DOI: 10.1021/ACS.JPCC.1C05314. URL: https://pubs.acs.org/doi/full/10.1021/acs.jpcc.1c05314.

[158] David R. Tallant and John C. Wright. "Selective laser excitation of charge compensated sites in CaF2:Er3+". In: *The Journal of Chemical Physics* 63.5 (Sept. 1975), pp. 2074–2085. ISSN: 0021-9606. DOI: 10.1063/1.431545. URL: /aip/jcp/article/63/5/2074/783729/Selective-laser-excitation-of-charge-compensated.

[159] Rui Tan et al. "Monodisperse Hexagonal Pyramidal and Bipyramidal Wurtzite CdSe-CdS Core-Shell Nanocrystals". In: *Chemistry of Materials* 29.9 (May 2017), pp. 4097–4108. ISSN: 15205002. DOI: 10.1021/acs.chemmater.7b00968. URL: https://pubs.acs.org/sharingguidelines.

[160] C. W. Thiel, Thomas Bttger, and R. L. Cone. "Rare-earth-doped materials for applications in quantum information storage and signal processing". In: *Journal of Luminescence* 131.3 (Mar. 2011), pp. 353–361. ISSN: 0022-2313. DOI: 10.1016/J.JLUMIN.2010.12.015.

[161] Jianjun Tian and Guozhong Cao. "Semiconductor quantum dot-sensitized solar cells". In: *http://dx.doi.org/10.3402/nano.v4i0.22578* 4.1 (Jan. 2013), p. 22578. ISSN: 2000-5121. DOI: 10.3402/NANO.V4I0.22578. URL: https://www.tandfonline.com/doi/abs/10.3402/nano.v4i0.22578.

[162] T. Uda, K. T. Jacob, and M. Hirasawa. "Technique for enhanced rare earth separation". In: *Science* 289.5488 (Sept. 2000), pp. 2326–2329. ISSN: 00368075. DOI: 10.1126/SCIENCE.289.5488.2326/ASSET/F64E012E-1996-4C6D-A636-9C6E8859A607/ASSETS/GRAPHIC/SE3808865004.JPEG. URL: https://www.science.org/doi/10.1126/science.289.5488.2326.

[163] Hendrik Utzat et al. "Coherent single-photon emission from colloidal lead halide perovskite quantum dots". In: *Science* 363.6431 (Mar. 2019). ISSN: 10959203. DOI: 10.1126/SCIENCE.AAU7392/SUPPL{_}FILE/AAU7392{_}UTZAT{_}SM.PDF. URL: https://www.science.org/doi/10.1126/science.aau7392.

[164] Stefano Vezzoli et al. "Exciton Fine Structure of CdSe/CdS Nanocrystals Determined by Polarization Microscopy at Room Temperature". In: *ACS Nano* 9.8 (2015), pp. 7992–8003. ISSN: 1936086X. DOI: 10.1021/acsnano.5b01354.

[165] J. Wang et al. "Epitaxial BiFeO3 multiferroic thin film heterostructures". In: *Science* 299.5613 (Mar. 2003), pp. 1719–1722. ISSN: 00368075. DOI: 10.1126/SCIENCE.1080615/SUPPL{_}FILE/WANG.SOM.PDF. URL: https://www.science.org/doi/10.1126/science.1080615.

[166] Ping Wang et al. "The important role of surface ligand on CdSe/CdS core/shell nanocrystals in affecting the efficiency of H2 photogeneration from water". In: *Nanoscale* 7.13 (Apr. 2015), pp. 5767–5775. ISSN: 20403372. DOI: 10.1039/c4nr07343f. URL: https://pubs.rsc.org/en/content/articlehtml/2015/nr/c4nr07343f%20https://pubs.rsc.org/en/content/articlelanding/2015/nr/c4nr07343f.

[167] Yonghong Wang et al. "CdSe@CdS Dot@Platelet Nanocrystals: Controlled Epitaxy, Monoexponential Decay of Two-Dimensional Exciton, and Nonblinking Photoluminescence of Single Nanocrystal". In: *Journal of the American Chemical Society* 141.44 (2019), pp. 17617–17628. ISSN: 15205126. DOI: 10.1021/jacs.9b06932.

[168] W. L. Warren et al. "Defect-dipole alignment and tetragonal strain in ferroelectrics". In: *Journal of Applied Physics* 79.12 (June 1996), pp. 9250–9257. ISSN: 0021-8979. DOI: 10.1063/1.362600. URL: /aip/jap/article/79/12/9250/495873/Defect-dipole-alignment-and-tetragonal-strain-in.

[169] R. Witte et al. "Evidence for enhanced ferromagnetism in an iron-based nanoglass". In: *Applied Physics Letters* 103.7 (Aug. 2013), p. 73106. ISSN: 00036951. DOI: 10.1063/1.4818493/150276. URL: /aip/apl/article/103/7/073106/150276/Evidence-for-enhanced-ferromagnetism-in-an-iron.

[170] Gary Wolfowicz et al. "Parasitic erbium photoluminescence in commercial telecom fiber optical components". In: *Optics Letters, Vol. 46, Issue 19, pp. 4852-4854* 46.19 (Oct. 2021), pp. 4852–4854. ISSN: 1539-4794. DOI: 10.1364/OL.437417. URL: https://opg.optica.org/viewmedia.cfm?uri=ol-46-19-4852&seq=0&html=true%20https://opg.optica.org/abstract.cfm?uri=ol-46-19-4852%20https://opg.optica.org/ol/abstract.cfm?uri=ol-46-19-4852.

[171] A. K. Yadav et al. "Observation of polar vortices in oxide superlattices". In: *Nature 2016 530:7589* 530.7589 (Jan. 2016), pp. 198–201. ISSN: 1476-4687. DOI: 10.1038/nature16463. URL: https://www.nature.com/articles/nature16463.

[172] Xiaobing Yan et al. "Self-Assembled Networked PbS Distribution Quantum Dots for Resistive Switching and Artificial Synapse Performance Boost of Memristors". In: *Advanced Materials* 31.7 (Feb. 2019), p. 1805284. ISSN: 1521-4095. DOI: 10.1002/ADMA.201805284. URL: https://onlinelibrary.wiley.com/doi/full/10.1002/adma.201805284%20https://onlinelibrary.wiley.com/doi/abs/10.1002/adma.201805284%20https://onlinelibrary.wiley.com/doi/10.1002/adma.201805284.

[173] Yanpeng Yao and Huaxiang Fu. "Charged vacancies in ferroelectric PbTiO3: Formation energies, optimal Fermi region, and influence on local polarization". In: *Physical Review B - Condensed Matter and Materials Physics* 84.6 (Aug. 2011), p. 064112. ISSN: 10980121. DOI: 10.1103/PHYSREVB.84.064112/FIGURES/4/MEDIUM. URL: https://journals.aps.org/prb/abstract/10.1103/PhysRevB.84.064112.

[174] Jing Yu et al. "Recent Advances on Pulsed Laser Deposition of Large-Scale Thin Films". In: *Small Methods* (2023), p. 2301282. ISSN: 2366-9608. DOI: 10.1002/SMTD.202301282. URL: https://onlinelibrary.wiley.com/doi/full/10.1002/smtd.202301282%20https://onlinelibrary.wiley.com/doi/abs/10.1002/smtd.202301282%20https://onlinelibrary.wiley.com/doi/10.1002/smtd.202301282.

[175] W. William Yu et al. "Experimental determination of the extinction coefficient of CdTe, CdSe, and CdS nanocrystals". In: *Chemistry of Materials* 15.14 (July 2003), pp. 2854–2860. ISSN: 08974756. DOI: 10.1021/cm034081k. URL: https://pubs.acs.org/sharingguidelines.

[176] Rongfeng Yuan et al. "A composite electrodynamic mechanism to reconcile spatiotemporally resolved exciton transport in quantum dot superlattices". In: *Science Advances* 9.42 (Oct. 2023). ISSN: 2375-2548. DOI: 10.1126/SCIADV.ADH2410. URL: https://www.science.org/doi/10.1126/sciadv.adh2410.

[177] Marco Zanella et al. "Self-assembled multilayers of vertically aligned semiconductor nanorods on device-scale areas". In: *Advanced Materials* 23.19 (May 2011), pp. 2205–2209. DOI: 10.1002/ADMA.201100539.

[178] V. Železný et al. "The variation of PbTiO3 bandgap at ferroelectric phase transition". In: *Journal of Physics: Condensed Matter* 28.2 (Dec. 2015), p. 025501. ISSN: 0953-8984. DOI: 10.1088/0953-8984/28/2/025501. URL: https://iopscience.iop.org/article/10.1088/0953-8984/28/2/025501%20https://iopscience.iop.org/article/10.1088/0953-8984/28/2/025501/meta.

[179] Qinghui Zeng et al. "Synthesis and optical properties of type II CdTe/CdS core/shell quantum dots in aqueous solution via successive ion layer adsorption and reaction". In: *Journal of Physical Chemistry C* 112.23 (June 2008), pp. 8587–8593. ISSN: 19327447. DOI: 10.1021/JP711395F/ASSET/IMAGES/LARGE/JP-2007-11395F{_}0001.JPEG. URL: https://pubs.acs.org/doi/full/10.1021/jp711395f.

[180] D. L. Zhang et al. "Structure Evolution and Multiferroic Properties in Cobalt Doped Bi4NdTi3Fe1-xCoxO15-Bi3NdTi2Fe1-xCoxO12-δ Intergrowth Aurivillius Compounds". In: *Scientific Reports 2017 7:1* 7.1 (Mar. 2017), pp. 1–8. ISSN: 2045-2322. DOI: 10.1038/srep43540. URL: https://www.nature.com/articles/srep43540.

[181] Lipeng Zhang et al. "Oxygen vacancy formation energies in PbTiO3/SrTiO3 superlattice". In: *Physical Review Materials* 2.6 (June 2018), p. 064409. ISSN: 24759953. DOI: 10.1103/PHYSREVMATERIALS.2.064409/FIGURES/5/MEDIUM. URL: https://journals.aps.org/prmaterials/abstract/10.1103/PhysRevMaterials.2.064409.

[182] Pingping Zhang et al. "Direct in situ photolithography of perovskite quantum dots based on photocatalysis of lead bromide complexes". In: *Nature Communications 2022 13:1* 13.1 (Nov. 2022), pp. 1–10. ISSN: 2041-1723. DOI: 10.1038/s41467-022-34453-9. URL: https://www.nature.com/articles/s41467-022-34453-9.

[183] Qingsong Zhang, Tahir Cagin, and William A. Goddard. "The ferroelectric and cubic phases in BaTiO3 ferroelectrics are also antiferroelectric". In: *Proceedings of the National Academy of Sciences of the United States of America* 103.40 (Oct. 2006), pp. 14695–14700. ISSN: 00278424. DOI: 10.1073/PNAS.0606612103/SUPPL{_}FILE/INDEX.HTML. URL: https://www.pnas.org/doi/abs/10.1073/pnas.0606612103.

[184] Zhen Zhang and John T. Yates. "Direct observation of surface-mediated electron-hole pair recombination in TiO2(110)". In: *Journal of Physical Chemistry C* 114.7 (2010), pp. 3098–3101. ISSN: 19327447. DOI: 10.1021/jp910404e.

[185] Danylo Zherebetskyy et al. "Hydroxylation of the surface of PbS nanocrystals passivated with oleic acid". In: *Science* 344.6190 (June 2014), pp. 1380–1384. ISSN: 10959203. DOI: 10.1126/SCIENCE.1252727/SUPPL{_}FILE/ZHEREBETSKYY.SM.PDF. URL: https://www.science.org/doi/10.1126/science.1252727.

[186] Tian Zhong and Philippe Goldner. "Emerging rare-earth doped material platforms for quantum nanophotonics". In: *Nanophotonics* 8.11 (Nov. 2019), pp. 2003–2015. ISSN: 21928614. DOI: 10.1515/NANOPH-2019-0185/ASSET/GRAPHIC/J{_}NANOPH-2019-0185{_}FIG{_}002.JPG. URL: https://www.degruyter.com/document/doi/10.1515/nanoph-2019-0185/html.

[187] Jianshi Zhou and Gregory A. Fiete. "Rare earths in a nutshell". In: *Physics Today* 73.1 (Jan. 2020), p. 66. ISSN: 0031-9228. DOI: 10.1063/PT.3.4397. URL: https://physicstoday.scitation.org/doi/abs/10.1063/PT.3.4397.

[188] Leonardo Z. Zornberg, Paul A. Gabrys, and Robert J. MacFarlane. "Optical Processing of DNA-Programmed Nanoparticle Superlattices". In: *Nano Letters* 19.11 (Nov. 2019), pp. 8074–8081. ISSN: 15306992. DOI: 10.1021/ACS.NANOLETT.9B03258/ASSET/IMAGES/LARGE/NL9B03258{_}0005.JPEG. URL: https://pubs.acs.org/doi/full/10.1021/acs.nanolett.9b03258.

[189] Pavel Zrazhevskiy, Mark Senaw, and Xiaohu Gao. "Designing multifunctional quantum dots for bioimaging, detection, and drug delivery". In: (2009). DOI: 10.1039/b915139g. URL: www.rsc.org/csr.

Appendix A

Supporting Information for Chapter 2

A.1 3D Printed Solid-State Sample Holder

The measurement of PLQY of colloidal QD solution samples has become fairly standardized using an integrating-sphere set-up[69, 25] since it is easy to prepare solutions with optical density in the range of 0.05 0.2. In contrast, the optical density of self-assembled QD thin films is on the order of 0.01. Previous works have reported the QY of solid-state materials with a few hundred nanometer thickness measured in an integrating sphere[122] or of mono-

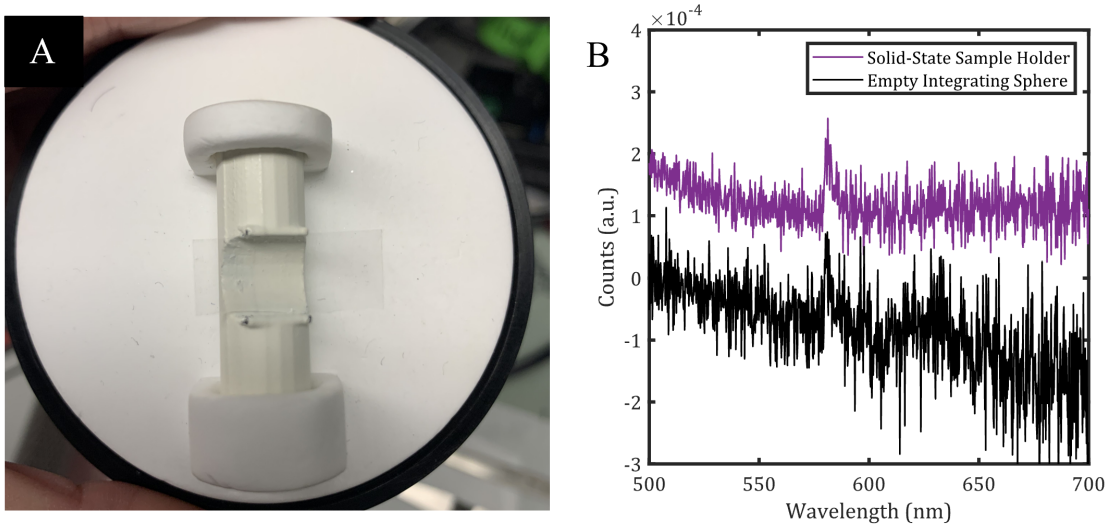

Figure A.1: **3D-Printed Solid State Sample Holder.** **A** Image of solid-state sample holder shown with a film mounted in the integrating sphere slit. **B** Photoluminescence spectra of solid-state holder and the empty integrating sphere.

layer TMDs using a dye dispersed in polymer film as a reference.[143] However, to estimate the relative QY of a thin sample using a reference film, a specialized confocal PL microscope with transmission spectroscopy capacity is required. Additionally, analytical methods have been developed to measure the photothermal quantum yield of nanoparticles with very small Γ_{nr}.[69] However, this technique is fairly time intensive and has only been realized for solution and films with multilayer thicknesses. Hence, measuring the PLQY of a thin film directly in an integrating sphere is a valuable tool.

A solid-state sample holder was 3D printed to fit precisely where the custom-built cuvette is mounted, and the middle slits allow for a thin film of that size to slide into the holder. The solid-state sample holder was designed to be the same size and shape as the custom cuvette used for the integrating sphere (Fig. A.1A). A slit in the middle of the holder allows a thin film approximately the size of half a cover slip (11 mm x 22 mm) to easily be inserted and removed from the holder. The film is positioned in the middle of the holder to parallel the integrating sphere's laser entry slit to ensure optimal excitation of the sample by the laser. One of the major sources of error in measuring the PLQY using an integrating sphere is the variability in position when mounting the film which gives vastly different results depending on how the sample is oriented relative to the excitation source. By using a solid-state sample holder that constrains the spatial and angular position of the thin film inside the integrating sphere, the sample is placed in the direct path of the excitation which prevents loss of photons in indirect excitation schemes that can lead to inaccurate PLQY values. The solid-state holder allows us to mount the thin film reproducibly to securely perform measurements with long acquisition times to improve the signal to noise ratio.

The PL spectra of the solid-state sample holder shows that the holder does not emit at the wavelength region of interest of our QD samples (Fig. A.1B). Comparison of the spectra of the solid-state sample holder with the empty integrating sphere shows no perceivable difference. The small peak present in both spectra at 570 nm signifies that there is some impurity in the integrating sphere. However, this impurity is outside of our wavelength range of interest, and it is accounted for in the measurement due subtraction of a blank reference.

A.2 Nanocrystal Size Analysis

A size and shape analysis on TEM images of the monolayer thin films is performed to generate a size distribution of the diameter (Fig. A.2A, D, G) and feret diameter (Fig. A.2B, E, H) of the ensemble of nanocrystals for each sample. The distribution in diameter assumes that the nanocrystals are isotropic and fits an outline of a circle around each nanocrystal reporting the diameter of the outlined circles whereas the distribution of feret diameter considers any anisotropic shapes of nanocrystals and reports the longest distance across the nanocrystals, performing no fitting of the nanocrystal into a particular shape. The differ-

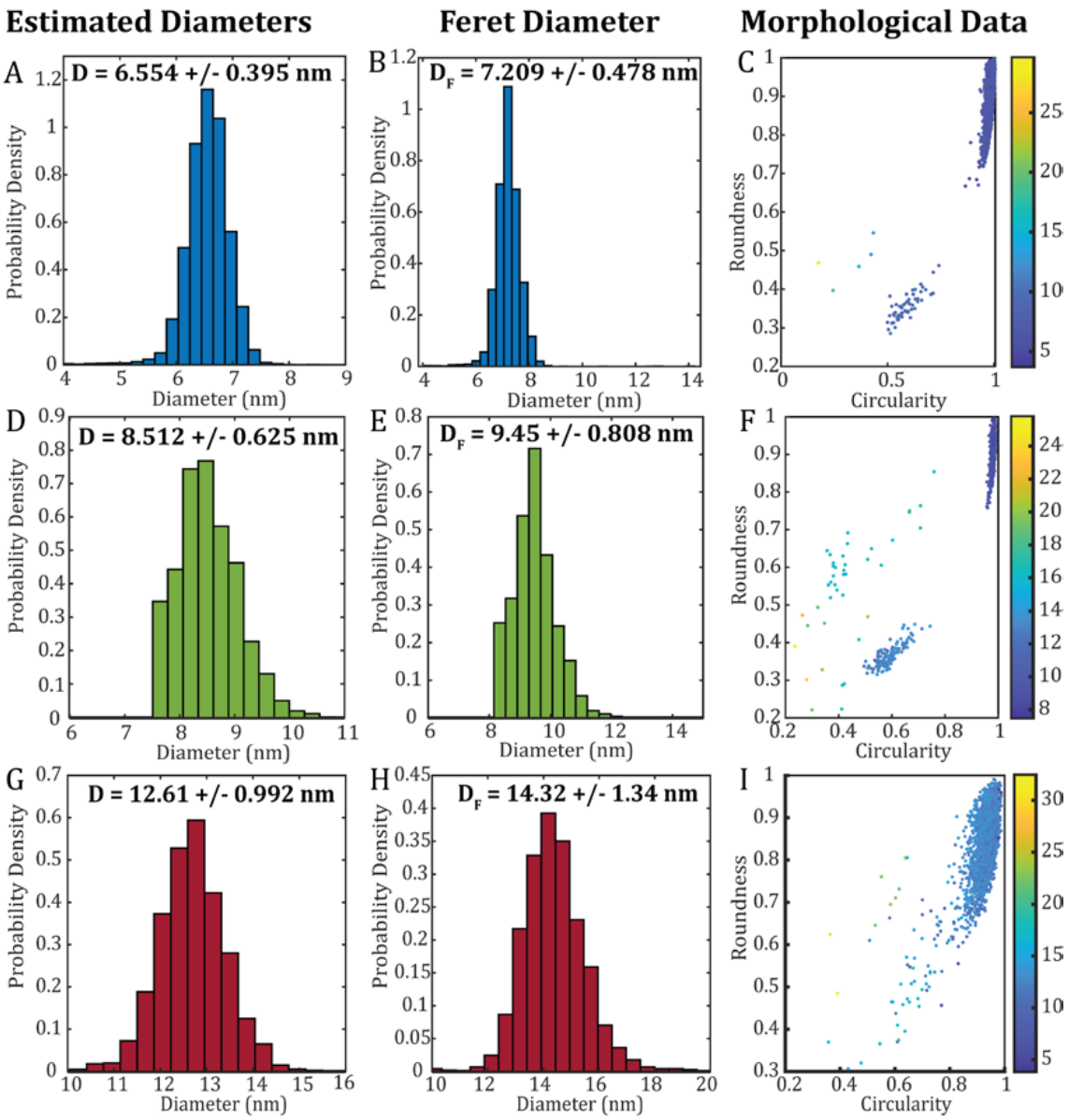

Figure A.2: **Size and Shape Analysis of QDs Based on TEM Images.** Estimated diameter of **A** CdSe/3MLCdS, **D** CdSe/6MLCdS, **G** and CdSe/9MLCdS. Feret diameter of **B** CdSe/3MLCdS, **E** CdSe/6MLCdS, **H** CdSe/9MLCdS, and **C,F,I** circularity of the samples. Colorbar represents diameters of QDs in the circularity plot.

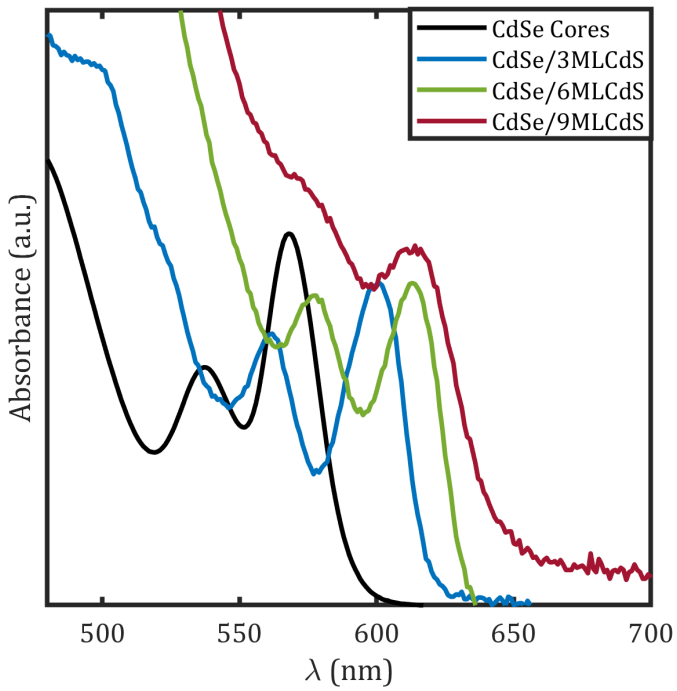

Figure A.3: **Absorbance Spectra for each QD Sample.** Spectra is focused on region of the first exciton peak.

ence between the diameter and feret diameter of the nanocrystal ensemble corresponds to how spherical the nanocrystals are. The greater the difference between the diameter and the feret diameter, the greater the deviation of the shape of the nanocrystal from a circle. The circularity of the samples (Fig. A.2C, F, I) compares the two diameters and depicts how circular the QDs are with the more circular QDs having a circularity and roundness value of 1. As we increase the shell thickness of our films, the greater the difference between the feret and regular diameter of the QDs and the less circular they become.

A.3 Absorption of CdSe/CdS Samples in Octane Solution

As we increase the shell thickness, the first exciton absorption peak redshifts (Fig. A.3). There is a large red shift from the CdSe core to the samples with CdS shell. As the shell thickness increases, a small systematic red shift in the first exciton absorption peak is observed due to the improvement in confinement of the hole wavefunction.

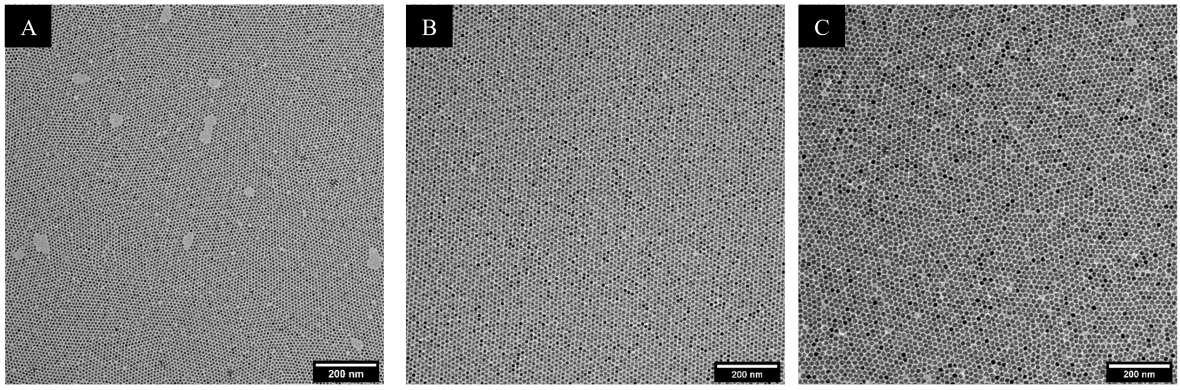

Figure A.4: **Lower Magnification TEM Images of QD Superlattices.** Lower magnification TEM images of **A** CdSe/3MLCdS, **B** CdSe/6MLCdS, and **C** CdSe/9MLCdS. Scale bars are 200 nm.

A.4 Lower Magnification TEM Images

At lower magnification, we observe the spatial order of the QD superlattices and confirm the micrometer monolayer coverage of all 3 films (Fig. A.4A-C).

A.5 FFT of Higher Magnification TEM Image

At higher magnification, the CdSe/3MLCdS (Fig. A.5A) and CdSe/9MLCdS (Fig. A.5C) superlattices appear to have more crystallographic order and as a result, the FFT processing (Fig. A.5B, D) of these images appear to have discrete points like that of CdSe/6MLCdS (Fig. 2.1C) rather than the ring like structures. This indicates that at lower magnification, we observed multiple different structural domains, forming the ring-like FFT images.

A.6 Time Resolved Photoluminescence Fits (TRPL)

Time resolved photoluminescence (TRPL) was fitted to different exponential curves for all 3 QD samples in colloidal solution and monolayer thin films. The data was fit to the first two decades (from $10^4 - 10^2$ counts) which represent 99% of the counts measured. Typically for QDs in colloidal solution, the first decade is fit to a monoexponential function to correspond

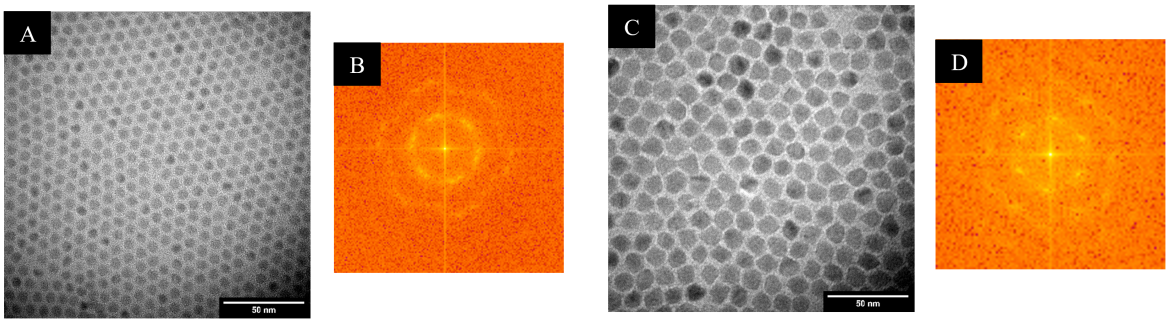

Figure A.5: **Higher Magnification TEM Images of QD Superlattices.** Higher magnification TEM image of **A** CdSe/3MLCdS with its **B** corresponding Fast Fourier transform and of **C** CdSe/9MLCdS and the **D** corresponding FFT of those images. Scale bar in **A** and **C** are 50 nm.

to the radiative lifetime of the exciton in solution.[71, 12] However, QDs with an inorganic shell typically have a multiexponential decay.[109, 71] Additionally, slower non-radiative recombination processes may be present in the monolayer thin film, we want to study a larger portion of the decay. To be consistent, we need to carefully fit the TRPL data of the films and solution to calculate the radiative rates. To do so, we consider a few different fits: monoexponential, biexponential, and stretched exponentials which have been previously used to fit TRPL data for QDs.[109]

In Figure A.6A and B, we fit the colloidal solution to a monoexponential and biexponential fit respectively.[71] The monoexponential fit appears to fit the first decade of the data well, but not the second decade as can be observed for the CdSe/9MLCdS whereas the biexponential fit seems to fit the entire range well. Hence, for the colloidal solution we choose to use a biexponential fit (eq. A.1) for our analysis. Similarly, the first decade of the monolayer thin film can fit well with a monoexponential function (Fig. A.6C) but a biexponential function is needed to fit the latter portion of the decay (Fig. A.6D). QDs with an inorganic shell typically have a multiexponential decay.[71, 109] Therefore, the biexponential fit seems to reasonably represent the data. An additional fit of the monolayer thin films using a stretched exponential (or Kohlrausch) function (eq. A.2) is shown in Figures A.6E and F. Stretched exponential functions have been used to describe complex systems that may have other factors affecting the system like FRET.[109] For systems that can be experiencing FRET, the $\beta = 1/6$, $1/3$ and $\frac{1}{2}$ for 1 to 3 dimensional systems respectively.[109] In Figure A.6E, a stretched exponential fit appears to represent the data as well as the biexponential fit. However, if we restrict β to be $1/3$ since we have a monolayer 2D superlattice, the fit is not representative of the data (Fig. A.6F).

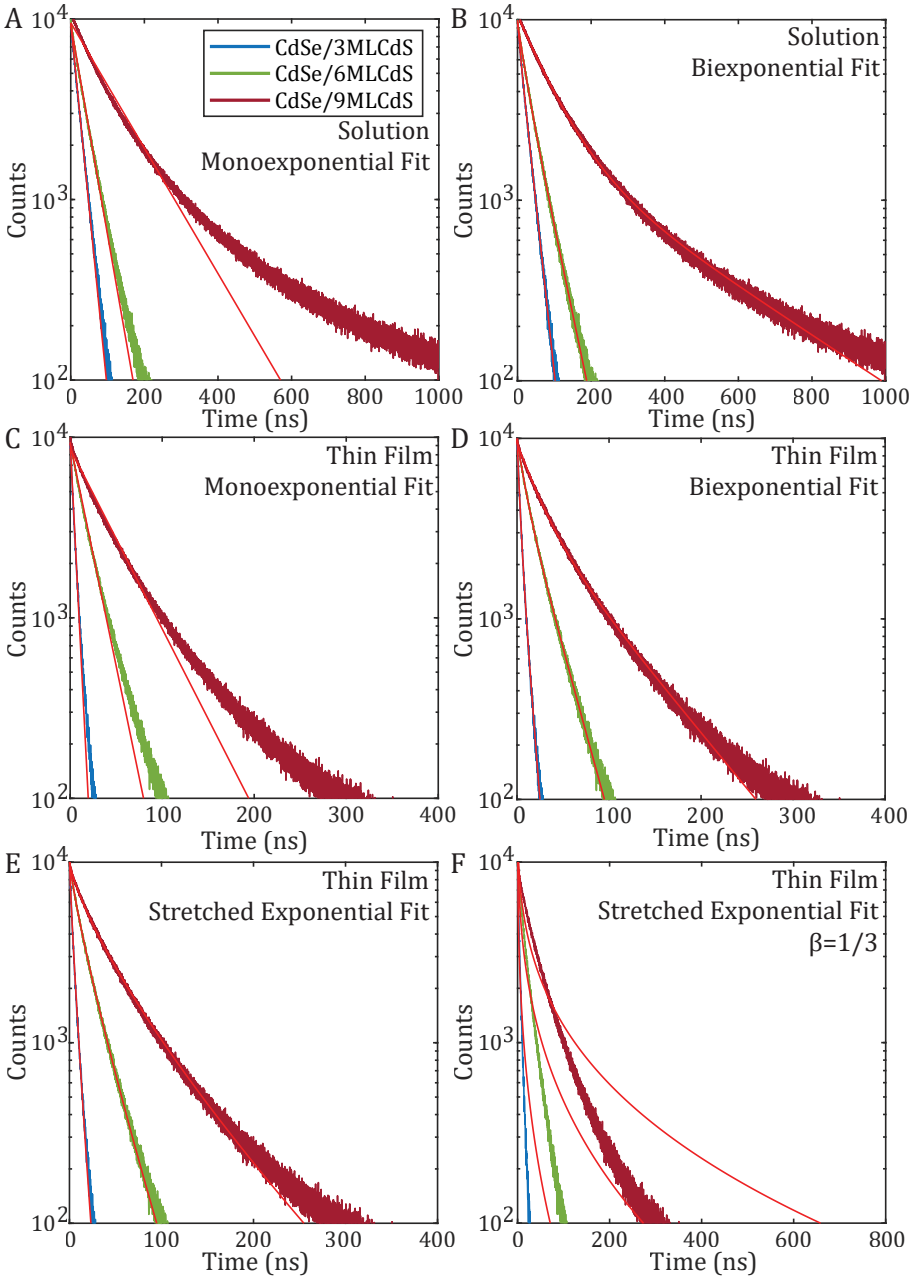

Figure A.6: **Time Resolved Photoluminescence Spectra with Exponential Fits.** TRPL for colloidal solution samples were fit with a **A** monoexponential and a **B** biexponential function. TRPL for monolayer thin films were fit with **C** a monoexponential, **D** biexponential, **E** stretched exponential and **F** a stretched exponential where β= 1/3 constraint is applied. TRPL data for CdSe/3MLCdS is shown in blue, CdSe/6MLCdS is shown in green and CdSe/9MLCdS is shown in dark red while the fits are in red for all plots.

$$Counts = A_1 e^{k_1 t} + A_2 e^{k_2 t} \tag{A.1}$$

$$Counts = A e^{k_1 t^{\beta}} \tag{A.2}$$

$$\tau_1 = -1/k_1 \tag{A.3}$$

From fitting the colloidal, we can extract the amplitudes (A_1 and A_2) and rate (k_1 and k_2) of both components of the decay. By taking the inverse of the rate (eq. A.3), we can obtain the two lifetime values for the faster (τ_1) and slower (τ_2) component of the decay (Table A.1).

$$\tau_{avg} = \frac{A_1\tau_1^2 + A_2\tau_2^2}{A_1\tau_1 + A_2\tau_2} \tag{A.4}$$

With all these components, we can calculate the average lifetime (τ_{avg}) (eq. A.4)[35, 179] of each sample. This τ_{avg} (Table A.1) is representative of the decay for each sample and can be used to calculate the recombination rates for each sample.

We also tabulate the fit results from fitting the thin films TRPL to a stretched exponential curve in Table A.2. Since the β value is much larger than what is expected for 2D systems, we ultimately choose to use the τ_{avg} for the recombination rate calculations.

A.7 PLQY of Thin Films

The PLQY of the 3 thin films was measured (Fig. A.7A-C) using the solid-state sample holder (Fig. A.1A). Each trial corresponds to a new film made from the same sample via self-assembly in the liquid-air interface and transferred to a glass cover slip. The average of the 5 trials is shown in black with the error bars corresponding to the standard deviation in PLQY values at each excitation wavelength. Although there is a small variance in PLQY value for each trial, the measurements were reproducible at providing a similar range of values.

A.8 Recombination Rates Using Stretched Exponential Fits for the QD Thin Films TRPL Data.

Recombination rates for monolayer thin films are calculated using τ from the stretched exponential fit results reported in Table A.2 and are compared to the recombination rates for the samples in colloidal solution using τ_{avg}. We observed the same trends in Γ_r (Fig. A.8A),

Table A.1: Biexponential Fitting Results of TRPL data for QD thin films (film) and colloidal solution (sol) samples.

Sample	A_1	τ_1 (ns)	A_2	τ_2 (ns)	τ_{avg} (ns)
CdSe/3MLCdS$_{sol}$	$14.21 \pm 0.29\%$	5.80 ± 0.16	$85.79 \pm 0.34\%$	22.98 ± 0.05	20.54 ± 0.70
CdSe/6MLCdS$_{sol}$	$32.12 \pm 0.93\%$	19.69 ± 0.32	$67.88 \pm 0.97\%$	44.88 ± 0.23	36.79 ± 1.34
CdSe/9MLCdS$_{sol}$	$80.03 \pm 0.16\%$	79.62 ± 0.22	$19.97 \pm 0.17\%$	324.15 ± 1.68	128.65 ± 1.36
CdSe/3MLCdS$_{film}$	$60.33 \pm 1.64\%$	2.67 ± 0.05	$39.67 \pm 1.70\%$	6.75 ± 0.12	4.29 ± 0.24
CdSe/6MLCdS$_{film}$	$42.03 \pm 0.69\%$	8.58 ± 0.10	$57.97 \pm 0.74\%$	23.47 ± 0.13	17.21 ± 0.42
CdSe/9MLCdS$_{film}$	$57.39 \pm 0.38\%$	22.57 ± 0.13	$42.61 \pm 0.40\%$	70.27 ± 0.32	42.89 ± 0.58

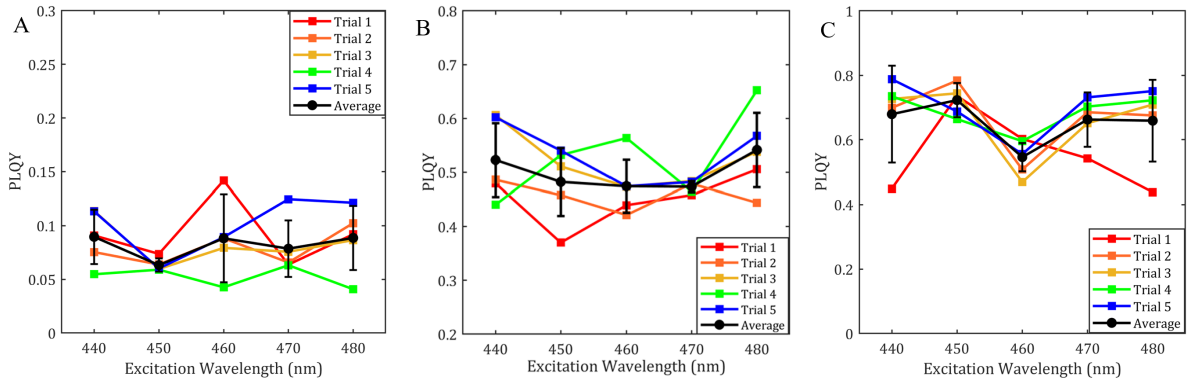

Figure A.7: **Photoluminescence Quantum Yield Measurements of QD Thin Films.** PLQY of **A** CdSe/3ML, **B** CdSe/6MLCdS, and **C** CdSe/9MLCdS thin films. Each color corresponds to a different measurement and the average quantum yield is shown in black with corresponding error bars.

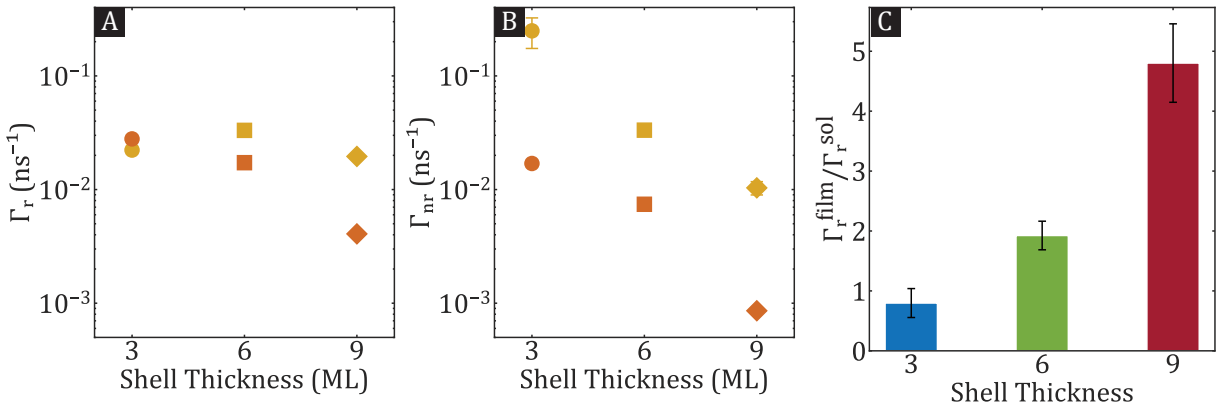

Figure A.8: **Recombination Rates Calculated Using Stretched Exponential Fits for the QD Thin Films TRPL Data.** **A** Γ_r and **B** Γ_{nr} of colloidal solution (orange) vs monolayer thin film (yellow) for the three different QD samples as a function of shell thickness. The rates for the QD thin films were calculated using the τ from the stretched exponential fit results reported in Table A.2. Corresponding y-axis error bars come from uncertainty of TRPL fits and PLQY measurements. **C** Radiative rate ratio for all three QD samples. Error bars were determined based on Γ_r uncertainties.

Table A.2: Stretched Exponential Fit Results of TRPL data for QD thin films.

Thin Film Sample	τ (ns)	β
CdSe/3MLCdS	3.685 ± 0.003	0.8332 ± 0.0005
CdSe/6MLCdS	15.04 ± 0.01	0.8323 ± 0.0004
CdSe/9MLCdS	33.43 ± 0.03	0.7541 ± 0.0006

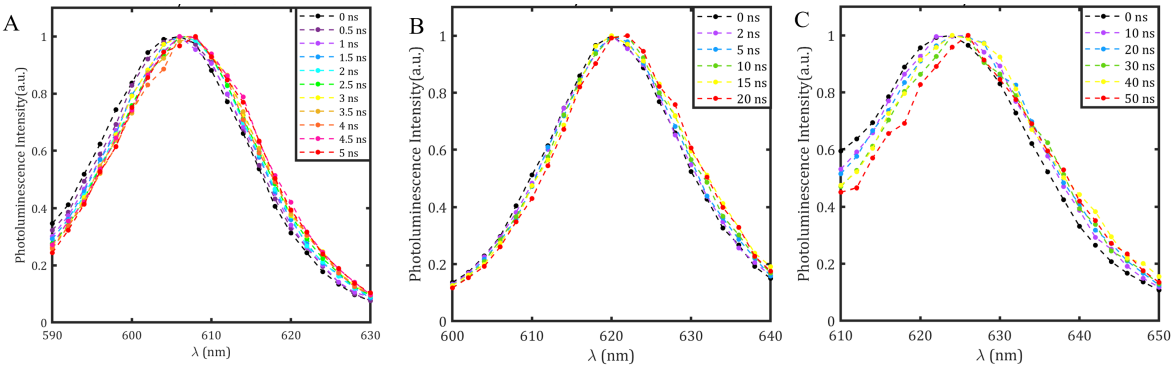

Figure A.9: **Time Resolved Emission Spectra of QD Monolayer Thin Films.** TRES of **A** CdSe/3MLCdS, **B** CdSe/6MLCdS, **C** CdSe/9MLCdS thin films.

Γ_{nr} (Fig. A.8B) and ${\Gamma_r}^{film}/\ {\Gamma_r}^{sol}$ (Fig. A.8C) as that reported in Figures 2.3 and 2.4 where all rates are larger for the monolayer thin films than in colloidal solution except for the Γ_r for CdSe/3MLCdS. Although using different fits for the TRPL data can lead to different Γ_r and Γ_{nr} values, the change from colloidal solution to monolayer thin films is the same.

A.9 Time Resolved Emission Spectra (TRES)

Time Resolved Emission Spectra (TRES) measurements were performed on monolayer thin film samples (Fig. A.9A-C) where the number of counts at each emission wavelength was measured as a function of time. The time scale chosen for each sample corresponds to τ_{avg} determined in section A.6. The data is normalized to better show any energy shifts over time. Essentially no shift is observed for the CdSe/3MLCdS and the CdSe/6MLCdS over time whereas a small shift is observed for CdSe/9MLCdS. This shift is much smaller than what has been reported for other QD solid systems where FRET has been observed9. A potential explanation for this lack of shift is due to the monodispersity in QD size of the samples which can result in a homogeneous energy landscape for the thin film.[73] Therefore, the lack of red shift does not necessarily signify a lack of FRET but rather indicates a uniformity in the energy of the film.

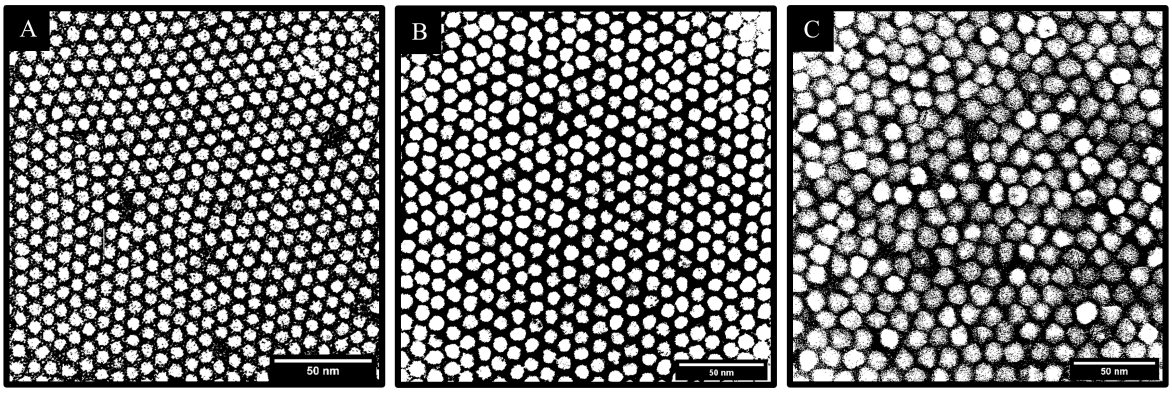

Figure A.10: **Binary TEM Images of Superlattices.** Binary TEM images of QD monolayer thin films of **A** CdSe/3MLCdS, **B** CdSe/6MLCdS, and **C** CdSe/9MLCdS. The white pixels in the image correspond to inorganic QD regions and black pixels in the image correspond to either air or organic ligands. Scale bars are 50 nm.

A.10 Effective Medium Approximation

To determine if the change in environment from solution to film is the cause of the differences in Γ_r. In solution, n corresponds to the index of refraction of the solvent which in our case is octane ($n = 1.40$). However, for the monolayer thin films, the index of refraction is made up of quantum dot inorganic material CdSe/CdS (n=2.53 for CdS and n=2.59 for CdSe), air (n=1.00), and the organic ligands passivating the QD surface (n= 1.46 for oleylamine and oleic acid).

The effective medium approximation was done on the samples based on the TEM images. The binary of the TEM images (Fig. A.10A-C) was used where each white pixel corresponds to inorganic material and the black pixels either correspond to air or the organic ligand passivating the nanocrystal surface.[81] The air/ligand ratio and inorganic ratio of the images correspond to the black and white pixel ratios respectively. Whereas the number of black pixels was divided by the total number of pixels in the image to obtain the amount of air/ligand in the image. The same process was done with the white pixels to obtain the amount of inorganic material in the image. We can then calculate what n is for the thin film samples by using the Bruggeman's Model for circular and spherical inclusions (eq A.5) where we average the index of refraction of the different components that make up the thin films. Based on size analysis of CdSe core and CdSe/CdS QDs, the QDs studied have roughly a 1:1, 2:1, and 3:1 CdS: CdSe ratio for CdSe/3MLCdS, CdSe/6MLCdS, and CdSe/9MLCdS

respectively. Hence, we can use a refractive index of 2.56, 2.55, 2.54 for the inorganic materials. Since we cannot know how much of the film is made up of air vs organic ligand passivating the surface, we can calculate two different refractive indexes: 1) where the film is only air and inorganic material and 2) where the film is made up of only organic ligand and inorganic material. The former will therefore be an underestimation of n and the latter will be an overestimation of n with the true n value being somewhere in -between those two values (Table A.3).
Bruggeman's Model for Circular and Spherical Inclusions:

$$\Sigma\delta_i \frac{\sigma_i - \sigma_e}{\sigma_i + (n-1)\sigma_e} = 0 \tag{A.5}$$

$$\Gamma_r = \frac{\omega^3 n|\mu_{12}|^2}{3\pi\epsilon_0\hbar c^3} \tag{A.6}$$

If we revisit the $\Gamma_r$equation (eq A.6) and assume that all the other variables should be equal for the solution samples and the thin film samples, then the difference in radiative rate between solution and thin film should be proportional to the change in n from solution to monolayer thin film. Since we calculated 2 potential n values for the films depending on if it's organic ligand or air surrounding it, we can do the same for the refractive index ratio. The n_{sol}/n_{film} (just air) overestimates the ratio because we are assuming that there is just air between the QDs which would underestimate the n_{film} value. The opposite is true for n_{sol}/n_{film} (just ligand) where we assumed that there is just ligand between the QDs. The true n_{sol}/n_{film} ratio will fall between those two extremes. However the radiative rate ratio for CdSe/3MLCdS is much smaller than and for CdSe/9MLCdS is much larger than the refractive index ratio range. Therefore, the change in environment from solution to thin film does not solely explain the discrepancies in Γ_r.

A.11 Change in Transition Dipole Moment

The transition dipole moment (μ) is the other variable in eq s5 that must be considered to understand the increase in Γ_r for the monolayer thin films as opposed to in solution. In solution, the QDs are dispersed in solvent and are considered to not be interacting with each other due to the large interparticle spacing. For the monolayer thin films, the QDs self-assemble into a superlattice in which the nanocrystals may also have a favored crystallographic orientation on the glass substrate. Therefore, the monolayer thin films may not only have great spatial order, but crystallographic order as well. Crystallographic alignment has previously been shown in 1D-nanorods,[177, 47] 2D-plates,[112] and even hexagonal quantum dots.[119] Although these nanocrystals are spherical and should have isotropic emission, size and shape, size analysis (Fig. A.2) of the TEM images show that the ferret diameter of these QDs is larger than the regular diameter. The longer ferret diameter signifies that the QDs are not perfectly spherical, especially with increasing shell thickness. Since we know

Table A.3: Results of Effective Medium Approximation.

Sample	Area of Image (nm^2)	Total Pixels	Black Pixels	White Pixels Ratio	Air Ligand	Inorganic Ratio	n just air	n just ligand
CdSe/3MLCdS	190 x 190	7452900	4054215	3398685	0.544	0.456	1.71	1.96
CdSe/6MLCdS	218 x 218	613089	315738	297351	0.515	0.485	1.75	1.98
CdSe/9MLCdS	227 x 227	10621081	5287867	5333214	0.498	0.502	1.77	2.00

Table A.4: Comparison of Radiative Rate Ratio with Refractive Index Ratio

Sample	$\Gamma_{r,\mathrm{sol}}$	$\Gamma_{r,\mathrm{film}}$	$\frac{\Gamma_{r,\mathrm{sol}}}{\Gamma_{r,\mathrm{film}}}$	$\frac{n_{\mathrm{sol}}}{n_{\mathrm{film}}}$ (just air)	$\frac{n_{\mathrm{sol}}}{n_{\mathrm{film}}}$ (just ligand)
CdSe/3MLCdS	2.8 ± 0.1	1.6 ± 0.5	1.75	0.82	0.71
CdSe/6MLCdS	1.72 ± 0.07	2.4 ± 0.3	0.72	0.80	0.70
CdSe/9MLCdS	0.41 ± 0.01	1.2 ± 0.2	0.34	0.79	0.70

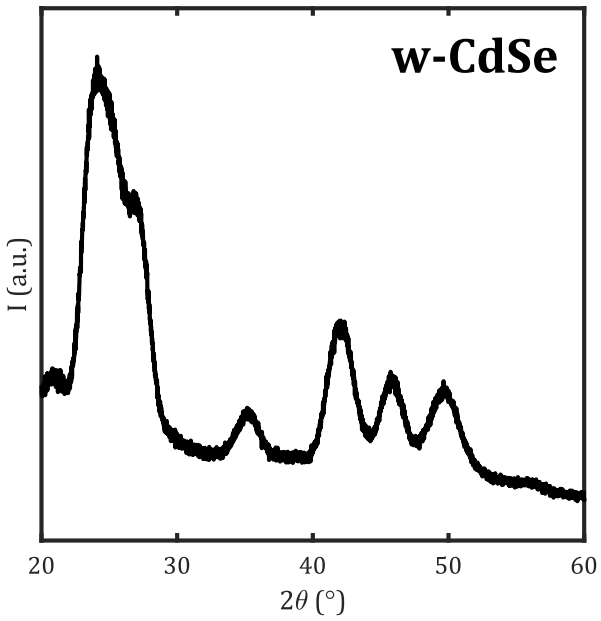

Figure A.11: **X-Ray Diffraction of Wurtzite CdSe Cores.**

the CdSe cores studied have a wurtzite crystal structure from x-ray diffraction of CdSe core samples (Fig. A.11) and the CdS shell growth procedure does not change the crystal structure of the QD,[96] their shape may become more hexagonal than spherical with increasing shell thickness16. Although not perfectly spherical nor hexagonal, the QDs could have a crystallographic alignment on the substrate favoring a specific orientation. Alignment of crystallographic orientation of the QD thin films will result in alignment of the transition dipole moment. If this alignment is present, μ in eq A.6 is greater for the monolayer thin films than in colloidal solution. This increase in μ can lead to optical anisotropies in the thin films that can be modeled in a cavity-like structure and results in an enhancement of Γ_r.[147]

One measurement that cooperates the crystallographic orientation and dipole alignment of the QD thin films is polarized emission measurements where the photoluminescence in-

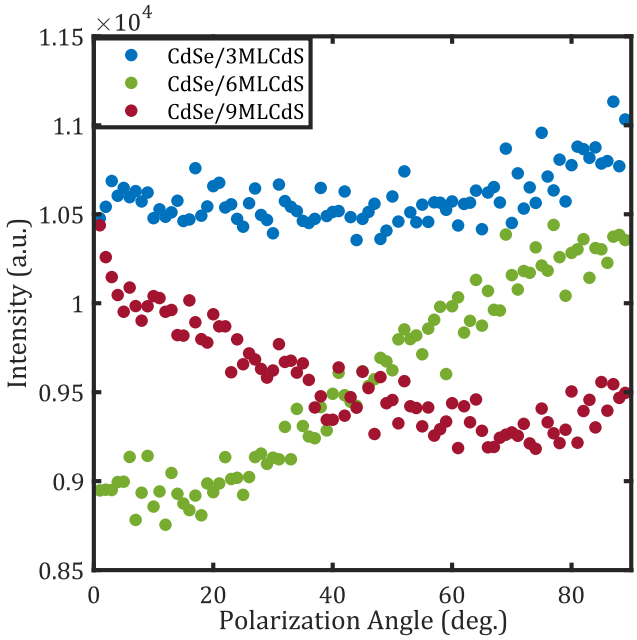

Figure A.12: **Polarized Emission Spectra of QD Monolayer Thin Films.**

tensity is measured as a function of the angle dependency of the emission polarizer (Fig. A.12).[164] For these measurements, the emission polarizer is rotated from 0° to 90° and the counts are measured at each sample's center emission wavelength. For the CdSe/3MLCdS sample, there is a small polarization angle dependency on intensity as the intensity changes from 1.05×10^4 to 1.11×10^4. The CdSe/9ML has some polarization angle dependency from 1.05×10^4 to 0.95×10^4 and CdSe/6MLCdS has the most polarization angle dependency as it changes from 0.9×10^4 to 1.05×10^4. However, in Fig. 2.4 the CdSe/9MLCdS sample has the highest radiative rate ratio from thin film to solution which does not correspond to the angle-dependency photoluminescence trend. Therefore, we cannot make any conclusions about the crystallographic alignment of the QD monolayer thin films without additional structural studies of the superlattice order.

A.12 Ligand Removal in Colloidal Solution

To verify if the removal of ligands from the QD surface can alter the recombination rates, we systematically remove ligands from the QD surface and check how the recombination rates change in colloidal solution. Antisolvent washes in acetone have been reported to remove cadmium oleate ligands from the QD surface.[5, 28] The removal of cadmium oleate ligands

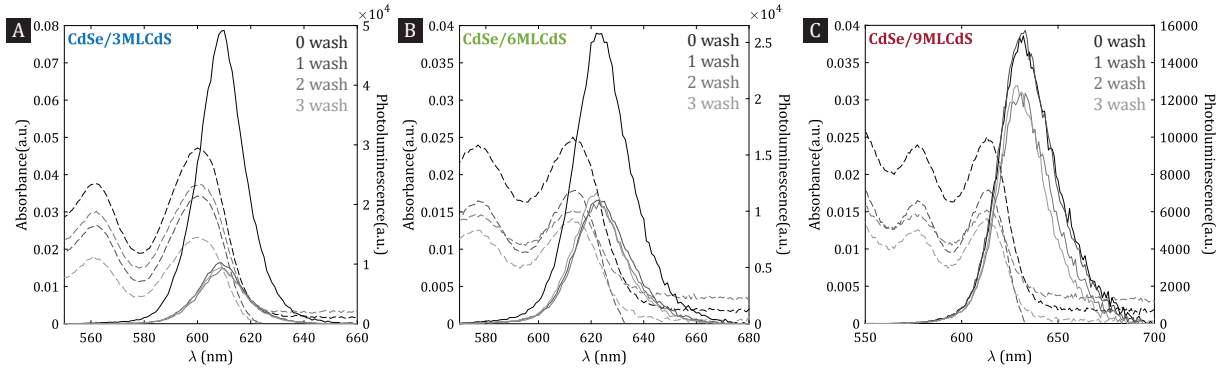

Figure A.13: **Absorbance and Photoluminescence of QDs in Colloidal Solution with Additional Washes.** Absorbance and PL of **A** CdSe/3MLCdS, **B** CdSe/6MLCdS, and **C**CdSe/9MLCdS with additional antisolvent washes.

will result in unpassivated sulfur sites that lead to a partially negative charged QD surface. Optical characterization of QD samples was done after additional antisolvent washes. In Figure A.13A-C, the absorbance and photoluminescence of the three samples is shown with the additional antisolvent washes. There are no significant changes in absorbance and PL peak positions and linewidth with additional washes. There is an initial decrease in luminescence intensity with the first couple of washes as expected based on the literature[28] but after the first (CdSe/3MLCdS and CdSe/6MLCdS) and second (CdSe/9MLCdS) washes no change in luminescence intensity is observed. Samples with a higher absorbance intensity do have a higher PL intensity but the change in PL with the first initial wash is greater than the differences in absorbance intensity.

Additionally, the TRPL of the three samples in colloidal solution decrease faster with additional washes (Fig. A.14 A-C). In other words, τ_{avg} becomes smaller with each additional wash for all samples. This trend is most apparent for the CdSe/9MLCdS sample (Fig. A.14C). Similarly, the PLQY also changes with additional washes. Initially the PLQY slightly increases with the first (CdSe/3MLCdS and CdSe/6MLCdS) and second (CdSe/9MLCdS) additional washes. However, with more washes, the PLQY of all three samples decreases. The decrease in PLQY is most extreme for the CdSe/3MLCdS which has the weakest wavefunction confinement and can result in charge carrier trapping with additional surface trap states.

With τ_{avg} and PLQY measured, we can calculate Γ_r (Fig. A.15A) and Γ_{nr} (Fig. A.15B) for the three samples in colloidal solution with additional washes. We compare how Γ_r and Γ_{nr} change with additional antisolvent washes relative to the rates before any additional washes (Wash 0). We observe that both Γ_r and Γ_{nr} increase with additional washes for all three samples. Eventually, after 3 washes, the Γ_r for CdSe/3MLCdS decreases below the

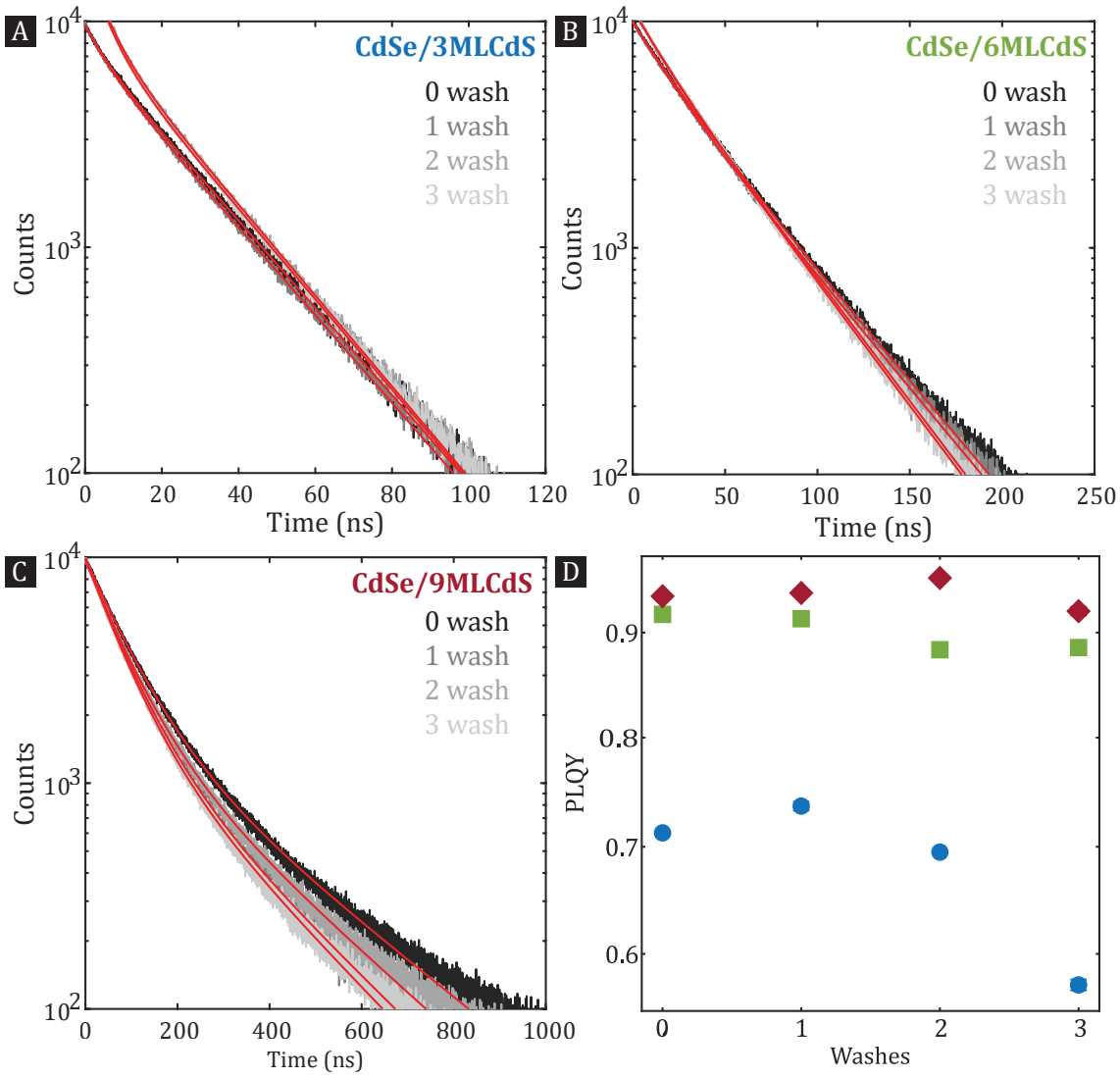

Figure A.14: **Optical Characterization of QDs in Colloidal Solution with Additional Washes.** TRPL of **A** CdSe/3MLCdS, **B** CdSe/6MLCdS, and **C** CdSe/9MLCdS. **D** PLQY values for CdSe/3MLCdS (blue circle), CdSe/6MLCdS (green square), and CdSe/9MLCdS (red diamond). First two decades of TRPL decay were fit to a biexponential curve shown in red.

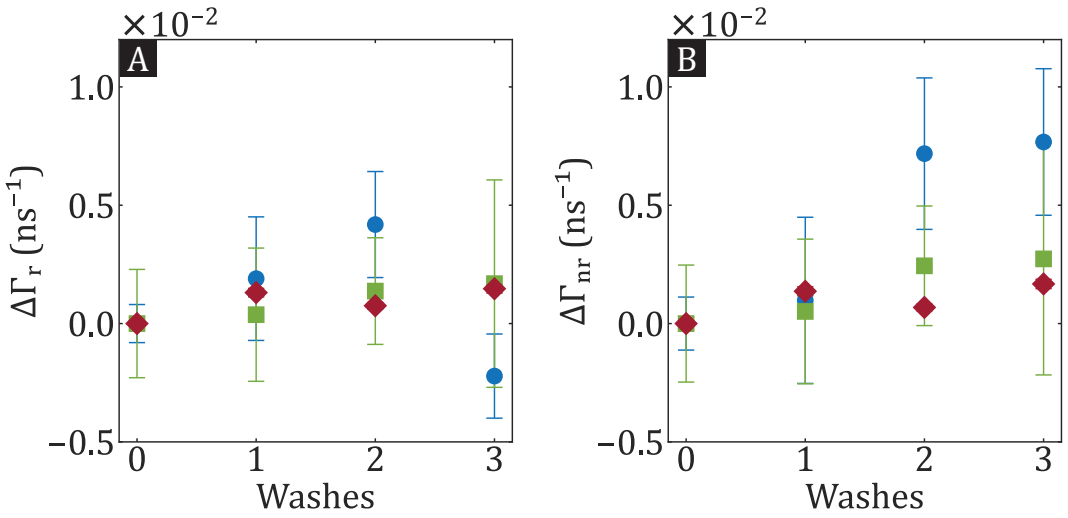

Figure A.15: **Change in Recombination Rate with Ligand Removal of QDs in Colloidal Solution.** Change in **A** Γ_r and **B** Γ_{nr} with additional antisolvent washes for CdSe/3MLCdS (blue circle), CdSe/6MLCdS (green square), and CdSe/9MLCdS (red diamond) colloidal solution. Change in rate was determined in reference to the initial rate before additional antisolvent washes.

pre-wash rate. These changes that we have observed are similar to the observed changes between colloidal solution and monolayer thin films although not as drastic. These results support our hypothesis that the removal of ligands can lead to changes in Γ_r.

Appendix B

Supporting Information for Chapter 6

B.1 Resonant Fluorescence Microscope

Resonant fluorescence measurements were done in a home-built microscope set-up (Fig. B.1) constructed at the Molecular Foundry at Lawrence Berkeley National Lab. Samples were excited with a Newport Velocity Tunable (TLB-6300-LN) laser with tunable emission from 1520 nm (6579 cm^{-1})-1570 nm (6369 cm^{-1}) and a nominal linewidth of $\leq$300 kHz (narrower than any feature discussed here). The excitation passed through a polarizing beam-splitter and the fluorescence with polarization orthogonal to the excitation was detected to suppress scattered laser light. A dual chopper set-up was used to do photoluminescence measurements at resonant excitation-emission frequencies. The choppers were rotating at the same frequency (77 Hz) but with a phase offset to minimize laser scattering. Additional prevention of laser scattering was done by using different chopper blades. The excitation chopper blade only exposed the laser to the sample 10% of the time while the detection chopper blade only collected the sample emission 50% of the time. An achromatic doublet lens was used instead of an objective to focus the laser on the sample to image a larger area of the sample. The sample was maintained in either a liquid He or liquid N_2 environment under vacuum in a Janis ST-500 cryostat, The emission was dispersed on to an InGaAs AndorCCD camera connected to a Princeton Instruments SpectroPro 300 with a spatial resolution of 0.1 nm.

B.2 Relative Peak Intensities

Relative intensities of the photoluminescence (PL) of Er^{3+}-doped PTO deposited in different substrates at 7 K (Fig. B.2a) and 77 K (Fig. B.2b). At both temperatures, samples with a higher fraction of *c*-domains have a brighter PL.

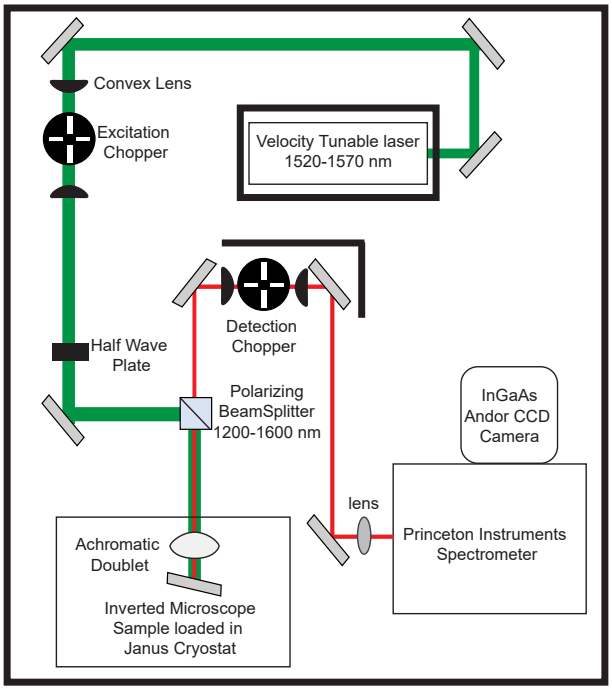

Figure B.1: **Diagram of Resonant Fluorescence Microscope Setup.**

B.3 Peak Fits for Er^{3+}-doped PTO Samples at 7 K

Peak fits for the Er^{3+}-doped PTO samples on STO (Fig. B.3) and DSO (Fig. B.4) at 7 K. Peaks were fit to a Gaussian curve with a linear background. The three peaks fitted correspond to the $Y_1 \rightarrow Z_1$ (Fig. B.3a and B.4a), $Y_1 \rightarrow Z_2$ (Fig. B.3b and B.4b), and $Y_1 \rightarrow Z_3$ (Fig. B.3c and B.4c) transitions. Residual of fits provided next to each peak fit to show the goodness of fits. Fit results are reported in Table B.1.

B.4 Peak Fits for Er^{3+}-doped PTO Samples at 77 K

Peak fits for the Er^{3+}-doped PTO samples on LSAT (Fig. B.5), STO (Fig. B.6), DSO (Fig. B.7), GSO (Fig. B.8) and NSO (Fig. B.9) at 7 K. Peaks were fit to a Gaussian curve with a linear background. The three peaks fitted correspond to the $Y_1 \rightarrow Z_1$ (Fig. B.5a-B.9a), $Y_1 \rightarrow Z_2$ (Fig. B.5b-B.9b), and $Y_1 \rightarrow Z_3$ (Fig. B.5c-B.9c) transitions. Residual of fits provided next to each peak fit to show the goodness of fits. Fit results are reported in Table B.2.

Table B.1: Gaussian fit results reporting frequency (Freq.), intensity and linewidth from Figures B.3 and B.4. Freq. from Literature (Lit.) from reference [155].

Transition	Freq. from Lit. (cm^{-1})	STO			DSO		
		Freq. (cm^{-1})	Intensity (arb. units)	Linewidth (cm^{-1})	Freq. (cm^{-1})	Intensity (arb. units)	Linewidth (cm^{-1})
$Y_1 \rightarrow Z_1$	6511.7	6516.08	954.96	1.4	6516.66	629.35	0.99
$Y_1 \rightarrow Z_2$	6497.49	6501.27	7066.52	1.86	6503.06	954.91	2.2
$Y_1 \rightarrow Z_3$	6398.23	6403.15	3224.14	1.64	6403.99	507.47	1.96

Table B.2: Gaussian fit results reporting frequency (Freq.), intensity and linewidth from Figures B.5, B.6, B.7, B.8, and B.9. Freq. from Literature (Lit.) from reference [155].

		LSAT			STO		
Transition	Freq. from Lit. (cm^{-1})[155]	Freq. (cm^{-1})	Intensity (arb. units)	Linewidth (cm^{-1})	Freq. (cm^{-1})	Intensity (arb. units)	Linewidth (cm^{-1})
$Y_1 \rightarrow Z_1$	6511.7	6515.82	2230.89	2.36	6515.81	3623.92	2.41
$Y_1 \rightarrow Z_2$	6497.49	6501.39	30101.09	2.2	6501.34	14655.47	2.19
$Y_1 \rightarrow Z_3$	6398.23	6403.98	8918.9	2.42	6403.91	870.85	2.44
		DSO			GSO		
Transition	Freq. from Lit. (cm^{-1})	Freq. (cm^{-1})	Intensity (arb. units)	Linewidth (cm^{-1})	Freq. (cm^{-1})	Intensity (arb. units)	Linewidth (cm^{-1})
$Y_1 \rightarrow Z_1$	6511.7	6516.28	607.68	2.46	6516.5	238.42	2.57
$Y_1 \rightarrow Z_2$	6497.49	6501.44	5405.47	2.13	6501.8	2839.2	2.25
$Y_1 \rightarrow Z_3$	6398.23	6404.13	349.34	2.55	6404.47	254.66	2.58

		NSO		
Transition	Freq. from Lit. (cm^{-1})	Freq. (cm^{-1})	Intensity (arb. units)	Linewidth (cm^{-1})
$Y_1 \rightarrow Z_1$	6511.7	6516.54	337.88	2.43
$Y_1 \rightarrow Z_2$	6497.49	6501.87	2575.09	2.35
$Y_1 \rightarrow Z_3$	6398.23	6404.3	278.17	2.7

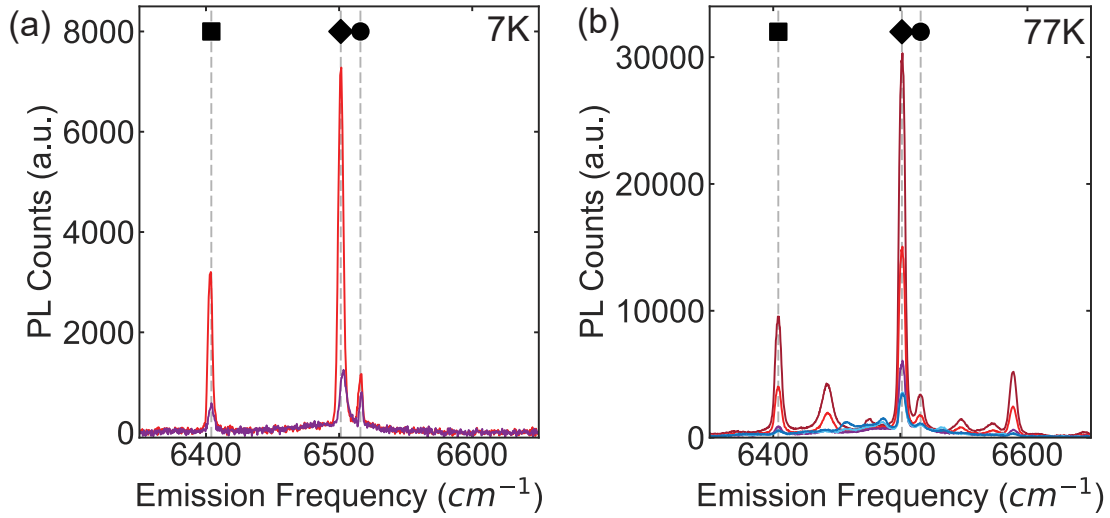

Figure B.2: **Relative Intensity of Er^{3+}-doped PTO. a** Relative PL spectra of Er^{3+}-doped PTO on STO (red) and on DSO (purple) at 7 K excited at 6515 cm^{-1} and **b** Relative PL spectra of Er^{3+}-doped PTO on LSAT (dark red), STO (red), DSO (purple), GSO (light blue), NSO (dark blue) at 77 K excited at 6500 cm^{-1}.

B.5 Temperature Dependent Photoluminescence

Temperature dependent PL of Er^{3+}-doped PTO on STO. Temperature dependent PL measurements were done for 2 temperature regimes: the liquid He temperature regime from 13 K-55 K (Fig. B.10a) and the liquid nitrogen temperature regime from 77 K-191 K (Fig. B.10b). All spectra was measured with an excitation frequency of 6500 cm^{-1}. Peaks corresponding to $Y_1 \rightarrow Z_1$, $Y_1 \rightarrow Z_2$, and $Y_1 \rightarrow Z_3$ transitions were fit to Gaussian peaks with a linear background. Peak fit results were plotted as a function of temperature for the three transitions in both the liquid He regime (Fig. B.11) and the liquid N_2 regime (Fig. B.12).

For the liquid He temperature regime, the normalized PL counts increase with temperature up until 35 K and then begins to decrease at higher temperatures (Fig. B.11a-c). At 35 K, there is enough energy to thermally populate different states. Both the emission frequency (Fig. B.11d-f) and linewidth (Fig. B.11g-i) increase with temperature which is expected due to changes in the population of states with thermal energy.

For the liquid N_2 temperature regime, the normalized PL counts (Fig. B.12a-c) decreases with temperature while the change in emission frequency (Fig. B.12d-f) and linewidth (Fig. B.12g-i) increase. The only exception to this trend is the change in linewidth for the $Y_1 \rightarrow Z_1$

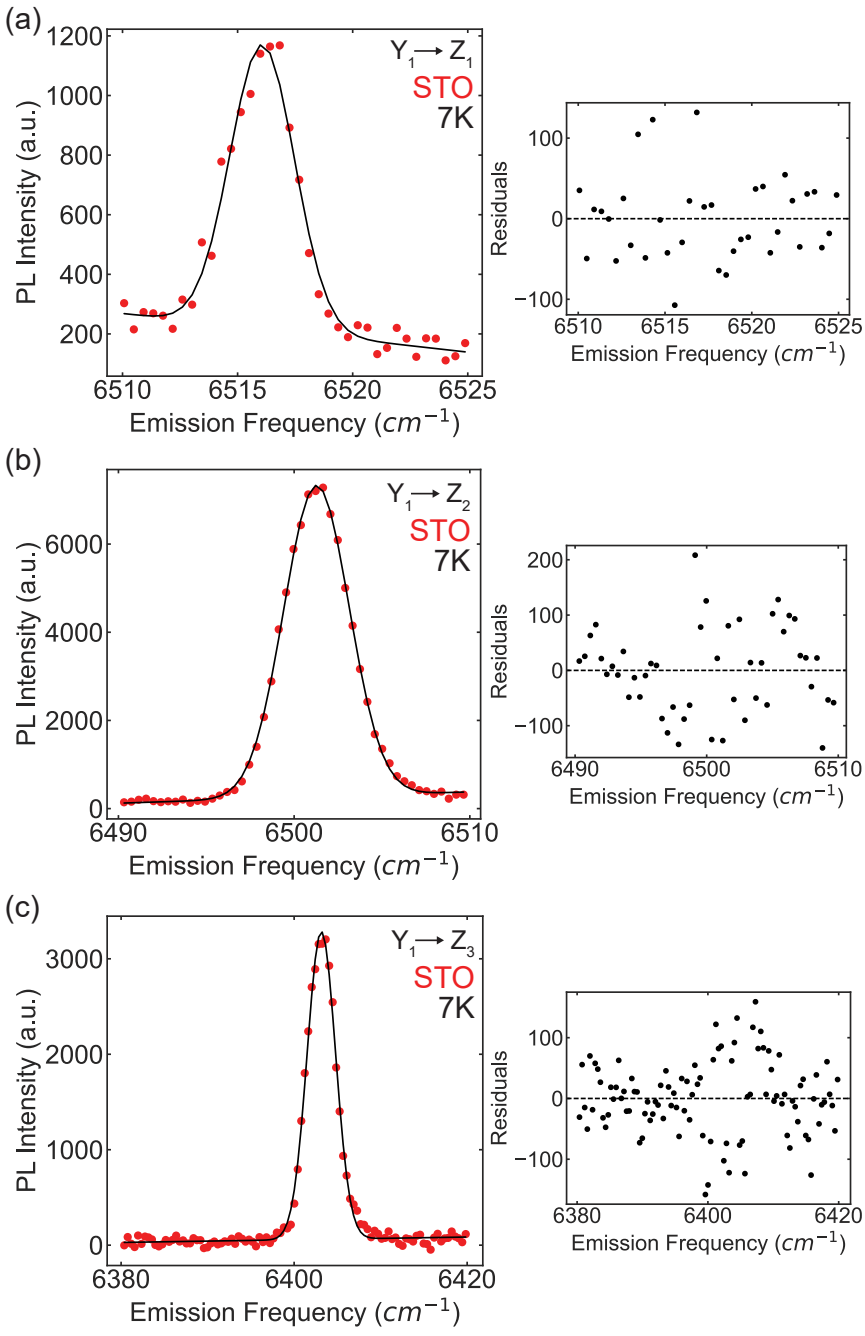

Figure B.3: **Fits for Er^{3+}-doped PTO on STO at 7 K.** Gaussian fits for the **a** $Y_1 \rightarrow Z_1$, **b** $Y_1 \rightarrow Z_2$, and **c** $Y_1 \rightarrow Z_3$ transitions. Fits (black solid line) shown on top of data (red circle). Corresponding residual from fits shown to the right of each plot

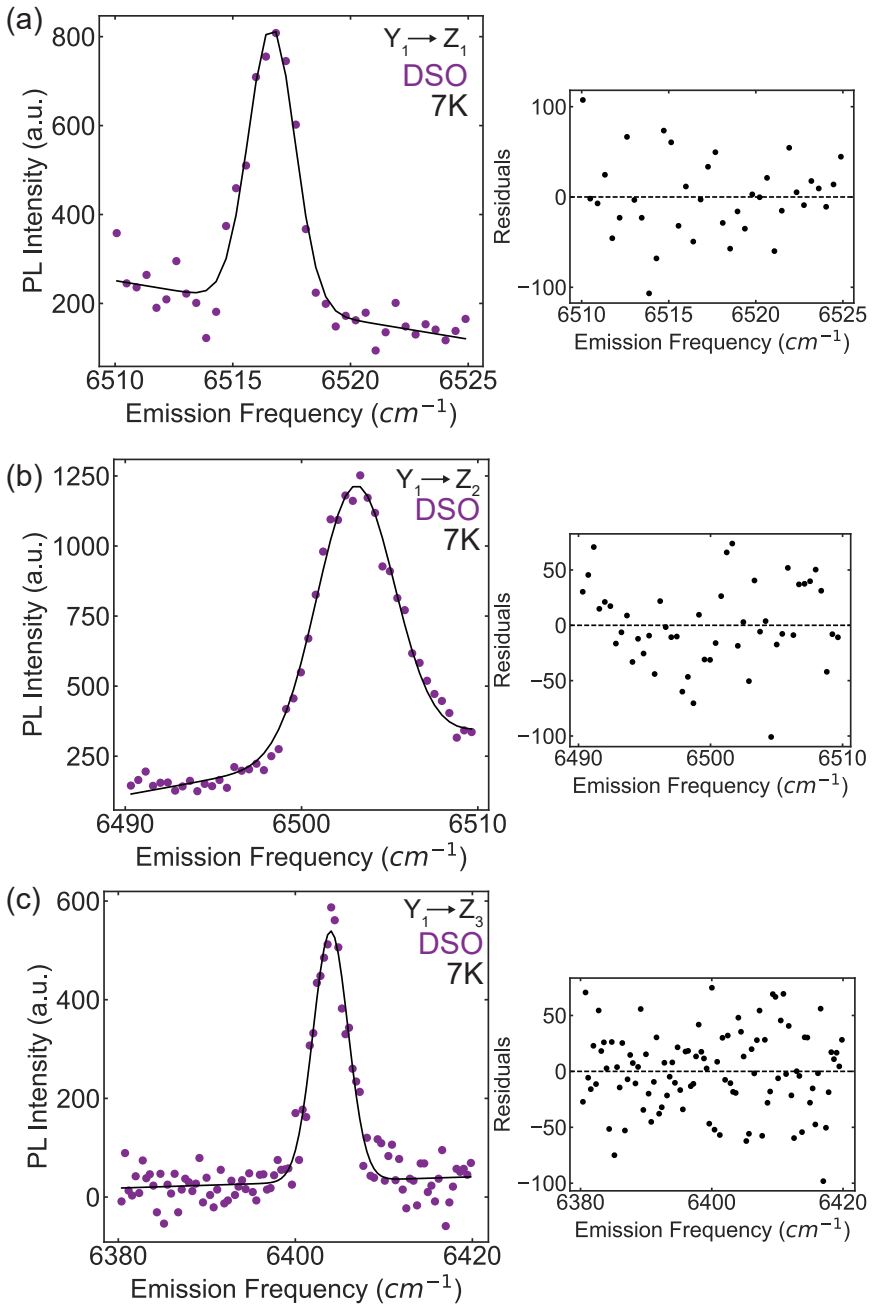

Figure B.4: **Fits for Er^{3+}-doped PTO on DSO at 7 K.** Gaussian fits for the **a** $Y_1 \rightarrow Z_1$, **b** $Y_1 \rightarrow Z_2$, and **c** $Y_1 \rightarrow Z_3$ transitions. Fits (black solid line) shown on top of data (purple circle). Corresponding residual from fits shown to the right of each plot.

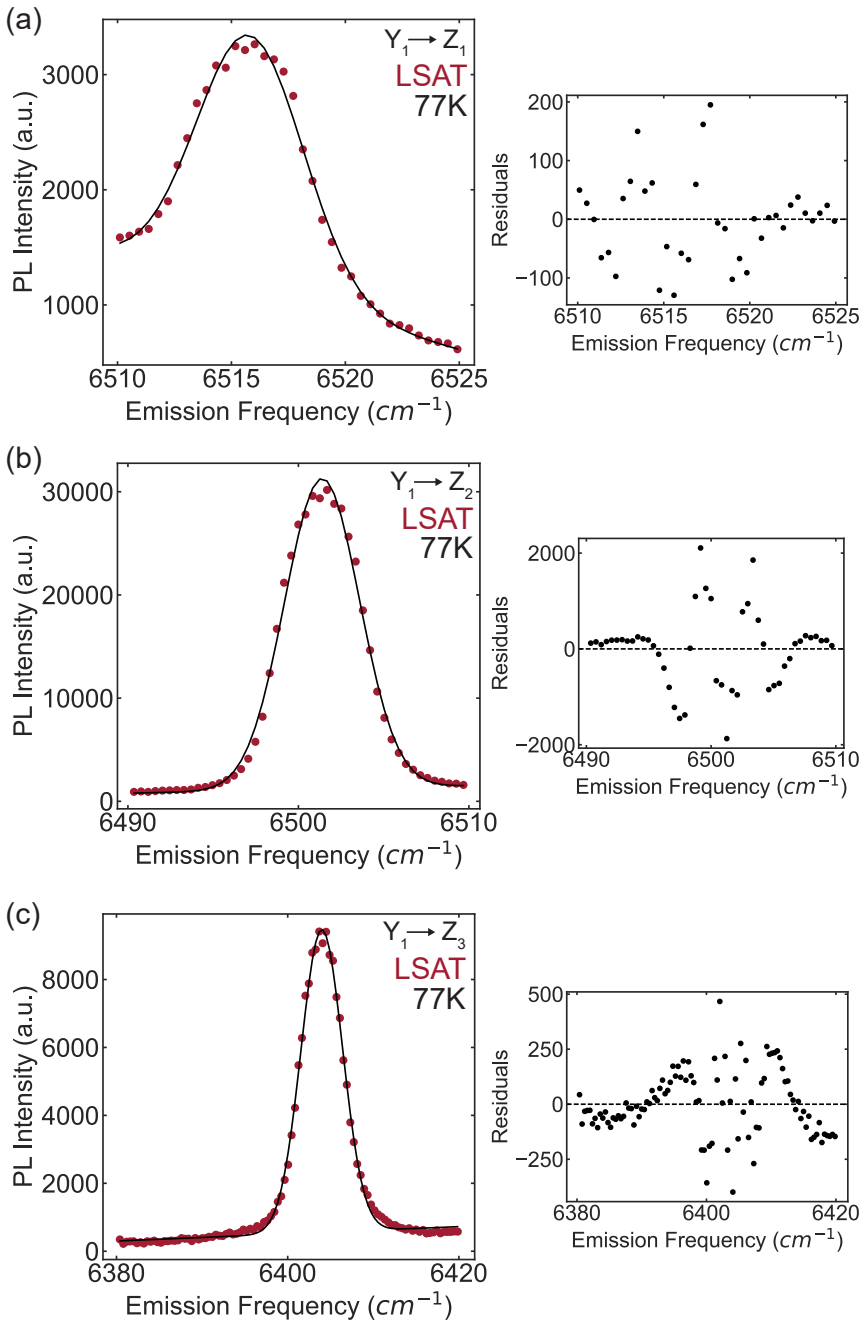

Figure B.5: **Fits for Er^{3+}-doped PTO on LSAT at 77 K.** Gaussian fits for the **a** $Y_1 \rightarrow Z_1$, **b** $Y_1 \rightarrow Z_2$, and **c** $Y_1 \rightarrow Z_3$ transitions. Fits (black solid line) shown on top of data (dark red circle). Corresponding residual from fits shown to the right of each plot

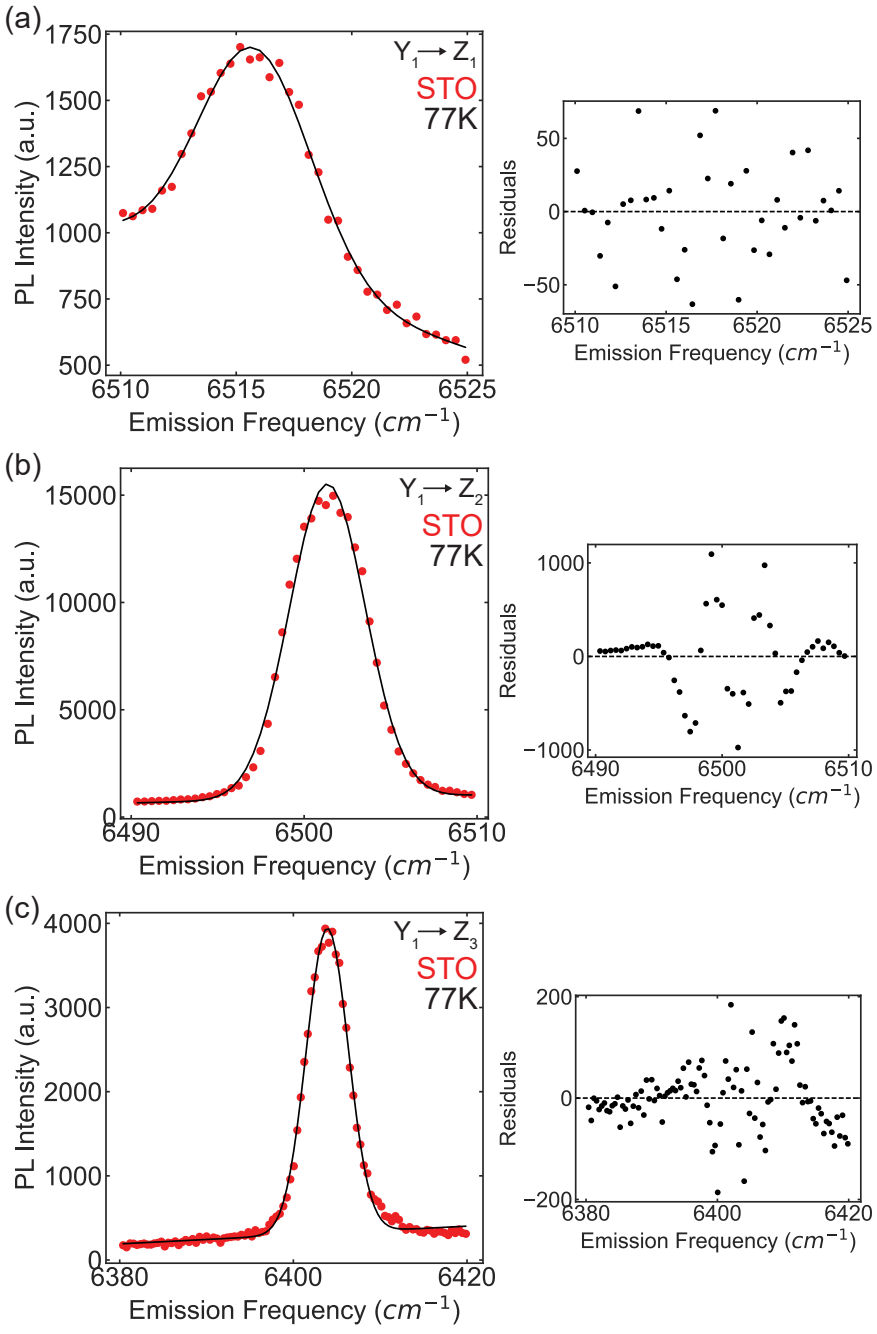

Figure B.6: **Fits for Er^{3+}-doped PTO on STO at 77 K.** Gaussian fits for the **a** $Y_1 \rightarrow Z_1$, **b** $Y_1 \rightarrow Z_2$, and **c** $Y_1 \rightarrow Z_3$ transitions. Fits (black solid line) shown on top of data (red circle). Corresponding residual from fits shown to the right of each plot

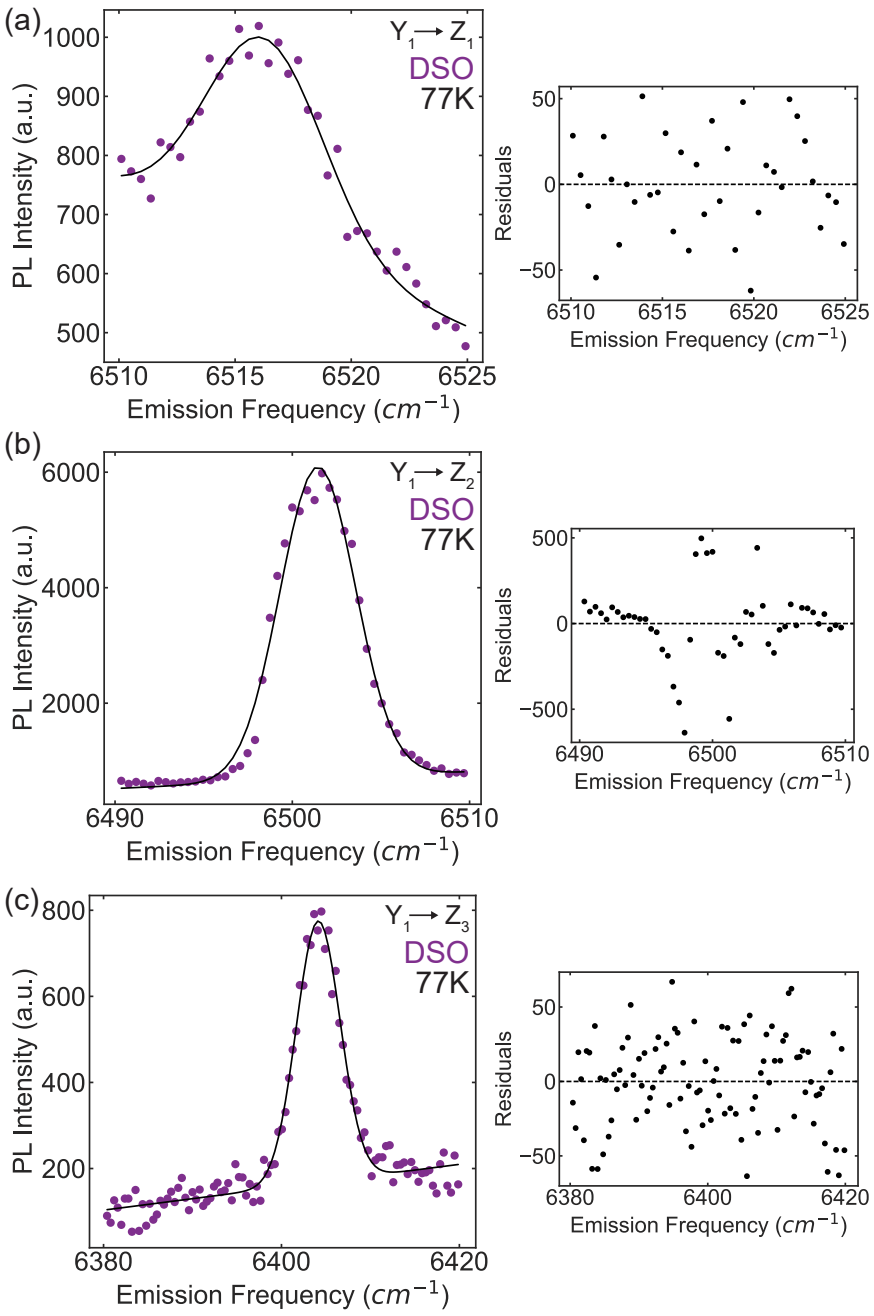

Figure B.7: **Fits for Er^{3+}-doped PTO on DSO at 77 K.** Gaussian fits for the **a** $Y_1 \rightarrow Z_1$, **b** $Y_1 \rightarrow Z_2$, and **c** $Y_1 \rightarrow Z_3$ transitions. Fits (black solid line) shown on top of data (purple circle). Corresponding residual from fits shown to the right of each plot

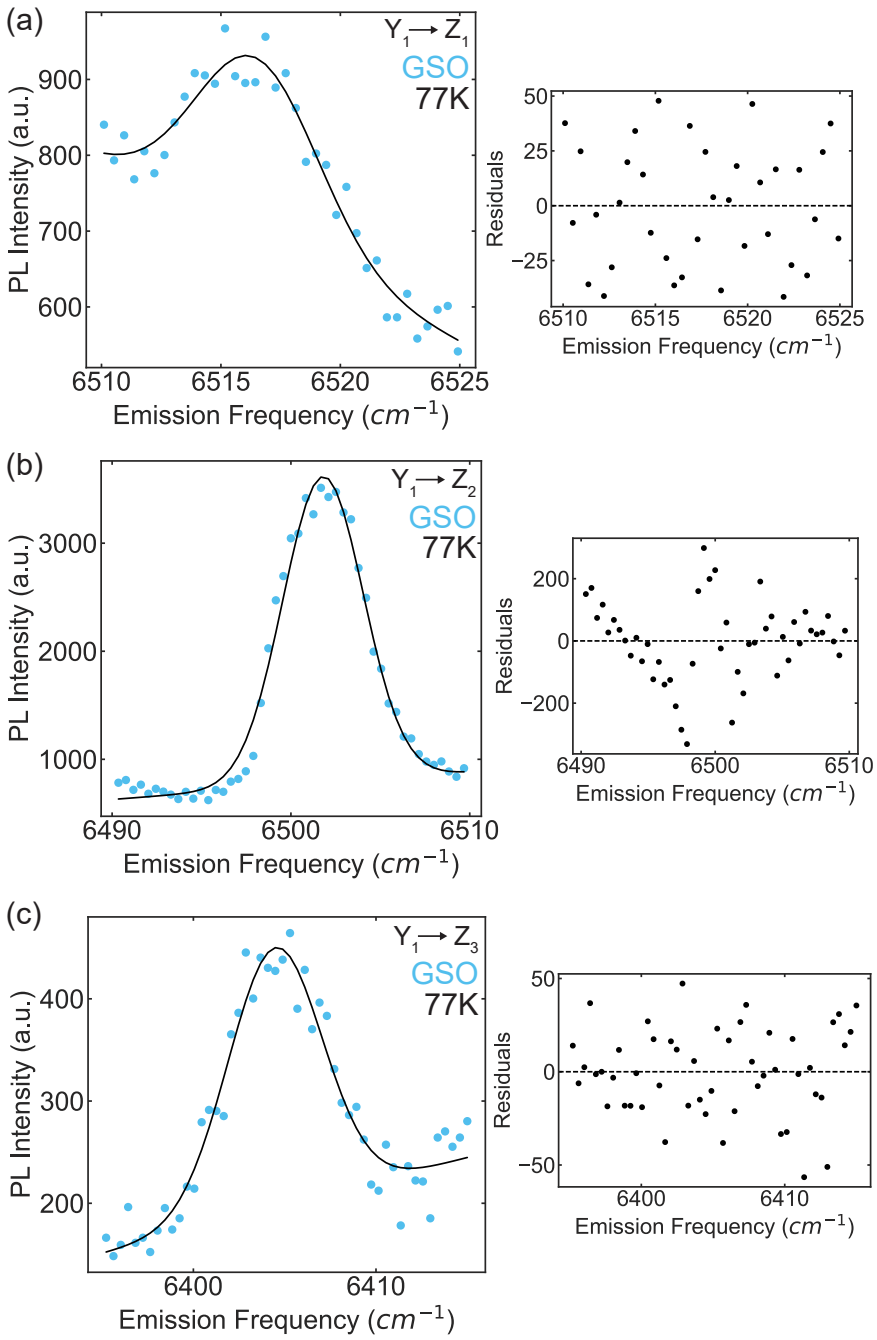

Figure B.8: **Fits for Er^{3+}-doped PTO on GSO at 77 K.** Gaussian fits for the **a** $Y_1 \rightarrow Z_1$, **b** $Y_1 \rightarrow Z_2$, and **c** $Y_1 \rightarrow Z_3$ transitions. Fits (black solid line) shown on top of data (light blue circle). Corresponding residual from fits shown to the right of each plot

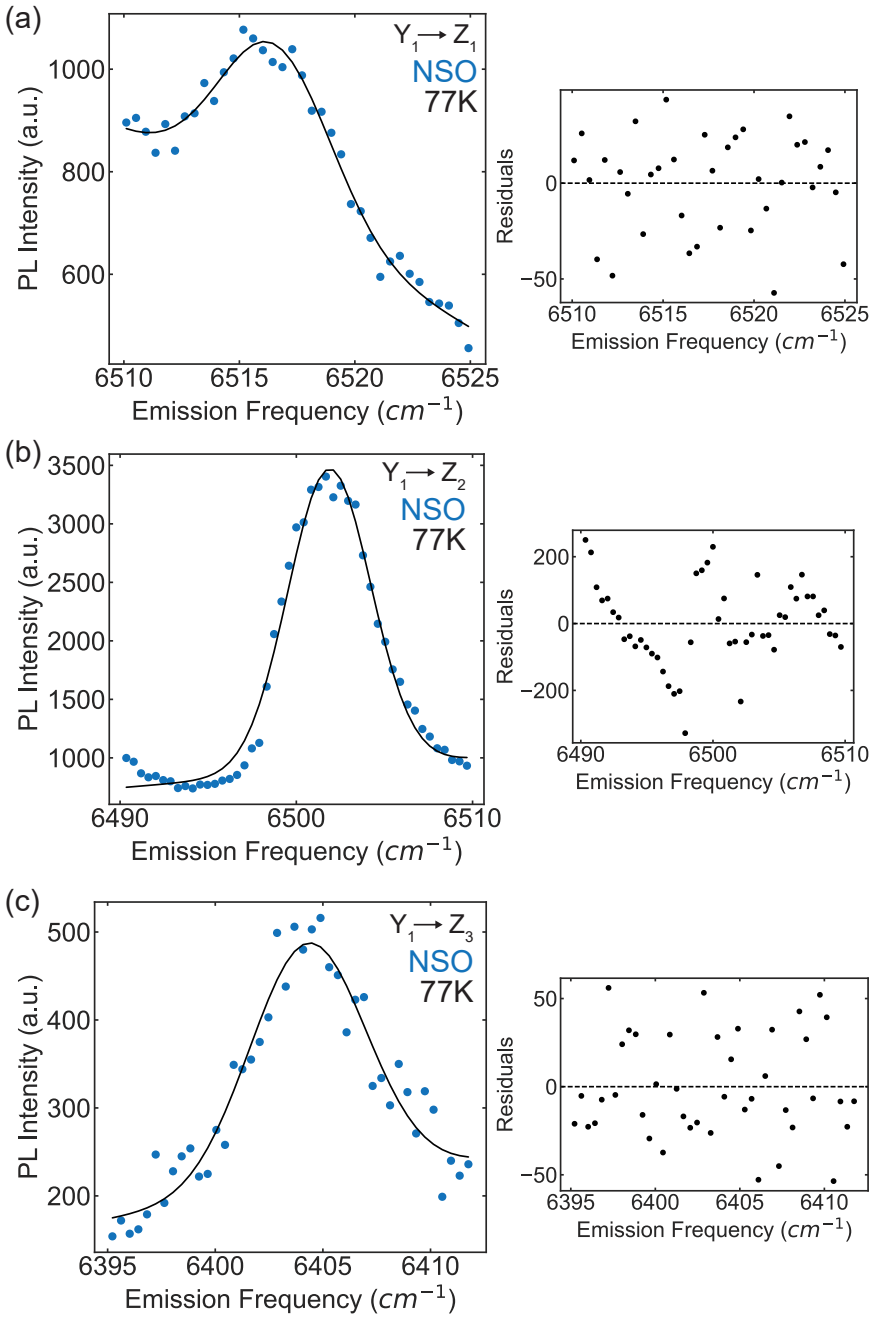

Figure B.9: **Fits for Er^{3+}-doped PTO on LSAT at 77 K.** Gaussian fits for the **a** $Y_1 \rightarrow Z_1$, **b** $Y_1 \rightarrow Z_2$, and **c** $Y_1 \rightarrow Z_3$ transitions. Fits (black solid line) shown on top of data (dark blue circle). Corresponding residual from fits shown to the right of each plot

transition (Fig. B.12 g).

B.6 Additional Peaks in Er^{3+}-doped PTO on GSO and NSO

Peak fits for additional peaks in Er^{3+}-doped PTO samples on GSO (Fig. B.13) and NSO (Fig. B.14) excited at 6500 cm^{-1} at 77 K. Peaks were fit to a Gaussian curve with a linear background. Residual of fits provided next to each peak fit to show the goodness of fits. Fit results are reported in Table 6.1.

Additional comparisons of PL of Er^{3+}-doped PTO samples and their respective substrates at resonant excitation frequencies to the additional peaks. In Figure B.15a, Er^{3+}-doped PTO on GSO (light blue) and GSO substrate (black) are excited at 6533 cm^{-1} (dashed line). At this excitation frequency, a different spectra is observed than at 6500 cm^{-1}. The peaks at this excitation frequency are present for both sample and substrate. Since Gd^{3+} does not have any transitions in this spectral range,[42] we believe these peaks are due to Er^{3+} impurities within the GSO substrate. On the other hand, in Figure B.15b, when Er^{3+}-doped PTO on NSO (dark blue) is excited at 6456 cm^{-1} (dashed line), peaks at 6456 cm^{-1}, 6486 cm^{-1} and 6500 cm^{-1} are observed. These peaks are also present at the 6500 cm^{-1} excitation. Additionally, no peaks are observed when the NSO substrate (black) is excited at 6456 cm^{-1} except for some counts at that frequency due to residual laser scattering. Lastly, in Figure B.15c, Er^{3+}-doped PTO on GSO (light blue) and GSO substrate (black) are excited at 6456 cm^{-1} (dashed line). Besides for the peak resonant to the excitation frequency, a peak at 6533 cm^{-1} is also observed for both the sample and substrate. The PL of the Er^{3+} impurities in GSO are much brighter than the Er^{3+} in PTO at this excitation frequency. Hence, we cannot differentiate if the source of those additional peaks are the Er^{3+} dopants in PTO sample or the Er^{3+} impurities in the GSO substrate.

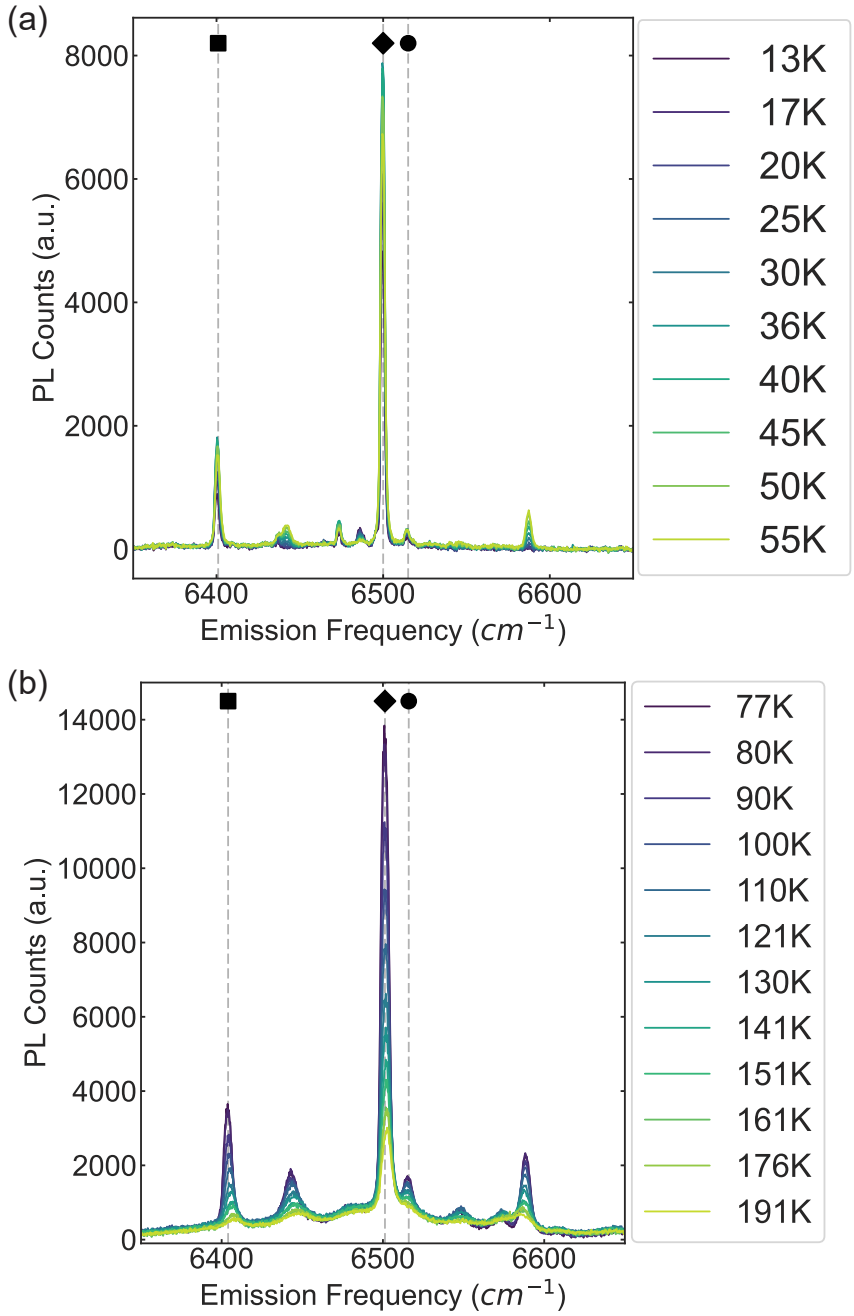

Figure B.10: **Temperature Dependent Photoluminescence.** PL for Er^{3+}-doped PTO on STO between **a**liquid He and liquid N_2 temperatures and between **b**liquid N_2 and room-temperature.

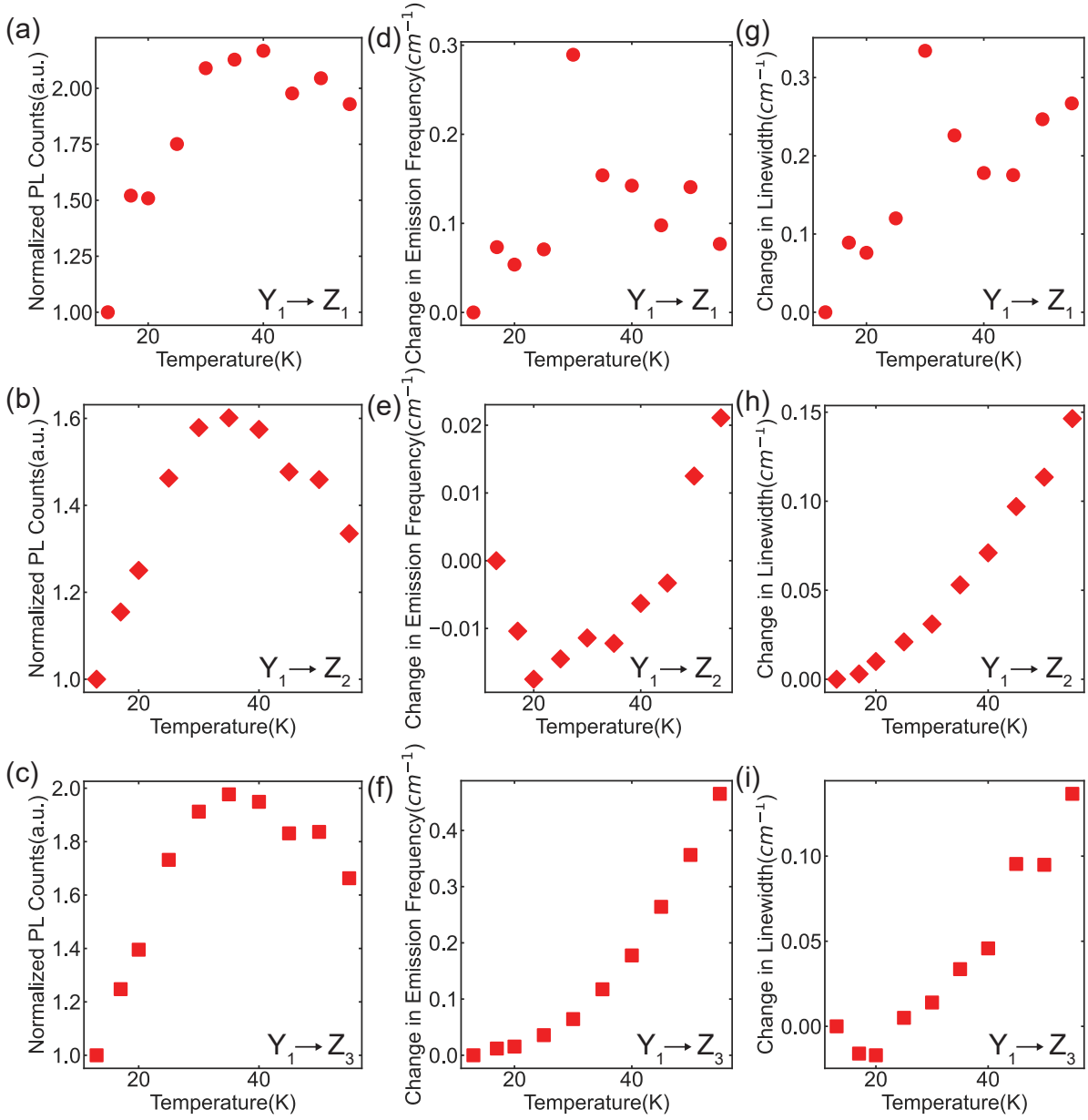

Figure B.11: **Fit Results from Temperature Dependent Data at Liquid He Temperature Regime.** Change in **a-c** PL counts, **d-f** emission frequency and **g-i** peak linewidth for the $Y_1 \rightarrow Z_1$, $Y_1 \rightarrow Z_2$, and $Y_1 \rightarrow Z_3$ transitions respectfully at different temperatures. PL counts were normalized with respect to each peak at 13 K. Change in emission frequency and linewidth were also determined with respect to each peak at 13 K.

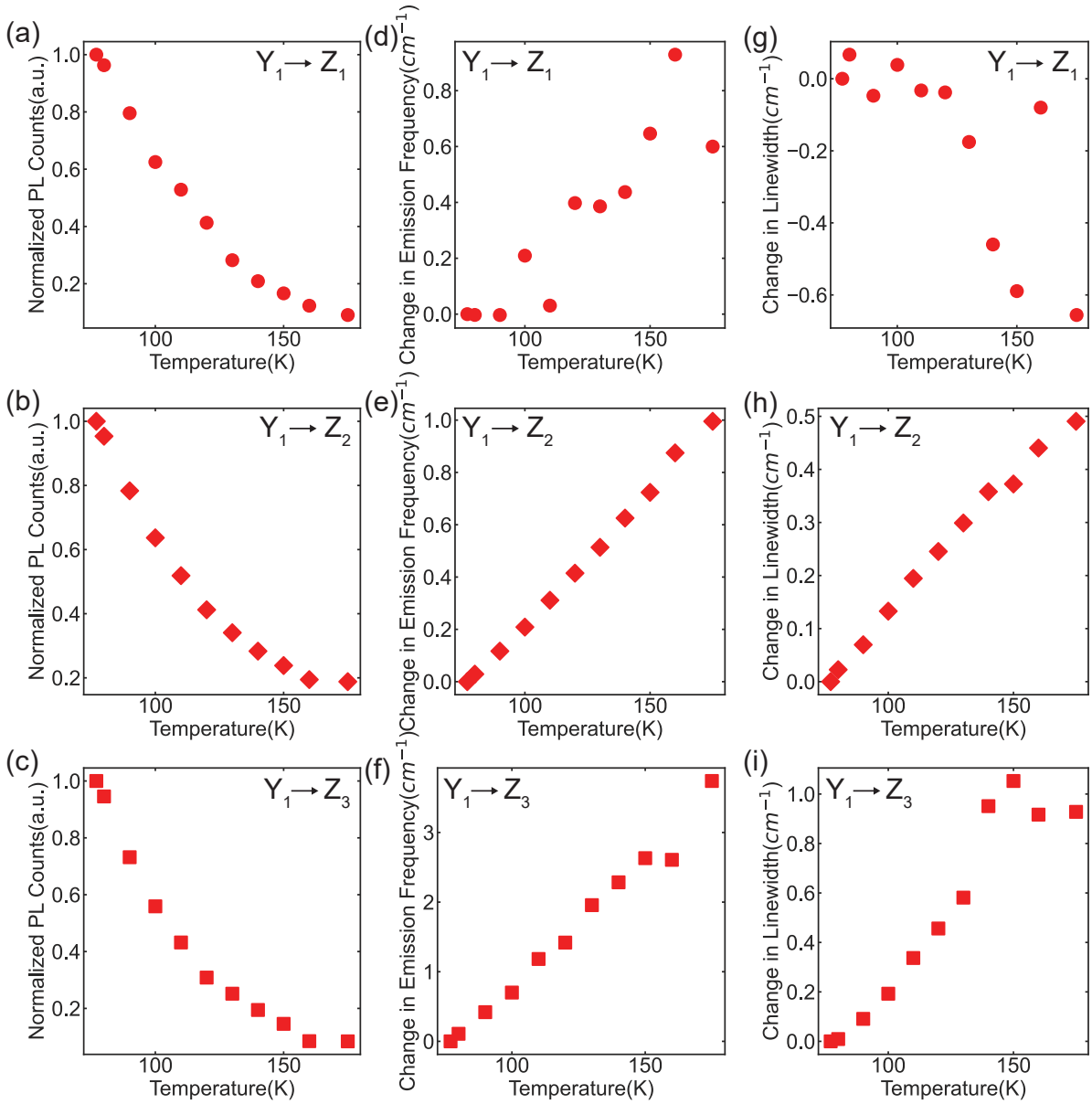

Figure B.12: **Fit Results from Temperature Dependent Data at Liquid N_2 Temperature Regime.** Change in **a-c** PL counts, **d-f** emission frequency and **g-i** peak linewidth for the $Y_1 \rightarrow Z_1$, $Y_1 \rightarrow Z_2$, and $Y_1 \rightarrow Z_3$ transitions respectfully at different temperatures. PL counts were normalized with respect to each peak at 77 K. Change in emission frequency and linewidth were also determined with respect to each peak at 77 K.

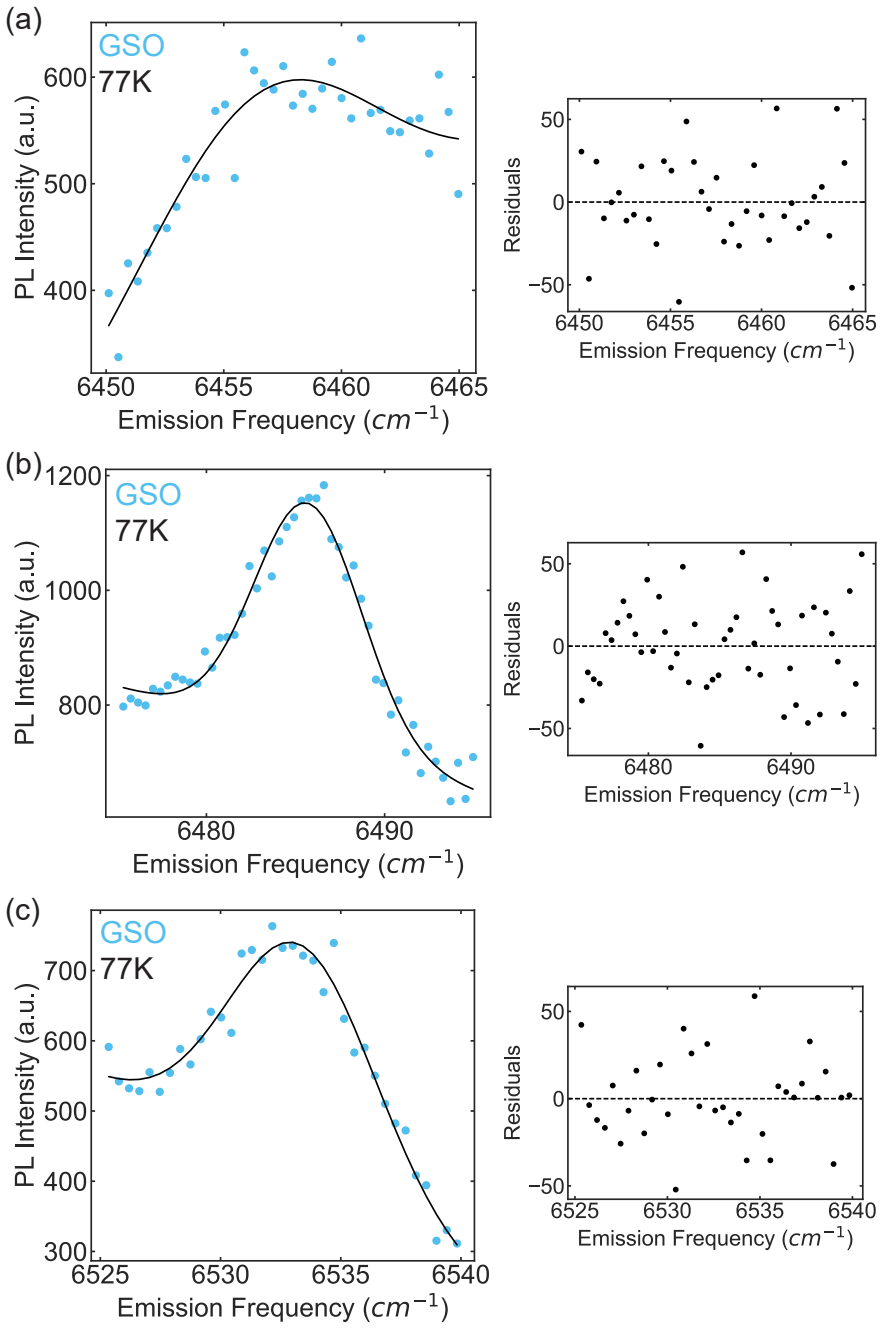

Figure B.13: **Fits for Additional Peaks in Er^{3+}-doped PTO on GSO at 77 K.** Gaussian fits for additional peaks at **a** 6456 cm^{-1}, **b** 6485 cm^{-1}, and **c** 6533 cm^{-1}. Fits (black solid line) shown on top of data (light blue circle). Corresponding residual from fits shown to the right of each plot.

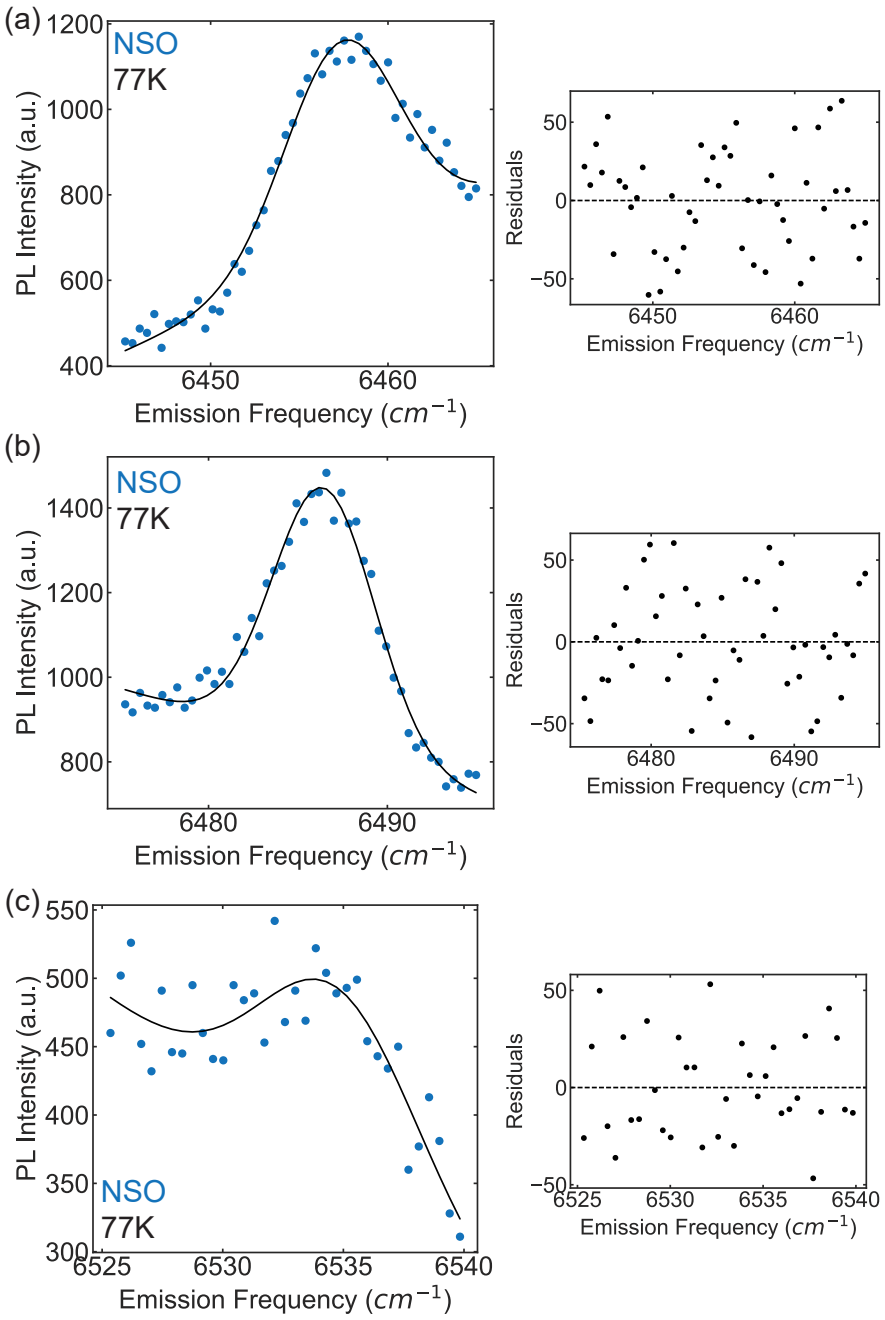

Figure B.14: **Fits for Additional Peaks in Er^{3+}-doped PTO on NSO at 77 K.** Gaussian fits for additional peaks at **a** 6457 cm^{-1}, **b** 6486 cm^{-1}, and **c** 6535 cm^{-1}. Fits (black solid line) shown on top of data (dark blue circle). Corresponding residual from fits shown to the right of each plot.

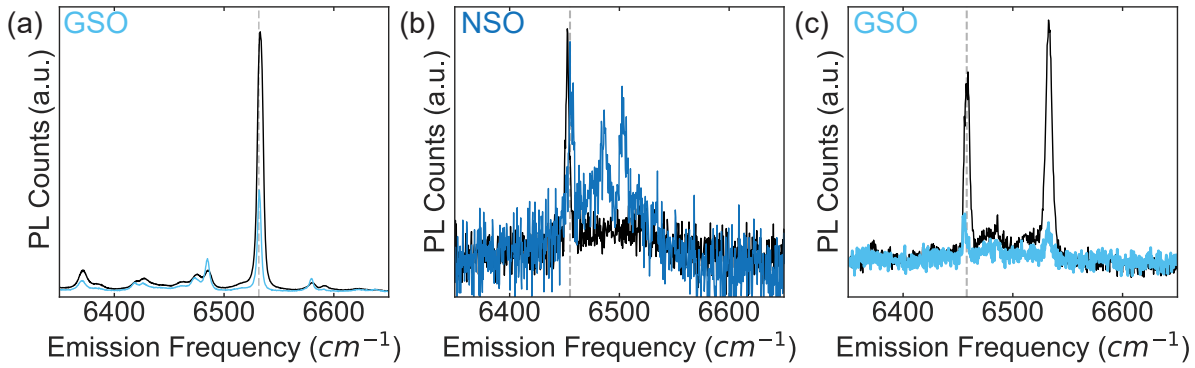

Figure B.15: **Comparison of PL of Er^{3+}-doped PTO and Substrates at Different Resonant Frequencies. a** PL of Er^{3+}-doped PTO on GSO (light blue) and GSO substrate (black) excited at 6533 cm^{-1}, **b** PL of Er^{3+}-doped PTO on NSO (dark blue) and NSO substrate (black) excited at 6456 cm^{-1}, and **c** PL of Er^{3+}-doped PTO on GSO (light blue) and GSO substrate (black) excited at 6456 cm^{-1}. All measurements were done at 77 K. Dashed line corresponds to excitation frequency.